RICE UNIVERSITY

Neutral Strange Particle Spectra with Direct Daughter Particle Identification in 11.6A GeV/c Au+Au Collisions

by

Kristofer K. Kainz

A Thesis Submitted
in Partial Fulfillment of the
Requirements for the Degree

DOCTOR OF PHILOSOPHY

Approved, Thesis Committee:

Dr. William J. Llope,
Senior Faculty Fellow, Chair
Department of Physics and Astronomy

Dr. Billy E. Bonner, Professor
Department of Physics and Astronomy

Dr. Richard A. Wolf, Professor
Department of Physics and Astronomy

Houston, Texas

September, 2001

ABSTRACT

Neutral Strange Particle Spectra with Direct Daughter Particle Identification in 11.6A GeV/c Au+Au Collisions

by

Kristofer K. Kainz

The BNL-AGS Experiment 896 intended to measure neutral strange particles, including the Λ hyperon and K_s meson, by recognizing and reconstructing their charged decay daughters. As designed, E896 had no means of directly identifying the species of these daughters, which is a powerful tool for the rejection of certain background processes that can mimic the signatures of such decays. A Time-Of-Flight (TOF) detector system was thus added to this experiment to provide a means for direct particle identification of the charged decay products. The detectors were constructed and installed in the E896 apparatus, and experimental data was collected with these new detectors during several runs of the experiment both with single hadron beams and central collisions of gold nuclei at a beam momentum of 11.6 GeV/c/N. Software was written to calibrate the raw TOF detector information, to make the crucial association of tracks in the experiment to hits in the TOF system, and to optimize the

timing performance and particle identification capabilities. This software was then used to form samples of reconstructed neutral strange particles under the more stringent criteria possible with the addition of the TOF information to the E896 data. The transverse mass distributions of Λ hyperons and K_s mesons from central 11.6 GeV/c/N Au+Au collisions, obtained from the analyses including direct daughter particle identification, will be presented and compared with other experiments and a theoretical model.

Acknowledgments

The tasks of designing, building, repairing, and commissioning the TOF detector in E896, and analyzing the data recorded by it, would be nearly impossible for one student to handle alone. I have been fortunate to have received much assistance in nearly every aspect of this project.

I am most grateful to William J. Llope, my research advisor at Rice, for granting me the opportunity to participate in the E896 experiment and for expressing confidence in my performance within it. The success of the E896 TOF project is due, in a very large part, to his guidance and assistance throughout all of its stages: design, construction, commissioning, and data analysis. Most every prediction he has made regarding the capabilities of the TOF detector and analysis has come true, which I have always found impressive. Hopefully my own efforts played a role in that.

Much thanks go to Professor Billy E. Bonner, the Director of Rice University's Bonner Lab, and Pamuela Reynolds, the Bonner Lab Administrator. They have generously provided my monetary support for my research and the presentations of my work at numerous collaboration meetings and conferences. Many thanks also go to Rose Berridge and Bridgitt Ayers, for their help on countless administrative matters within the Physics and Astronomy Department. I am also grateful to Prof. Bonner and Professor Richard A. Wolf for their gracious review of this Thesis.

Many thanks also go to the spokespersons of the E896 Collaboration, Hank Crawford and Tim Hallman, for consistently supporting my effort, and for facilitating our interactions with the other collaborators within E896. The helpful comments I have received from E896's collaborators have guided the direction of this analysis.

I have also received much assistance from the Collaboration in commissioning the TOF detector hardware; several people in particular stand out. Christopher Stokely had devoted a substantial amount of effort into refurbishing the TOF detector hardware. John Mitchell's vast technical expertise was essential in the design, construction, and refurbishing of nearly every detector in E896, especially TOF and the ECD, as well as the triggering and data acquisition systems. Salvo Costa and Jo Schambach had provided much-needed assistance in troubleshooting the TOF Fastbus DAQ hardware and calibration. Al Casper at BNL had uncovered and solved some serious problems with the TOF high voltage system. Without the kind assistance of the above, the entire E896 TOF project could not have been brought to completion.

I am also grateful to those who provided assistance throughout the TOF data analysis. Sean Kelly had developed the track reconstruction software package upon which the TOF extrapolation and calibration code is superimposed; and had performed the initial filtering, which provided a sample of neutral particle decay candidates to which the TOF data was applied. He has given much-needed assistance and advice on these and countless other software matters.

Both Bill Llope and Frank Geurts have done much work to procure and configure the Mammoth tape drive and Cheetah SCSI drive onto the Linux machines at Bonner Lab, thus dramatically hastening the progress of my data analysis. They have also devoted much time to porting the StAF analysis software onto Linux, and to resolving countless platform-related compilation problems. Many thanks go to their efforts for enabling me to keep jobs running on all of the Pentium II processors.

Contents

Abstract ii

Acknowledgments iv

List of Figures xi

List of Tables xxvii

1 Introduction 1

2 The Experiment 896 9

2.1 Overview of E896 10

2.1.1 Goals of the Experiment 10

2.1.2 Basic Features of the E896 Experiment 12

2.2 E896 Hardware 13

2.2.1 E896 Coordinate System 14

2.2.2 Beamline Elements 15

2.2.3 Trigger Elements and Trigger Definition 17

2.2.4 Forward Detectors 27

2.2.5 Silicon Drift Detector Array 31

2.3 Particle Identification in E896 31

2.3.1 Particle Identification without TOF 32

2.3.2 PID through Separation of Time versus Momentum 36
2.3.3 Quantities Measured from a Slat-based TOF System 37
2.3.4 Pertinent Quantities for TOF PID 41
2.3.5 Method of TOF PID in E896 41
2.4 E896 Time-Of-flight Detector Hardware 42
2.4.1 Overview of the TOF Detector System 42
2.4.2 Time-Of-Flight Central Wall 44
2.4.3 Time-Of-Flight Side Walls 49
2.4.4 TOF PMT High-Voltage System 54
2.4.5 TOF Electronics 55
2.5 Data Acquired from E896 and TOF 59
2.5.1 April 1998 Gold Ion Beam Run 59
2.5.2 September 1998 Single Hadron Beam Run 62

3 TOF Analysis Software: Extrapolation and Calibration 64

3.1 Association of DDC Tracks to TOF Slats 65
3.1.1 Track Extrapolation from DDC to TOF 65
3.1.2 Track-to-slat Matching and Track Path-length Calculations . . 72
3.1.3 Flight Time Calculations 84
3.1.4 Summary of Track-to-slat Association 87
3.2 TOF Signal Calibration 89

3.2.1 ADC Pedestal Correction 89
3.2.2 TDC Gain Correction 97
3.2.3 TDC Slew Corrections 99
3.2.4 TDC Run-dependent Offset Corrections 111
3.2.5 TDC Constant Offset Corrections 114
3.2.6 TOF Time Measurement Resolution 119
3.2.7 Summary of TOF Signal Calibration 123

4 Corrections and Physics Results **125**

4.1 Reduction of V_0 Candidate Set 126
4.1.1 Run and Event Cuts to V_0 Candidates 127
4.1.2 Geometric and Kinematic Cuts to V_0 Candidates 129
4.1.3 Time-Of-Flight Cuts to V_0 Candidates 145
4.1.4 Measured Λ Hyperon Yields and Spectra 151
4.1.5 K_s Meson Observables 158
4.2 Acceptance Corrections 161
4.2.1 Geometric Acceptance 162
4.2.2 Reconstruction Efficiency 163
4.2.3 Correction Factor Results 168
4.3 Results, Comparisons, and Discussion 172
4.3.1 Transverse Mass Distributions 175

4.3.2 Slope Parameter Dependence upon Rapidity 183

4.3.3 Production Magnitudes for Λ Hyperons and K_s Mesons 196

4.3.4 Λ Hyperon and K_s Meson Proper Lifetimes 204

5 Summary and Conclusions **217**

References **221**

List of Figures

2.1 Schematic of the top view of a hypothetical $H_0 \rightarrow \Sigma^-$ p $\rightarrow \pi^-$ n p decay occurring in a magnetic field. 11

2.2 The E896 apparatus viewed from above. The line which spans the figure corresponds to the path of the non-interacting beam. Not shown in this figure are the upstream detector elements (the Beam Counters, Beam Vertex Detector, and Veto Counter) and the Multiplicity Telescope (located just upstream of the collimator). 14

2.3 A drawing of the Exit Charge Detector, showing the key components. 20

2.4 A schematic of the ECD outputs and their contribution to the E896 trigger. 24

2.5 The Armenteros variables $p_\perp$ versus α as defined by Equation 2.7 for V_0 candidates reconstructed from E896 central events. 35

2.6 The inverse velocity versus momentum for primary pions, kaons, and protons in the E896 TOF geometry simulated in GEANT. This plot was obtained from Reference [18]. 38

2.7 The flight time versus the particle momentum for TOF-incident secondary pions and protons from RQMD $b < 4$ fm events propagated through the E896 geometry in GEANT. 39

2.8 A photograph of the E896 TOF detector system, looking approximately downstream and from below. 43

2.9 Top view of a portion of the Bakelite structure designed by E877 to hold the Central Wall slats. This drawing was taken from [5]. 47

2.10 A diagram of the ADC and TDC electronics of the E896 TOF system. Only signal cables from one PMT are shown. The other PMT has similar cabling. 60

3.1 The software tasks performed on the data from E896 Au98 events that were earlier found to contain at least one V_0 candidate. 66

3.2 The extrapolator accuracy versus the TOF hole number for the actual slat hit, for p98 events, with the DDC wire map used before the error was uncovered. 70

3.3 The extrapolator accuracy versus the TOF hole number for the actual slat hit, for p98 events. 72

3.4 The extrapolator accuracy distribution for p98 track-to-slat matches upon the central TOF array. 73

3.5 The y coordinate given by the extrapolator code versus the difference between the bottom and top raw TDC values, for Au98 tracks matched to a sample slat. 75

3.6 A scenario in which the actual TOF slat hit by a particle, according to vertical coordinate comparisons, is not the same as the slat intercepted by the particle's DDC track extrapolated to TOF. 77

3.7 The difference between the extrapolator y and the TOF y coordinate (converted to units of distance), for matches to a sample TOF slat from Au98 events. 79

3.8 The correctness-of-match efficiency versus TOF hole number is plotted in the left frame. The right frame shows the number of tracked particles per slat. 80

3.9 The signal-to-background ratio versus the TOF hole number, without any track quality cuts applied to the tracks matched to TOF slats. . . 81

3.10 The upper frames plot the difference between the calculated path length and the path length given by GEANT, for the positive daughters of fiducial Monte Carlo Λ hyperons. The lower frames show the differences in the corresponding flight times. 83

3.11 The upper drawing illustrates a situation in which the extrapolator estimate and the actual TOF slat hit are not equal. The method to correct for this is shown in the lower drawing. 84

3.12 The same distributions in Figure 3.10, after the momentum vector rotation and path length recalculation. 85

3.13 The V_0 candidate topology and a listing of the pertinent quantities for the flight time calculation of each leg of the topology. 86

3.14 Comparisons of path length and flight time differences between the track extrapolation code and GEANT, for the decay daughters of simulated neutral particles. 88

3.15 The phase of the ramp generator output (the "sawtooth" profile on the bottom) with respect to the 60 Hz AC waveform (top profile). 90

3.16 A distribution of ADC measurements taken from the ramp generator output, from 100k Au98 central events. 92

3.17 The dependence of the TOF PMT pedestal value upon the ramp ADC, for four sample TOF PMTs. 93

3.18 An example of a "profile histogram" used to correct for the pedestal effects in the TOF PMT ADC distributions. 95

3.19 The pedestal distributions for the top PMT of TOF hole number 67, without any event-by-event correction (dotted line), and after the ramp ADC correction (solid line). 96

3.20 A diagram of the electronics used in the Time Calibrator data acquisition. 98

3.21 The top frame shows the TDC distribution of time-calibrator stop pulses. A Gaussian fit is applied to one of these pulses (the fourth from the right) The bottom frame is a plot of the centroid of each stop-pulse peak in the top plot, versus the time (in ps) after the start pulse. 100

3.22 The "time walk" or "slewing" effect. 101

3.23 TDC versus ADC for an individual TOF PMT (left frame), and ⟨TDC⟩ versus ⟨ADC⟩ for the same slat (right frame). 104

3.24 The slat average time versus ⟨ADC⟩ distributions to which the slew function is fitted. The left-hand frame is a scatter plot; the right-hand frame is a two-dimensional histogram filled with the hits in the left-hand frame. The fit of the slew function is also plotted in the second frame; the parameters are $t_0 = 44288 \pm 152$, $C = 26585 \pm 3973$. . . . 105

3.25 The top two frames show the slat average time versus ⟨ADC⟩ distributions before and after the slew correction for a single TOF slat. The fit parameters for this TOF hole were found to be $t_0 = 32030$ ps and $C = 28308$ ps$/\sqrt{ADC\ channel}$. The bottom two frames are the projections of the top two frames onto the vertical axis. 107

3.26 The variance in the slat average TDC value, ⟨TDC⟩, versus the hole number before and after the slew correction (top frame), and the ratio of these (bottom frame). 109

3.27 The sigma of the slat average time (⟨time⟩) distributions for 50 channel-wide gates in the ⟨ADC⟩ values, for four sample TOF slats as labeled on the horizontal axes. 110

3.28 The mean slat average time (⟨time⟩) value versus the run number, for four sample slats. 112

3.29 The spread in the peak slat average time (⟨time⟩) value for each slat, over five Au98 runs that were recorded over a period of six days. . . . 113

3.30 A diagram illustrating the method used to determine the constant timing offset for each TOF slat. 116

3.31 The left frame shows the slat average time versus momentum distribution from Au98 data for a single slat. The right-hand frame shows the same distribution for RQMD protons. 117

3.32 The left-hand frame shows the measured slat average time, with the predicted GEANT flight time versus momentum subtracted, versus the momentum. The right-hand frame is a projection of the data in the left-hand frame onto the vertical axis. 118

3.33 Measured flight time (after all ADC and TDC corrections were made) minus calculated flight time, for $\Lambda \rightarrow$ p candidates in the data set. . . 120

3.34 The solid circles in the above frame indicate the widths of the $TOFmeas-TOFcalc$ distribution for $\Lambda \rightarrow$ p candidates incident upon each TOF slat as labeled on the horizontal axis. The resolution in TOF_{calc} is indicated by the down triangles. If a 120 ps start/stop ($TOFmeas$) resolution is added in quadrature to $\sigma_{TOFcalc}$ (open circles), the result agrees well with the resolution of $TOFmeas-TOFcalc$ extracted from the experimental data. 121

4.1 The cuts applied to the Pass II V_0 candidates (with calibrated TOF detector information associated with the daughters) to reduce the data to a clean set of Λ hyperons or K_s mesons. Asterisks (*) denote the specific cuts that were revised to favor K_s mesons instead of Λ hyperons. 128

4.2 The ramp ADC distribution from a run during which the maximum sawtooth value was set too high, causing the overflow seen on the right hand side of the distribution. 130

4.3 The distribution of x locations of V_0 candidates extrapolated back to the target (left frame), and the target y distribution (right frame). The dotted lines denote the boundaries of the target cuts used in this analysis. 132

4.4 The vertex residual distribution in x (left frame), and the vertex residual in y (right frame). The units are in centimeters. The dotted lines denote the boundaries of the vertex residual cuts. 134

4.5 Schematic of a neutral particle decaying upstream of the DDC. The vertical line denotes the DDC upstream face. The magnetic fields are weaker on the left-hand side of that line. The dotted lines denote the actual paths of the daughter particles. The solid lines to the left of the DDC upstream face denote the apparent daughter trajectories (extrapolated from the "solid line" tracks deposited in the DDC) if the magnetic fields inside and outside the DDC were taken to be the same. 136

4.6 Calculated Λ hyperon mass versus vertex z for reconstructed Monte Carlo Λ hyperons with helix extrapolation upstream (left frame) and with Runge-Kutta extrapolation upstream (right frame). The vertical dotted line denotes the upstream face of the DDC. 138

4.7 The number of hit DDC wires associated with the negative daughter track of the V_0 candidate versus the number of hit wires assigned to the positive daughter, for digitized GEANT K_s mesons. The dotted lines denote the boundaries of the wire hit correlation cut. 140

4.8 The transverse momentum versus rapidity for Λ hyperon candidates, from $\sim$ 11 million central events, that survive all geometric and kinematic cuts except the phase space cut. The dotted line depicts the boundary of this phase space cut. 143

4.9 The Λ hyperon invariant mass distributions before (left frame) and after (right frame) the various geometric and kinematic cuts. For details about these cuts, refer to the text earlier in this subsection. 144

4.10 The TOF hole hit distribution of $\Lambda \rightarrow$ p candidates (which survive the geometric and kinematic cuts) extrapolated to TOF. The dotted lines denote the boundaries of the TOF Central Wall. 147

4.11 The distribution of $y_{tracking} - y_{TOF}$ for $\Lambda \rightarrow$ p candidates matched to TOF Central Wall slats. 149

4.12 The measured flight time versus momentum for the positive daughter track of Λ hyperon candidates that are successfully matched to TOF Central Wall slats. 150

4.13 The Λ hyperon invariant mass distributions for $\Lambda \rightarrow$ p candidates matched to TOF slats, before (upper left frame) and after (upper right frame) applying the TOF "p-band" cut. The lower left frame shows the invariant mass distribution for $\Lambda \rightarrow$ p candidates rejected by the TOF PID cut. 153

4.14 The (y, p_T) distributions for $\Lambda \rightarrow$ p candidates matched to TOF slats, before (left frame) and after (right frame) applying the TOF "p-band" cut. 154

4.15 The (y, p_T) distribution for $\Lambda \rightarrow$ p candidates that reside in the "not-p-band" region. 155

4.16 The K_s meson invariant mass distribution for V_0 candidates within the "not-p-band" region of Figure 4.12. 156

4.17 The left frame is an Armenteros plot of the Λ hyperon candidates before applying any TOF PID cuts. The right frame is the plot for hits in the "not-p-band" region of the time-vs.-momentum plot. The square on each frame defines the Armenteros region used to estimate the probability of a "true" $\Lambda \rightarrow$ p being matched to a TOF slat that gives a "not-p-band" measurement. 157

4.18 The K_s meson invariant mass distribution of those V_0 candidates which survive the geometric, kinematic, and TOF-related cuts that were optimized to purify the K_s meson sample. 159

4.19 The (y, p_T) distribution of those V_0 candidates which survive the geometric, kinematic, and TOF-related cuts optimized to purify the K_s meson sample. 160

4.20 An example of the invariant mass distribution compiled from Monte Carlo V_0 candidates reconstructed within a particular (y, p_T) bin in the acceptance calculations. 169

4.21 The Λ hyperon correction factors obtained in this analysis without TOF cuts (solid lines), compared with those obtained in the earlier DDC Λ hyperon analysis [14] (dotted lines). 170

4.22 Comparison of the Λ hyperon correction factors including TOF cuts and corrections (crosses) with those obtained without the TOF cuts (solid circles). 171

4.23 The correction factors (TOF cuts and corrections included) for Λ hyperons and K_s mesons in the regions of (y, p_T) where the DDC+TOF acceptances overlap. 173

4.24 The rapidity distribution for V_0 candidates reconstructed from Monte Carlo Λ hyperons generated within a particular (y, p_T) bin. The dotted lines define the rapidity range within which the Monte Carlo Λ hyperons were originally generated. 174

4.25 The differential yield versus transverse mass for corrected Λ hyperons in E896, without TOF cuts. The markers represent the data from this analysis; the solid lines denote the Boltzmann fit results. The dotted lines represent the fits to the produced Λ hyperon distribution from the analysis described in Reference [14]. 179

4.26 The Λ hyperon differential yields versus transverse mass for produced Λ hyperons in this analysis, with TOF cuts (markers and solid lines) and without TOF cuts (dotted lines). 180

4.27 Λ hyperon differential yield versus transverse mass. The markers and solid lines represent corrected Λ hyperon spectra obtained using TOF cuts and corrections. The dotted lines are the fits to the Λ hyperon spectra from RQMD, $b < 4$ fm. 181

4.28 A comparison of the K_s meson transverse mass spectra obtained from this analysis with TOF cuts included (markers and solid lines), and from RQMD (dotted lines). 182

4.29 Transverse mass spectra for Λ hyperons, TOF cuts included, for four different rapidity bins. For each rapidity bin, the fit is performed over the m_T range covered by the DDC+TOF detector acceptance. 184

4.30 Transverse mass spectra for Λ hyperons from RQMD, $b < 4$ fm, for four different rapidity bins. Denoted at the bottom of each frame are the E896 TOF Λ hyperon temperatures measured for each rapidity bin. 186

4.31 The Λ hyperon inverse slope parameter versus rapidity, for the E896 TOF-cut data (circles), RQMD (squares), E891 [38] (up triangles), E877 [6] (down triangles and diamonds), and the E896 SDDA data [30] [35] (stars). 187

4.32 Results of the "fireball model" fit to the temperature-vs.-rapidity values for E896 TOF-cut Λ hyperons (left frame) and for RQMD Λ hyperons (right frame). 188

4.33 Results of the "fireball model" fit to E896 SDDA Λ hyperon data alone (left frame) and to the SDDA and TOF Λ hyperon data taken together (right frame). 189

4.34 The transverse mass plots and Boltzmann fits for K_s mesons obtained from the E896 TOF analysis. 191

4.35 The transverse mass plots and Boltzmann fits for K_s mesons obtained from RQMD, $b < 4$ fm. Denoted at the bottom of each frame are the E896 TOF K_s meson temperatures measured for each rapidity bin. . . 192

4.36 The K_s meson inverse slope parameter versus rapidity, for K_s mesons from the E896 TOF analysis (circles) and from RQMD $b < 4$ (squares). Also included are charged kaon temperatures from E866 [39] (up triangles for K^+, down triangles and diamonds for K^-) and K^+ meson temperatures reported by E877 [40] (stars). 193

4.37 The solid curves represent fits of the "fireball model" function to the temperature-vs.-rapidity plots for K_s mesons from the E896 TOF analysis (left frame) and for K_s mesons from RQMD (right frame). The dotted lines show the fits to the Λ hyperon values from Figure 4.32. . 194

4.38 Fits of the "fireball model" function to the temperature-vs.-rapidity plots for kaons when fitting only to the mid-rapidity charged kaons (left frame) and when including the E896 TOF K_ss in the fit as well (right frame). 195

4.39 The "intercept parameter" (the point on the $m_T - m_0 = 0$ axis crossed by the fitted Boltzmann curve) versus rapidity, for Λ hyperons from the E896 TOF analysis (circles) and from RQMD (squares). 197

4.40 The intercept parameter (scaled to conform to Equation 4.19) versus rapidity, for Λ hyperons from the E896 TOF analysis (circles) and from E891 [38] (up triangles). 199

4.41 The intercept parameter (scaled to conform to Equation 4.20) versus rapidity, for Λ hyperons from the E896 TOF analysis (circles) and from E877 [6] (down triangles and diamonds). The error bars for the E896 TOF intercepts are smaller than the marker size. 200

4.42 The integrated dN/dy values versus rapidity for Λ hyperons from the E896 TOF analysis, RQMD, E891, E877, and the E896 SDDA analysis. 202

4.43 The dN/dy values versus rapidity for SDDA and TOF Λ hyperons, along with a Gaussian fit applied to these data. 203

4.44 The intercept parameter versus rapidity for K_s mesons from the E896 TOF analysis (circles) and from RQMD (squares). 205

4.45 The integrated dN/dy values versus rapidity for K_s mesons from the E896 TOF analysis (circles) and from RQMD (squares). 206

4.46 Distribution of $d/\gamma\beta$ for K_s mesons from the present analysis, corrected for acceptance. The error bars represent the combined uncertainties of the data sample and the correction factors. 209

4.47 Acceptance-corrected distributions of $d/\gamma\beta$ for Λ hyperons in the present analysis, without TOF cuts (left frame) and with TOF cuts included (right frame). The solid lines denote exponential fits over the full $d/\gamma\beta$ range. The dotted line in the right frame denotes the fit over the range 20 cm $< d/\gamma\beta <$ 100 cm. 210

4.48 Uncorrected count rates for Λ hyperons versus the quantity $\gamma\beta$ (left frame) and decay length d (right frame). Solid lines denote count rates for all Λ hyperons in the sample. Dashed (dotted) lines represent Λ hyperons with $d/\gamma\beta$ greater than (less than) 15 cm. 212

4.49 Uncorrected count rates for Λ hyperons versus the x (upper left), y (upper right), and z (lower left) coordinates of the decay vertex. Solid lines denote count rates for all Λ hyperons in the sample. Dashed (dotted) lines represent Λ hyperons with $d/\gamma\beta$ greater than (less than) 15 cm. 213

4.50 Uncorrected count rates for Λ hyperons versus rapidity (left frame) and transverse momentum (right frame). Solid lines denote count rates for all Λ hyperons in the sample. Dashed (dotted) lines represent Λ hyperons with $d/\gamma\beta$ greater than (less than) 15 cm. 214

4.51 Acceptance-corrected distributions of $d/\gamma\beta$ for Λ hyperons, TOF cuts included, for rapidity less than 3.0 (left frame) and rapidity greater than 3.0 (right frame). The solid lines denote exponential fits. 215

List of Tables

3.1 The overview of the parameters relevant to extrapolation of DDC tracks to the TOF array. 71

3.2 The uncertainties assumed for the path length and momentum for the parent and daughter legs of the $\Lambda \rightarrow$ p candidates. 122

4.1 The percentages by which each individual geometric and kinematic cut reduces the peak and off-peak sections of the Λ hyperon invariant mass distribution from this work and from Reference [14] as labeled. 145

Chapter 1
Introduction

Experiment 896 [1] at the Brookhaven National Laboratory Alternating Gradient Synchrotron (BNL-AGS) was designed to detect neutral strange particles that originate from the nuclear matter produced in "violent" collisions of gold ions. Such particles would be identified by reconstructing them from the tracks left behind by their charged decay products. E896's primary goal was to detect the decay signature of the hypothesized [2] H_0 di-baryon in very violent head-on, or "central," collisions of $11.6A$ GeV/c/N ^{197}Au on a fixed ^{197}Au target. The detector geometry was optimized to detect the H_0 di-baryon if its lifetime ranges from $c\tau \sim 4$ cm to 100 cm. [1] Such a system is also sensitive to decay signatures from the Λ hyperon and K_s meson as well, since these neutral strange particles have similar lifetimes and also decay into charged particles that can be measured. Thus, another experimental goal of E896 is the measurement of the production of Λ hyperons and K_s mesons.

In reconstructing neutral strange particles, the original plan of the experiment was to apply mass assumptions to the tracked decay products of neutral particle candidates. However, there exist background processes, such as interactions of neutrons and photons with the particle tracking detector, that can resemble the decays of Λ hyperons, K_s mesons, or H_0 di-baryons. Were a means of direct particle identifica-

tion available for the decay products of these candidates, some of these background processes could be recognized and suppressed.

To provide this direct daughter particle identification and reduce background, an additional detector system, a Time-Of-Flight (TOF) scintillator array, was added to the E896 apparatus. This detector measures the flight time of charged particles. A particle's flight time, when combined with the particle momentum obtained from the curvature of the particle's associated track, can establish a direct identification of the mass of the particle.

Software was developed to extract flight time measurements from the TOF detector's raw response signals. The required software tasks are comprised of two broad categories: track extrapolation and TOF signal calibration.

In the track extrapolation stage, the daughter particle from the neutral decay must be associated with the TOF counter struck by that same particle. This task is complicated in that there exist no supplementary detectors to provide particle space points between E896's tracking detector and the TOF array, and that, despite the presence of five to ten particle tracks and twenty to forty TOF counter hits during an event, the daughter particle track must be uniquely matched to the "correct" TOF counter in a very complicated environment. The goal of the extrapolation software is to optimize the efficiency of the track-to-slat matching, despite these challenges.

The TOF signal calibration software converts the raw TOF detector output gen-

erated by a particle hit upon the counter into a flight time measurement of that particle relative to the start of the heavy ion event. Factors which distort these flight time measurements are the presence of "dirty AC" contamination in the detector electronics and output signal, the dependence of the time measurement upon the signal size, and the electronic offsets to the signal arrival time, both constant (due to cable-length differences among TOF signal channels) and time-dependent (due, for example, to slow temperature variations). The objective of the calibration software is to remove all of these signal distortions, and thus optimize the resolution of the flight time measurements.

Measured flight times were then associated with the daughter particles of Λ hyperon and K_s meson candidates that were reconstructed in approximately 11 million central collisions of a 11.6A GeV/c ^{197}Au beam upon a ^{197}Au target. Cuts were applied to the measured particle flight times, as well as to specific aspects of the decays of the reconstructed candidates, to yield samples of Λ hyperons and K_s mesons with certain backgrounds suppressed for the first time.

Production rates for strange particles are of interest, since strange matter does not exist within the beam or target ions prior to the collision. The production rates of strange particles are sensitive to the thermodynamic evolution of the hot, dense matter produced in heavy ion collisions. Also, if a deconfinement of quarks and gluons were to occur, the amount of strange matter produced in the collision should

increase. [1] Strange quarks are produced through mechanisms such as $g + g \rightarrow s + \overline{s}$, in addition to strange particle production through hadronic interactions such as π + nucleon $\rightarrow \Lambda$ + kaon.

The production of particles in heavy ion experiments is usually studied as a function of rapidity and transverse momentum (or transverse mass). The rapidity is defined as:

$$y = \frac{1}{2}\ln(\frac{E + p_L}{E - p_L}) \tag{1.1}$$

where E is the total energy of the particle, and p_L is the component of the particle momentum parallel to the beam momentum in the laboratory frame. In a heavy ion collision, one can identify three "sources" of particles. Depending on how "head-on," or central, the collision is, there are cold remnants of the target nuclei and projectile, and a hot, dense nuclear system formed where the projectile and target nuclei overlap (the "participant region"). The remnants of the beam and target nuclei and the hot collision zone emit particles, which are measured in the laboratory. The "target source" is at rest in the laboratory and emits particles with a laboratory rapidity distribution y_{lab} centered at zero. The "projectile source" moves with approximately the velocity of the incident beam. The particles it emits are strongly forward focused in angle due to the Lorentz boost between this source and the laboratory frames. For 11.6 GeV/c/nucleon ^{197}Au+^{197}Au collisions, the laboratory rapidity of the particle

source is $y_{lab} = 3.2$. As the projectile and target studied here are of equal mass, the hot collision zone moves in the laboratory with one half of the velocity of the incident projectile, and hence this source emits particles that are seen with rapidities centered at 1.6.

Particle measurements as a function of transverse momentum p_T, or transverse mass $m_T = \sqrt{p_T^2 + m_0^2}$, are of interest. A nonzero p_T value for a particle is related to a physical scattering in the collision, since the transverse momentum of the target ion and beam ion before the collision is zero. Also, the rate of decrease in the yield of measured particles with an increase in transverse momentum is typically assumed to be indicative of a "temperature" of the source at the time these particles are emitted. That is, the transverse momentum "spectra," *i.e.* dN/dp_T or $(1/m_T)(dN/dm_T)$, are commonly extracted experimental quantities, and the slopes of these distributions are often inverted and called "temperatures," in units of MeV (where $c = 1$).

Comparisons of measured and experimental acceptance corrected temperatures and production magnitudes for Λ hyperons and K_s mesons with those from other experiments will be made. In order to make direct comparisons of the present experimental results, it is necessary to apply certain corrections to the experimental spectra in order to account properly for effects such as detector geometry and software inefficiencies. These "acceptance corrections" required detailed simulations of the experiment. These simulations will be described in section 4.2.

Comparisons will also be made with the RQMD model [3] [4]. RQMD simulates the collision of nuclei from the moment they begin to overlap to the point when all of the strong interactions among the particles in the participant zone have subsided. RQMD is an example of a transport model. As such, it allows one to study how the various interactions within the participant matter affect the spectra of the particles produced during the collision, thus providing insight into the evolution of the matter in the beam-target overlap region.

RQMD presumes two stages in the evolution of the participant matter and the production of particles. In the first stage, the overlap of the beam and target nuclei excites the color string fields among the quarks within the participant nucleons. These strings fragment, producing more hadrons in the process. The second stage of RQMD features rescattering among the hadrons produced from string fragmentation and the participant nucleons. Interactions among the nucleons and hadrons are modeled at the quark level. The paths of the quarks from the ingoing hadrons are denoted, and "Glauber" type collisions are modeled. To determine the experimentally unknown cross sections such as $K + K$, an additive quark model is applied. For collisions involving unstable hadrons, the cross section for an unstable hadron is taken to be equal to the cross section for the stable hadron with the same quark content. For example, $\sigma_{\Delta+} \approx \sigma_p$. In the second stage of RQMD, particle production is achieved through energy loss in the inelastic collisions as well as through the decay of resonances. Most

of these interactions can be treated as two-particle collisions. Pauli blocking effects are also included where appropriate. These successive interactions (often referred to as a "cascade") continue until equilibrium, or "freeze-out," is achieved, at which point the produced hadrons propagate freely. The above prescription for RQMD operation is referred to as "cascade mode," as it assumes no other physical processes beyond those expected from a series of nucleon+nucleon interactions.

The RQMD predictions to be presented later in this Thesis were obtained with the RQMD software operated in cascade mode. Alternately, by setting a switch within the RQMD software, the model could simulate more exotic physics processes in the dense participant matter beyond the aforementioned string fragmentation and hadron collisions. One such process features, in the initial string formation and fragmentation stage, the fusion of overlapping independent color string fields into chromoelectric flux tubes, or "ropes." Another process, which can be applied at the hadronic scattering stage of RQMD, assigns an effective mass to an ingoing baryon in close proximity to other baryons. This simulates the effect of a "mean field," which sets up a force to which the ingoing hadrons are subject.

Comparisons with the RQMD model have been made in several prior studies of AGS data [5] [6]. The goal of this analysis is to search for deviations of the RQMD predictions from our data. Should the data and RQMD agree, observations can be made regarding the appropriateness of the mechanisms incorporated into the RQMD

model to simulate central Au+Au collisions.

The E896 experimental goals, method, and apparatus, and the TOF particle identification method and hardware, are described in Chapter 2. The extrapolation and calibration software is presented in Chapter 3. In Chapter 4, temperatures are extracted for Λ hyperons and K_s mesons including TOF particle identification (PID). The temperature and rate measurements are compared with those from other AGS experiments and from the RQMD v2.4 model operated in "cascade mode." Chapter 5 presents the conclusions.

Chapter 2
The Experiment 896

This chapter describes the goals and methods of the BNL-AGS Experiment 896 (E896), along with the hardware elements designed and implemented to meet them. These hardware elements include those which define and determine the beam trajectory, those that establish the central event trigger, and those that provide trajectories for charged decay products from neutral particles produced in the central Au+Au collisions. Missing from the original E896 proposal was the hardware required for direct particle identification of charged daughters from neutral particle decays. This motivated the implementation of a Time-Of-Flight (TOF) detector. The particle identification techniques in E896, without and with the inclusion of TOF measurements, will be described. Also presented will be the principles of particle identification using a slat-based TOF system, both in general and specific to E896. A description of the E896 TOF hardware will be given next. The hardware components of the TOF system will then be described. This chapter closes with a description of the data sets acquired by E896 during 1998 using gold ion beams and single hadron beams. Also described are the problems encountered with the TOF hardware during data acquisition, and the measures taken to solve them.

2.1 Overview of E896

2.1.1 Goals of the Experiment

E896 was proposed [1] to study the production of strange matter in the collisions of ∼11 GeV/c/N ^{197}Au+^{197}Au ions. The primary experimental goal of E896 was to unambiguously identify a hypothesized six-quark di-baryon (with the quark composition *uuddss*) called the H_0 [2], by reconstructing it from its tracked decay products. The design and placement of the elements of the E896 apparatus, to be described in detail in section 2.2, were optimized for the detection of the H_0 di-baryon via the decay channel $H_0 \rightarrow \Sigma^-$ p $\rightarrow \pi^-$ n p, which is schematically illustrated in Figure 2.1. The H_0 passes through a magnetic field, where it is expected to decay with a 30 percent probability into a Σ^- baryon and a proton. The Σ^- baryon decays with known properties into a neutron and negative pion. The magnetic field induces the curvatures of the charged particles in the decay. A distinguishing feature of this signature is the kink present in the negative track that emerges from the $\Sigma^- \rightarrow \pi^-$ n decay.

This optimization for an H_0 di-baryon acceptance also enables E896 to detect other weakly-decaying strange neutral particles, such as the Λ hyperon and K_s meson. These particles have lifetimes of the order of the predicted H_0 di-baryon lifetime. They also have high branching ratios for charged-particle decay, enabling the production of curved tracks from which the daughter momenta can be measured and the parent

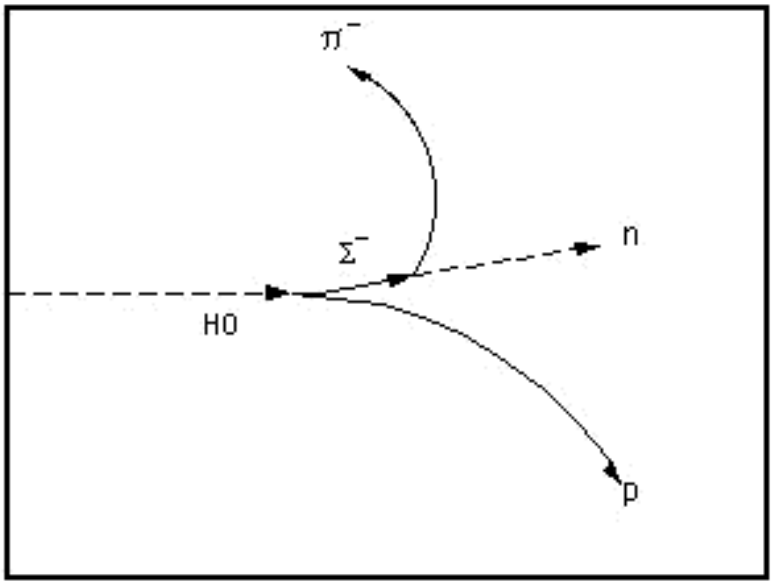

Figure 2.1 Schematic of the top view of a hypothetical $H_0 \rightarrow \Sigma^-$ p $\rightarrow \pi^-$ n p decay occurring in a magnetic field.

particle reconstructed. Thus, an additional experimental goal of E896 is to measure the spectra of Λ hyperons and K_s mesons over a broad range of rapidity and transverse momentum in the E896 acceptance.

2.1.2 Basic Features of the E896 Experiment

The heavy ion interactions studied by E896 take the form of 11.6 GeV/c/nucleon fully-ionized gold ions incident upon a fixed gold target. Such heavy ion interactions yield high rates of production for Λ hyperons. [7] Higher rates of Λ hyperon production per event would imply conditions favorable for the formation of the H_0 di-baryon, as the Λ hyperon has the quark content uds, while the H_0 di-baryon is comprised of the quarks $uuddss$.

As originally proposed, E896 is sensitive to a wide range of H_0 di-baryon masses and lifetimes (from $c\tau \sim 4$ cm to $c\tau \sim 100$ cm). E896 attempts to reduce the charged-particle backgrounds in the environment within which the H_0 di-baryon and other neutral strange particles are reconstructed by using strong magnetic fields. It can handle high beam rates, allowing for a beam luminosity several times greater than the predicted H_0 di-baryon cross section. The experiment is also sensitive to several of the predicted H_0 di-baryon decay channels, not just Σ^- + p, but also Λ + p + π^-, and Λ + n. Finally, E896 also provides a specific consistency check of the $H_0 \rightarrow \Sigma^-$ p decay topology by attempting to detect the neutron from the $\Sigma^- \rightarrow$ n π^- channel.

Though the above capabilities make E896 a potentially definitive H_0 di-baryon search experiment, the ability to confirm the identities of one or more of the charged decay products of the H_0 di-baryon would make such a verification, and other E896 analyses, even more conclusive. The identities of the decay products of the Λ hyperon and K_s meson can also be confirmed, yielding a purer sample of these particles. This motivates an additional detector for E896 that can provide a direct determination of the mass of the decay products of Λ hyperon, K_s meson, and H_0 di-baryon candidates, rather than require mass assumptions for these decay daughters. Such a determination can be made by providing a particle flight time measurement to complement the momentum and position measurement of a neutral parent's decay products. To accomplish this, the Rice University effort in E896 has proposed, built, and commissioned a Time-Of-Flight detector (TOF).

2.2 E896 Hardware

Before describing the TOF particle identification (PID) method and TOF hardware, all of the other E896 apparatus elements, most of which are shown in Figure 2.2, will be described. First, the E896 coordinate system will be defined, and the key beamline elements will be described. The detectors that signal a Au+Au collision as being central will be discussed next. After that, the two distinct particle track detector systems in E896, the "SDDA" and the "DDC," are described. Greater emphasis is placed on the DDC and the other forward detectors, since TOF information

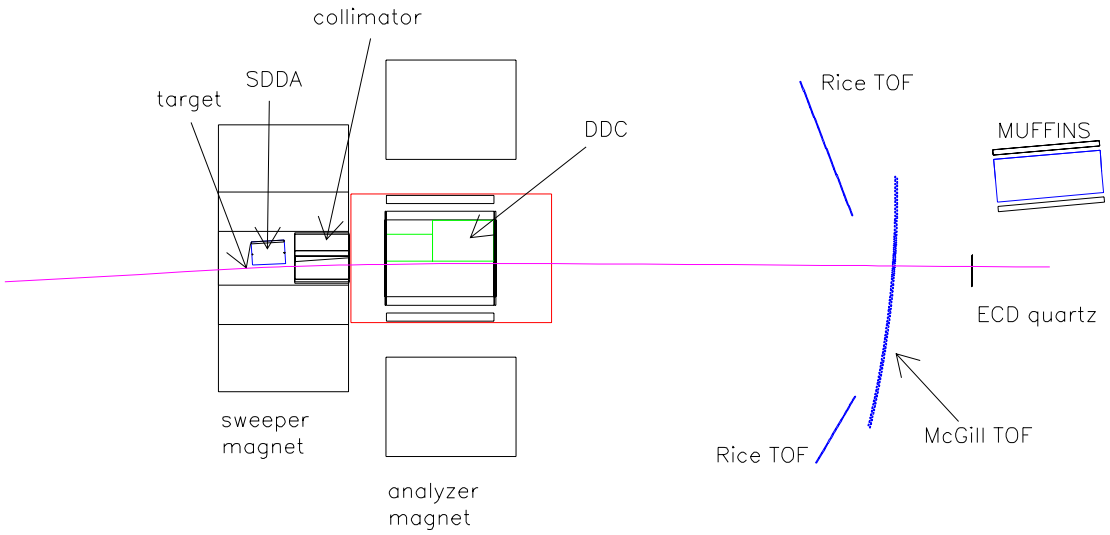

Figure 2.2 The E896 apparatus viewed from above. The line which spans the figure corresponds to the path of the non-interacting beam. Not shown in this figure are the upstream detector elements (the Beam Counters, Beam Vertex Detector, and Veto Counter) and the Multiplicity Telescope (located just upstream of the collimator).

is applied to tracks reconstructed from the DDC detector data.

2.2.1 E896 Coordinate System

The axes of the E896 coordinate system are defined as follows. The z axis bisects the sweeper and analyzer magnets (described later). As one moves downstream, the z coordinate increases. The path of the non-interacting beam is roughly parallel to the z axis. The downstream face of the analyzer magnet is defined to be $z = 500$ cm. Positive values of the x coordinate are to beam left of the z axis, and negative x values are to beam right. The y axis is vertical, with y becoming more positive

when moving upward and negative when moving downward. The target is situated at about $z = 253$ cm, $x \approx$ -8 cm, and $y \approx 0$.

2.2.2 Beamline Elements

Beam

E896 was situated on the C5 line at the Brookhaven National Laboratory Alternating Gradient Synchrotron (BNL-AGS). The beam momentum was 11.6 GeV/c per nucleon, corresponding to a projectile rapidity in the laboratory frame of 3.2. Beam bunches entered the C5 line from the AGS in spills of roughly 1 s duration, with about 3 s between spills. Over most of the run, the beam intensity was 75k ions per spill.

Beam Vertex Detectors

To measure the beam trajectory and reconstruct the beam upon the target, the Beam Vertex Detector (BVD) was implemented about 1 m upstream of the target. The BVD is comprised of two sets of drift chambers, separated by about 1 m. Each drift chamber consists of two planes of vertical wires (to measure an x-coordinate) and two planes of horizontal wires (for a y-coordinate measurement). The position resolution of the BVD was determined to be about 1 mm. The mean angle of the beam at the target, as established by the BVD, was 3.09 degrees in the xz-plane [8].

Target

The stationary target used for nearly all of the recorded heavy-ion interactions was made from gold foil. To achieve beam-target interactions with a 10 percent probability, the thickness of the target was set to 2.5 mm.

Sweeper Magnet

The target was situated within the bore of a superconductor magnet, called the "sweeper magnet," with a peak field of 6.2 T. This magnet deflects the beam-like fragments and most of the produced charged particles away from the downstream tracking detectors. Thus, the sweeper magnet serves to suppress primary and other produced particles that would otherwise reduce the efficiency for tracking the neutral particles of interest, namely the H_0 di-baryon, Λ hyperon, and K_s meson.

Collimator

To contribute to the suppression of primary and other particle backgrounds, a collimator was installed at the downstream end of the sweeper bore. The collimator was constructed using blocks of tungsten and lead, both of which have very high interaction cross sections. A gap in the collimator permits a fraction of the neutral particles to pass through it, eventually to decay downstream in a cleaner environment.

2.2.3 Trigger Elements and Trigger Definition

The hardware elements described in this section are used to establish whether a central Au+Au collision occurred. When such an event occurs, the data from all detectors in E896 are written to magnetic tape for offline analysis.

Beam Counters

To determine that an event took place, it must first be established that a gold ion beam particle had approached the target. This is done using two Beam Counters (BCs) located 4 m and 3 m upstream of the target. Each BC consists of a quartz Čerenkov radiator mounted within the evacuated beam pipe, and read out by two fast Hamamatsu R2083 photomultiplier tubes (PMTs). The start time measurement resolution of the BCs is about 30 ps.

The BCs serve two purposes. First, they establish that exactly one beam particle approaches the target during an event. A BC signal that is too large indicates the presence of two gold ions traveling close to each other in time. The trigger rejects such an event. Also, the signal from one of the BC PMTs is used to establish the start of the Au+Au event. This serves as the start pulse for the TDC units employed by the downstream detectors.

Veto Counter

About one half of a meter upstream of the target was placed a so-called Veto Counter. This detector is comprised of a piece of glass with a 1 cm diameter hole in the middle, and a PMT for readout. The Veto Counter detects (and rejects) events in which beam "halo" is present (*i.e.* a particle or particles of generally low charge that may accompany a beam ion), as well as events in which the beam interacted upstream of the counter.

Multiplicity Telescope

Just downstream of the target, and upstream of the collimator, is the Multiplicity Telescope (MLT) [9], the primary centrality detector for E896. Its design is based on the transverse energy detector constructed and implemented in AGS Experiment 878 [10].

The MLT is comprised of four lead slabs, each 1 in. thick, with a scintillator slab placed downstream of each lead slab. The lead-scintillator blocks are arranged around the upstream face of the collimator. Photons convert into electrons and positrons inside the lead. The electrons and positrons produce light inside the scintillator, which is read out by a fast PMT.

The MLT primarily detects photons that result from the decays of π^0 mesons produced in the Au+Au interaction by converting a fraction of these to charged par-

ticles using the lead layers. The number of photons detected is proportional to the number of primary charged particles produced in the participant region. That primary charged particle multiplicity is strongly anti-correlated with the event centrality. Thus, as the event becomes "more central," the MLT detector response increases.

Exit Charge Detector

A second centrality detector, the Exit Charge Detector (ECD), was built at the Bonner Nuclear Laboratory at Rice University and added to the E896 apparatus. The ECD measures the total charge of the surviving beam fragments and spectator protons. Thus, as the event centrality increases, the total spectator mass decreases (there are fewer and smaller forward-rapidity fragments), and the ECD response decreases.

Figure 2.3 shows a drawing of the ECD and its key hardware elements. The ECD is comprised of a 30 cm $\times$ 20 cm $\times$ 2 mm quartz Čerenkov radiator situated just inside the front face of a 30 cm $\times$ 60 cm $\times$ 10 cm light integration volume. At the top and bottom of the ECD are two PMTs. Charged particles which pass through the quartz radiator generate photons, which reflect off of the inside walls of the light integration volume until they reach the PMTs. The ECD is placed about 6 m downstream of the target, and oriented so that the non-interacting beamline and beam fragments pass through the quartz radiator.

The dimensions of the ECD radiator were determined through the use of a sim-

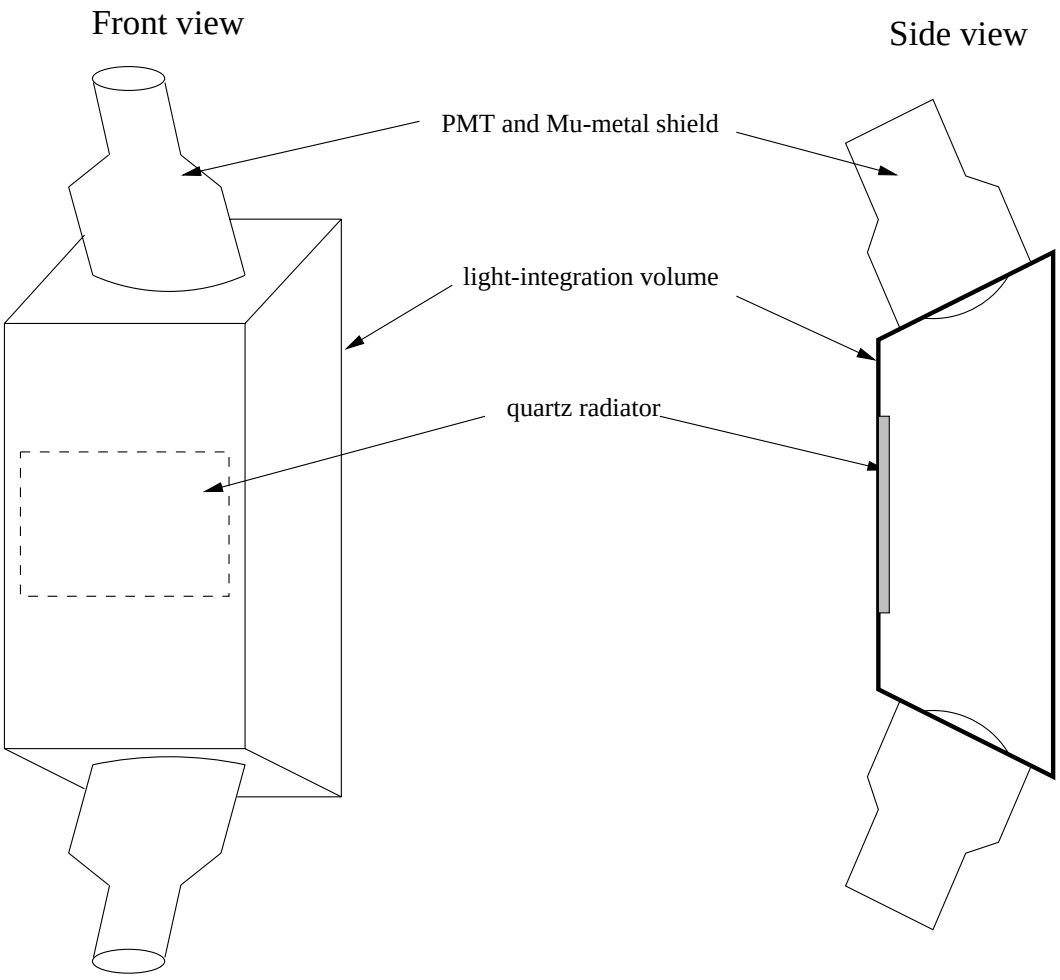

Figure 2.3 A drawing of the Exit Charge Detector, showing the key components.

ulation program known as GEANT [11], which was also widely used in many of the TOF-related simulations, such as the calculation of the constant timing offsets (subsection 3.2.5) and the acceptance calculations (section 4.2). GEANT is a software package which reads in the attributes of the E896 detector geometry supplied by the user, and propagates particles (whose initial positions and momenta are also supplied by the user) through the system. The entire experimental geometry, including both active and inactive parts of detectors and other components of the apparatus, is defined. Effects such as particle decay, hadronic interactions with the detector media, and multiple coulomb scattering are simulated by GEANT. Information such as hit location, particle species, or charge for simulated particle hits upon designated detector elements can be stored into constructs referred to as ntuples and analyzed for the information of interest.

Based on GEANT simulations performed in 1996 [12], the radiator area was made large enough to intercept projectile fragments with $A/Z \geq 2$, yet small enough to keep hits from other charged particles (especially $Z = 1$ particles from the participant region) to a minimum. The 2 mm thickness kept the probability of gold beam interactions below 5 percent, yet the radiator was still thick enough to produce enough light to give a measurable response to a $Z = 2$ particle. The 60 cm vertical dimension of the ECD light integration volume was long enough to keep the probability of $Z = 1$ hits upon the ECD PMT photocathodes themselves below 10 percent, yet

short enough to keep the surface area inside the ECD low and thus minimize the loss of signal due to absorption inside the light integration volume.

The light integration volume has its interior walls lined with Tyvek paper. Tyvek is white and fibrous, making it highly and diffusively reflective. The diffusiveness helps to reduce the dependence of the ECD response upon the hit location of the particle upon the radiator.

The ECD PMTs are RCA/Burle 8854 PMTs. They exhibit a fast 3 ns rise time, which is essential for the use of the ECD as a trigger element. The photocathode diameter is a wide 4.5 inches, which reduces the overall number of PMTs required to cover the top and bottom of the light integration volume to obtain usable signals.

Since the amount of light produced by a particle passing through a Čerenkov radiator is proportional to the square of the particle's charge, and since the size (and charge) of the surviving beam fragment increases as the impact parameter increases, a large ECD signal indicates a peripheral beam-target interaction (or no interaction at all). Thus, the ECD PMT signals are used as the basis for a beam-interaction trigger.

Figure 2.4 is a schematic of the ECD signals in the E896 trigger logic, and how they help define the central trigger and interaction trigger. Each of the four ECD PMT anode pulses was amplified by a factor of 20. These amplified pulses were paired up and linearly summed. These summed signals were each sent to a Phillips

704 discriminator, set at a relatively low threshold. If one of the linear sums fails to exceed the discriminator threshold, the event could be regarded as central. In this way, the amplified ECD pulses help to define the central event trigger.

Similarly, the non-amplified ECD PMT anode pulses are paired up and linearly summed, and sent to discriminators with a relatively high threshold. Those thresholds would be exceeded if the ECD signals are characteristic of a gold ion response. If one of the non-amplified linear sums does not exceed this threshold, a beam-particle interaction is suspected to have occurred, and the minimum-bias trigger is satisfied.

Several important conclusions emerged over the course of the analysis of ECD data taken during the gold ion beam run of January 1997. First, while studying the widths of the ECD signal pulse size (ADC) distributions, an additional contribution to the ADC signal (pedestal) due to contamination by ambient "dirty" AGS power was observed. Since the problem was recognized in January of 1997, electronics were developed and implemented in the Au98 run to remove this "dirty" AGS ground contamination from the TOF PMT ADCs. The procedure is described in subsection 3.2.1.

Another observation from the 1997 ECD analysis was that a significant number of beam interactions take place outside of the target. Aside from the beam-target interactions, the ECD analysis in Reference [12] measured a 22 percent probability of gold beam interactions taking place upstream of the ECD. An accounting of each of

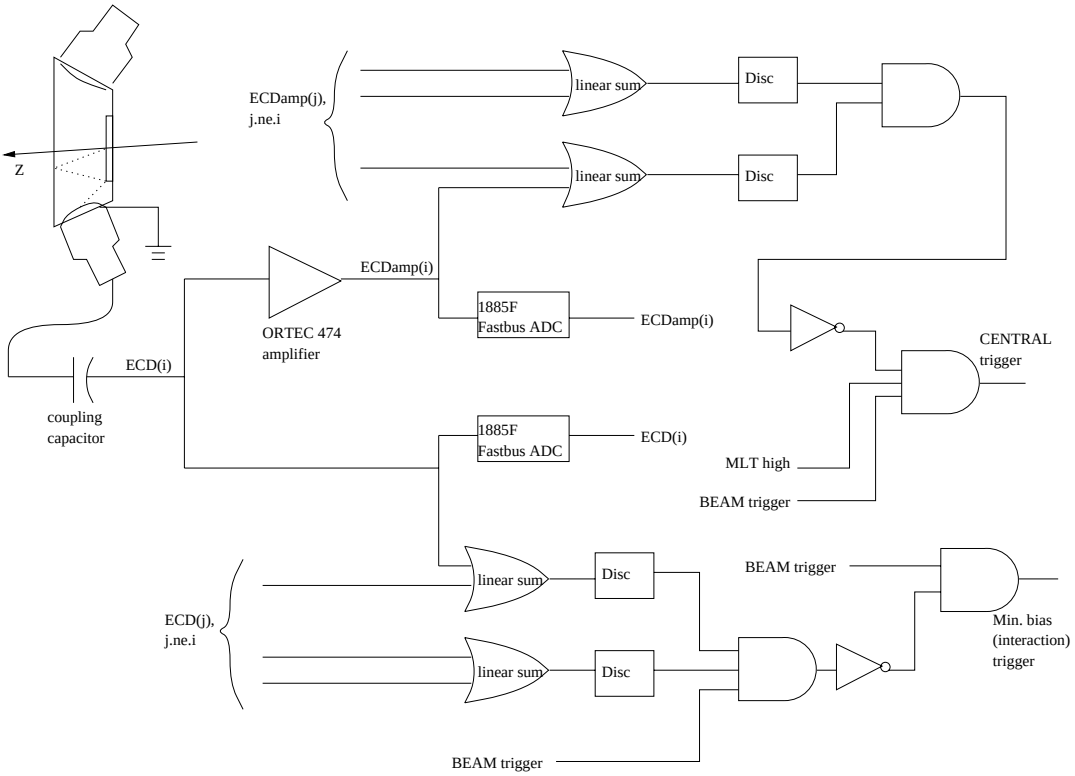

Figure 2.4 A schematic of the ECD outputs and their contribution to the E896 trigger.

the beamline elements (including the BCs, BVDs, DDC materials, air, and collimator) was able to explain these measured non-target interactions to within 2 percent. Because of these significant downstream interactions, the ECD was used in later runs as a trigger element but with rather loose cuts as an interaction trigger, rather than as a centrality trigger.

Definition of the Central Event Trigger

E896 sought to restrict its analysis to events in which a substantial number of mid-rapidity particles are produced, and the remnant of the incident beam particle is either very small or nonexistent. The objective of the E896 central event trigger is to flag those events and to store to tape the output from all detectors if the trigger is satisfied.

The central event trigger uses all of the detectors described earlier in this section. First, both BCs must register a minimum signal (indicating a particle approaching the target), while the Veto Counter registers no signal above threshold:

$$INGEO = BC1(low) * BC2(low) * \overline{VETO} \tag{2.1}$$

Also, the downstream BC must measure a signal above a threshold indicating a gold ion, but should not measure a signal consistent with a gold ion plus some other charged particle(s):

$$BEAM = INGEO * BC2(mid) * \overline{BC2(high)} \tag{2.2}$$

Finally, for a central event trigger, the MLT response must be above a threshold, and the amplified ECD signals must fall below a threshold, indicating many produced particles and the lack of a surviving beam ion, respectively:

$$CENTRAL = BEAM * MLT(high) * \overline{ECDamp(low)} \tag{2.3}$$

The discriminator levels for the MLT are set such that only the 10 percent most central beam-target interactions are selected. Thus, using a 10 percent interaction target, about one percent of the beam particles undergoes an interaction that satisfies the present central trigger.

The central event trigger will also reject an event if either BC detects consecutive minimum signals within 500 ns of each other. This is done to provide "before and after" protection. If the previous event occurred only slightly earlier, hits from the earlier event and the current event would pile up in the detectors, confusing the information from the event of interest with erroneous detector signals. The 500 ns separation allows particles from the previous event to completely clear away from the detectors.

2.2.4 Forward Detectors

The main particle tracking detector in E896, and the one whose data is used in the analyses described in this Thesis, is the Distributed Drift Chamber (DDC) [13]. The hardware elements that comprise the forward detectors, along with the DDC itself, are the analyzer magnet, the MUFFINS array, and the TOF array. A detailed description of the TOF hardware is given later in this chapter; the other forward detectors are described first.

Distributed Drift Chamber

The Distributed Drift Chamber consists of planes of parallel (anode) wires, separated by (cathode) sheets parallel to the wire planes. A negative high voltage is placed on the cathode planes, while the anode wires are held at ground. This sets up an electric field (drift field) between the wires and the cathode planes. The planes and wires are placed within an inert gas environment. When a charged particle passes through the drift chamber in the proximity of an anode wire, it ionizes gas molecules along its path. These ions in the gas are drawn toward the anode wires by the drift field, ionizing more of the gas molecules along the way. The arrival time of the ion cascade upon an anode wire, relative to the start of the event, is recorded. Since the dependence of this ion cascade's drift velocity upon the distance from the wire has been calibrated [14], the measured drift time can determine the distance of closest

approach of the original charged particle to the anode wire. Full three-dimensional track reconstruction was provided by rotating the orientation of wires in alternating planes. The pattern $xx'uu'xx'vv'xx'...$ was adopted, where the wires in the u and v planes were rotated $\pm$ 15 degrees relative to the vertically-oriented x-plane wires.

Combining the distance-of-closest-approach information from several drift chamber wires in the vicinity of the particle's flight path allows for a very precise determination of the flight path. This allows the calculation of the daughter particle momentum as obtained from the radius of curvature of the track. The position and momentum of a neutral parent leading to a pair of charged tracks can also be reconstructed if both of these "daughter" tracks are reconstructed in the DDC active volume.

The DDC in E896 had to be capable of recording data at high rates. At the same time, the probability of interactions between the particles from the event and the DDC hardware had to be kept minimal. This was achieved by using a gas mixture of 50 percent helium and 50 percent ethane. The He/C_2H_6 mixture minimized effects such as multiple coulomb scattering, delta-ray production, and interactions of photons and neutrons within the DDC active volume. At the same time, the gas mixture provided sufficient gain for the ionization cascade and an understandable drift velocity.

The DDC consists of 12 drift chamber modules, with 12 planes of wires per module. Higher resolution at the upstream end of the DDC was desired, since most of the

neutral vertices would be reconstructed there. Thus, the spacing between the wires in the upstream DDC modules was 3 mm, while 4 mm spacing was used for the downstream modules. The DDC active volume is 67.5 cm in x, 20 cm in y, and 100 cm in z. The final position measurement resolution of the DDC was about 150 μm.

The DDC was placed 1.3 m downstream of the target. This was far enough downstream so that many of the primary charged particles produced in the event were deflected clear of the DDC active volume by the sweeper field. This also placed the DDC's phase space acceptance in the region of high (near beam-like) rapidity and low transverse momentum. Provided that the triggered events were highly central, the DDC could thus measure particles produced by the participant region at the extreme forward rapidities to complement the measurements of the SDDA (see subsection 2.2.5) that are made closer to mid-rapidity.

Analyzer Magnet

To measure the momentum of the particles that deposit tracks in the DDC, the DDC is placed in a magnetic field. Such a field was provided by a standard BNL 48D48 magnet, hereafter referred to as the analyzer magnet. The analyzer magnet generates a 1.7 T magnetic field which, throughout the DDC active volume, is vertically oriented and nearly constant. This allowed [14] the use of a helical model to determine the radius of curvature r for DDC tracks in the xz-plane, and thus calculate the momentum p_{xz}, using the equation below:

$$|p_{xz}| = qB|r| \tag{2.4}$$

where q is the particle charge, and B is the magnetic field amplitude. The momentum component in the yz plane, p_y, is obtained using the equation below:

$$|p_y| = |p_{xz}| \tan\theta \tag{2.5}$$

where θ is the angle between the tangent of the track and the xz plane. Assuming that the magnetic field inside the DDC has no components in the x or z directions, the momentum component p_y is constant for the DDC track.

Multi-functional Neutron Spectrometer

A consistency check of a possible $H_0 \rightarrow \Sigma^-$ p $\rightarrow \pi^-$ n p decay signature in the DDC is possible by detecting the neutron from the Σ^- decay. The Multi-functional Neutron Spectrometer (MUFFINS) [15] was implemented for this purpose. MUFFINS is an array of 29 scintillator disks, oriented vertically and stacked one behind the other. The array of disks is placed about 2 m downstream of the DDC, parallel to and just to beam left of the neutral line. A neutron signal in MUFFINS is characterized by the absence of a signal in several of the upstream disks and a strong signal in the remaining downstream disks. Relative signal strengths measured from the six PMTs placed on each disk can determine the trajectory of the incident neutron. This

trajectory can be traced back toward the DDC to see if it could have emerged from a $H_0 \rightarrow \Sigma^-$ p $\rightarrow \pi^-$ n p topology.

2.2.5 Silicon Drift Detector Array

Besides the DDC, the other detector used in E896 to track charged particles and reconstruct the topologies of weakly decaying strange neutral particles is the Silicon Drift Detector Array (SDDA) [16]. The SDDA consists of fifteen n-type silicon wafers, each with dimensions of 6.3 cm $\times$ 6.3 cm $\times$ 300 μm. The detector is positioned inside of the sweeper bore, 10 cm downstream of the target and to the beam left of the noninteracting beamline. This positions the SDDA for the detection of mid-rapidity particles ($1.6 < y < 2.4$), and for unstable neutral particles with lifetimes as low as half that of the Λ hyperon. The data acquisition rate of the SDDA is lower than that of the DDC (about two events are recorded per spill) because of the slower drift times within the silicon than within the DDC.

2.3 Particle Identification in E896

Neutral particle searches in E896 can be improved by adding the capability for direct identification of charged daughter particles. This can provide a more powerful consistency check on an H_0 di-baryon decay topology, and also can yield a "cleaner" sample of Λ hyperons and K_s mesons. Such direct PID is done in E896 by performing flight time measurements to complement the momentum measurements of particles

that pass through the DDC.

For this purpose, a Time-Of-Flight (TOF) hodoscope was designed, commissioned, and used in experimental runs. This section describes how PID is performed in E896, without and with TOF. The details of the E896 TOF detector hardware are presented in section 2.4.

2.3.1 Particle Identification without TOF

Neutral Vertex Reconstruction

E896 detects neutral particles by reconstructing them from the tracks deposited by their charged decay products. Each pair of positive and negative tracks is compared to see if they appear to have a common origin, also called a neutral vertex, inside the DDC. Such a pair is referred to as a V_0 candidate. If a V_0 candidate is found in the DDC in an event, then the location of the vertex is determined, and the momentum vector of the V_0 candidate is reconstructed from the momenta of the reconstructed daughters.

The invariant mass M of the V_0 candidate is calculated in the manner given by Equation 2.6:

$$M^2 = m_+^2 + m_-^2 + 2E_+E_- - 2\vec{p_+} \cdot \vec{p_-} \tag{2.6}$$

where m_i, E_i, and $\vec{p_i}$ are the mass, total energy, and momentum of the daughter particle of charge i.

A peak on an invariant mass distribution compiled from several V_0 candidates indicates the presence of a parent neutral particle of that mass within the detector acceptance. For neutral particles of known mass (Λ hyperons and K_s mesons), an invariant mass peak can confirm the copious production and detection of these particle species, and gauge the effectiveness of the geometric and kinematic cuts to the V_0 candidates in removing specific backgrounds using cuts. For the H_0 di-baryon, the presence of a peak in the invariant mass histogram could demonstrate the H_0 di-baryon's existence, confirm the correctness of its assumed decay channels, and provide a mass measurement.

However, since the above analysis must assume the masses of the daughter tracks, the invariant mass distribution will include certain backgrounds. Examples of such backgrounds for neutral particles include V_0 candidates emerging from the interaction of neutrons or gammas within the DDC, K_s mesons mis-identified as Λ hyperons, and pairs formed from unrelated positive and negative tracks (*i.e.* combinatorial background).

Armenteros Variables

In lieu of direct identification of the species of the decay particles, there is a method that can be used to indicate the presence of unstable neutral particles. An "Armenteros plot," such as the example shown in Figure 2.5, depicts the daughter's transverse momentum $p_\perp$ (defined with respect to the parent momentum vector)

versus a quantity α defined in terms of the longitudinal momenta of the daughter particles, $p_{\parallel}$, in the manner of Equation 2.7:

$$\alpha = \frac{p_{\parallel}^{+} - p_{\parallel}^{-}}{p_{\parallel}^{+} + p_{\parallel}^{-}} \tag{2.7}$$

Neither $p_{\perp}$ nor α require mass assumptions for their computation.

For unstable neutral particles of a specific mass M, the Armenteros variables $p_{\perp}$ and α, based on the daughter kinematics, are related in the manner presented in Equation 2.8:

$$p_{\perp}^{2} + (\alpha - \alpha_0)\frac{\beta^2 M^2}{4} = \frac{Q^2}{2} \tag{2.8}$$

where β is the parent velocity, and

$$\alpha_0 = \frac{m_{+} - m_{-}}{m_{+} + m_{-}} \tag{2.9}$$

and

$$Q^2 = M^2 - m_{+}^{2} - m_{-}^{2} \tag{2.10}$$

is the energy released by the decay.

Bands will appear on the Armenteros plot that can be associated with the decay of specific neutral particles. The dark band on the right-hand side of the plot in

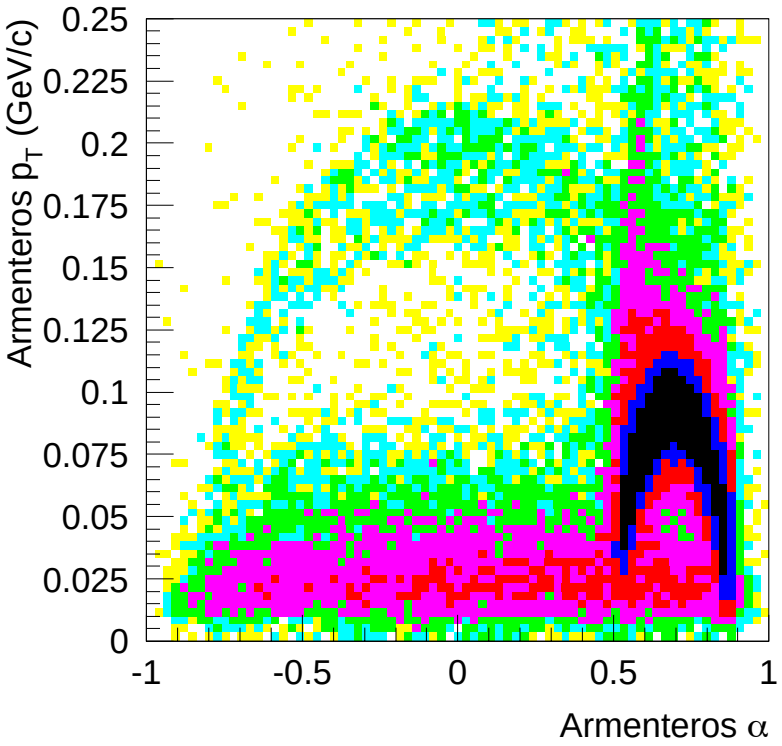

Figure 2.5 The Armenteros variables $p_\perp$ versus α as defined by Equation 2.7 for V_0 candidates reconstructed from E896 central events.

Figure 2.5, symmetric about $\alpha \sim 0.7$ and peaked at about $p_\perp \sim 0.1$, corresponds to the decay of Λ hyperons. A more faint band, which is symmetric about $\alpha = 0$ and peaked at about $p_\perp \sim 0.2$, represents the decay of K_s mesons. The flat band present at low $p_\perp$ is attributed to a background process in which e^+e^- pairs are reconstructed as V_0 candidates.

Though an Armenteros plot allows for the identification of specific neutral particles, the method still has significant shortcomings. First, there are regions of Ar-

menteros space where certain neutral particles (such as the Λ hyperon and K_s meson) overlap. Also, the spread in the velocities of the decay particles broadens the Armenteros bands. This creates further overlap among Λ hyperons and K_s mesons, and smears the neutral-particle bands into regions of the Armenteros space covered by background V_0 candidates.

The Armenteros method is a statistical method with assumptions, and is not a form of direct particle identification. Such a plot can be used to estimate backgrounds for Λ hyperons and K_s mesons, but not conclusively separate them. An Armenteros plot can be used to infer the number of Λ hyperons that were produced in a certain number of events, but it cannot be used to select any one V_0 candidate that is definitely a Λ hyperon or a K_s meson.

2.3.2 PID through Separation of Time versus Momentum

For primary particles (those which originate at the target), the measured flight time versus the measured momentum can readily determine the particle mass. If primary particles of different species are incident upon a given TOF slat, then for a sufficiently low momentum (the "cutoff momentum"), the particles of different species are observed to have measurably different flight times, as indicated by diverging "bands" on the time-vs.-momentum plot.

Figure 2.6 plots the inverse velocity $1/\beta$ versus momentum for simulated primary pions, kaons, and protons propagated through the E896 geometry using GEANT. The

error bars in each frame represent the spread in the TOF-measured $1/\beta$ for each momentum bin. That width is determined by the momentum resolution $\Delta p/p$ and time measurement resolution σ_{TOF} incorporated into the simulation. On each of the frames, a *cutoff momentum* can be defined such that, for momentum below that value, the error bars for distinct particle species do not overlap. For example, in the upper right frame (with $\sigma_{TOF} = 120$ ps and $\Delta p/p = 0.01$), the cutoff momentum for the separation of protons from kaons is about 5.6 GeV/c.

Figure 2.7 shows the parent-plus-daughter flight time versus momentum for secondary RQMD protons (upper band) and π^+ mesons (lower band) propagated through GEANT. Even though the parent-plus-daughter flight paths are less constrained than for primary particles, such daughters may also be separable below a certain cutoff momentum. Thus, flight time measurements can also be used to separate $K_s \rightarrow \pi^+$ from $\Lambda \rightarrow$ p.

The TOF detector analysis in E896 uses the technique of time-vs.-momentum band separation to reduce the background of the invariant mass histograms, and thus provide a cleaner sample of Λ hyperons and K_s mesons that can be used to study the heavy-ion collisions from which they were created.

2.3.3 Quantities Measured from a Slat-based TOF System

TOF systems in different experiments are designed to measure the same physical quantities for charged particles. First, TOF systems are designed to measure the

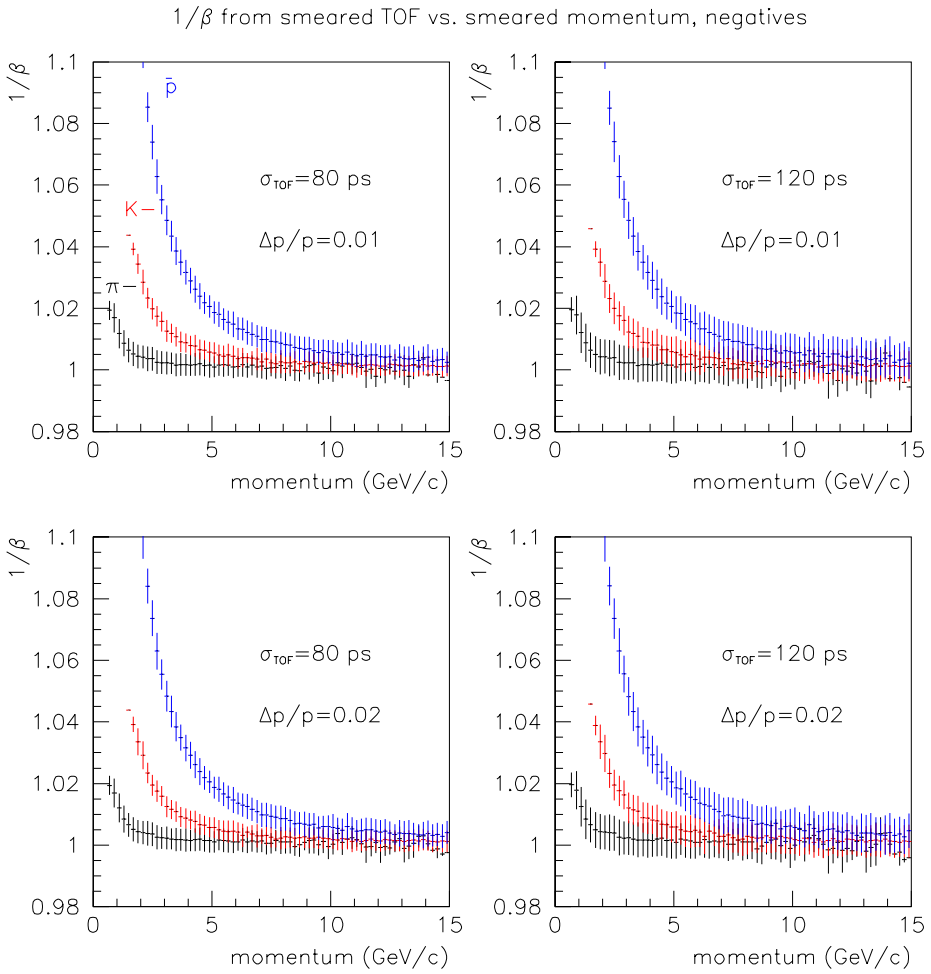

Figure 2.6 The inverse velocity versus momentum for primary pions, kaons, and protons in the E896 TOF geometry simulated in GEANT. This plot was obtained from Reference [18].

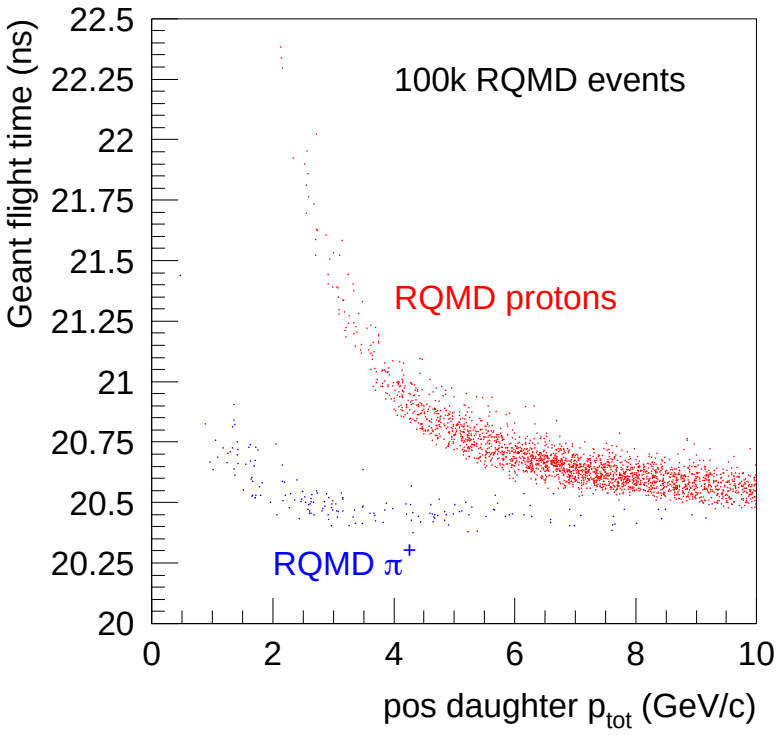

Figure 2.7 The flight time versus the particle momentum for TOF-incident secondary pions and protons from RQMD $b < 4$ fm events propagated through the E896 geometry in GEANT.

charge of an incident particle, since the area of the output signal of the TOF counter correlates with the charge squared. Charge measurements ensure that exactly one $Z = 1$ particle passed through the TOF counter during an event. It is difficult to resolve two particles that strike the same slat in the same event. TOF systems are typically optimized to avoid that situation.

Second, TOF systems measure a time, relative to the start of an event, when a particle strikes a given slat. The design of any TOF system strives for a time-measurement uncertainty as low as achievable. This allows particles of different mass to be separable via TOF at higher momentum. Figures 2.6 and 2.7 illustrate this point. Achieving narrower proton and pion bands translates to greater separability for protons and pions.

For each TOF counter, two measurements of signal size and signal arrival time are made, one at each end of the active element. Using two time measurements at opposite ends of the counter allows for a simultaneous flight time measurement (obtained from the average of the individual time measurements) and a hit location measurement (obtained from the difference between the two individual time measurements). Also, using two measurements per counter suppresses the dependence of signal size and time upon the hit location of the particle upon the counter.

Finally, the TOF system provides an additional global space point for the three-dimensional tracking of a charged particle. As stated above, the difference between

the two time measurements gives the vertical space point coordinate. The location of the struck TOF counter provides the other two coordinates.

2.3.4 Pertinent Quantities for TOF PID

A summary of the quantities required for PID in E896, and the detectors that provide these quantities, is given below:

- The *DDC* defines the particle path, needed to associate the particle with the correct TOF counter; and performs a measurement of the particle momentum and particle total path length.
- The *BCs* define the start signal for the TOF detector time measurement.
- The *TOF* detector itself provides the stop signal for the particle flight time measurements. It also provides a space point to aid in the association of a DDC track to the correct TOF counter; and a particle charge measurement, to ensure that exactly one $Z = 1$ particle struck the TOF counter in an event.

2.3.5 Method of TOF PID in E896

Particle identification in E896 proceeds as follows. First, the neutral vertices are constructed from the DDC tracks reconstructed from the central events. These V_0 candidates are required to satisfy a series of cuts to their geometric and kinematic quantities. These cuts are defined in section 4.1. Among these cuts are requirements that the V_0 candidate point back to the target, and that the daughter tracks' distance

of closest approach to each other at the presumed vertex is sufficiently small. After the geometric and kinematic cuts are applied, the measured flight times for the daughter tracks (after correcting for time-measurement offsets) are plotted versus the daughter track momentum. This time-vs.-momentum plot is used to determine whether the V_0 candidate daughter's flight time is consistent with that for a proton from a Λ hyperon decay, or a π^+ meson from a K_s meson decay.

The goals of this analysis of E896 data, using the TOF array for PID, are these. First, TOF information will be added to the daughter particles of Λ hyperon candidates found in an earlier pass through the data [14]. This will provide a better understanding of the backgrounds from the original analyses, and yield a cleaner sample of Λ hyperons to compare with other AGS experiments and with RQMD. TOF will also be used to identify K_s mesons. The spectra of K_s mesons in the E896 data will be measured.

2.4 E896 Time-Of-flight Detector Hardware

2.4.1 Overview of the TOF Detector System

A photograph of the E896 Time-Of-Flight array is shown in Figure 2.8. The E896 TOF detector system is a series of about 200 long, narrow scintillation counters, called "slats." The slats are grouped into three distinct arrays, called "walls." A highly granular 2 m wide "Central Wall," inherited from the decommissioned AGS Experiment 877, is positioned about the beamline to accept higher momentum charged particles

Figure 2.8 A photograph of the E896 TOF detector system, looking approximately downstream and from below.

from neutral particle decays. Located on each side of the Central Wall are two "Side Walls," one 1.3 m wide and the other 0.7 m wide; they were built at Rice University to improve the TOF acceptance for lower momentum decay products.

Each slat consists of a plastic scintillator rod, with photomultiplier tubes (PMTs) placed at each end to detect the light produced by a charged particle incident upon the slat. Each PMT response is read out on two signal lines. One line is sent to an analog-to-digital converter (ADC), which measures the area of the pulse from

the PMT anode. The ADC measurement correlates with the charge of the particle incident upon the slat and the amount of energy it deposits. The other signal line goes to a time-to-digital converter (TDC), which records the arrival time of the PMT pulse relative to the start of the Au+Au event. The TDC measurement correlates with the flight time of the particle and its hit location along the length of the slat.

To aid in describing the location of each TOF slat relative to the rest of the array, the following naming convention was developed. A TOF *hole* is a numbered placeholder for a TOF slat. The slat at the extreme beam left end of the TOF system (on the beam left Side Wall) is assigned hole number 1. As one proceeds in the beam right direction along the TOF array, the slats are given higher hole numbers, up to 200.

This section will first describe the motivation, hardware, and construction of the TOF Central and Side Walls. The electronic components, namely high voltage and data acquisition (DAQ) systems, will be described next.

2.4.2 Time-Of-Flight Central Wall

The TOF Central Wall was originally built by McGill University for BNL-AGS Experiment 877 [19]. In that experiment, the hodoscope was used to identify charged pions, kaons, and protons that were produced at their target, by providing flight time measurements to complement the momentum measurements for these particles. In Au+Au interaction data recorded in E877, the average flight time measurement

resolution among all scintillation counters in the array was about 85 ps [5].

The TOF Central Wall consists of 148 scintillator counters situated within 160 available TOF mounting holes, numbered by convention from 27 to 186. The six holes at each end of the Central Wall are vacant. Slats were also removed from ten holes (numbers 89 to 98) near the middle of the Central Wall to accommodate the passage of non-interacting gold beams through the experiment.

Each Central Wall slat is 70 cm long. The thickness of each slat is 1.5 cm. This allows for a sufficient dE/dx yield for minimum ionizing particles (MIPs), while at the same time keeps the nuclear interaction probability to a manageable 4 percent. Thirty-nine slats in the middle of the Central Wall (holes 62 to 100) are 1.0 cm wide; the remaining Central Wall slats are 1.7 cm wide. The high granularity of the Central Wall makes it well suited for detecting pions from K_s meson decay and protons from Λ hyperon decay, since these decay products tend to reside in regions of E896 where the overall charged particle multiplicity is high.

Figure 2.9 illustrates the mounting pattern for the Central Wall slats. The slats are arranged in a staggered two-row pattern within a Bakelite frame, with an overlap of 0.25 mm between the front and rear layers of slats. As the relative location of each TOF slat within the Bakelite frame is well known, to an accuracy of less than 1 mm, the Bakelite frame serves as the reference for the survey of the Central Wall's position with respect to the E896 coordinate system. The Central Wall slats were arranged in

an arc with a radius of curvature of 9.5 meters.

The scintillator material is Bicron BC404, with a fast decay time constant of 1.8 ns and large light output. The peak of the wavelength distribution of its emitted light is 408 nm, and the attenuation length is 160 cm. The PMTs affixed to the plastic are Hamamatsu R2076 8-stage PMTs. They have a fast 1.3 ns rise time and 0.36 ns transit time spread. Also, the R2076 photocathode's peak wavelength sensitivity of 410 nm matches well with the BC404 scintillator.

For the 1.7 cm wide Central Wall slats, the PMT photocathodes are glued directly to the ends of the plastic with BC600 optical cement. For the 1.0 cm wide slats, a 15 cm long UV-transparent Lucite light guide is glued between the plastic and the PMT photocathode. The slats are wrapped with a layer of clear plastic, which is surrounded by a layer of aluminum for reflection of light back into the slat, which is in turn surrounded by a layer of black plastic to protect the scintillator from external light.

The Central Wall, when acquired by E896 from E877, was not in a ready-to-operate condition. Much work was necessary to position the Central Wall, and repair the high voltage lines to, and signal lines from, each of the 296 PMTs.

The Central Wall's final location was a compromise between the optimal location suggested by GEANT simulations [18] and the constraints imposed by the locations of the MUFFINS array and the concrete radiation barriers to the E896 experimental

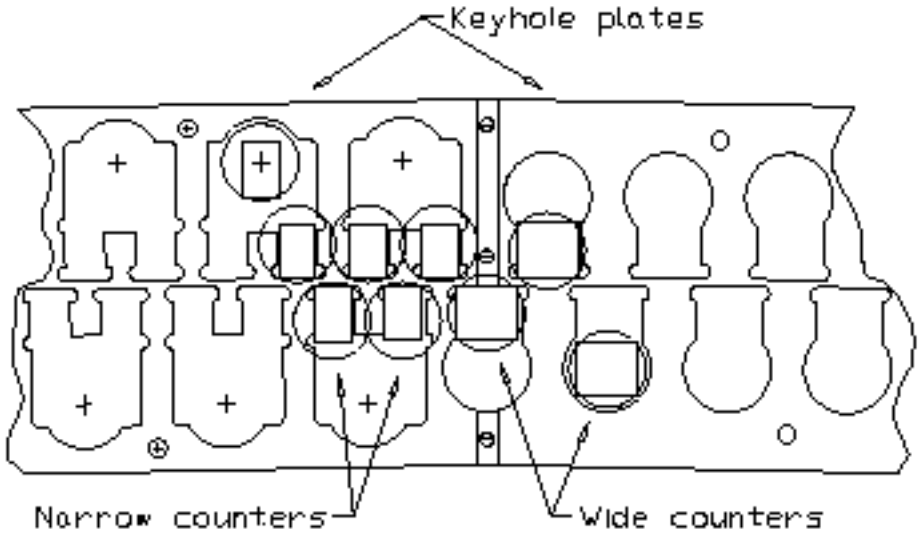

Figure 2.9 Top view of a portion of the Bakelite structure designed by E877 to hold the Central Wall slats. This drawing was taken from [5].

area. All TOF hardware was mounted so that no electrical contacts between TOF electronics (PMTs, discriminators, cable connectors) and the AGS "dirty ground" could be made. Bakelite wedges and electrical tape were heavily used for this purpose.

Intensive work was also necessary to repair the cables that carried the TOF PMT signals to the data acquisition (DAQ) electronics. The anode signals from the Central Wall PMTs were carried out through $\sim$ 10 ns long RG-111 Lemo cables, with Lemo connectors at the end. A special Lemo-compatible connector was installed at the TOF-detector end of each of the RG-58 cables that went from the detector to the DAQ electronics. This was done to conserve space. Many of the RG-58 Lemo connectors that were originally on the Central Wall signal cables were damaged or missing, and

had to be replaced.

Patch panels were installed at the edges of the TOF array to mount the RG-58 cables for an easily accessible and space-saving connection to the PMT Lemo cables. More patch panels were installed next to the TOF DAQ electronics to provide an interface between the RG-58 cables and the cables that went into the DAQ hardware.

Leading the RG-58 cables from the TOF detector to the DAQ electronics was also a tedious job. The RG-58 signal cables were combined in bunches of twelve. Though this reduced the amount of tangling among the roughly six hundred cables total, the cable bundle was very stiff and heavy. Cable trays were assembled atop the TOF array and inside the AGS floor to hold the cable bundles.

Once the signal cables were laid between the detector and the DAQ electronics, the opposite ends of each cable were mapped. This task was tedious in that six hundred cables needed to be mapped to the correct PMTs. The mapping was done by setting up a constant NIM pulse through each cable at the input near the detector, and using an oscilloscope to search for the associated output among the ends of the cables near the DAQ electronics.

Much of the high voltage cabling had disappeared when E896 acquired the Central Wall, and had to be replaced. About four hundred RG-59 75 Ω cables (to accommodate the Central Wall and Side Walls), each about 50 feet long, were fabricated. SHV connectors (Kings 1705-1) were installed on each end of the high voltage cables.

2.4.3 Time-Of-Flight Side Walls

The TOF Central Wall is ideal for detecting the π mesons from K_s meson decay and the protons from Λ hyperon decay. However, π^- mesons from Λ hyperons (and H_0 di-baryons), and π^+ mesons from $\overline{\Lambda}$ hyperons tend to have lower momentum, and are thus deflected to the left or right of the Central Wall.

The TOF Side Walls were thus built at Rice University and placed on the beam left and beam right sides of the Central Wall to intercept the π^- mesons from Λ hyperons (and H_0 di-baryons), and possibly π^+ mesons from $\overline{\Lambda}$ hyperons. These walls could also be used as an online trigger for events likely to contain a Λ hyperon or $\overline{\Lambda}$ hyperon, as described in subsection 2.5.2.

The scintillator slats in the Side Walls have a width of 5 cm, a thickness of 1 cm, and a length of 100 cm. The beam left Side Wall is comprised of 26 slats, whose assigned hole numbers range from 1 to 26. The beam right Side Wall has 14 slats, numbered 187 to 200. In each Side Wall, the slats are arranged side by side so that the 5 cm wide surface faces the target.

Bicron BC404, used in the Central Wall, was the plastic scintillator chosen for the Side Wall slats as well. At the opposite ends of each slat were affixed Hamamatsu model 1398 PMTs.

To make the slat surfaces reflective, the slats were wrapped in white Tyvek paper. Whereas aluminum foil is typical, Tyvek was used instead because it has a 30 percent

higher reflectivity than does aluminum foil. Tyvek was also used because it is much less electrically conductive than aluminum foil. This is of concern since the PMTs are operated at negative high voltage; this puts a negative voltage on the PMT photocathode, which comes in contact with the slat and its wrapping. When operating the PMTs at negative high voltage, the PMT anode, from which the signal is extracted, can be kept at ground. This removes the need to separate the time-varying PMT signal from the constant positive high voltage of the anode. However, the photocathode must be set at negative high voltage, so that the photoelectrons can accelerate toward the higher-stage dynodes and anode. If a conductive wrapping is used, the negative voltage on the cathode can induce a positive charge on the wrapping near the photocathode. This sets up a stray electric field that can distort the flight of the photoelectrons that are emitted from the photocathode. Also, since the top and bottom PMTs are, in general, operated at different voltages, the effect of the foil would be to try to equalize the photocathode potentials on each PMT. This also distorts the PMT signal.

The Tyvek paper was cut to a length of about 2 mm shorter than that of the plastic, to leave some room when affixing the PMT later; and to a width of about 15 cm, to allow for enough overlap when covering the plastic. The edges of the plastic were used to crease the Tyvek, to allow for good surface-to-surface contact between Tyvek and plastic. To minimize scratches to the plastic, cotton gloves were used

during this process. After wrapping the Tyvek around the plastic, the Tyvek was taped down, lengthwise across the overlap, using black 3M Super 33+ electrical tape.

Before the gluing stage, each PMT's dark current was tested. "Dark current" is the signal that arises from an electron cascade initiated by some process other than the photon-induced ejection of electrons from the photocathode. Dark current rates are typically of the order of milliseconds, and their pulse heights are rarely in excess of 50 mV ([17] p. 208). The PMT and base were shielded from exterior light. Because of the low dark-current rates, the signal line from the anode was sent to an image-intensifying oscilloscope. The typical applied voltage was -1500 V. Among the Hamamatsu 1398s tested, the pulse height of the dark current ranged from -6 mV to -80 mV; -15 mV was typical. Noisy or jagged-looking signals were typically due to faulty bases. Weak signals or "arc-ing" behavior (periodic increases of anode voltages from zero to tens of volts) indicated a defective PMT.

After the PMTs were tested, the wrapped slats were mounted vertically upright in preparation for the affixing of the PMTs to the slats. Epotek optical epoxy was used for this purpose. As light guides were not needed, none were used.

Five drops of the mixed epoxy were applied using a syringe at the center of the edge of the plastic where the PMT would be glued. Care was taken so that no visible air bubbles were created in the epoxy while mixing. The PMT was placed atop the epoxy puddle and plastic, and held in place with masking tape.

After being mixed, the epoxy remains quite fluid for about two hours, but fully hardens in about twelve hours. When the epoxy was fully cured, the slats were turned upside down, and PMTs were glued to the opposite ends of the plastic.

Once the PMTs were glued to each end of the Side Wall slats, the remaining unexposed scintillator surfaces were wrapped with about four layers of white plastic plumber's tape. Such tape is diffusively reflective, and is flexible enough to adapt to the contours of the edges of the plastic and PMT.

The next step was to "light-tighten" the slats; that is, to prevent any external light from reaching the scintillator plastic or the PMT. Black photographic plastic was cut to about the same dimensions as was the Tyvek, and wrapped tightly around the slat. At each end of the slat, the black plastic wrap/scintillator plastic/photocathode junction was then covered with about three layers of black 3M Super 33+ electrical tape.

The base was then attached to the PMT, and held in place first using splints of electrical tape, along the length of the PMT-base assembly, and then with the tape wrapped around the PMT-base junction.

A layer of single-stick foam insulating tape, 1/2 in. wide and 3/8 in. thick, was then wrapped around the PMT. A magnetic shield was slipped over the base and onto the PMT, being secured in place by the foam tape, until it rested against the end of the scintillator plastic. The magnetic shield/scintillator junction and the magnetic

shield/base junction were then covered with black electrical tape.

After the slats were fully wrapped, they were each tested for light leaks in a darkened tent. A small flashlight was shined over the entire surface of the slat while the PMT anode signal was monitored. If a light leak (indicated by a pronounced increase in anode pulse height and oscilloscope trigger rate) was detected, it was sealed with black silicone and/or black electrical tape. The overall slat responsiveness was checked using a ^{90}Sr "beta gun" source near the center of the slat.

During these tests, the applied PMT voltage was -1400 V, and the oscilloscope trigger level was set between 50 and 200 mV. The resulting pulse heights from the ^{90}Sr source ranged from -100 mV to -800 mV.

Once the finished slats were tested for response to the ^{90}Sr source and for light-tightness, they were placed onto a frame fashioned from four aluminum Unistrut segments, two in front of the slat array and two in back, and oriented perpendicularly to the slats. The slats were placed side by side between the aluminum Unistrut, with single-stick foam insulating tape, 1 in. wide and 3/8 in. thick, affixed to the edges of the aluminum Unistrut surfaces that faced the slats. The friction of the foam held the slats in place, and the sponginess of the tape prevented damage to the scintillator plastic.

To further secure the PMT/base/magnetic shield assemblies so that they would not sag and create strain upon the epoxy joints, sheets of Plexiglas were affixed to the

Unistrut pieces on the back of the slat array, and the magnetic shields were bonded to the Plexiglas with an RTV-like compound. The front and rear segments of the aluminum Unistrut were bolted together, and the entire array was then bolted to a support structure fashioned from steel Unistrut in the E896 experimental area.

The reference points for the position survey of the Side Walls were chosen to reside upon the front face of the Side Wall slats. The survey targets were placed near the four corners of each Side Wall scintillator array, between the first and second slats from the left and right sides of each Side Wall.

2.4.4 TOF PMT High-Voltage System

For the Central Wall and the two Side Walls, voltage was applied to all of the PMTs using two LeCroy 1440 series high voltage power supply crates. The voltages were distributed to each PMT using LeCroy model 1443N negative high voltage cards, with each card having 16 SHV ports. LeCroy 1445A crate controllers were used to set the voltages on each port. A VT100 terminal was used to communicate with the 1445As via a GPIB interface. RG-59 shielded-high-voltage cables were used to apply the 1443N voltages to the PMTs.

After the Side Wall arrays were reinstalled among the E896 detectors, the PMT gains were set. The ^{90}Sr source was placed at the center of the slat, and the PMT voltage was adjusted until the anode pulse height (after about 10 ns of cable delay) was -300 mV, provided that the PMT photocathode was sufficiently robust. The

pulse amplitudes, rather than the pulse areas, were matched among all PMTs, so as to provide the best possible time measurement.

For the Side Wall PMTs, operating voltages ranged from −1200 V to −1900 V, with −1500 V being typical. The Central Wall PMTs were generally set much higher, typically −1700 V to −2200 V. [18] [5]

2.4.5 TOF Electronics

Figure 2.10 illustrates the signal lines and electronic elements through which the TOF PMT response signals propagate, and denotes the propagation time between each element. The transit time for both the ADC and TDC signal lines, from the PMTs at the detector to the Fastbus DAQ, was about 600 ns, though this varied by about ± 30 ns among all of the signal lines. This long transit time was due to the distance of the TOF system's Fastbus electronics from the detector array itself, a configuration inherited from E877.

Despite the considerable attenuation of the PMT anode signal over this distance, the ADC signal lines went directly from the PMTs to the Fastbus DAQ modules, without shaping or amplification. Ground noise on the ADC lines was measured to be ± 3 mV peak-to-peak.

Once the ADC signals arrived at the data acquisition electronics via RG-58/U 50 Ω coaxial cables, they were sent into breakout boxes, and directed into 110 Ω twisted pair ribbon cables to be plugged into the ADC modules. Although the Fastbus ADC

modules were designed to receive 50 Ω input, which would suggest the use of 50 Ω coaxial ribbon cables, the 110 Ω twisted pair ribbon cables were used instead. This was because of a scarcity of working 50 Ω coaxial ribbon cables, and the fragility of the ones that were available. Also, the 50 Ω ribbon cables were shown to be highly susceptible to noise from the Fastbus power supply. The peak-to-peak noise measured within the 50 Ω ribbon cables was 33 mV, compared with only 4.4 mV peak-to-peak noise measured within the 110 Ω twisted-pair cables.

Despite the impedance mismatch, signal attenuation and reflection was not a problem. To test this, a 985 mV pulse was sent from just beyond the TOF detector into a sample ADC signal line en route to the Fastbus DAQ. The pulse at the end of the twisted pair cable that would go into the ADC module had a height $PH1 =$ 213 mV. The first reflection had a pulse height that was 6.3 percent of $PH1$'s height, and an area that was 1/14 that of $PH1$. The height of the second reflection was 0.6 percent of $PH1$'s height. The separation between each of these reflections was 1082.5 ns, or about one microsecond. Thus, the reflections would fall well outside the ADC gate width of 200 ns. Moreover, with a beam rate of about 10^5 beam particles per spill, subsequent triggers are on average too far apart in time for ADC-signal reflections from one event to affect the ADC measurement in a subsequent event.

Both the ADC and TDC signals traveled through about 600 ns of cable from the TOF PMTs to the data acquisition electronics. The reason for the long signal

travel time is as follows. First, the start pulse must arrive at the data acquisition electronics about 50 ns before the stop pulses. Formation of the start pulse involves a decision made by the central trigger logic. This decision typically takes hundreds of nanoseconds to make. The timing stop signals must therefore be delayed, by hundreds of nanoseconds, so that they are closer in time to the start pulse at the data acquisition electronics. The delay can be achieved electronically, although the use of cables to propagate the signal is a better method, in that it enables the data acquisition electronics to be placed far away from the detector in the E896 beamline.

However, the attenuation of the signal within a cable leads to both a pulse height decrease and a rise time increase. The latter is detrimental to fast timing. To minimize the rise time increase, one propagates the fastest possible timing signal from the TOF PMT to the data acquisition electronics. This is done by putting the PMT pulse through a discriminator close to the PMT anode. The discriminator output has a rise time of about 1.5 ns, compared with the 2 to 3 ns rise time for the PMT anode pulse.

The TDC signals first went into Phillips 706 300 MHz NIM-standard leading edge discriminators, about 10 ns after leaving the photocathode. These discriminator levels were set to -50 mV, high enough to avoid triggering on either ground noise or dark current, yet low enough so that the pulse's leading edge was linear where it crossed the discriminator threshold. The output of the Phillips 706s is a standard NIM pulse.

Prior to going into the Fastbus DAQ, the TDC signals then went via 4 ns of cable into CAMAC-standard leading edge discriminators (Phillips model 7106), about 6 ns in advance of the Fastbus DAQ. The CAMAC discriminator levels were also set at -50 mV, for the same reason as those located 10 ns from the TOF PMTs. The output of the CAMAC discriminators were ECL-standard signals, which were sent to the LeCroy 1875A Fastbus TDC modules via 110 Ω twisted pair cables.

The ADC modules used in the TOF Fastbus DAQ were LeCroy model 1885F charge-integrating ADCs. Each 1885F module has 96 channels; five such modules were required to accommodate all of the TOF PMTs. Because the 1885Fs have an inherent dead time of 50 ns after the leading edge of the ADC gate, the TOF ADC signals were delayed so that they would arrive 60 to 70 ns after the start of the 200 ns wide ADC gate. Thus, the ADC gate could accommodate the entire PMT pulse, whose baseline width at the ADC input was typically 130 ns or less.

The TDC modules were LeCroy model 1875A 12-bit (and one 10-bit 1872A) Fastbus common-start TDCs. The 1875A modules each have 64 channels; seven modules were necessary to accommodate the TOF PMTs, and duplicates of the Beam Counter TDCs. The common start pulse was derived from the Beam Counter-driven trigger. The intrinsic dead time of the 1875A TDCs after receipt of the common start pulse is 45 ns. Thus, the TDC stop signals were timed to arrive about 60 to 80 ns after the start signal. This put the TDC signals' arrival times in the region of best linearity

for the 1875As. [5]

The digital data from the ADC and TDC modules were exported from the E896 TOF DAQ system via an 1821/ECL interface to a VME 1190 memory buffer. The data in the memory buffer was written to Mammoth exabyte tape as part of the E896 data stream for offline analysis.

2.5 Data Acquired from E896 and TOF

2.5.1 April 1998 Gold Ion Beam Run

The AGS produced 11.6 GeV/c/N gold ion beams down the C5 line and onto a 10 % gold target from April 1 to April 30 of 1998. During this "Au98 run," several TOF electronics problems were encountered and resolved. The Fastbus DAQ hardware, which was inherited from E877, was particularly troublesome. Pins would become bent through frequent removal and reinstallation of faulty ADC and TDC modules, and would require replacement. The power supply needed to be replaced once. Problems were also traced to improper voltages being placed on the modules. The so-called ECL card, which serves as the interface between the Fastbus crate and the VME 1190 memory unit, became defective and was replaced several times. Servicing the above hardware elements resolved problems such as stuck BUSY signals (which would freeze the entire E896 DAQ and trigger systems), and stuck bits or dropped bits from the Fastbus crate output (which led to erroneous addresses in the raw data).

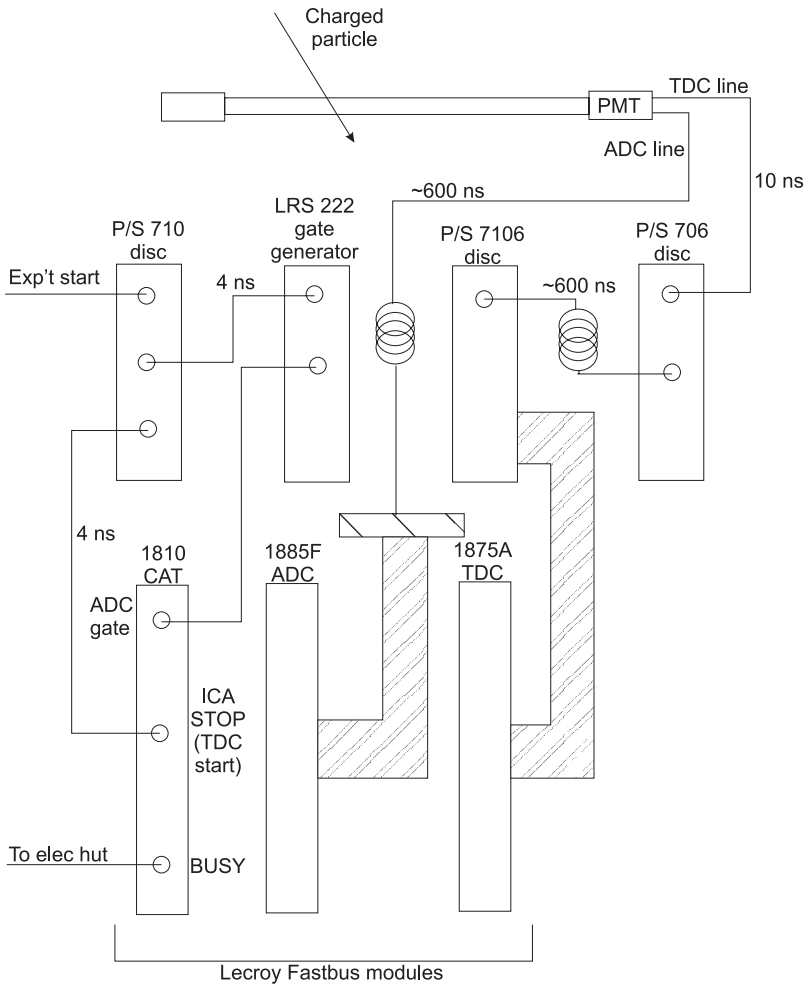

Figure 2.10 A diagram of the ADC and TDC electronics of the E896 TOF system. Only signal cables from one PMT are shown. The other PMT has similar cabling.

The TOF high voltage system also encountered problems. A LeCroy 1442 unit (which applied the high DC voltages to the ports on the 1443N cards) repeatedly tripped during the run. This problem was traced to a cooling fan in the high voltage crate that had stopped, causing the 1442 unit above it to overheat and shut down. Replacing the fans solved the high voltage problems for the remainder of the Au98 run.

An additional problem was that the signals from the Side Wall PMTs required an additional ~ 110 ns in order to fall within the final ADC and TDC gates used in the Central Wall. The necessary RG-58 cable segments were manufactured and added to the eighty Side Wall PMT signal lines.

Throughout the Au98 run, about 92 million central collisions were recorded. Of these, the TOF Central Wall was fully functional during about 67 million events, and the Side Walls were on line to record about 57 million events.

The analyses documented in the remainder of this Thesis used about 11 million of these central events. One reason the analysis was restricted to this subset of the events was because of a decrease in the DDC efficiency observed in many of the other runs when the beam rate exceeded $75k$ particles per spill. Also, only those runs were used for which the raw data was available from the independent analysis pass, called "Pass II," to compile the run-dependent timing offsets described in subsection 3.2.4.

2.5.2 September 1998 Single Hadron Beam Run

The "p98 run" was conducted during September of 1998, when the AGS was providing single hadron beams. The bulk of E896's data taking featured a 15 GeV/c beam incident upon a beryllium target to produce Λ hyperons for a polarization measurement [14]. Since about 60 percent of π^- mesons from fiducial Λ hyperon decay were expected to be incident upon the Beam Left Side Wall, the TDC signals from that wall were "ORed" together and added to the beam trigger. An event was written to tape only if at least one of the slats of the Beam Left side wall recorded a hit. Thus, only those events likely to contain a Λ hyperon were written to tape. This "Λ hyperon trigger" enhanced the rate of V_0 candidate detection per triggered event by about five times that observed for the minimum bias trigger. This TOF trigger thus significantly improved the event sample size in the Λ polarization analysis.

During a 24 hour period in September 1998, a dedicated "TOF calibration" run was performed. The target was removed and the beam was stepped horizontally across the entire TOF array using the beamline and E896 magnets.

The beam momentum was 4.0 ± 0.5 GeV/c, to allow for greater deflection by the magnets and an ability to direct particles onto a wider range of TOF slats. The "D10" magnet upstream of the target and the sweeper magnet were adjusted to steer the beam over regions of TOF slats. For some of these upstream magnet settings, single particle tracks were also present in the DDC. This would eventually serve as

a powerful tool to tune the DDC-to-TOF track extrapolation software and to verify the positions of the DDC and TOF detectors relative to each other and to the rest of the E896 detectors. The analyzer magnet was operated at both current polarities, to simulate tracks of opposite curvature within the same magnetic field.

Both the Au98 and p98 events were used to develop the TOF analysis software and to calibrate the TOF detector output. This software is described in detail in the next chapter.

Chapter 3
TOF Analysis Software: Extrapolation and Calibration

At a collaborating institution, a pass through all of the raw Au98 data [14] reconstructed tracks and V_0 candidates using the DDC data in each E896 event. This massive computing effort is referred to as "Pass II." Those events which contained a V_0 candidate were selected, and the geometric and kinematic quantities for each V_0 candidate found within these events were saved. Cuts to the trajectory and momentum quantities for those V_0 candidates (similar to those described in greater detail in section 4.1) were then applied to obtain a somewhat cleaner sample of Λ hyperons and K_s mesons from these V_0 candidates.

The Rice E896 data analysis sought to remove even more background from these Λ hyperon and K_s meson candidates by adding flight-time information to the previous V_0 candidate analyses. This process consisted of two stages. First, the V_0 candidate daughter tracks were propagated from the DDC to the TOF array, and assigned to the corresponding struck TOF slat. The raw TDC and ADC data from that slat were then converted into a measured flight time of the daughter and parent, relative to the event start time.

A significant amount of new software was required to perform these tasks. The details of this track extrapolation and TOF signal calibration are the subject of this

chapter. Figure 3.1 summarizes the software tasks performed upon the filtered Au98 data, and the order in which they were applied. The processes performed first are those which propagate the V_0 candidate daughter track to the TOF array, match the track to the slat, and calculate the expected flight time based on momentum information alone for comparison to the measured flight time. Once the track-to-slat association is made, the slat's ADC values are corrected for noise effects, and the TDC values are corrected for gain, time-walk ("slewing"), [19] [20] and time-measurement offsets, as described.

3.1 Association of DDC Tracks to TOF Slats

3.1.1 Track Extrapolation from DDC to TOF

The first step in matching a DDC track to a struck TOF slat is to propagate in software the track's location at the DDC to the correct location upon the TOF array. Parameters in this propagation are the precise locations of the DDC and TOF, the measured three dimensional magnetic field between them, and the algorithms used to extrapolate the track in software.

Three complicating factors must be overcome. First, Au98 central-event data cannot efficiently be used to test the DDC-to-TOF extrapolation, since such events have about five to ten DDC tracks and twenty to forty struck TOF slats. Far more useful would be a data set whose events consist of exactly one DDC track and exactly one struck TOF slat. Such a data set was compiled during the September 1998 proton

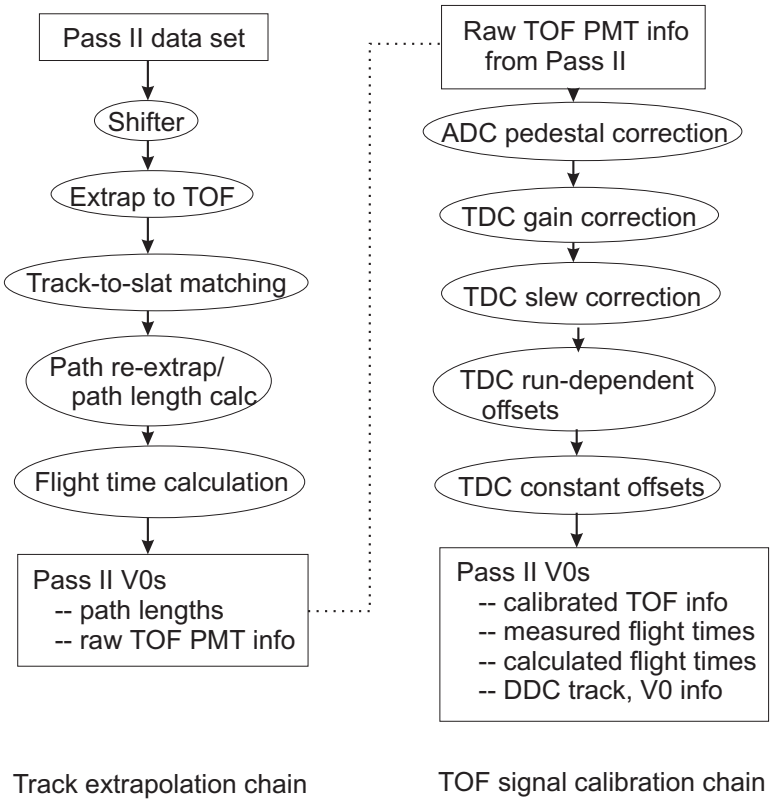

Figure 3.1 The software tasks performed on the data from E896 Au98 events that were earlier found to contain at least one V_0 candidate.

run ("p98") as described in subsection 2.5.2, and used in this track extrapolation study.

Another complicating factor is the strong variation of the magnetic fields with position between the DDC and TOF. These analyzer fringe fields were mapped [21] and implemented into the present software. The remaining required component is the track stepping algorithm that accommodates the strongly varying fringe fields. Three different track extrapolation algorithms were employed in the different regions within the E896 apparatus:

- *Helix extrapolation* involves propagating the track circularly in the xz plane, and linearly in the y direction. It was used to propagate tracks interior to the DDC, where the magnetic fields were nearly constant.

- *Runge-Kutta extrapolation*, based on the GEANT [11] GRKUTA routine, is performed in steps of 1 cm in the z direction. It was employed in the z range spanning from the DDC track's downstream endpoint to about 40 cm upstream of the TOF array. In this area, the analyzer fringe fields are highly nonuniform.

- *Linear extrapolation* simply involves extending the track in the direction provided by the momentum vector at the point of origin of the extrapolation. It was used in the vicinity of the TOF array, where the magnetic fields were negligible.

A third complicating factor in proper track-to-slat matching is that there is a two to three meter flight path between the DDC and TOF. This is a long flight path

between a tracking detector and a TOF detector in typical experiments. This allows affects such as particle scattering over small angles in air to contribute to the matching uncertainty.

The following variables are used during the track to slat matching calculations:

• The *extrapolator estimate* is the hole number of the TOF slat that the extrapolator code predicts is struck by a specific DDC track.

• The *actual TOF slat hit* is the hole number of the struck TOF slat closest in proximity to the extrapolator estimate, possibly under additional constraints described below.

• The *extrapolator accuracy* is the *extrapolator estimate* minus the *actual TOF slat hit*. "Perfect matching" gives an extrapolator accuracy of zero across the entire TOF array, for all particle momenta and path lengths.

The objective of the track extrapolation study is to bring the peak value of the extrapolator accuracy among all matches as close to zero as possible. Also, the width of the extrapolator accuracy distribution is used to estimate the multiple coulomb scattering (MCS) effect upon the particle propagation from the DDC to TOF, as described in more detail below.

While the Au98 data-filtering pass was conducted throughout 1999, an error was discovered in the surveyed coordinates of the DDC wire map such that the DDC was 6.51 cm too far downstream. This wire map error was actually discovered during the

development and testing of the present track extrapolation code. Figure 3.2 plots the extrapolator accuracy versus the actual TOF slat hit for p98 tracks, before (left frame) and after (right frame) the DDC wire map offset was discovered. In the left frame, as the actual TOF hole hit increases, the extrapolator accuracy (extrapolator estimate minus actual TOF hole hit by the p98 track) steadily becomes more negative. The effect suggests that the p98 tracks are not being sufficiently deflected within the extrapolation software.

This "extrapolator undershoot" was in fact not due to a deficiency of the present code, but rather to the DDC wire map being located too far forward in z, relative to the analyzer magnet field map. There was not enough analyzer fringe field to sufficiently deflect the p98 tracks, hence the undershoot. After ruling out all other possible sources for the undershoot problem (extrapolator code, TOF geometry, magnetic field map values), a $\sim$6 cm shift of the DDC wire map was found to resolve the systematic undershoot, and render the extrapolator accuracy constant with respect to the location on the TOF array. Once the suggestion was made to the E896 collaboration that the accepted position of the DDC wire map may be incorrect, a measurement was taken in the E896 experimental area in November of 1999. This indeed indicated that the DDC position was actually 6.51 cm farther upstream than was the DDC position in the default wire map in use by the collaboration as a whole. Erroneous transverse mass and rapidity distributions were being obtained in other E896 analyses, and this

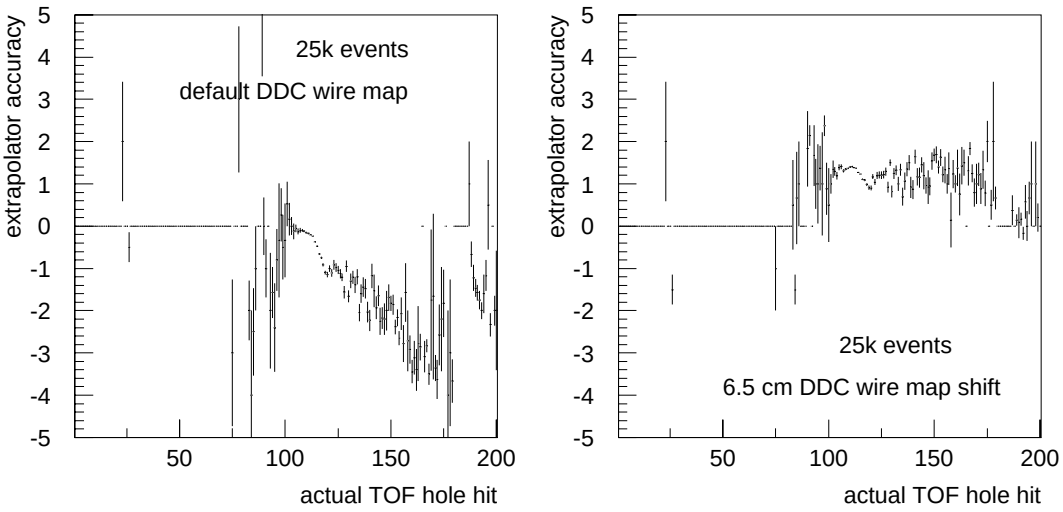

Figure 3.2 The extrapolator accuracy versus the TOF hole number for the actual slat hit, for p98 events, with the DDC wire map used before the error was uncovered.

discovery of the DDC wire map error remedied this problem.

Correcting the DDC wire map for this shift yielded the plot shown in the right-hand frame of Figure 3.2. The extrapolator accuracy became constant with respect to the actual TOF hole hit by the p98 particle. A shift of the TOF Central Wall geometry of $\sim$ 2 cm toward beam right had yielded an extrapolator accuracy near zero across the entire TOF Central Wall.

The geometry and field parameters that were eventually applied are summarized in Table 3.1. An additional -3.5 mrad rotation of the wire map was necessary in order for the V_0 candidates found in the earlier pass to point back to the correct target location. Thus, the position coordinates of the tracks found and fitted during

the data-filtering pass needed to be shifted and rotated, and the track momentum coordinates needed to be recalculated.

parameter	*setting*
Magnetic field maps	default mapped fields
DDC wire map	z range: 484.64 cm to 494.64 cm;
	-3.5 mrad rotation in xz plane
TOF Central Wall	shifted 2.4 cm toward beam right in x
TOF Side Walls	default surveyed positions

Table 3.1 The overview of the parameters relevant to extrapolation of DDC tracks to the TOF array.

The extrapolator accuracy versus the actual TOF slat hit, after the DDC wire map problem was fixed, is plotted for p98 events in Figure 3.3. For the regions of the TOF array covered by p98 tracks, the mean extrapolator accuracy is indeed very close to zero, and within statistical uncertainties constant with respect to the TOF slat location. This indicates that the track extrapolation from the DDC to TOF is now being handled appropriately in the present software.

Figure 3.4 shows the extrapolator accuracy distribution for p98 hits upon the TOF Central Wall. This is basically the projection of Figure 3.3 onto its vertical axis. The width of this distribution is about 0.6 slat widths, or about 1 cm. This is consistent with the spreads in the extrapolator accuracy distributions versus hole number apparent in Figure 3.3.

This horizontal 2 cm resolution in the track propagation to TOF can be shown

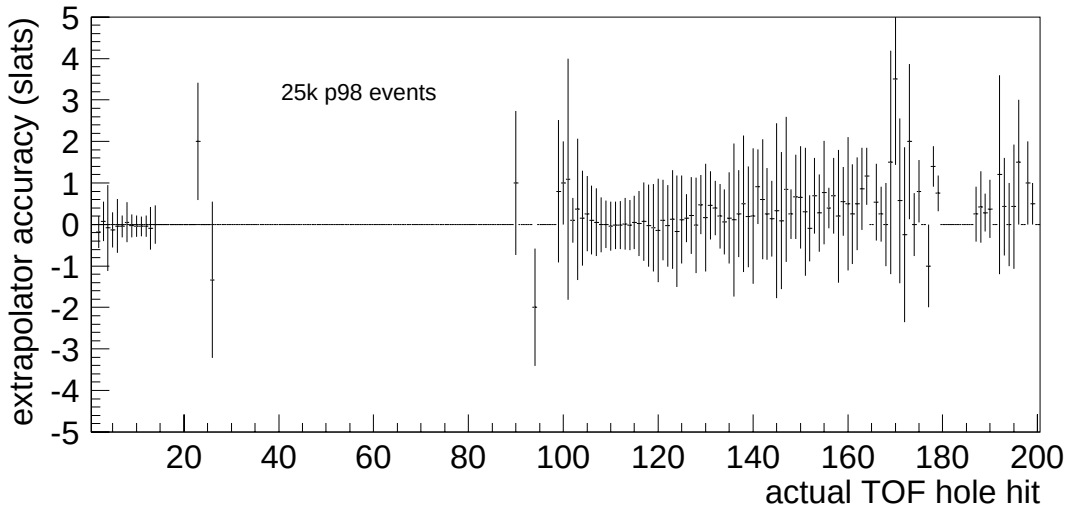

Figure 3.3 The extrapolator accuracy versus the TOF hole number for the actual slat hit, for p98 events.

to be consistent with multiple coulomb scattering (MCS) effects. MCS is present in the actual particle flight, but as it is a stochastic process and there are no detectors intermediate to the DDC and TOF, this smearing cannot be estimated track by track. A 2 cm resolution in the vertical direction based on the known errors in the DDC track reconstruction is also predicted [14], and will be apparent in the track-to-slat matching studies to be described next.

3.1.2 Track-to-slat Matching and Track Path-length Calculations

In the track propagation results just described, the horizontal resolution of the extrapolator estimate is approximately one slat width. About 30 percent of the time, the extrapolator estimate and the actual TOF hole struck by the particle will not be

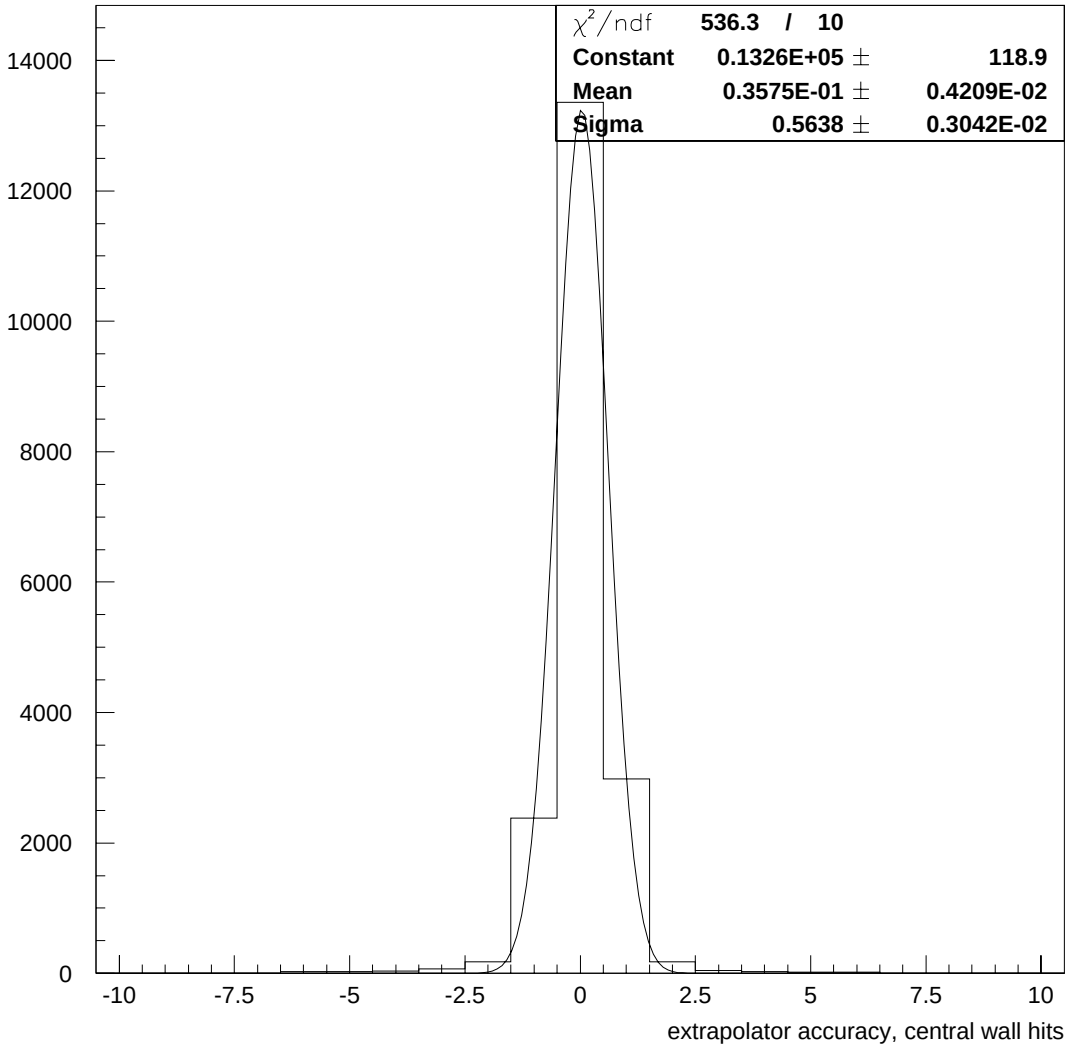

Figure 3.4 The extrapolator accuracy distribution for p98 track-to-slat matches upon the central TOF array.

the same, leading to the possibility of incorrect track to slat matches. In fact, when including downstream scattering at a low level, the struck TOF slat corresponding to the extrapolated track may be as many as two slat widths to beam left or beam right of the extrapolator estimate.

The presence of twenty to forty struck TOF slats in Au98 central events thus complicates the matching of a TOF slat to a DDC track, in that the $\pm$ 2 slat range about the extrapolator estimate for a given track may feature more than one struck TOF slat. In such a situation, a physical quantity which can be determined by both the track extrapolation code and the TOF slat data is needed to resolve this ambiguity.

The vertical coordinate of a track's incidence upon a TOF slat is such a quantity. Figure 3.5 plots the difference between the bottom and top TDC values from a struck TOF slat, TDC_{diff}, versus the y coordinate at the TOF wall predicted by the extrapolator code, "$y_{tracking}$." The tight linear correlation is interpreted as those tracks correctly matched to the slat shown in this figure. Thus, if there exist several struck TOF slats in the vicinity of the extrapolator estimate, the struck TOF slat whose TDC_{diff} value is most consistent with the y coordinate of the extrapolated track is chosen for the track-to-slat match.

The algorithm used to match a unique struck TOF slat to an extrapolated track can be described with the aid of Figure 3.6. The track-to-slat matching algorithm

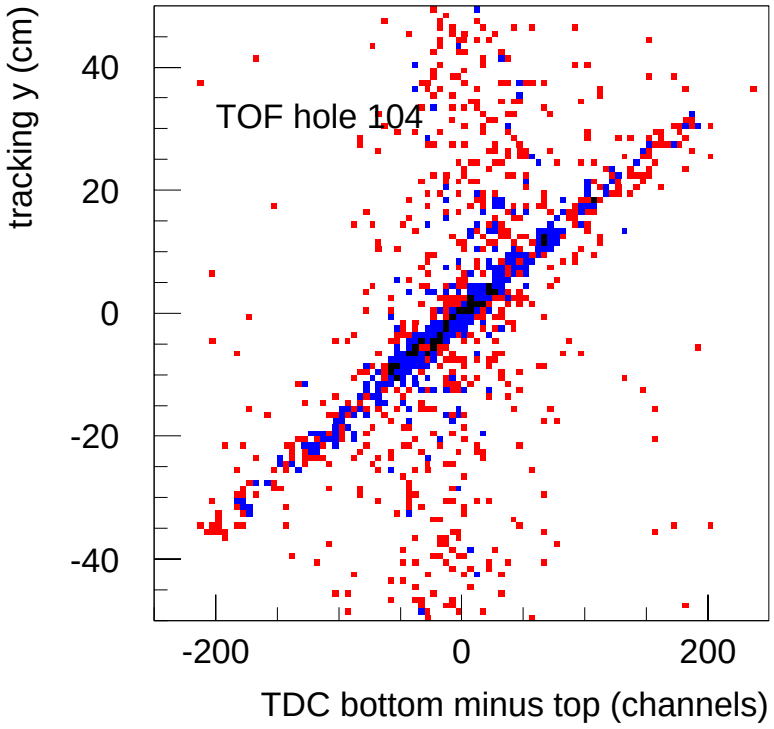

Figure 3.5 The y coordinate given by the extrapolator code versus the difference between the bottom and top raw TDC values, for Au98 tracks matched to a sample slat.

checks for hits on all TOF slats within two slat widths of the extrapolator estimate (the center slat in Figure 3.6). The slat whose y coordinate inferred from TOF TDC information (represented by circles in Figure 3.6) is most consistent with the extrapolator y coordinate (represented by X's) is matched to the track. In Figure 3.6, the track would be matched to the slat immediately to the left of the extrapolator estimate.

The matching algorithm thus proceeds as follows. First, for each of the struck slats within two slat widths of the extrapolator estimate, the values of TDC_{diff} were obtained. These TDC_{diff} values were converted to "y_{TOF}" values, using the linear dependence between $y_{tracking}$ and TDC_{diff} such as that apparent in Figure 3.5. The quantity

$$\Delta y = |y_{tracking} - y_{TOF}| \tag{3.1}$$

was then computed for each struck slat. The slat with the minimum Δy was matched to the extrapolated track.

Figure 3.7 shows the Δy distribution for all matches of tracks to a given TOF slat. That distribution is used to define the quantities that gauge the success of the track-to-slat matching algorithm. The Δy distribution can be fitted with a function that is comprised of the sum of two Gaussians, one "peak" and one "background." The curve in Figure 3.7 depicts the fit to the background distribution. The number of

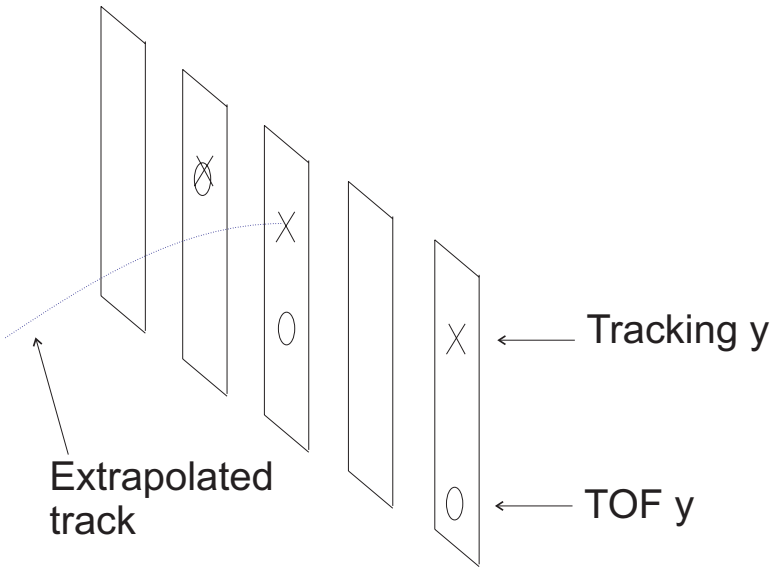

Figure 3.6 A scenario in which the actual TOF slat hit by a particle, according to vertical coordinate comparisons, is not the same as the slat intercepted by the particle's DDC track extrapolated to TOF.

correct matches is the area underneath the "peak" Gaussian, above the "background" Gaussian curve. The number of incorrect matches mistakable for good matches is taken to be the area underneath the background Gaussian curve, in the range from $\mu \pm 3\sigma$, where μ and σ are the mean and width, respectively, of the peak Gaussian. Note that the width of this distribution is about 2 cm, consistent with the horizontal resolution of the track extrapolation. The sigma of the Δy distribution is also about 2 cm. This vertical extrapolation resolution is consistent with the horizontal resolution of 2 cm seen in the track propagation study.

From these curve integrals, along with the total number of track-to-slat matches, the following match-quality variables are defined for each TOF slat:

- *correctness-of-match efficiency*: ϵ_{match} = good matches/all matches
- *signal-to-background ratio*: SN = good matches/mismatches

The quantity ϵ_{match} was determined for matches in which no track-quality cuts were applied, and for matches to "good" tracks, *i.e.* those with over 80 wire hits in the DDC assigned to them during the reconstruction. The left frame of Figure 3.8 shows ϵ_{match} versus the TOF hole number, without and with the wire-hit-per-track cut. Across the entire TOF array, ϵ_{match} ranges from 30 percent to 60 percent. Losses in efficiency may be attributed to downstream interactions of particles between the DDC and TOF. The match efficiencies increase substantially with the "good" track cut; the quantity ϵ_{match} then ranges from 70 percent to 90 percent. The right frame

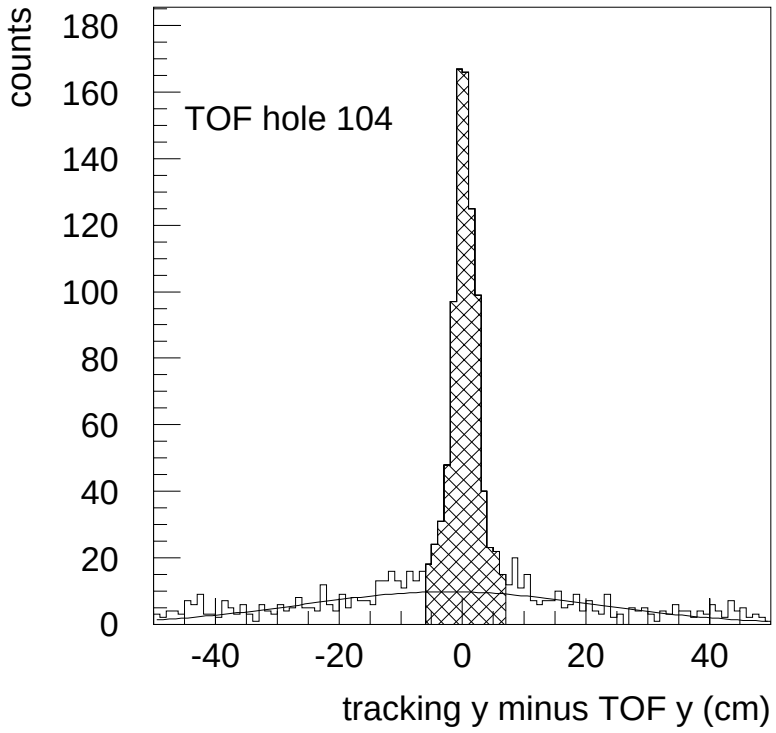

Figure 3.7 The difference between the extrapolator y and the TOF y coordinate (converted to units of distance), for matches to a sample TOF slat from Au98 events.

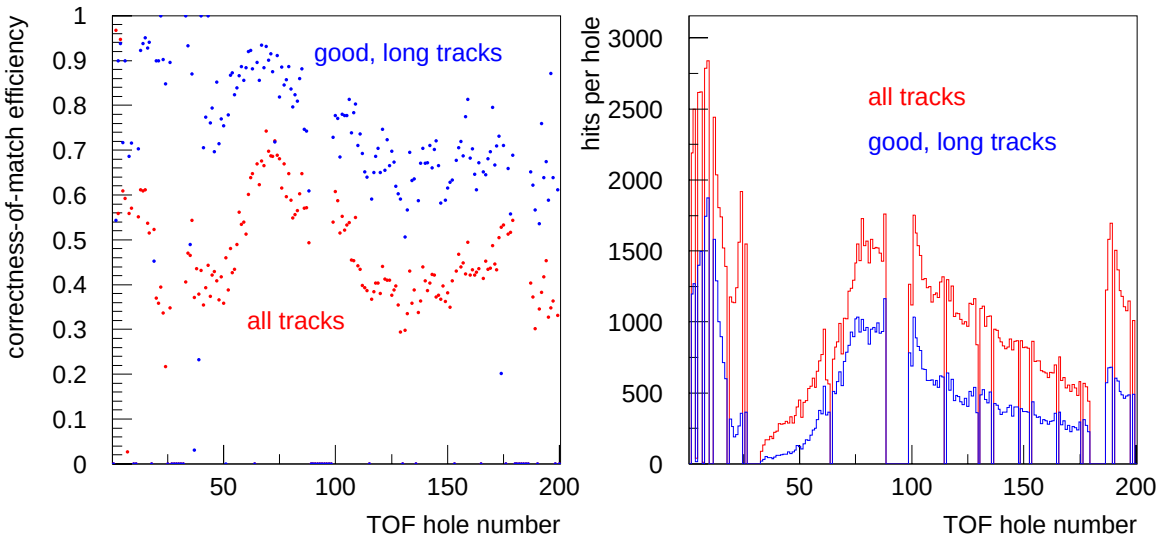

Figure 3.8 The correctness-of-match efficiency versus TOF hole number is plotted in the left frame. The right frame shows the number of tracked particles per slat.

of Figure 3.8 shows the distribution of extrapolated track hits per hole number. The trend in ϵ_{match} versus hole number follows that for the particle hit rate, *i.e.* the "occupancy," versus the hole number for DDC tracks extrapolated to the TOF array.

The signal-to-background ratio versus the TOF hole number is shown in Figure 3.9. As does ϵ_{match}, SN tends to peak near the neutral line, which passes through TOF hole 56; in this region, tracked charged-particle multiplicities are high while non-tracked particle multiplicities are low, making for more precise matching. ϵ_{match} is also high over the beam-left TOF Side Wall; particles which hit this wall have shorter flight paths, and thus a lesser probability of experiencing DSIs or MCS. An increase in DSI probability with flight path length may also explain the decrease in

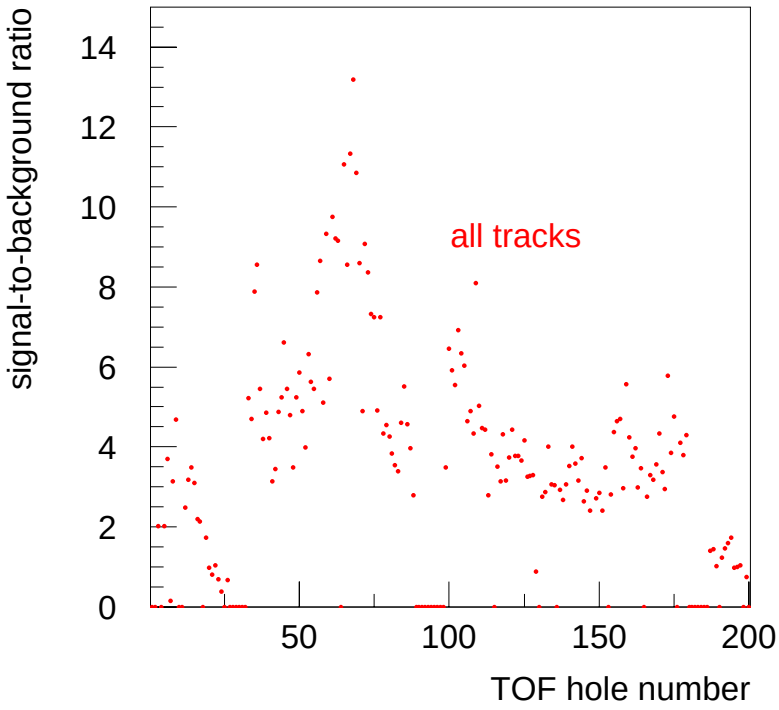

Figure 3.9 The signal-to-background ratio versus the TOF hole number, without any track quality cuts applied to the tracks matched to TOF slats.

ϵ_{match} (as well as SN) over the beam-right half of the TOF array. The quantity ϵ_{match} tends to dip around TOF hole 125. In this region, many non-tracked projectile-like protons are present, greatly increasing the probability of mismatches.

Figure 3.10 plots the extrapolated path length minus GEANT path length for simulated tracks from Monte Carlo Λ hyperons. Because the path length is calculated during the extrapolation to TOF, a deviation of the extrapolator accuracy from zero points to a systematic error in the path length calculation. This is especially apparent

for matches on the TOF Central Wall such that the extrapolator accuracy = ± 1 slat width. Since the Central Wall slats are set in a staggered double-layer pattern, the calculated path length may be off by 1.5 cm. The double peak behavior is due to the staggering of the Central Wall slats.

Thus, an algorithm was implemented to correct the path length calculation for matched tracks whose extrapolator accuracy was nonzero. The method is illustrated in Figure 3.11. First, the downstream endpoint of the DDC track and the midpoints of the actual TOF hole hit and the extrapolator estimate are used to define an angle θ_{xz} in the xz plane. The momentum vector of the track at the downstream endpoint is then rotated by θ_{xz}. The track is then re-extrapolated to TOF, and the path length is recalculated.

The result of this path-length recalculation, for the simulated V_0 candidate daughters depicted in Figure 3.10, is shown in Figure 3.12. The double-peak behavior is removed from the distributions, and the extrapolated path lengths are now more consistent with the GEANT path length. There will be more discussion of the accuracy of the extrapolator code's calculations using more detailed methods later in this chapter.

Although the differences between the extrapolator code's calculation and the GEANT software's calculation are not all centered at zero, the mean is within the sigma for all comparisons except for the difference between calculated time and GEANT time for positive daughters whose extrapolator accuracy was equal to +1 (lower right

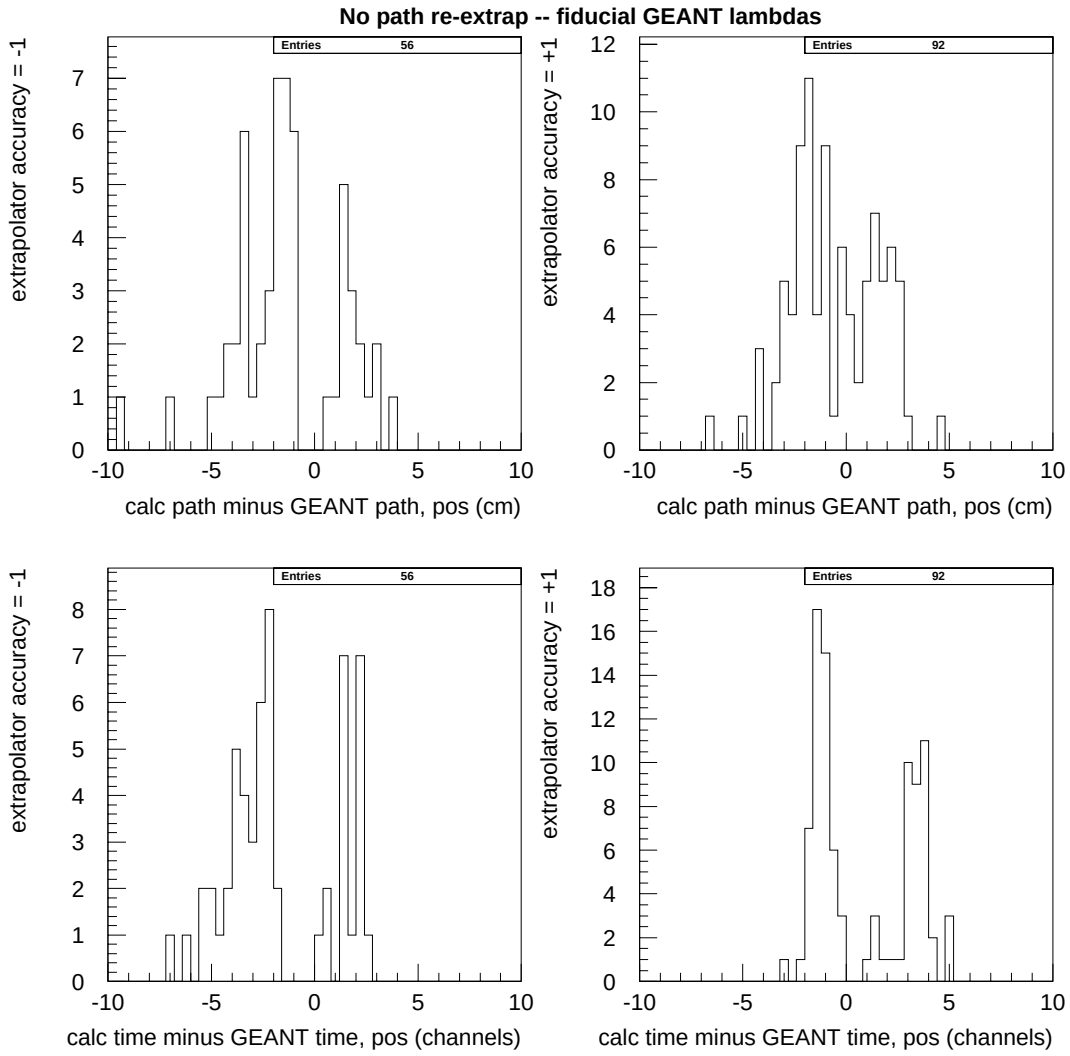

Figure 3.10 The upper frames plot the difference between the calculated path length and the path length given by GEANT, for the positive daughters of fiducial Monte Carlo Λ hyperons. The lower frames show the differences in the corresponding flight times.

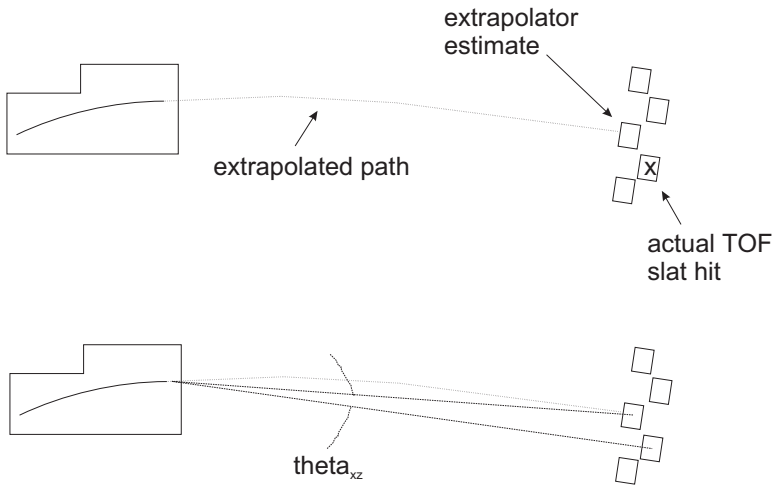

Figure 3.11 The upper drawing illustrates a situation in which the extrapolator estimate and the actual TOF slat hit are not equal. The method to correct for this is shown in the lower drawing.

frame).

3.1.3 Flight Time Calculations

With the path length calculations of the V_0 candidate daughter particles complete, all that remains is to calculate the flight time of the combination of daughter track and parent, for the $\Lambda \rightarrow \pi^- p$ and $K_s \rightarrow \pi^+\pi^-$ assumptions for V_0 candidates. Figure 3.13 schematically illustrates a V_0 candidate topology, the required quantities for reconstruction of each component of that topology, and the manner in which they are obtained. For each segment of the V_0 candidate topology, the flight times were calculated using Equation 3.2:

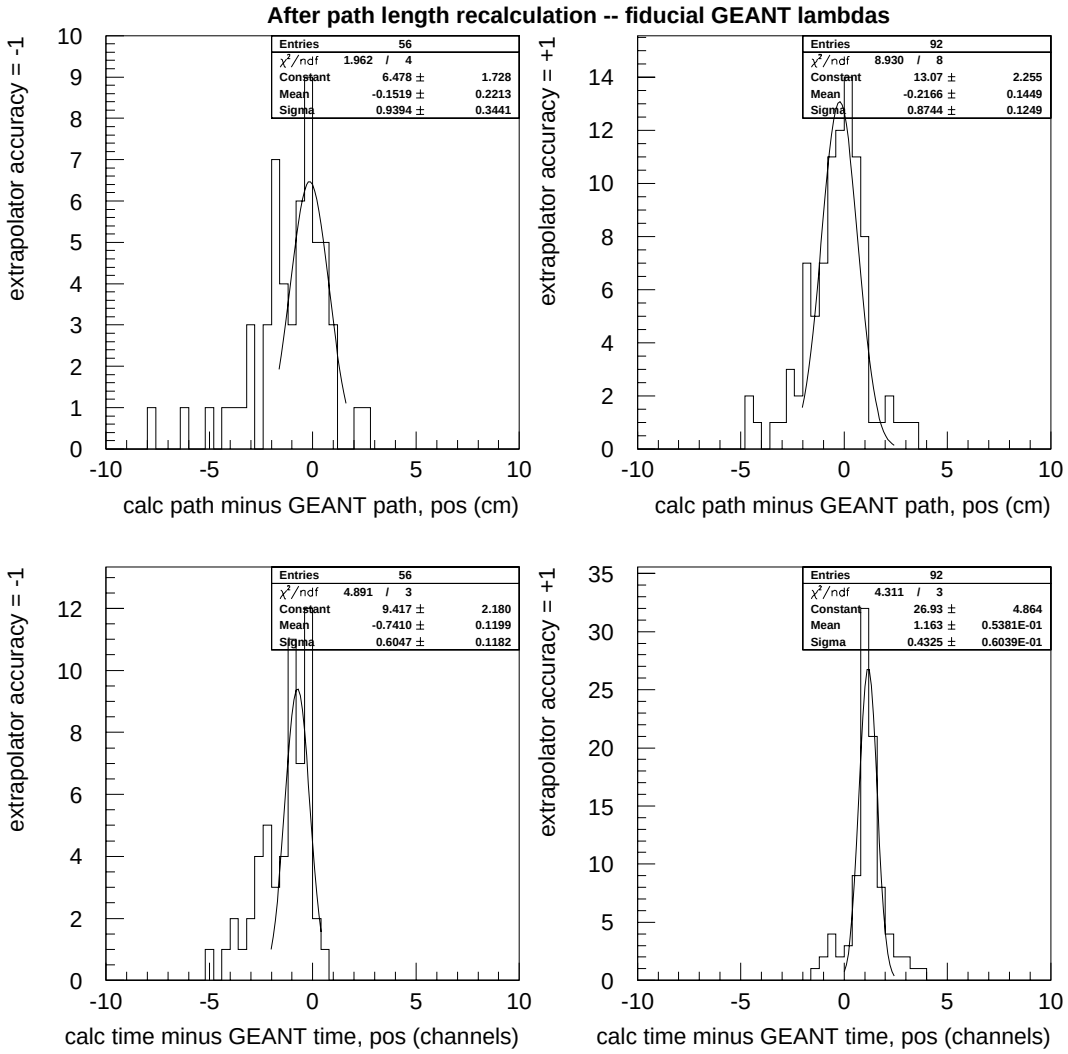

Figure 3.12 The same distributions in Figure 3.10, after the momentum vector rotation and path length recalculation.

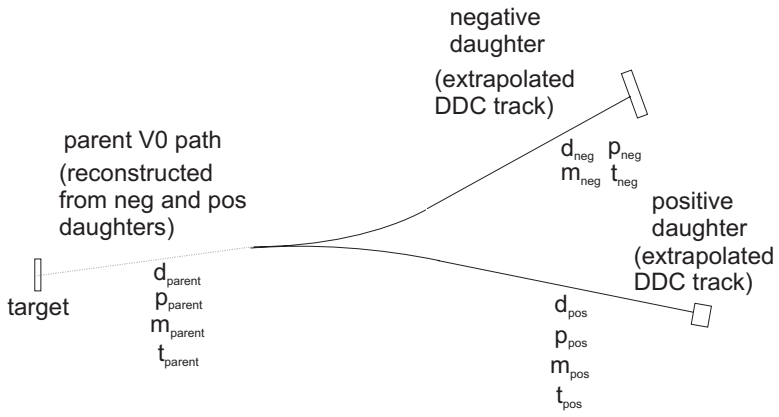

Figure 3.13 The V_0 candidate topology and a listing of the pertinent quantities for the flight time calculation of each leg of the topology.

$$t = \frac{d}{c}\sqrt{1 + \frac{m^2}{p^2}}. \tag{3.2}$$

Digitized simulated Λ hyperons were used to determine the accuracy of the extrapolator code's calculation of parent and daughter flight times. The results are shown in Figure 3.14. The upper frames compare the path length calculations from the track extrapolation code and from GEANT, and the bottom frames compare the flight time calculations. The left frames show the correspondence between calculated flight time and GEANT flight time for the positive daughter and the right frames show the same for the negative daughter. Gaussian fits are applied to each distribution. For the positive daughters, the extrapolator code can reproduce GEANT's calculation of path length with 1 cm resolution (upper left frame), and flight time to within 30 ps

(lower left frame). For the negative daughters, the path length calculation resolution, for the extrapolator code as compared with GEANT, is about 2.5 cm, and the flight time calculation resolution is about 40 ps.

3.1.4 Summary of Track-to-slat Association

The extrapolation code can propagate DDC tracks to the TOF array with an uncertainty of about 2 cm along both the horizontal and vertical axes. The uncertainty is consistent with particle deflections expected from MCS.

The correctness-of-match efficiencies for well-fitted DDC tracks extrapolated to TOF varies from 70 to 90 percent. The dependence of ϵ_{match} upon the TOF hole location can be explained in terms of the tracked charged-particle densities and flight path lengths for tracks incident upon different regions of TOF.

Compared with GEANT's calculation, the path lengths and flight times of the V_0 candidate daughter tracks calculated using the track extrapolation code exhibit an uncertainty of $\sim$1 cm and $\sim$30 ps for the positive daughter, and $\sim$2.5 cm and $\sim$40 ps for the negative daughter.

After applying the extrapolation, matching, and path and time calculation software to the filtered V_0 candidates, the path lengths and flight times of the V_0 candidate daughters are now determined. Also, for each of the V_0 candidate daughters which match to a TOF slat, raw TOF TDC and ADC information can be associated with the daughter particle. These raw TDC and ADC values are converted into flight

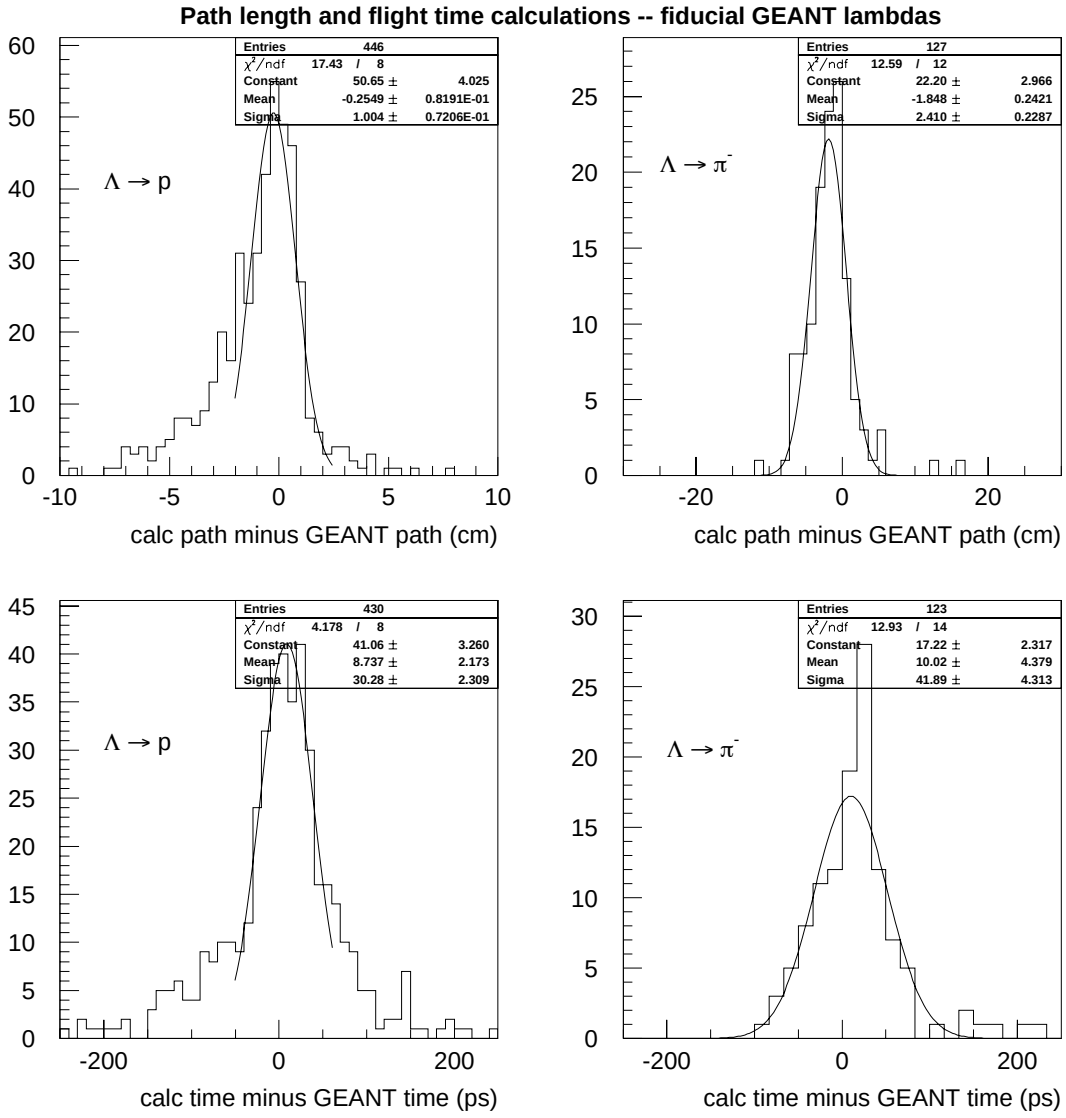

Figure 3.14 Comparisons of path length and flight time differences between the track extrapolation code and GEANT, for the decay daughters of simulated neutral particles.

times measured relative to the event start using software that accounts for various electronic effects in the raw data. The next section describes these TOF calibration tasks.

3.2 TOF Signal Calibration

3.2.1 ADC Pedestal Correction

When using PMTs in modern heavy-ion experiments, it is common that there is a certain amount of noise on the detector ground, which when digitized in an ADC results in varying baseline ADC values, *i.e.* pedestals. The source of ADC pedestal noise can be traced to points of contact between the "clean" AC power supply, used to power the TOF PMTs and the Fastbus ADC modules, and the ambient "dirty" AGS ground. Identifying and removing the ADC pedestal in software requires an independent variable that correlates in time with the dirty AGS ground. In the US, AC power operates in a standard 60 Hz cycle, hence the time dependence of the ADC pedestal also exhibits a 60 Hz cycle.

To provide to the E896 data stream a variable that correlates linearly with the phase of the 60 Hz AC cycle, a AC line-synchronized ramp generator was built at Rice University [22]. Figure 3.15 shows the phase of the ramp generator output with respect to the 60 Hz sinusoidal waveform. This generator uses the 60 Hz waveform from any AC power supply as a reference to produce a sawtooth waveform whose period is $1/(60\text{ Hz}) = 16.\overline{6}$ ms. The zero crossing of the 60 Hz AC waveform fires a

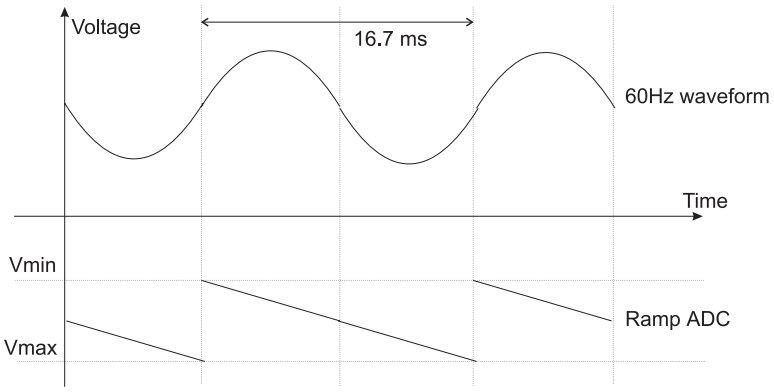

Figure 3.15 The phase of the ramp generator output (the "sawtooth" profile on the bottom) with respect to the 60 Hz AC waveform (top profile).

"one-shot" that resets the ramp generator output.

The ramp generator output is connected to a spare Fastbus ADC channel in the E896 TOF DAQ crate. Since the ADC gate width of 200 ns (see subsection 2.4.5) is five orders of magnitude smaller than the sawtooth period, the ramp ADC effectively measures the exact height of the sawtooth at the same time as an experiment event occurs. Thus, the ramp ADC measures the time the ADCs and TDCs are gated with respect to a clock synchronized with the AC power line (60 Hz).

The distribution of measured ramp ADC values over a single run is shown in Figure 3.16. The horizontal axis is ADC counts. The low end of the horizontal scale at ~ 3000 corresponds to $t = 0$, while the ramp ADC value of ~ 25000 corresponds to $t = 16.\overline{6}$ ms. The low end of the distribution is offset from zero using a knob on the

ramp generator box. The gap in the distribution seen around channel number 5000 is an artifact of the dual range mode of operation of the Fastbus ADC module. If an ADC measurement exceeds 4095 channels, the internal gain of the ADC switches from low range to high range. If the high-range ramp ADC values are simply shifted offline so that this gap is eliminated, the resulting distribution could be scaled to values of time in 60 Hz cycle, from $t = 0$ to $t = 16.\overline{6}$ ms.

Figure 3.17 shows the dependence of four sample TOF PMT pedestals upon the ramp ADC. In each frame, the pedestal dependence upon 60 Hz phase is single valued. Also, the TOF pedestal at the minimum ramp value is about equal to that at the maximum ramp value. Different groups of PMTs exhibit a distinct shape of the 60 Hz correlated pedestal. This indicates that several distinct ambient grounds, each with a different phase relative to the 60 Hz cycle, have somehow come in contact with the E896 detector electronics.

The event-by-event pedestal correction technique is as follows [12]. The pedestal values for each of the TOF PMTs are extracted versus the ramp ADC from the first five thousand events of each raw data file. For each TOF PMT not struck by a particle (TDC = 0), the pedestal ADC value is plotted versus the ramp ADC value in a profile histogram, an example of which is shown in Figure 3.18. A profile histogram is an HBOOK [23] structure which displays the average value (and its uncertainty) of the ordinate variable, for each bin in the abscissa. The frame shows the mean value of the

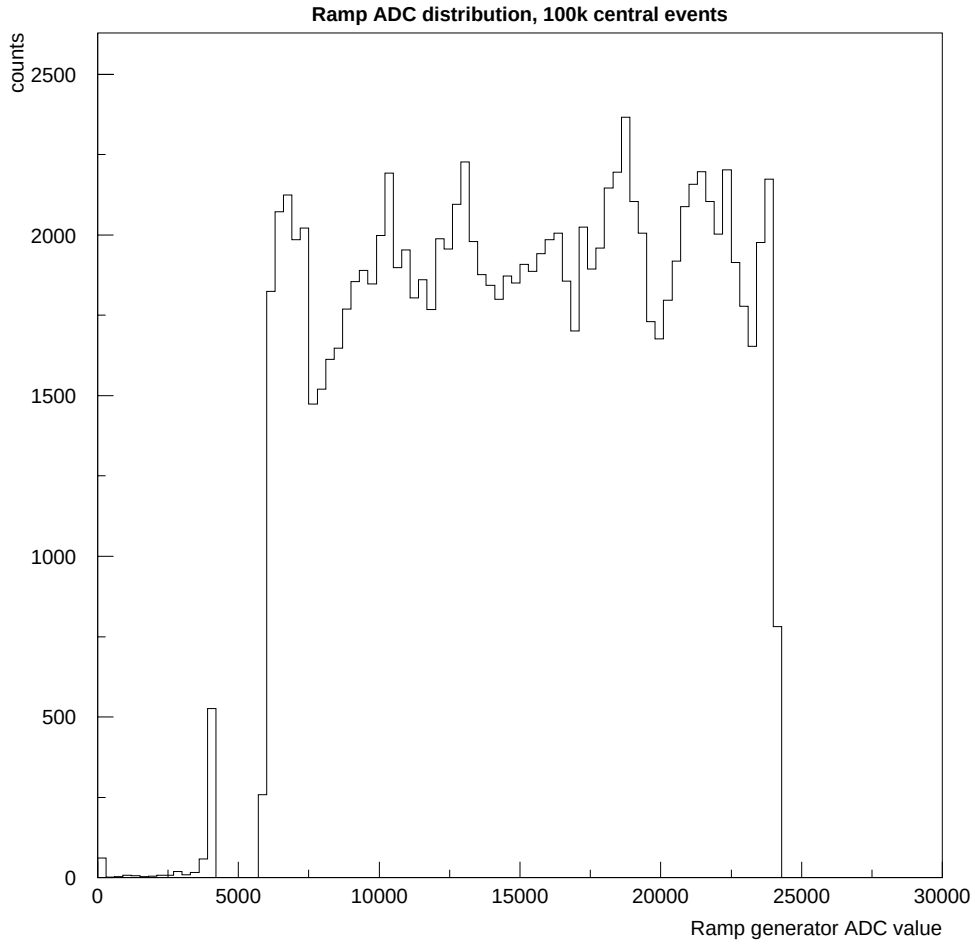

Figure 3.16 A distribution of ADC measurements taken from the ramp generator output, from 100k Au98 central events.

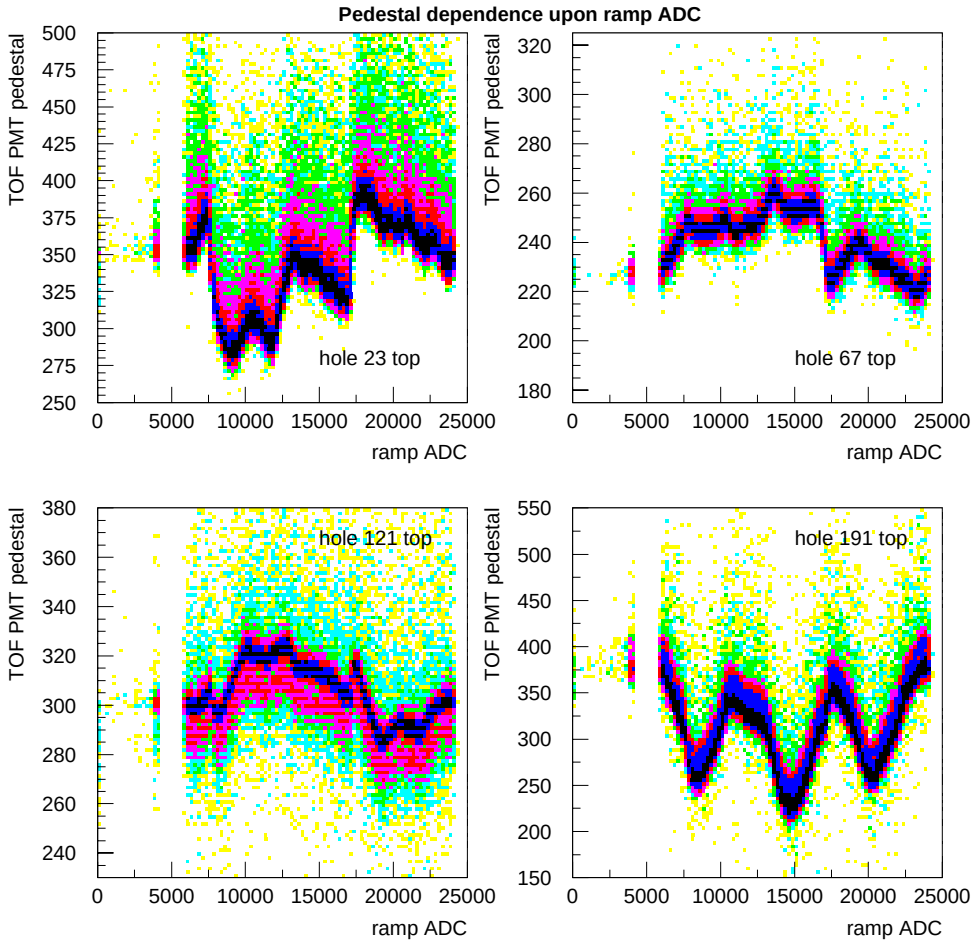

Figure 3.17 The dependence of the TOF PMT pedestal value upon the ramp ADC, for four sample TOF PMTs.

TOF PMT pedestal with respect to the ramp ADC value. The error bars represent the standard deviation of each point about its mean value.

In a later pass through the data, the TOF PMT ADC values are thus corrected in the following manner. The average pedestal value for each TOF PMT at a given value of the ramp ADC is determined by using that PMT's associated profile histogram as a lookup table. The resulting pedestal is then subtracted from the experimental ADC value if the slat is struck or not, yielding an ADC value free from the effects of 60 Hz noise. This algorithm removes both the intrinsic ADC pedestal (inherent within the DAQ electronics) and the pedestal variation due to all correlated noise sources.

Figure 3.19 shows a typical TOF PMT ADC pedestal distribution, without a correction for the correlated noise (dashed line) and with the ramp ADC correction (solid line). After the ramp ADC correction was applied, the pedestal widths are reduced to about three ADC channels. The three channel pedestal width is expected from the sum of the effects of the PMT dark current, the long cables, and the intrinsic pedestal within the Fastbus ADC module.

With this electronics and related correction, the measured ADC values are now not smeared by correlated noise. The next correction to be discussed is the TDC gain calibration.

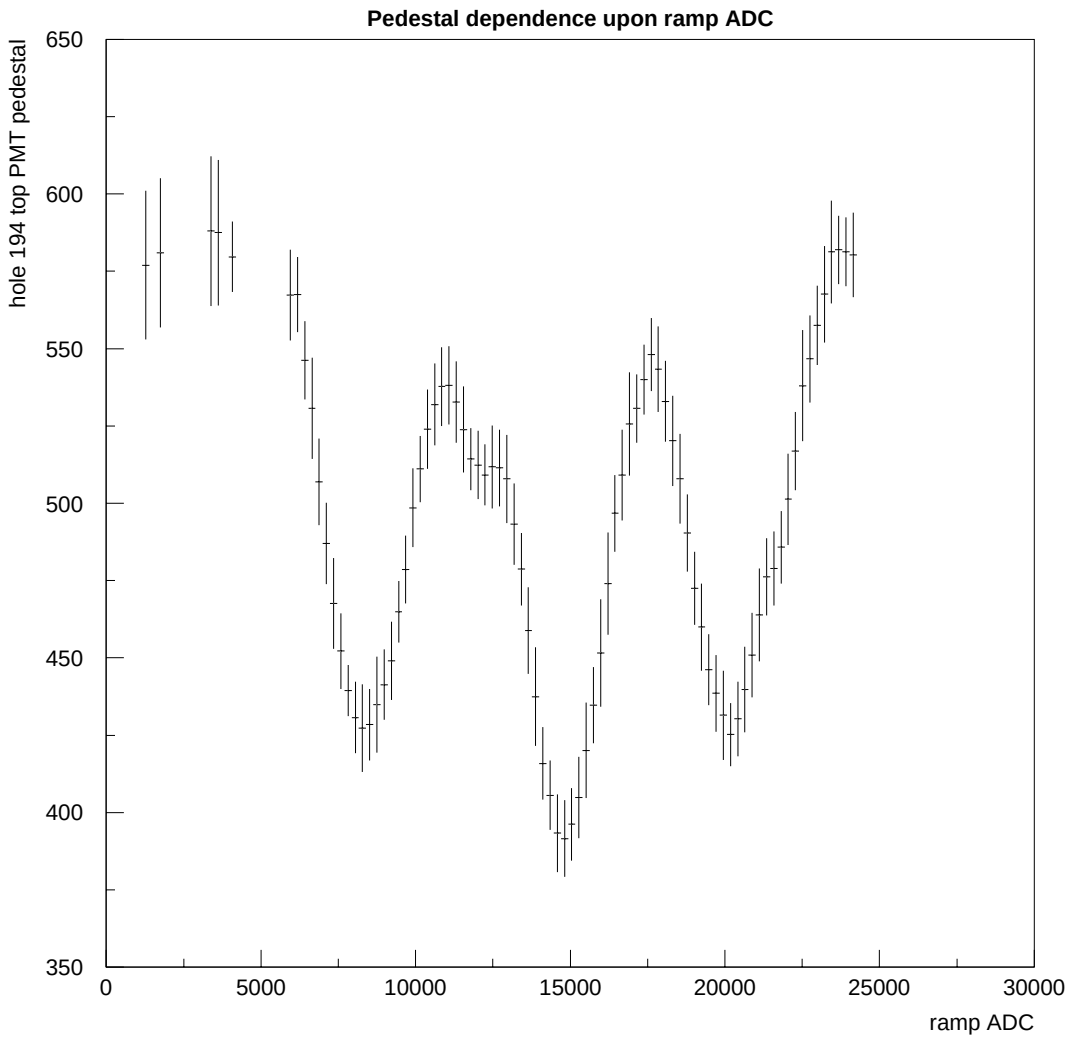

Figure 3.18 An example of a "profile histogram" used to correct for the pedestal effects in the TOF PMT ADC distributions.

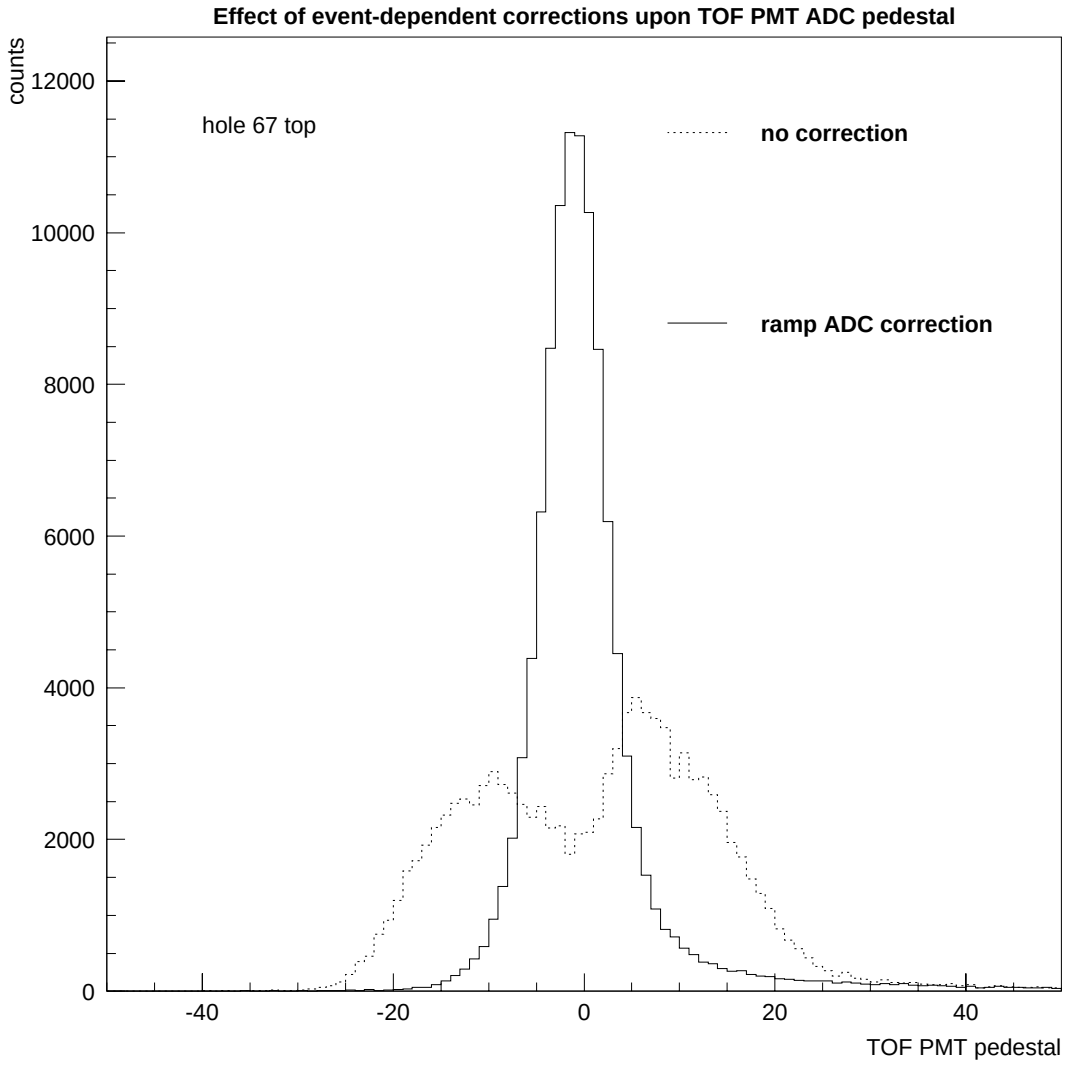

Figure 3.19 The pedestal distributions for the top PMT of TOF hole number 67, without any event-by-event correction (dotted line), and after the ramp ADC correction (solid line).

3.2.2 TDC Gain Correction

The output of the Fastbus TDC module is an integer ranging from 0 to 4095, whose value depends upon the time span between the trigger-induced common start pulse and the stop pulse generated by the PMT of a struck TOF slat. Thus, the first step toward converting a raw TDC value into a flight time is to determine the gain factor for each TDC channel, or the time span for a single digital TDC count.

Nominally, the LeCroy 1875A TDC channel widths are 25 ps [24]. These values are of the order of 25 ps per channel as quoted by the manufacturer, but may vary by ± 10 percent from this specification. This deviation must be measured from each TOF TDC channel to allow the proper conversion of TDC channel to ps for each TDC signal line. Thus, for each TDC channel, a direct measurement of the gain factor is required. This involved the collection of specific timing calibration data, as now described.

The data acquisition for this time calibration was done using the circuit and trigger logic shown in Figure 3.20. The E896 pulser-trigger signal was used as the start pulse of the DAQ and as the TDC common start. A Tennelec 850 NIM Time Calibrator (TC) module generated stop pulses that followed the local start pulse by integer multiples of 10 ns. The NIM stop pulse from the TC was fanned out and sent to a NIM-to-ECL converter, and then connected to a specific 1875A TDC input via twisted-pair ribbon cables. About 80k TC pulses were collected for each TDC

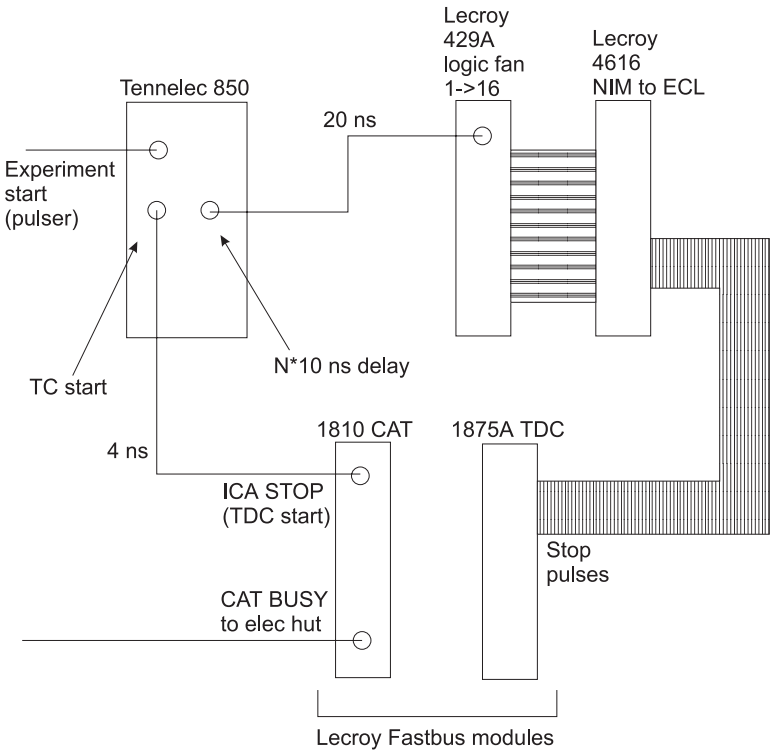

Figure 3.20 A diagram of the electronics used in the Time Calibrator data acquisition.

channel, and the data was written to Mammoth tape for offline analysis.

The distribution of TC start-stop intervals was plotted for each TDC channel in the TOF system. An example plot of one such channel is shown in the top frame of Figure 3.21. A Gaussian was fitted to each peak. The bottom frame of Figure 3.21 shows a plot of the fitted centroid of each Gaussian peak versus the interval number multiplied by 10 ns, the defined separation time between these by the TC. A line was then fitted to the plot in the lower frame. The slope of this line is the gain calibration

for this TDC channel. The present Fastbus TDCs are known to be nonlinear over certain parts of their operating range [5]. Therefore, in the present gain calibrations, only the seven peaks to the right of the lowest TDC peak in Figure 3.21 are used in the linear fit. For a sample TDC channel, omitting the lowest-TDC peak reduced the measured gain factor by 0.1 ps/channel.

The TC gain factor measurements were taken immediately after the end of the April 1998 Au run, and again in September 1998. The retest in September showed a change in the gain factors of about 0.12 percent. This suggests that the TDC gain factors were stable over time.

3.2.3 TDC Slew Corrections

As illustrated in Figure 3.22, an intrinsic feature of PMTs, namely PMT-anode pulse-height variations, lead to variations in the times at which the leading edge of the PMT pulses cross the discriminator threshold. As the height of the pulse becomes greater (corresponding to greater pulse area and thus larger measured ADC), the pulse's leading edge crosses the discriminator threshold sooner, relative to the time of creation of the pulse. The resulting measured TDC value decreases. This correlation is a simple artifact of how PMTs operate when used with leading edge discriminators, and is referred to as the "time-walk," or "slewing," effect. [25]

This effect could be remedied in real time by using constant fraction discriminators. However, the relationship between measured time and measured signal size,

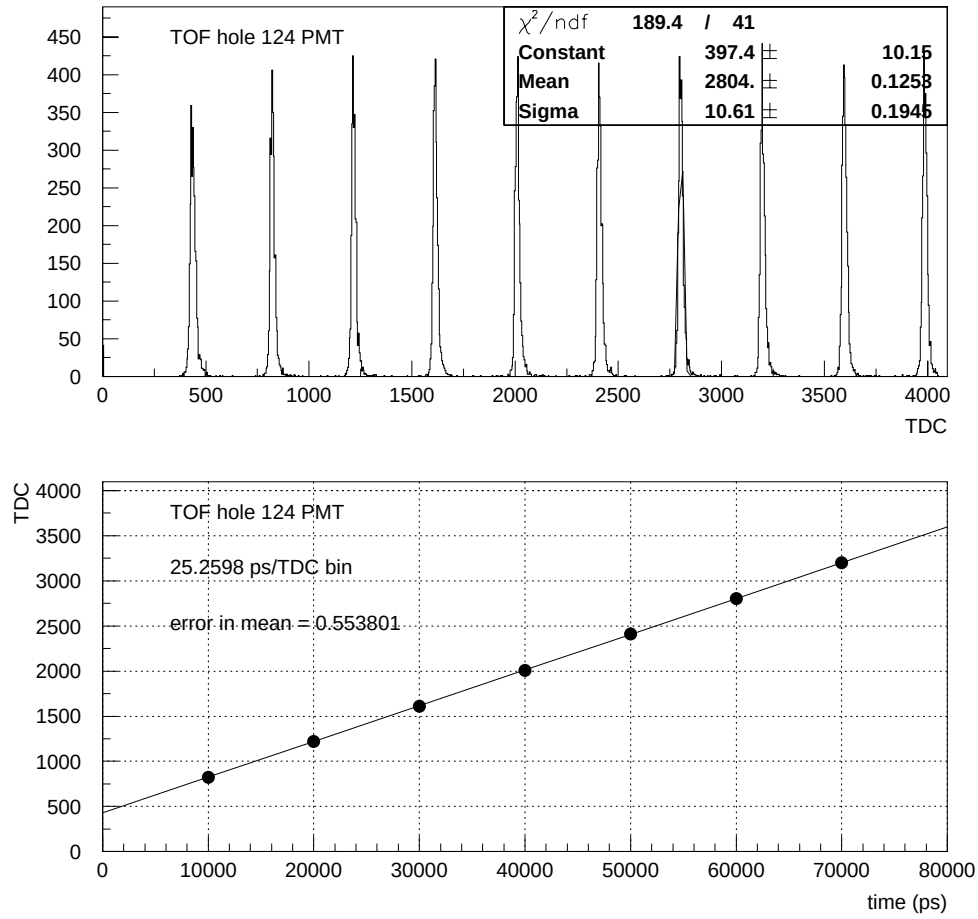

Figure 3.21 The top frame shows the TDC distribution of time-calibrator stop pulses. A Gaussian fit is applied to one of these pulses (the fourth from the right) The bottom frame is a plot of the centroid of each stop-pulse peak in the top plot, versus the time (in ps) after the start pulse.

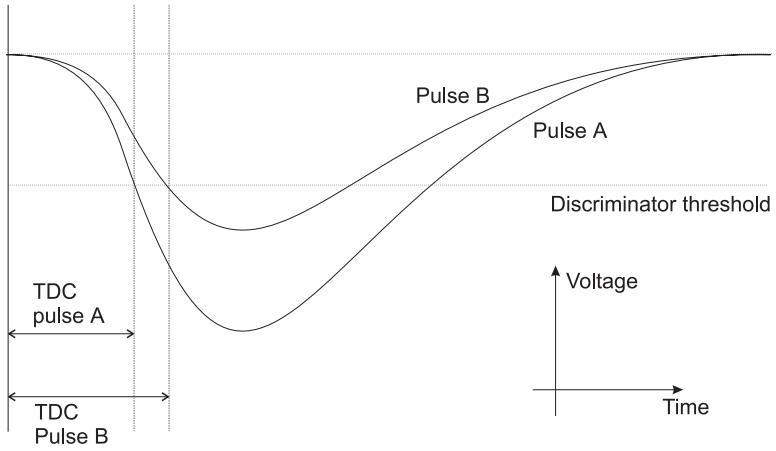

Figure 3.22 The "time walk" or "slewing" effect.

as illustrated in Figure 3.22, is typically easy to understand and correct offline. For various reasons, it is preferable to implement leading edge discriminators and offline correct for the slewing effect.

There are many examples of slewing corrections which all differ slightly [19] [5] [25] [20] [26]. The method attempts to remove the slewing using the ADC value as an indication of the PMT pulse height, so that the TDC is then equal to the flight time of the particle plus some offset.

The measured time dependence upon pulse area can be assumed to take the form [19] [5]

$$t = t_0 + C/q^n \quad (C \geq 0) \tag{3.3}$$

where t is the measured (uncorrected) time, *i.e.* the TDC value, and q is the total charge of the PMT anode signal, *i.e.* the ADC value. In Equation 3.3, the measured time t is the sum of the measured time without the slew effect (an offset t_0) and a factor related to the signal area.

The parameter n depends upon the shape of the PMT anode pulse. If the leading edge of the pulse is assumed to be linear, then $n = 1$. Usually, the leading edge is assumed to have a parabolic shape [19] [20]; in that instance, $n = 0.5$. In the E896 TOF slew fitting, the slew function used is that shown in Equation 3.4:

$$t = t_0 + C/\sqrt{\langle ADC \rangle} \quad (C \geq 0) \tag{3.4}$$

where $\langle$ADC$\rangle$ is the slat average ADC, taken to be the geometric mean between the slat's individual PMT ADC values: $\sqrt{ADC_{top} ADC_{bottom}}$.

For each TOF slat, data from Au98 central events were used to compile histograms of slat average time "$\langle$time$\rangle$" (the arithmetic mean of the gain-corrected TDC values from each PMT, $\frac{time_{top}+time_{bottom}}{2}$) versus the slat average ADC. The slew function of Equation 3.4 was then fitted to each histogram, and the slew parameters were obtained for each slat. No cuts to track quality or particle charge were applied. The slew parameters for each slat were obtained from plots of slat average time ($\langle$time$\rangle$) versus slat average ADC ($\langle$ADC$\rangle$). This was done for two key reasons. First, $\langle$time$\rangle$ and $\langle$ADC$\rangle$ values are independent of the location of the particle hit upon a slat.

Only the spreads in particle flight path length and momentum smear the ⟨time⟩ and thus affect the slew fitting.

The second reason is illustrated by Figure 3.23, which plots, for a single slat, the TDC versus ADC for an individual PMT (left frame), and for the slat average between the slat's two PMTs (right frame). In the left-hand frame, though a slewing effect is observed, there are separate contours seen corresponding to different particle charges present ($Z = 1$, $Z = 2$, etc.), making a single slew fit more difficult. However, as the right-hand frame shows, these separate contours converge when plotting the slat average TDC versus the slat average ADC. A slew function can thus be easily fitted to this data with the highest possible statistical certainty.

For each TOF slat, the ⟨time⟩ and ⟨ADC⟩ values for all particle hits are projected onto two-dimensional histograms. An example of one of these is shown in Figure 3.24. The left frame of Figure 3.24 shows a scatter plot of the slat average time versus the slat average ADC for hits on a sample slat, while a two-dimensional histogram is depicted in the right frame. The fit points are obtained from that histogram by locating, for each ⟨ADC⟩ bin, the ⟨time⟩ bin with the most entries. This was done so that the "slow particle" hits, represented by the band on the ⟨time⟩-vs.-⟨ADC⟩ plot that rises from the MIP point, would not skew the fit. To hasten the fit, the average uncorrected ⟨time⟩ value is used as the seed for the fitting routine for the parameter t_0.

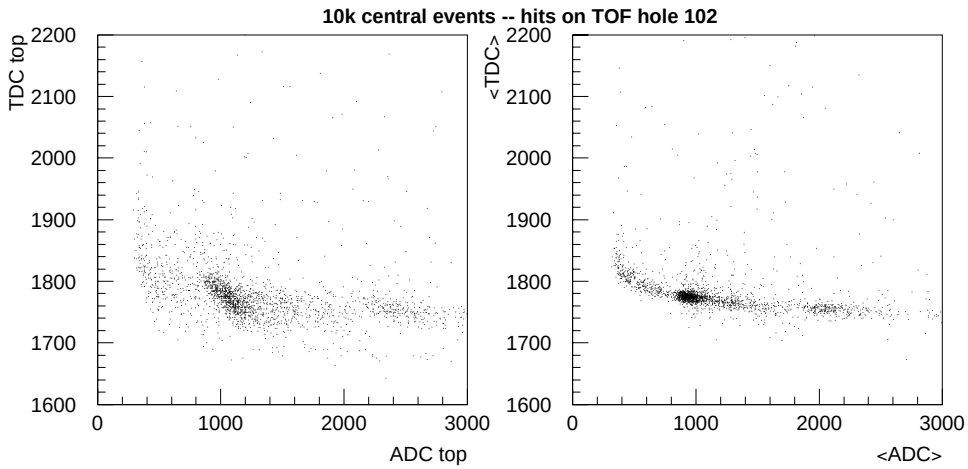

Figure 3.23 TDC versus ADC for an individual TOF PMT (left frame), and $\langle$TDC$\rangle$ versus $\langle$ADC$\rangle$ for the same slat (right frame).

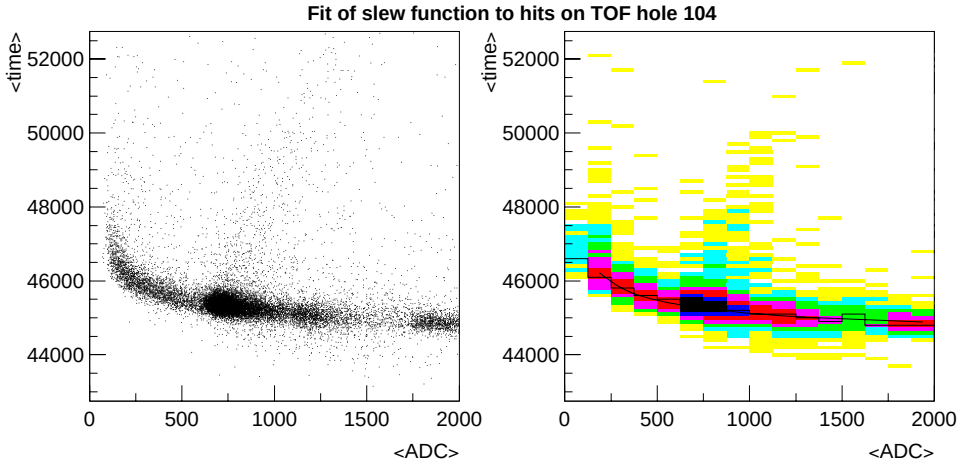

Figure 3.24 The slat average time versus $\langle \mathrm{ADC} \rangle$ distributions to which the slew function is fitted. The left-hand frame is a scatter plot; the right-hand frame is a two-dimensional histogram filled with the hits in the left-hand frame. The fit of the slew function is also plotted in the second frame; the parameters are $t_0 = 44288 \pm 152$, $C = 26585 \pm 3973$.

The slew corrections are applied by subtracting the quantity $C/\sqrt{\langle \mathrm{ADC} \rangle}$ from the $\langle \mathrm{time} \rangle$ value. The result is a $\langle \mathrm{time} \rangle$ distribution without slewing, *i.e.* is constant for all values of $\langle \mathrm{ADC} \rangle$, and is centered at the offset value t_0 also determined for each slat separately.

The top two frames of Figure 3.25 show the slat average time versus the slat average ADC distribution for a single TOF slat, before (left frames) and after (right frames) the slew correction. The upper frames are plots of the slat average time versus the slat average ADC before and after the slew correction. The lower frames are projections of the upper frames onto the (vertical) slat average time axis.

As expected, the slat average time value for the prompt hits is constant versus $\langle \mathrm{ADC} \rangle$ and is centered about the constant t_0. Also as expected, the slew correction shifts the prompt-particle slat average time versus $\langle \mathrm{ADC} \rangle$ values to earlier times. Thus, the modification of the measured flight time due to the time-walk effect is removed. Typically, the $\langle \mathrm{time} \rangle$ for the MIP peak is shifted to earlier times by about 900 ps. The bottom two frames of Figure 3.25 are projections of the top two frames onto the slat average time axis. They show that the width of the prompt-particle peak of the slat average time value is also reduced by the slew correction.

The performance of the slew correction over all of the slats in the TOF array is summarized in the plots of Figure 3.26, which show the $\langle \mathrm{TDC} \rangle$ width versus the hole number (top frame) and fractional decrease brought about by the slew correction

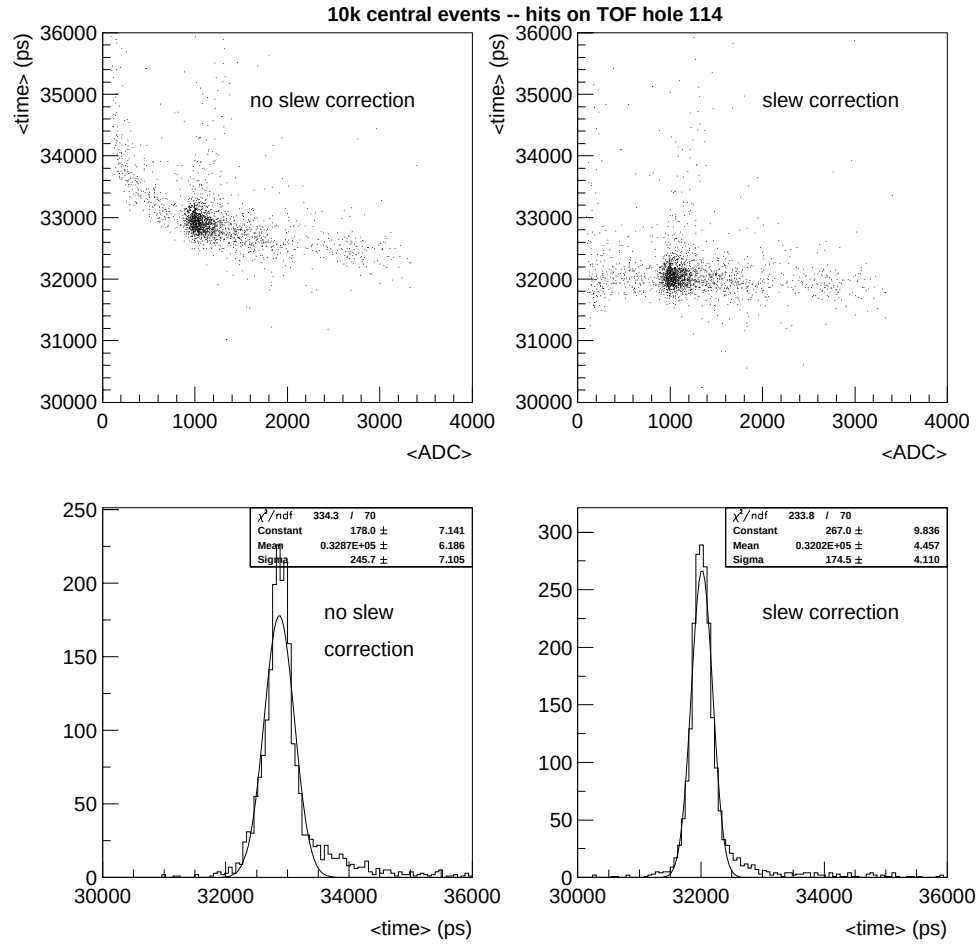

Figure 3.25 The top two frames show the slat average time versus $\langle \mathrm{ADC} \rangle$ distributions before and after the slew correction for a single TOF slat. The fit parameters for this TOF hole were found to be $t_0 = 32030$ ps and $C = 28308$ ps$/\sqrt{ADC\ channel}$. The bottom two frames are the projections of the top two frames onto the vertical axis.

(bottom frame). The fractional reduction of the ⟨TDC⟩ width for different TOF slats ranges from 10 percent to 40 percent. This reflects the different intrinsic rise times of the PMTs. Low rise time PMTs have a larger slewing correction.

To estimate the minimum-achievable TOF resolution without accounting for path length or momentum variations, a "perfect slew correction" can be performed. A tight cut is applied to the ⟨ADC⟩ value for a given slat, and the width of the resulting ⟨time⟩ value is measured. This is effectively an estimation of the ⟨time⟩ width in the absence of slewing effects, which can be used to check the performance of the full slewing correction. Figure 3.27 plots the ⟨time⟩ width in units of ps as a function of the central value of tight ⟨ADC⟩ gates, for four sample TOF slats. In the vicinity of the MIP ⟨ADC⟩ values, the ⟨time⟩ width is as low as 6 channels, or about 150 ps. This is thus the (quadrature) sum of the TOF start-stop electronic resolution and the timing resolution due to the experimental path length and momentum variations among particles striking this slat.

With the TDC values corrected for gain and time-walk effects, one last step remains in converting the raw TDC values from the TOF array into quantities that directly measure flight times. The timing offsets must now be determined and applied. The timing offset for each slat is evaluated in two stages. First, the drifts in the measured time values from run to run are determined and corrected. These drifts are simply electronic and temperature related. After that, the remaining constant

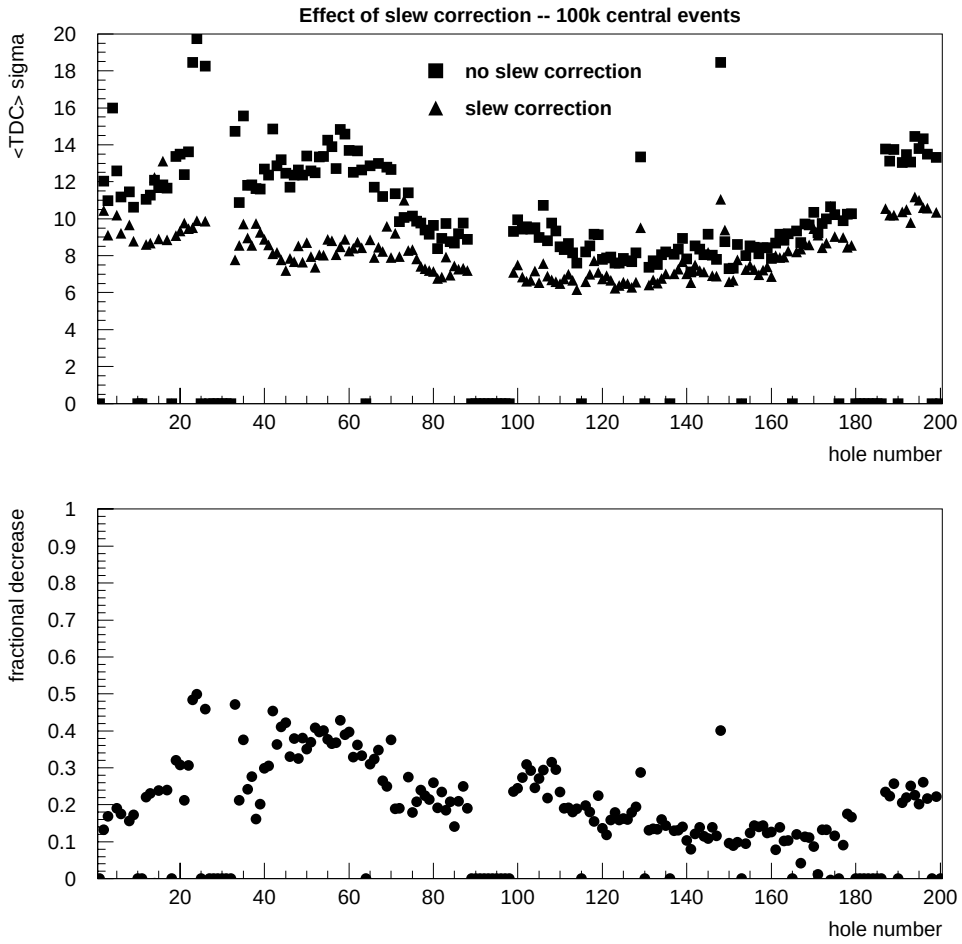

Figure 3.26 The variance in the slat average TDC value, $\langle \mathrm{TDC} \rangle$, versus the hole number before and after the slew correction (top frame), and the ratio of these (bottom frame).

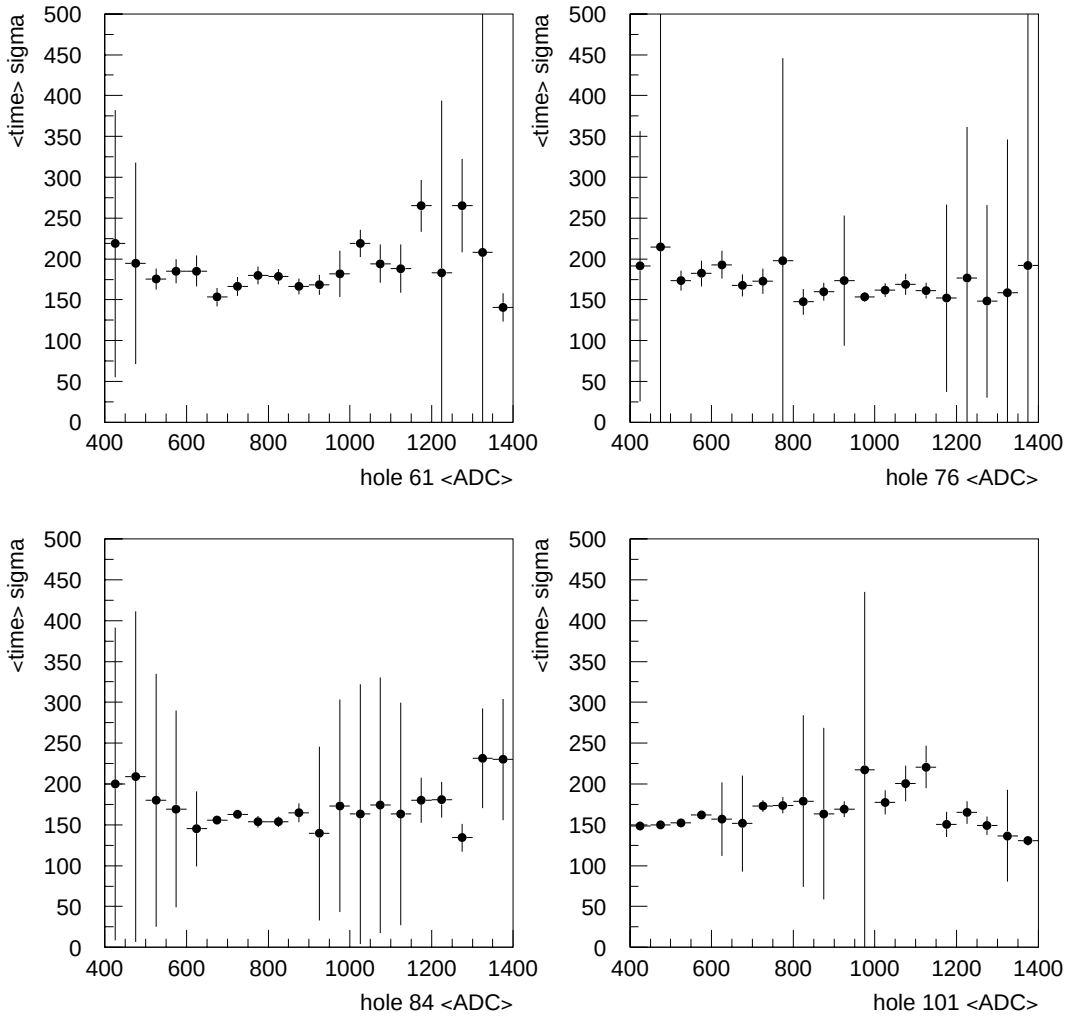

Figure 3.27 The sigma of the slat average time ($\langle$time$\rangle$) distributions for 50 channel-wide gates in the $\langle$ADC$\rangle$ values, for four sample TOF slats as labeled on the horizontal axes.

flight time offset is determined and applied. These are now described in turn.

3.2.4 TDC Run-dependent Offset Corrections

Between runs, the time measurements of the trigger and TOF systems may fluctuate due to changes in temperature or slow electronic changes to the trigger and TOF hardware, or experimental modifications such as the swapping of cables or the adjustment of discriminator levels. Figure 3.28 shows a plot of the mean value of a Gaussian fit to the measured slat average time distribution versus the run number for four sample TOF slats. One sees that these values vary significantly with the E896 run number. Figure 3.29 plots the maximum difference among the mean values of the slat average time distribution for each slat over five runs recorded during a six day span. The measured slat average time for a given slat can fluctuate run to run by up to 250 ps. This run-dependent drift must be corrected offline.

The correction method is as follows. From the first ten thousand events of each raw data file, the slat average time values are recorded and saved in a one-dimensional histogram for each slat. A Gaussian is fitted to the peak of this distribution, and the mean value and variance of the fit for each TOF hole are stored to an ASCII file for the given run.

The run-dependent offset corrections are applied in a later pass through the data, in the following manner. One of the Au98 runs is chosen arbitrarily as a reference. For a given run being analyzed, the mean values of the $\langle \text{time} \rangle$ distributions are extracted

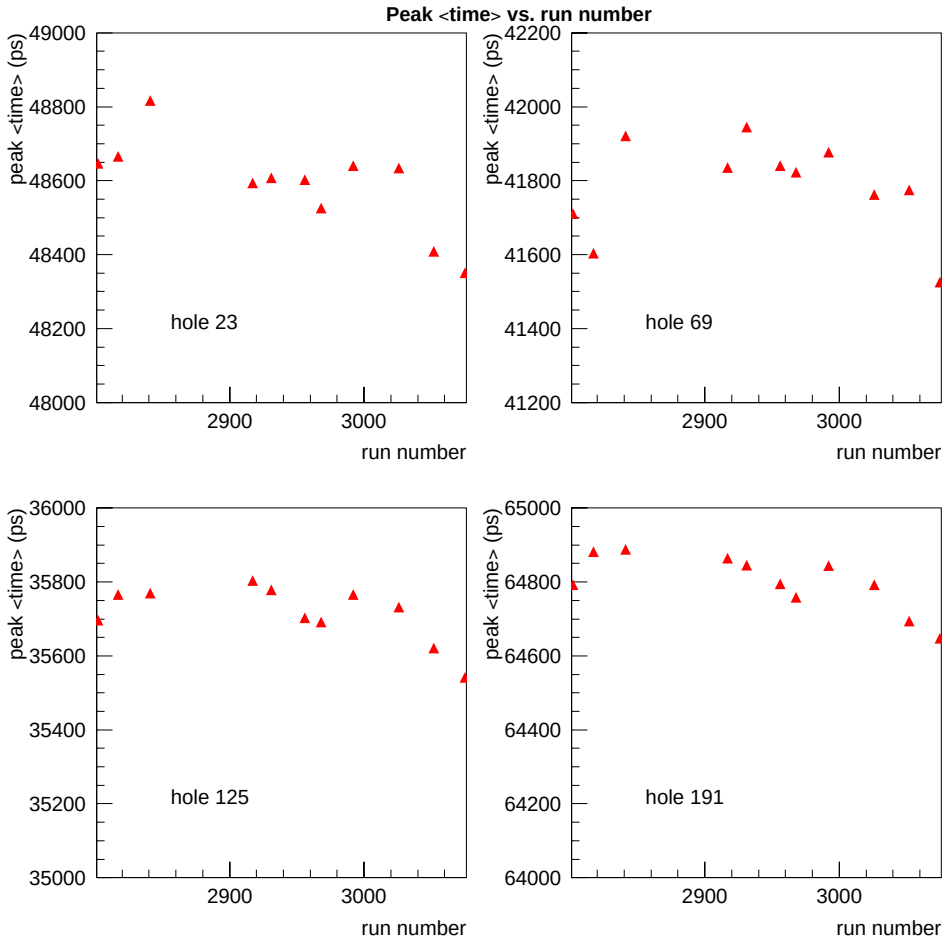

Figure 3.28 The mean slat average time ($\langle$time$\rangle$) value versus the run number, for four sample slats.

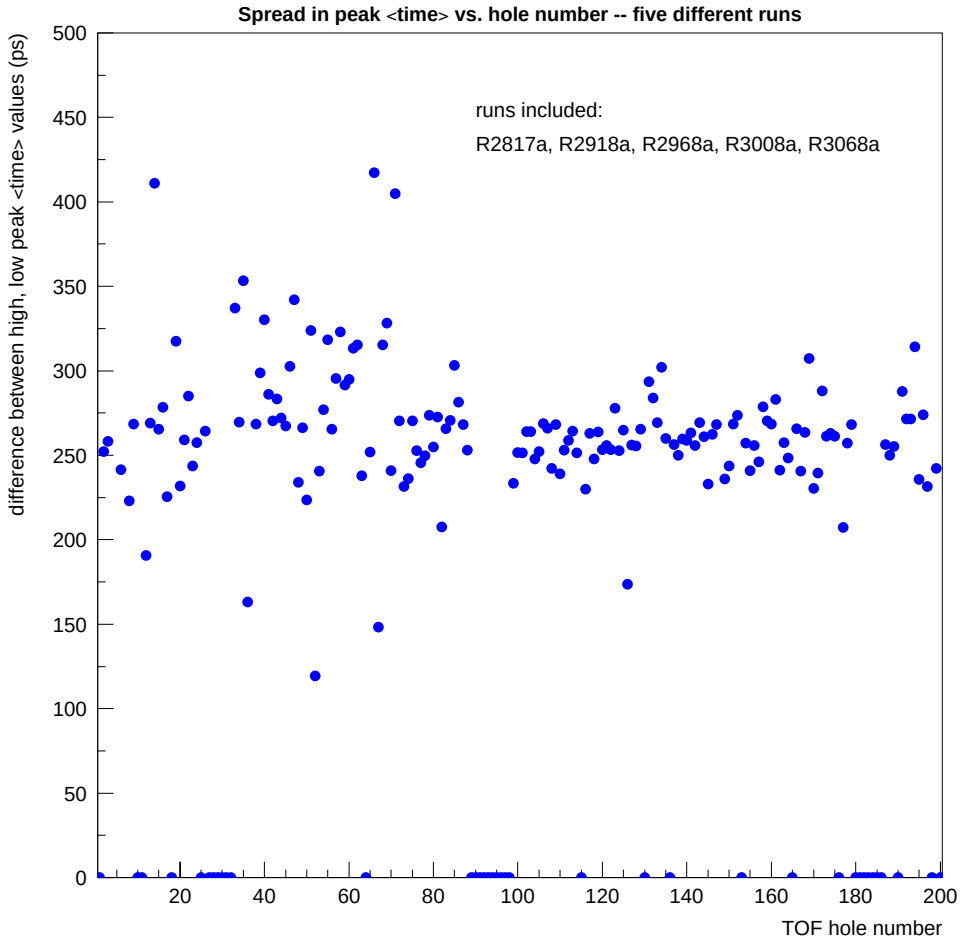

Figure 3.29 The spread in the peak slat average time ($\langle$time$\rangle$) value for each slat, over five Au98 runs that were recorded over a period of six days.

from the ASCII files for the run being analyzed and for the reference run. The run-dependent offset for that slat is obtained by taking the difference between the mean ⟨time⟩ values from the two ASCII files. The correction is applied by subtracting that offset from all of the ⟨time⟩ data within that slat for the given run. Thus, over all of the runs being analyzed, the mean ⟨time⟩ values for a given slat are made the same.

3.2.5 TDC Constant Offset Corrections

Once the run-dependent offsets to the TOF slat average time data have been calculated and applied, the remaining offset for each slat is a constant over all runs. Data from several runs are combined to compute this remaining offset that is due to the different overall cable lengths among the various TOF PMT TDC channels.

To compute the constant offset for each channel, the measured flight time must be compared to a calculated flight time for a given slat. Simulations are used here to provide a flight time estimate for TOF-incident particles produced in Au+Au collisions. RQMD [3] provides the primary and secondary protons and pions that are expected to hit the TOF slats. These RQMD central-event particles are propagated through the E896 geometry and onto the TOF array using GEANT. The particle flight time distributions as determined by GEANT are compared with the measured flight times from actual Au98 data.

Figure 3.30 schematically depicts time versus momentum curves for Au98 data and the simulations, to illustrate the method used to determine the constant offsets. The

upper curve is the time-vs.-momentum distribution for proton (or pion) candidates from Au98 data; all other corrections are already made to this data. The lower curve is the simulations prediction for protons from RQMD (or pions from RQMD). The constant offset for this slat is obtained by subtracting the bottom curve from the top curve.

For each slat, the slat average time versus momentum contour for Au98 is compared to that obtained from RQMD. Though the momentum distributions upon the slat given by RQMD might differ from Au98, the time-vs.-momentum points reside on the same contours, as all other aspects of the simulation are independently constrained. The constant offset is the value for each slat to subtract from the slat average time distribution in Au98 data such that the time-vs.-momentum band from the Au98 data lines up with that obtained from the simulation.

Examples of time versus momentum plots for Au98 data and from the simulations are shown in Figure 3.31. In the Au98 data (left frame), the proton band is readily apparent, but some pion hits are observed as well. Equation 3.2 can be easily fitted to the RQMD plot in the right frame. The resulting parameters are used to extract the constant timing offset from the Au98 slat average time versus momentum distribution for each slat, in the fashion outlined in Figure 3.30.

A plot of measured minus calculated slat average time versus momentum, for the same slat depicted in Figure 3.31, is shown in the left frame of Figure 3.32. Except

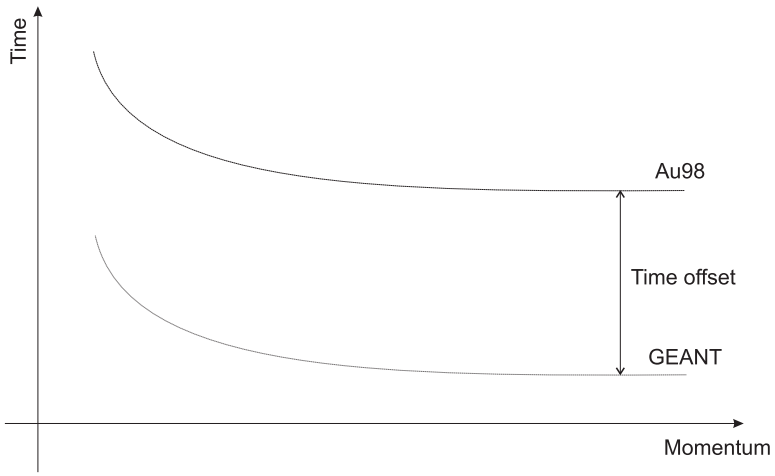

Figure 3.30 A diagram illustrating the method used to determine the constant timing offset for each TOF slat.

for a slight dip seen for momenta less than about 3 GeV/c, the distribution is nearly constant. The proton band apparent in Figure 3.31 is flattened considerably. The right frame of Figure 3.32 is the projection of the left-hand frame onto the slat average time axis. A Gaussian fit to this right-hand frame gives the constant offset for this slat.

The validity of this method of offset determination can be investigated by comparing the measured (and fully corrected) flight times for $\Lambda \rightarrow$ p candidates with calculated flight times based only on the tracking information and the $\Lambda \rightarrow$ p hypothesis. The $\Lambda \rightarrow$ p candidates in the data are extracted by cutting on various quantities related to the trajectory and kinematics of the V_0 candidates. Calculated

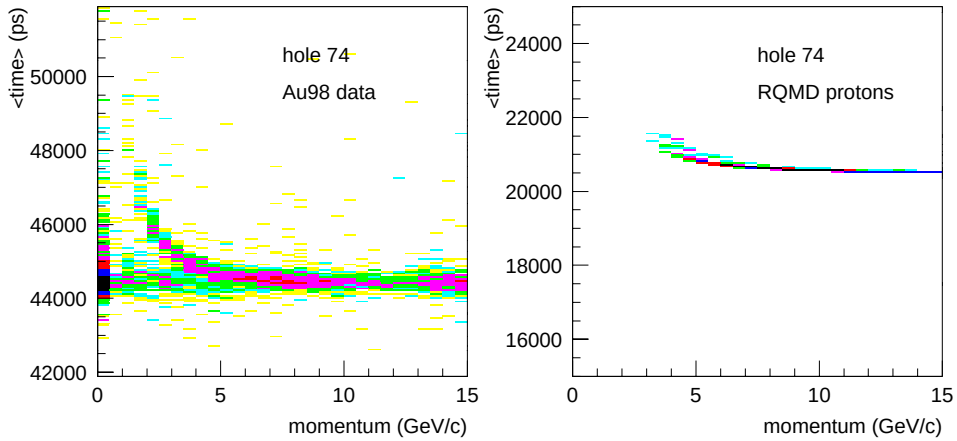

Figure 3.31 The left frame shows the slat average time versus momentum distribution from Au98 data for a single slat. The right-hand frame shows the same distribution for RQMD protons.

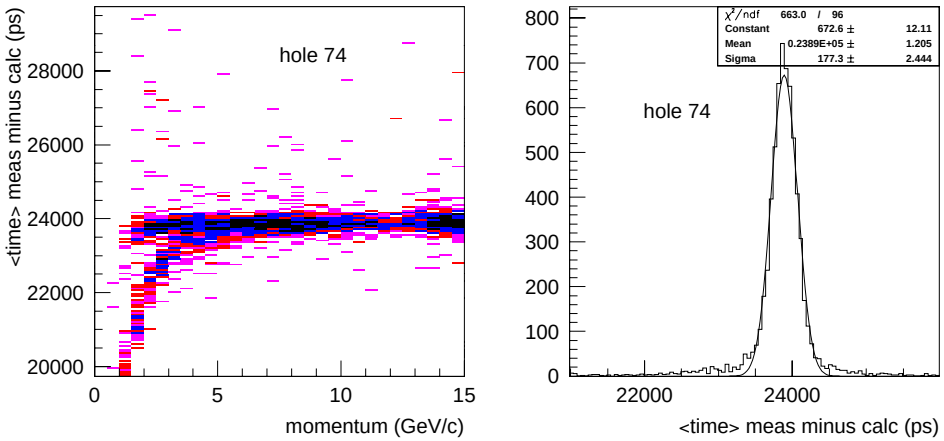

Figure 3.32 The left-hand frame shows the measured slat average time, with the predicted GEANT flight time versus momentum subtracted, versus the momentum. The right-hand frame is a projection of the data in the left-hand frame onto the vertical axis.

flight times are obtained by using the measured momenta, the path lengths determined by the extrapolator, and the mass assumptions for the parent and daughter (all of the quantities summarized in Figure 3.13). Figure 3.33 plots and fits to the difference between calculated and measured time for $\Lambda \rightarrow$ p candidates incident upon the TOF Central Wall. As seen in the statistics box of this figure, the calculated and measured flight times, averaged over the entire acceptance, agrees to approximately 24 ps. This is taken to be adequate for the present analyses.

3.2.6 TOF Time Measurement Resolution

An estimate of the TOF start/stop measurement resolution, $\sigma_{TOFmeas}$, is made by assuming that uncertainties in the measured flight time and the calculated flight time are independent, and hence can be added in quadrature to obtain the variance in the measured TOF minus calculated TOF:

$$\sigma^2_{TOFmeas-TOFcalc} \approx \sigma^2_{TOFmeas} + \sigma^2_{TOFcalc} \tag{3.5}$$

The calculation of $\sigma_{TOFmeas}$ was made using $\Lambda \rightarrow$ p candidates from the filtered Au98 data set. The quantity $\sigma_{TOFmeas-TOFcalc}$ was determined for each slat by plotting the distribution of $TOFmeas - TOFcalc$ for individual TOF slats (similar to that depicted in Figure 3.33), and fitting a Gaussian to determine the variance. The solid circles in Figure 3.34 denote the $\sigma_{TOFmeas-TOFcalc}$ for each TOF hole seeing hits from $\Lambda \rightarrow$ p daughters. The average value across all TOF slats is approximately 145 ps.

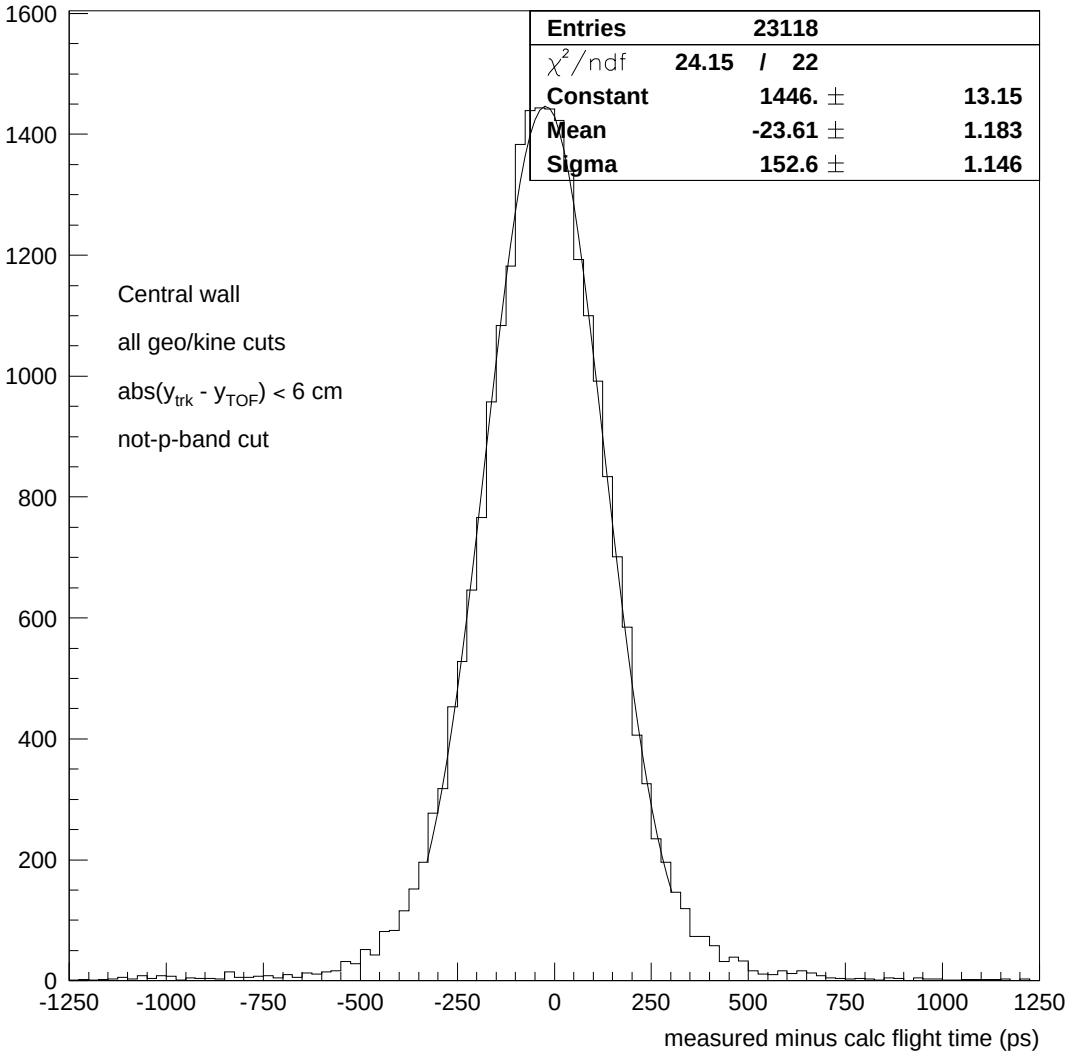

Figure 3.33 Measured flight time (after all ADC and TDC corrections were made) minus calculated flight time, for $\Lambda \rightarrow$ p candidates in the data set.

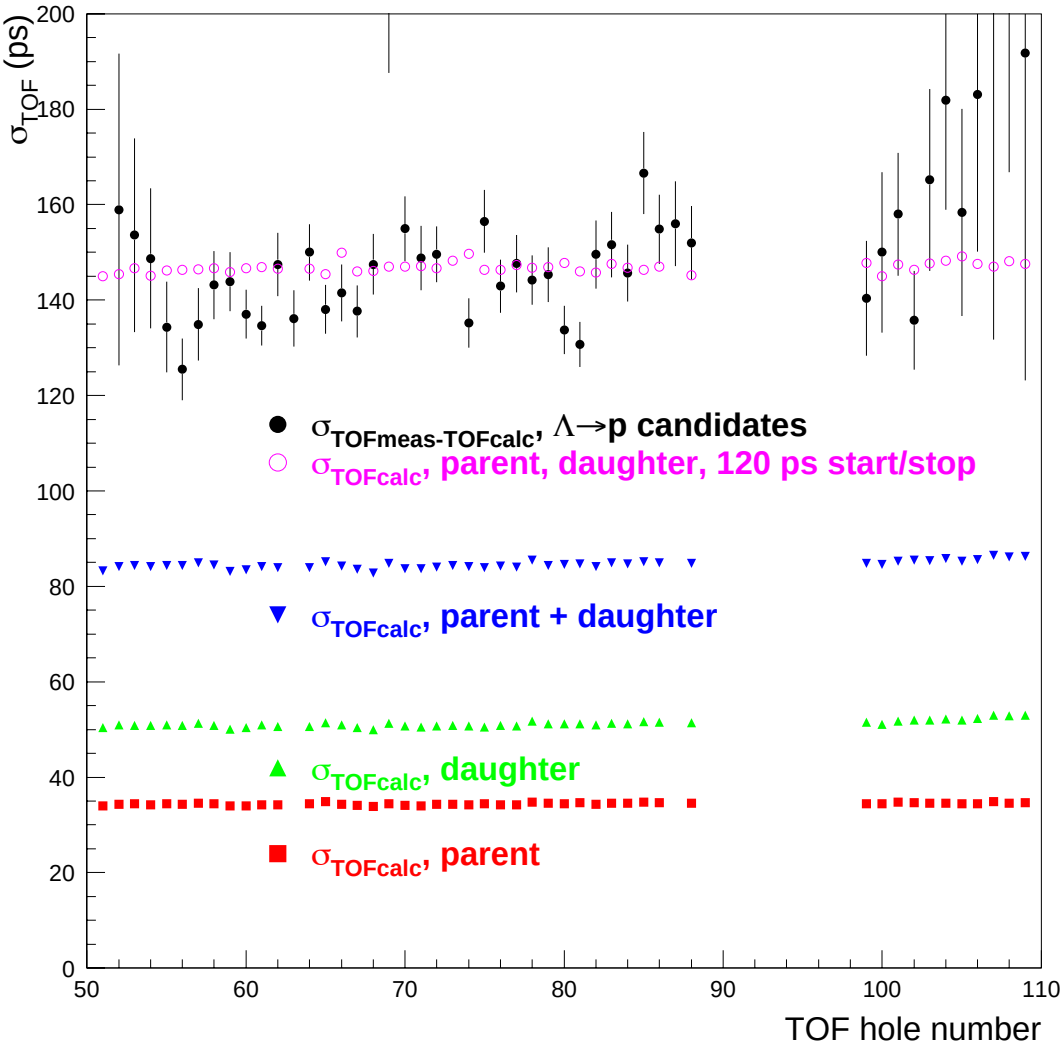

Figure 3.34 The solid circles in the above frame indicate the widths of the $TOFmeas - TOFcalc$ distribution for $\Lambda \rightarrow$ p candidates incident upon each TOF slat as labeled on the horizontal axis. The resolution in TOF_{calc} is indicated by the down triangles. If a 120 ps start/stop ($TOFmeas$) resolution is added in quadrature to $\sigma_{TOFcalc}$ (open circles), the result agrees well with the resolution of $TOFmeas - TOFcalc$ extracted from the experimental data.

The uncertainties in the calculated flight time for each slat were determined in the following manner. First, the peak values of parent path length and momentum, and daughter path length and momentum, were determined for the $\Lambda \rightarrow$ p candidates upon each slat. A smearing was then applied to each of these four quantities, using the path length and momentum uncertainties summarized in Table 3.2. The quantity *TOFcalc* was then redetermined using these smeared path lengths and momenta. The average value for $\sigma_{TOFcalc}$ across the TOF array was about 85 ps, as illustrated by the upside down triangles on Figure 3.34.

V_0 *quantity*	*uncertainty*
$\sigma_{d_{parent}}$	1.0 cm (vertex position resolution)
$\sigma_{p_{parent}}/p_{parent}$	1.0 % (V_0 momentum resolution)
$\sigma_{d_{daughter}}$	1.5 cm (path length calc. uncertainty)
$\sigma_{p_{daughter}}/p_{daughter}$	2.0 % (track momentum resolution)

Table 3.2 The uncertainties assumed for the path length and momentum for the parent and daughter legs of the $\Lambda \rightarrow$ p candidates.

Using the values for $\sigma_{TOFmeas-TOFcalc}$ and $\sigma_{TOFcalc}$ obtained above, the intrinsic start/stop timing resolution of the E896 TOF system was determined to be

$$\sigma_{TOFmeas} = \sqrt{\sigma^2_{TOFmeas-TOFcalc} - \sigma^2_{TOFcalc}} \approx 120ps \tag{3.6}$$

The open circles in Figure 3.34 depict the quantity $\sqrt{\sigma^2_{TOFcalc} + (120ps)^2}$ for each TOF slat. These values are by construction in agreement with the $\sigma_{TOFmeas-TOFcalc}$ values for each hole number.

3.2.7 Summary of TOF Signal Calibration

To uniquely match a struck TOF slat to an extrapolated DDC track in Au98 data, the correlation between y_{TOF} and $y_{tracking}$ was used. For long DDC tracks, the match efficiency across the TOF array ranges from 70 to 90 percent. After correcting the raw TOF data for correlated noise, TDC gain, time walk, and time-measurement offsets, the TOF measurement resolution was found to be about 120 ps.

The same wall had achieved a timing resolution of 85 ps in E877. However, E877 had more space points, provided by several drift chambers and multi-wire proportional chambers, to aid them in the extrapolation and path length calculation of particles incident upon their TOF system. Their path length and slat matching resolutions cannot be compared to those in E896. Also, E877 used their TOF system mainly for *primary* tracks, whose paths through the experiment are very well defined, with a geometry fixed at both ends by the target and at the slat. E896 is not designed to detect primary tracks, and in fact does its best to completely ignore these using the sweeper magnet. The resolutions of the V_0 candidate decay vertex and the daughter momentum and path determination must be incorporated into the overall timing resolution in E896. Most importantly, though, aging of the Central Wall system may have led to a deterioration in the timing resolution as well. The system was operated at high PMT gain in E877 for about two years, sat idle on the AGS floor for a few more years, and then ran at high gain in E896 for two years. PMT performance typically

degrades after such a treatment. Thus, the timing performance of the Central Wall in E877 and in E896 should not be expected to be similar, even though the physical stop detectors are the same.

After applying the above calibration tasks to the V_0 candidate daughters in the filtered data set, these V_0 candidate daughters are now associated with a measured flight time provided by the TOF detector. In a plot of these measured flight times versus the daughter particle momentum, such as that shown in Figure 4.12, a separation of daughter particle masses, and thus parent particles (*i.e.* Λ hyperons from K_s mesons) is apparent. The band which indicates the heavier $\Lambda \rightarrow p$ can be easily distinguished, and separated, from the band comprised of $K_s \rightarrow \pi$ and e^+e^- background up to a momentum of $\sim$ 5 GeV/c. TOF PID cuts involve separating the bands present in this time-vs.-momentum plot.

With the addition of TOF measurement information to the V_0 candidate daughters from filtered Au98 data, cuts to the measured flight times of the parent plus daughter can now be applied to yield purer samples of Λ hyperons or K_s mesons. The measured spectra of Λ hyperons and K_s mesons will be translated into produced particle spectra by correcting for the geometric acceptance of the E896 experimental apparatus and the reconstruction efficiency inherent in the software and the cuts applied to the V_0 candidates. These corrections, and the physics results then obtained, are described in the next chapter.

Chapter 4
Corrections and Physics Results

The previous chapter described the software applied to associate TOF timing information to the daughters of V_0 candidates found in the E896 main filtered data set. It remains to apply time-of-flight and other cuts to these V_0 candidates to obtain a lower-background sample of identified Λ hyperons and K_s mesons. These cuts are documented in section 4.1 below. Cuts are applied at the run and event level, to the geometric and kinematic quantities associated with the V_0 candidates, and to quantities provided by the TOF detector information associated with the candidate daughters. These cuts are optimized for the reconstruction and identification of either K_s mesons or Λ hyperons. The physics results so obtained will be first compared with those reported by an independent Λ hyperon analysis in E896 [14], as a consistency check. The invariant mass, rapidity y, and transverse mass ($m_T = \sqrt{p_T^2 + m_0^2}$) distributions for Λ hyperons and K_s mesons that survive all of these cuts will be presented.

Before these Λ hyperon and K_s meson measurements can be compared with those from other experiments and models, the measured particle distributions must be corrected for the geometric acceptance of the DDC and TOF detectors and for the software reconstruction efficiencies. Both quantities depend upon the rapidity and

transverse momentum of a candidate. Section 4.2 describes the acceptance calculations performed to compute these correction factors for Λ hyperons and K_s mesons. The Λ hyperon correction factors obtained without applying TOF cuts or corrections are compared to the correction factors from the previous Λ analysis (without TOF) [14], to evaluate the accuracy of the present calculations.

Once the cuts and corrections are included, projections of the produced particle spectra are described in section 4.3. Particle source temperature measurements at particle freeze out in different rapidity bins can be inferred from the transverse mass spectra assuming these can be fit using the Boltzmann distribution of Equation 4.18. The production yields and temperatures are then compared with results from other AGS experiments and with the predictions of the RQMD model. RQMD is operated in "cascade mode," with no rope formation or mean field interactions included, to predict the multiplicities and momenta of the particles produced in a $b < 4$ fm Au+Au collision. These predicted particle spectra are then filtered through the experimental acceptance in simulation. The effective temperatures for Λ hyperons and K_s mesons in the center-of-mass frame of the participant region will be determined from the present and previous results.

4.1 Reduction of V_0 Candidate Set

The flow chart in Figure 4.1 presents an overview of the cuts applied to the initial V_0 candidate set. This initial candidate set emerged from "Pass II," which was an

E896-wide effort to reduce the set of all raw events into a set of events which are known to contain a neutral vertex candidate. This "Pass II" data set is used at E896 institutions for all subsequent analyses. Cuts at the run and event level are described first. Next, the cuts applied to the geometric and kinematic quantities of the V_0 candidates are described, and the degree to which they reduce the size of the V_0 candidate set is quantified. Finally, the cuts to the TOF-related quantities for the V_0 candidate daughters are described.

4.1.1 Run and Event Cuts to V_0 Candidates

During the Au98 running period, central triggers were written to tape in blocks of about $200k$ events. Each block (or, "run") was normally written onto two Mammoth tapes, with about $100k$ events from the run on each tape.

This analysis concentrated on runs that were recorded during the last two weeks of the April 1998 running period. During this time, the TOF detector hardware, high voltage, and data acquisition systems were fully functional. For these runs, the rate at which the V_0 candidate filter had triggered on central events was about 8 percent.

Also, only those runs were used for which both the filtered V_0 candidate file and the corresponding unfiltered raw data file were available. The unfiltered raw events were needed to determine the relative timing offsets for each run (as described in Chapter 3).

The minimum and maximum levels of the ramp generator output were properly

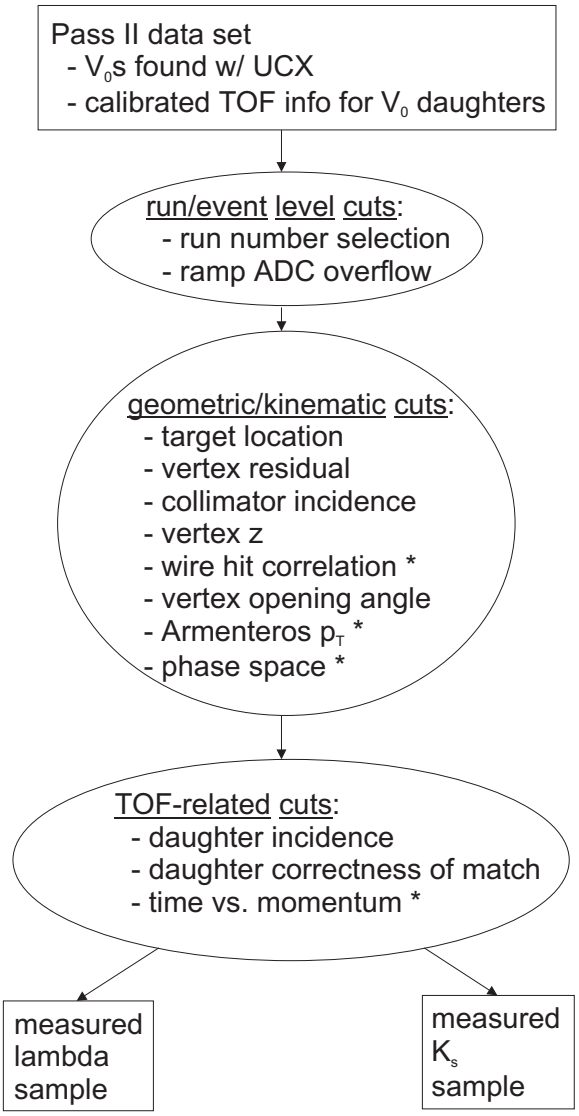

Figure 4.1 The cuts applied to the Pass II V_0 candidates (with calibrated TOF detector information associated with the daughters) to reduce the data to a clean set of Λ hyperons or K_s mesons. Asterisks (*) denote the specific cuts that were revised to favor K_s mesons instead of Λ hyperons.

set during the last two days of the Au98 running period. However, for the earlier runs, the ramp generator's outputs became too large due to electronic aging. This caused the sawtooth's maximum level to exceed the maximum charge measurable by the 1885F ADCs. Figure 4.2 shows the ramp ADC distribution for such a run. An overflow is observed at the high end of the distribution. The ramp ADC correlation with the phase of the 60 Hz cycle is undetermined in the overflow region. Such events are therefore not included in the data analysis, since a 60 Hz pedestal correction cannot be made without additional parameters such as "blackened PMT" values. The ramp ADC overflow rate varied from 13 to 15 percent during a five-day running period about a week before the end of the run. During the day before the overflow problem was solved, the overflow rate varied from 48 to 50 percent.

The final event samples used in the analysis are as follows. For distributions in which no ramp overflow cuts are applied (*i.e.* no TOF-related cuts are required), the Λ hyperon and K_s meson candidates are drawn from $N_{ev} = 11,728,613$ central triggers. After applying the ramp overflow cuts to the V_0 candidate events, and adjusting for the 8 percent V_0 candidate trigger rate in the filter, the number of central events from which Λ hyperons and K_s mesons are drawn is $N_{ev} = 9,447,838$.

4.1.2 Geometric and Kinematic Cuts to V_0 Candidates

To extract a cleaner sample of Λ hyperons (and K_s mesons as well), cuts were then applied to the V_0 candidate's observed trajectory and momentum. These geometric

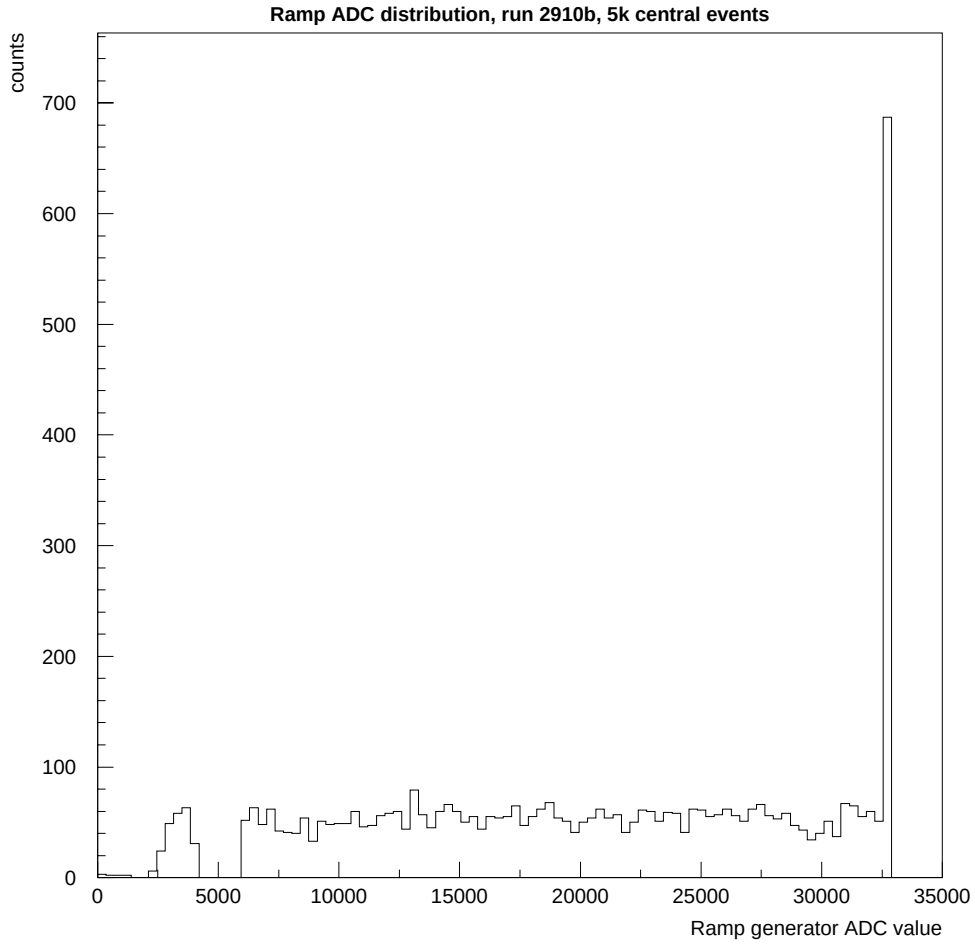

Figure 4.2 The ramp ADC distribution from a run during which the maximum sawtooth value was set too high, causing the overflow seen on the right hand side of the distribution.

and kinematic cuts are described below. Specific modifications of these cuts to optimize for the reconstruction of K_s mesons or Λ hyperons are noted where appropriate. The effectiveness of each cut in reducing the background of the Λ hyperon invariant mass distribution relative to the peak is tabulated, and compared with results from the independent E896 analysis. [14]

Target Cuts

A candidate was required to originate sufficiently close to the collision primary vertex at the z coordinate of the target. Thus, the reconstructed parent particle's momentum vector for each V_0 candidate was linearly extrapolated backwards to $z = 253$ cm, and the extrapolated parent x and y locations at the target (denoted $x_{z=253}$ and $y_{z=253}$) were determined. Figure 4.3 shows plots of these distributions of $x_{z=253}$ and $y_{z=253}$.

The target x and y cuts were then defined as

$$|x_{z=253} - x_{tgt}| < 1.0\,\text{cm} \tag{4.1}$$

and

$$|y_{z=253} - y_{tgt}| < 1.5\,\text{cm} \tag{4.2}$$

The average values $x_{tgt} = -7.739$ cm and $y_{tgt} = -0.741$ cm are the average target x

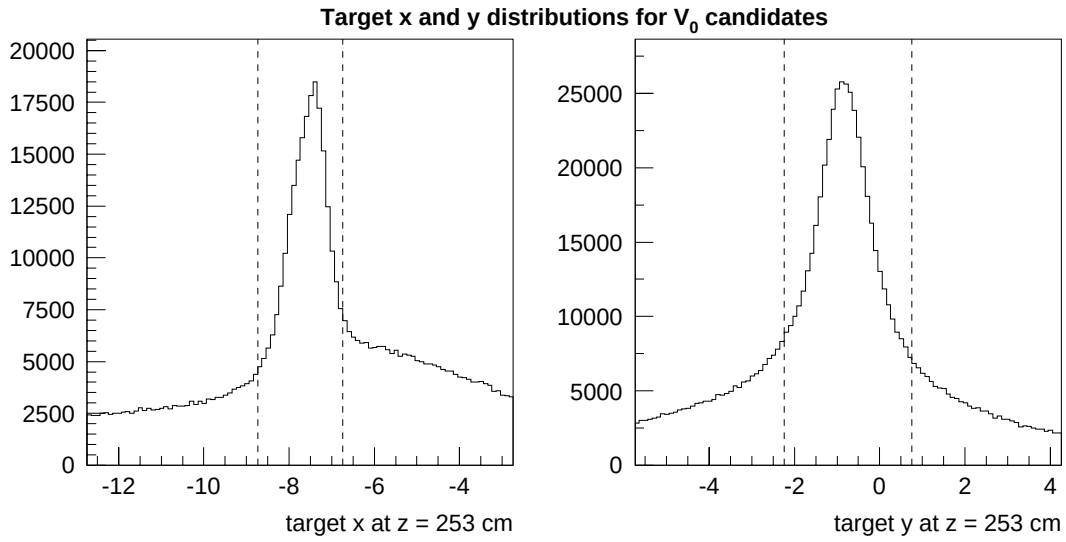

Figure 4.3 The distribution of x locations of V_0 candidates extrapolated back to the target (left frame), and the target y distribution (right frame). The dotted lines denote the boundaries of the target cuts used in this analysis.

and y locations for V_0 candidates extrapolated to the target over all runs.

Vertex Residual Cuts

The positive and negative daughter tracks of a valid neutral particle candidate were then required to converge sufficiently close together, such as would be expected if they were indeed produced during the decay of a neutral parent. Smaller distances of closest approach are generally assumed to correspond to better reconstructed V_0 candidates. Thus, a quantity called the *vertex residual* was defined in the following manner. For each coordinate i, where i represents either the x or y axis in E896:

$$vres_i = i_{vertex} - \frac{i_+ + i_-}{2} \tag{4.3}$$

where $vres_i$ is the i coordinate of the reconstructed vertex at the vertex z location, and i_+ and i_- are the values of the coordinate i for the positive and negative tracks extrapolated to the vertex z location. Figure 4.4 shows the vertex residual distributions. On the left frame is the distribution of $vres_x$, and on the right is the distribution of $vres_y$. For both frames, the units are in centimeters. One sees on the left frame that the width of the $vres_x$ distribution is about 0.001 cm. On the right frame, the width of the $vres_y$ distribution is about 0.01 cm.

The cut on the vertex residuals for neutral particles were defined as

$$|vres_x| < 0.006\,\text{cm} \tag{4.4}$$

and

$$|vres_y| < 0.04\,\text{cm} \tag{4.5}$$

These values are shown in Figure 4.4 as the vertical dashed lines.

Collimator Cut

A reconstructed neutral particle was also required to appear, via the reconstructed daughters, to have passed through the hole in the collimator. This cut required the

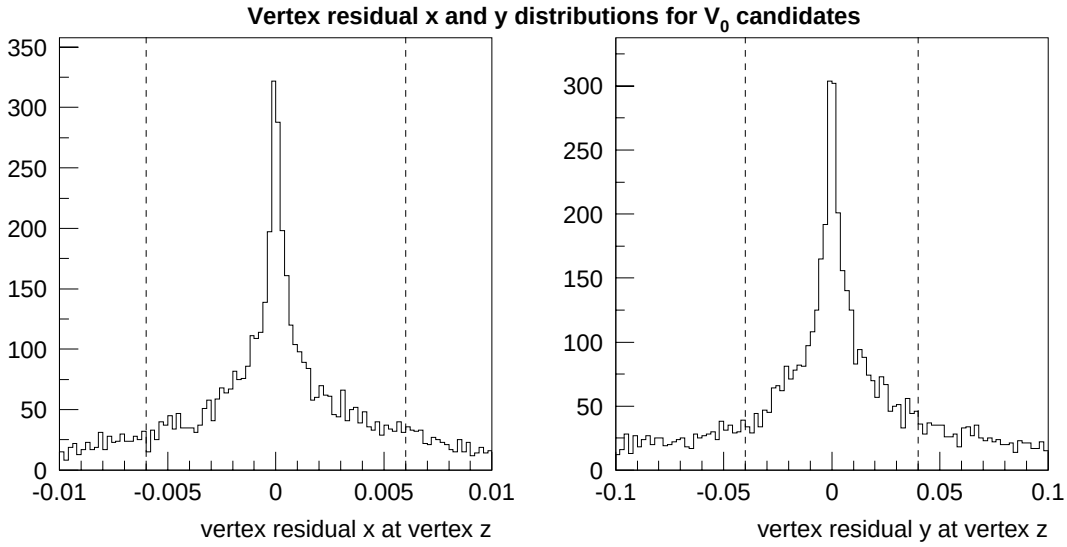

Figure 4.4 The vertex residual distribution in x (left frame), and the vertex residual in y (right frame). The units are in centimeters. The dotted lines denote the boundaries of the vertex residual cuts.

V_0 candidate trajectory, traced back to the target, to pass through both the upstream and downstream apertures of the collimator bore. This was intended to remove fake candidates originating from interactions of particles with the collimator.

Vertex z Cut

Some of the neutral vertices comprised from DDC tracks are reconstructed upstream of the actual active volume of the detector, as illustrated in Figure 4.5. In this figure is a schematic top view of a neutral particle decay inside a magnetic field. The vertical line denotes the upstream face of the DDC. The magnetic field to the left of the vertical line is weaker than the field inside the DDC (to the right of the vertical line). The dotted curved line to the left of the DDC upstream face represents the actual flight paths of the neutral particle's daughters. Though the magnetic field is quite constant inside the DDC, it decreases considerably as one moves upstream of the DDC front face. If the helix extrapolation that is performed inside the DDC is continued upstream in z (denoted by the solid lines in Figure 4.5), the apparent z coordinate of the vertex is downstream of the actual vertex z coordinate. To properly locate the z coordinate for upstream V_0 candidates, Runge-Kutta extrapolation is used in place of helix extrapolation in this region to propagate the DDC tracks through the weaker, uneven fringe fields upstream of the DDC as described in section 3.1.

According to Equation 2.6, if the opening angle calculated exceeds the actual

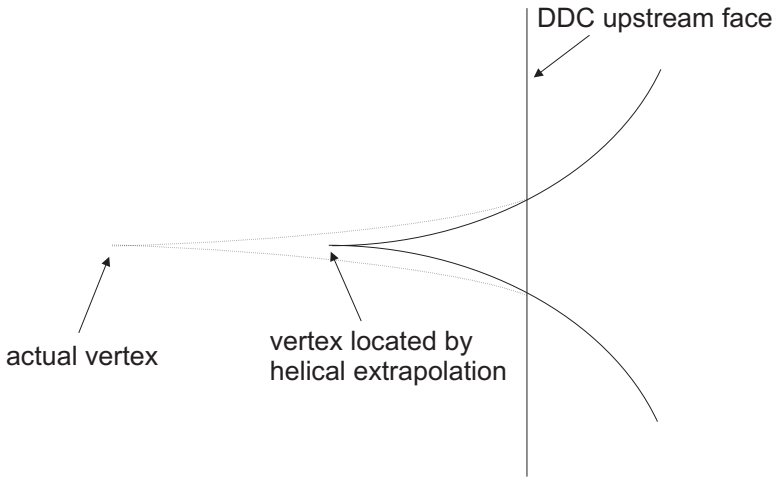

Figure 4.5 Schematic of a neutral particle decaying upstream of the DDC. The vertical line denotes the DDC upstream face. The magnetic fields are weaker on the left-hand side of that line. The dotted lines denote the actual paths of the daughter particles. The solid lines to the left of the DDC upstream face denote the apparent daughter trajectories (extrapolated from the "solid line" tracks deposited in the DDC) if the magnetic fields inside and outside the DDC were taken to be the same.

value, the dot product term is underestimated. Subtracting a systematically smaller dot product term results in a systematically larger invariant mass. Figure 4.6, which plots the calculated Λ hyperon mass versus vertex z for reconstructed V_0 candidates for helix extrapolation and for Runge-Kutta extrapolation, demonstrates this effect. Shown in the left frame is the calculated Λ invariant mass versus the calculated vertex z coordinate for Monte Carlo Λ hyperons that were digitized (*i.e.* their charged daughter tracks were converted into simulated raw DDC data) and reconstructed using helix extrapolation upstream of the DDC. The right frame plots the same quantities when Runge-Kutta extrapolation is used in place of helix extrapolation upstream of the DDC. The vertical dashed lines denote the upstream face of the DDC. The horizontal dashed lines denote the accepted Λ hyperon mass.

As illustrated in the left frame, using helix extrapolation to reconstruct upstream V_0 candidates leads to opening angles that are overestimated, resulting in invariant mass estimates that are too large. Though a re-fitting of upstream V_0 candidates using Runge-Kutta extrapolation upstream of the DDC can correct this problem (as shown in the right frame), a vertex z cut was imposed for simplicity and for consistency with the earlier Λ hyperon analyses [14], to allow direct comparisons. The vertex z coordinate, z_{vertex}, of a candidate was required to be such that

$$z_{vertex} > 381.5\,\mathrm{cm} \tag{4.6}$$

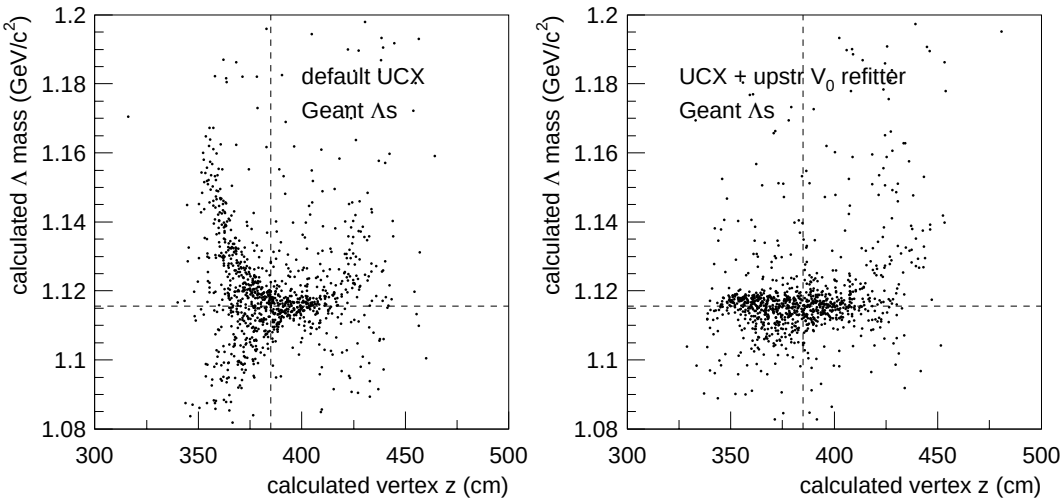

Figure 4.6 Calculated Λ hyperon mass versus vertex z for reconstructed Monte Carlo Λ hyperons with helix extrapolation upstream (left frame) and with Runge-Kutta extrapolation upstream (right frame). The vertical dotted line denotes the upstream face of the DDC.

which is about 4 cm upstream of the front face of the DDC active volume.

Wire Hit Correlation Cut

The wire hit correlation cut requires that the number of DDC wire hits associated with the positive track (N_+), relative to that quantity for the negative track (N_-), fall within a particular value. For Λ hyperons, this cut rejects pairings of a positive track with a too short negative track that could be mistaken for a pion. Figure 4.7, which plots N_- versus N_+ for digitized Monte Carlo K_s meson daughters, motivates the wire hit cut definition for K_s mesons. In this figure, the number of DDC wire hits associated with the negative track is plotted versus the number of wire hits associated

with the positive track for the digitized Monte Carlo K_s mesons. The dashed lines on the figure denote the boundaries of the wire hit correlation cut for K_s mesons. The positive and negative tracks are required to be of comparable length for K_s mesons.

For Λ hyperon candidates, this cut was defined, according to Reference [14] as:

$$|N_+ - (1.06)N_-| < 50 \tag{4.7}$$

while for K_s meson candidates, the cut is defined as:

$$|N_+ - (0.95)N_-| < 50 \tag{4.8}$$

Opening Angle Cut

A contribution to the background comes from pairings such that one or both of the daughter tracks have too high a momentum. In such a case, the V_0 candidate's apparent opening angle is suppressed with respect to actual parent decays. The opening angle cut was defined [14] as:

$$\theta_{lab\,frame} > 0.03 \text{ radians} \tag{4.9}$$

This value was chosen, along with the value for the Armenteros $p_\perp$ cut (defined next), in order to eliminate the low $p_\perp$ tail that was observed to contaminate the accepted Λ hyperon phase space. [14]

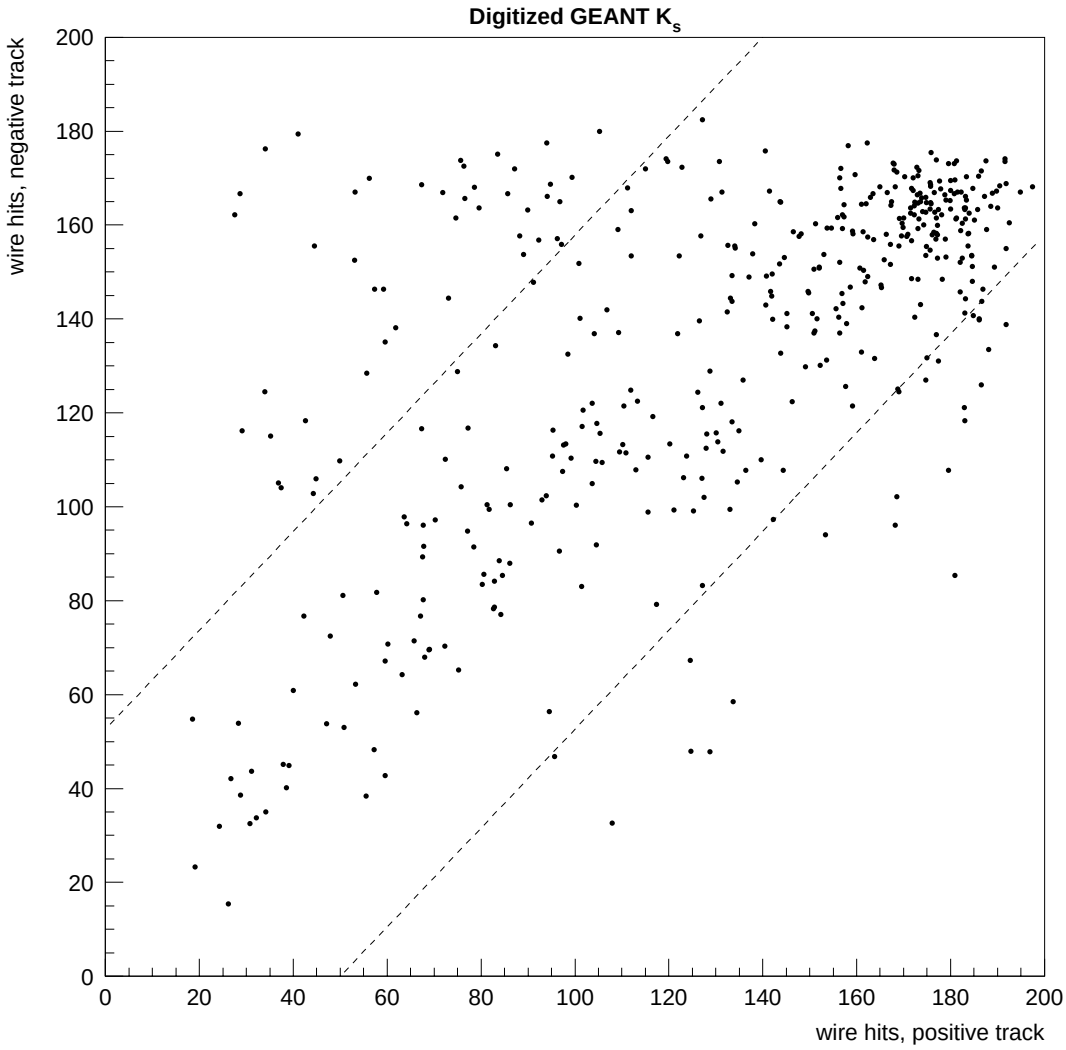

Figure 4.7 The number of hit DDC wires associated with the negative daughter track of the V_0 candidate versus the number of hit wires assigned to the positive daughter, for digitized GEANT K_s mesons. The dotted lines denote the boundaries of the wire hit correlation cut.

Armenteros $p_\perp$ Cut

Though the Armenteros variables (as plotted in Figure 2.5) cannot directly separate Λ hyperons and K_s mesons from all background processes, the Armenteros $p_\perp$ constraints for Λ hyperons and K_s mesons can reduce certain backgrounds in which the kinematics of the pair result in Armenteros $p_\perp$ and α values are inconsistent with the known properties of Λ or K_s decays. The Armenteros $p_\perp$ cut for Λ hyperons is defined as

$$p_\perp > 0.02\,\mathrm{GeV/c} \tag{4.10}$$

and, for K_s mesons, the cut is defined as

$$p_\perp > 0.1\,\mathrm{GeV/c} \tag{4.11}$$

Since the e^+e^- band on the Armenteros plot is largely below Armenteros $p_\perp = 0.02$ GeV/c (see section 2.3.1 and Figure 2.5), such a cut can remove some of the background from the Λ hyperon distribution, obviously at a loss of Λ hyperon signal. Similarly, a cut of Armenteros $p_\perp = 0.1$ GeV/c can separate much of the overlap between Λ hyperons and K_s mesons.

Phase Space Cut

The E896 and DDC detector geometry will accept Λ hyperons and K_s mesons only within a well defined range in rapidity and transverse momentum defined effectively by the edges of the DDC active volume and fiducial cuts applied in the offline software. The rejection of neutral particle candidates that fall outside of the (y,p_T) acceptance will be defined and applied more concretely in the section on acceptance corrections described below. A "crude" phase space cut was nonetheless defined in the form of a simple linear cut to the two-dimensional (y,p_T) plot for Λ hyperons. This cut is shown in Figure 4.8, which plots on a two-dimensional histogram the transverse momentum versus the rapidity for Λ candidates, from $\sim$ 11 million central events, which survive all of the other cuts described in this section. The dashed line in the figure denotes the "crude" phase space cut. The final phase space cut depends upon the acceptance calculations (described in the next section), and are performed bin by bin in (y, p_T) space.

Performance of Geometric and Kinematic Cuts

With the geometric and kinematic cuts to V_0 candidates defined above, it remains to determine how well these cuts remove backgrounds at the expense of neutral particle signal. A consistency check of the background removal in this analysis with that done earlier for Λ hyperons [14] is also discussed.

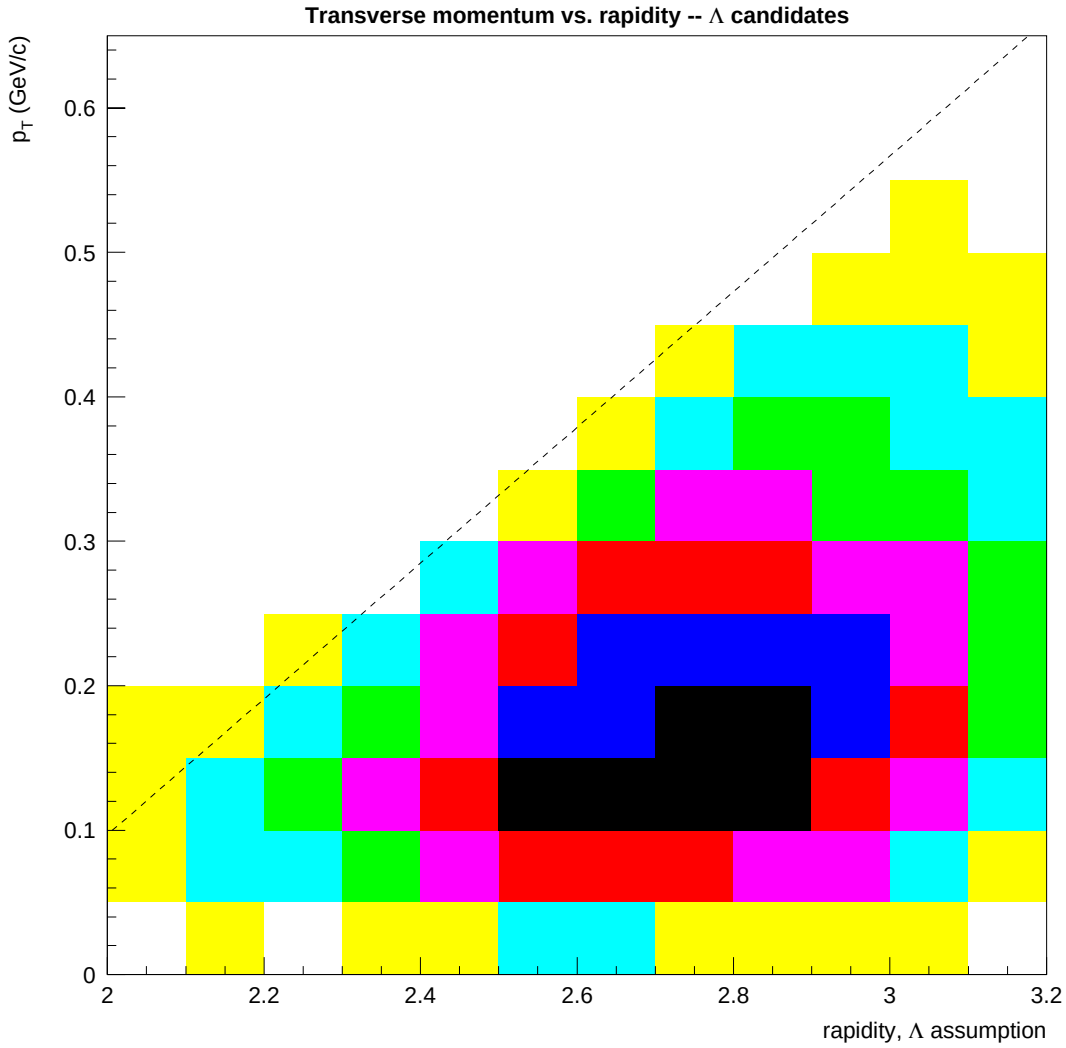

Figure 4.8 The transverse momentum versus rapidity for Λ hyperon candidates, from $\sim$ 11 million central events, that survive all geometric and kinematic cuts except the phase space cut. The dotted line depicts the boundary of this phase space cut.

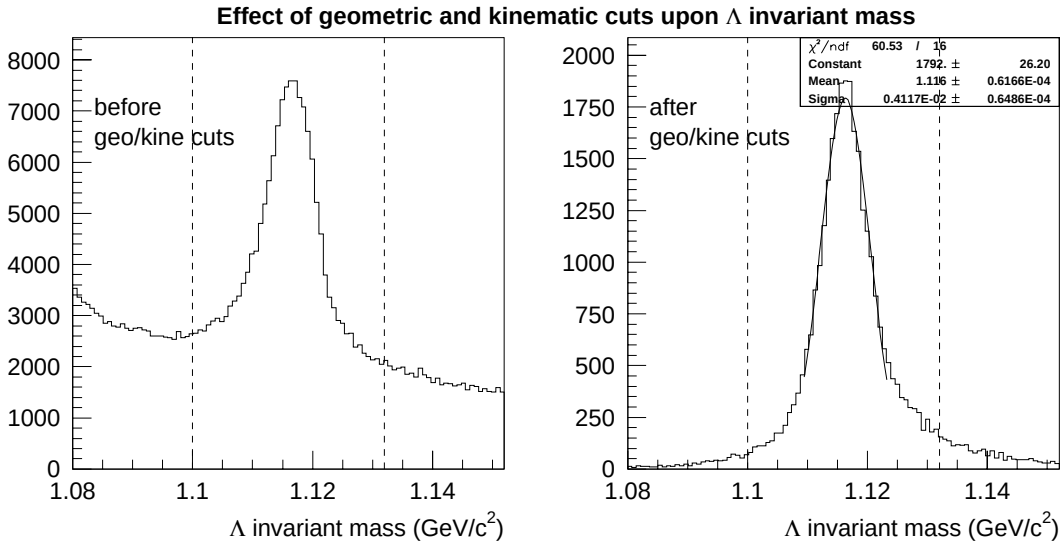

Figure 4.9 The Λ hyperon invariant mass distributions before (left frame) and after (right frame) the various geometric and kinematic cuts. For details about these cuts, refer to the text earlier in this subsection.

The diagnostic used is the percent reduction of the number of entries in the Λ hyperon invariant mass distribution within the invariant mass peak (defined as 1.1 GeV/c^2 $< m_\Lambda <$ 1.132 GeV/c^2) and outside of the peak (defined as 1.08 GeV/c^2 $< m_\Lambda <$ 1.1 GeV/c^2 and 1.132 GeV/c^2 $< m_\Lambda <$ 1.152 GeV/c^2). Figure 4.9 shows the Λ hyperon invariant mass distributions from the $\sim$ 11 million central events before (left frame) and after (right frame) the geometric and kinematic cuts. The geometric and kinematic cuts applied together sharply reduce the background, and yield a width of the invariant mass peak of about 4 MeV/c^2.

Table 4.1 summarizes the efficiencies of these cuts on the peak and off-peak re-

gions of the Λ hyperon invariant mass distributions, for each of the geometric and kinematic cuts applied individually. Also shown are the same reduction factors from the independent analysis. [14] Apart from background removal from the Armenteros $p_\perp$ cut, each of the reduction factors obtained from both analyses agree very well. One possible cause for the discrepancy in the Armenteros $p_\perp$ cut may be that the calculation of Armenteros $p_\perp$ in this analysis may be systematically too high. The source of this discrepancy is currently not understood.

cut	*on-peak reductions (%)*		*off-peak reductions (%)*	
definition	*This work*	*Ref. [14]*	*This work*	*Ref. [14]*
target x	48.4	47.2	82.7	79.3
target y	39.4	39.9	69.3	66.7
vertex res. x	36.0	36.1	49.3	48.2
vertex res. y	39.9	40.3	60.1	58.2
collimator	42.0	39.6	76.0	69.7
vertex z	28.7	27.1	11.8	15.5
wire hit correl.	11.9	12.9	23.3	25.5
opening angle	6.6	6.4	4.1	4.2
Armenteros $p_\perp$	8.7	8.3	22.2	40.7
phase space	42.7	47.1	78.3	78.5
all cuts combined	83.7		97.8	

Table 4.1 The percentages by which each individual geometric and kinematic cut reduces the peak and off-peak sections of the Λ hyperon invariant mass distribution from this work and from Reference [14] as labeled.

4.1.3 Time-Of-Flight Cuts to V_0 Candidates

All E896 analyses could apply no further cuts to the filtered V_0 candidate data set. Several estimates of contamination to the background of the resulting Λ hyperon

sample are available. The K_s meson contamination to the Λ sample was estimated to be $\sim$ 1.3 percent, and the contamination due to combinatorial background was estimated to be about 2 percent. [14]

The cuts described in this section are the extension of the previous analysis to remove Λ hyperon backgrounds that still exist after the geometric and kinematic cuts. These cuts, which use for the first time in E896 TOF detector measurements, will lead to cleaner samples of Λ hyperons and the first K_s meson distribution obtained from E896.

Positive Daughter Incidence upon Central TOF Wall

The first TOF-related cut to the remaining V_0 candidate sample requires that the positive daughter particle strike one of the slats of the TOF Central Wall. The motivating factors for this cut are the following. First, the most pertinent PID separation in this analysis involves distinguishing the $\Lambda \rightarrow$ p from the $K_s \rightarrow \pi^+$. TOF-related cuts to the negative daughter could serve as a consistency check. But with large uncertainties on the Beam Left Side Wall, π^- mesons from Λ hyperons and from K_s mesons are not easily separable via flight time measurements.

The second motivating factor is illustrated by Figure 4.10. This shows the TOF hole hit distribution of extrapolated positive daughters from V_0 candidates. Nearly all of the positive daughters from reconstructed Λ hyperons and K_s mesons are incident upon the Central Wall.

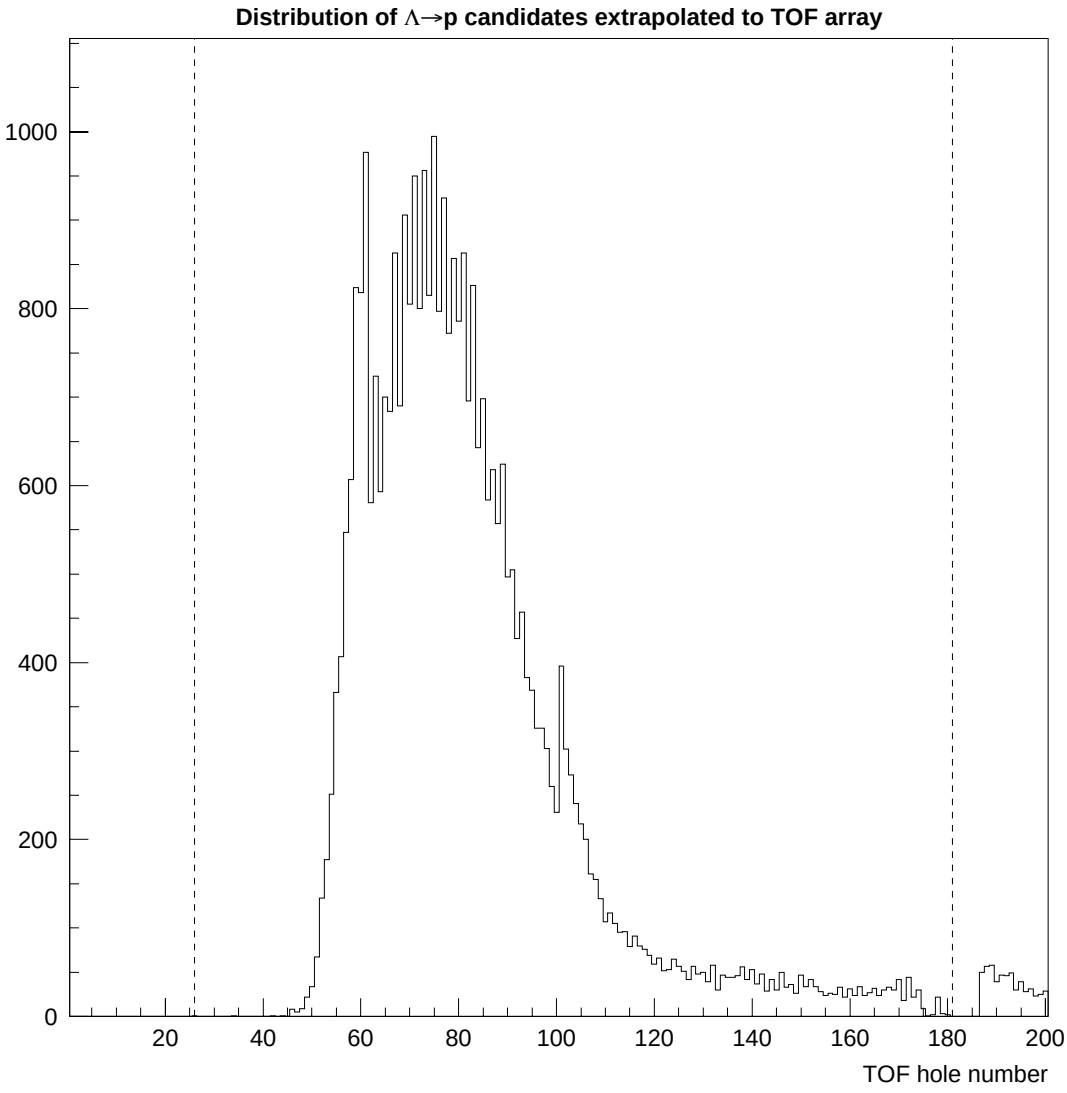

Figure 4.10 The TOF hole hit distribution of $\Lambda \rightarrow$ p candidates (which survive the geometric and kinematic cuts) extrapolated to TOF. The dotted lines denote the boundaries of the TOF Central Wall.

TOF y Consistency with Extrapolator y

After requiring the positive daughter to strike a TOF slat, a cut was applied to ensure the consistency of the y coordinate of the slat hit inferred from the difference between the slat's TDC values (y_{TOF}) and the y coordinate obtained from the extrapolation of the positive daughter track ($y_{tracking}$). These variables were introduced in subsection 3.1.2; also see Figure 3.5.

Figure 4.11 shows the distribution of $\Delta y = y_{tracking} - y_{TOF}$ for the matches to TOF of all positive daughters from V_0 candidates, after all geometric and kinematic cuts described earlier in this section. This y-consistency cut was defined such that the V_0 candidates in the hatched region of the above histogram are retained in the analysis. The peak centered at zero is interpreted as tracked positive daughters that are matched to the correct TOF slat. The y-consistency cut is defined as:

$$|\Delta y| < 6 \text{ cm} \tag{4.12}$$

Cuts to Flight Time versus Momentum

The final TOF-related cut to the V_0 candidate sample separates the $\Lambda \rightarrow$ p candidates from backgrounds using flight time measurements. Figure 4.12 shows a plot of the measured flight time versus track momentum for the positive daughter tracks of $\Lambda \rightarrow$ p candidates that have survived all of the other cuts defined in this section.

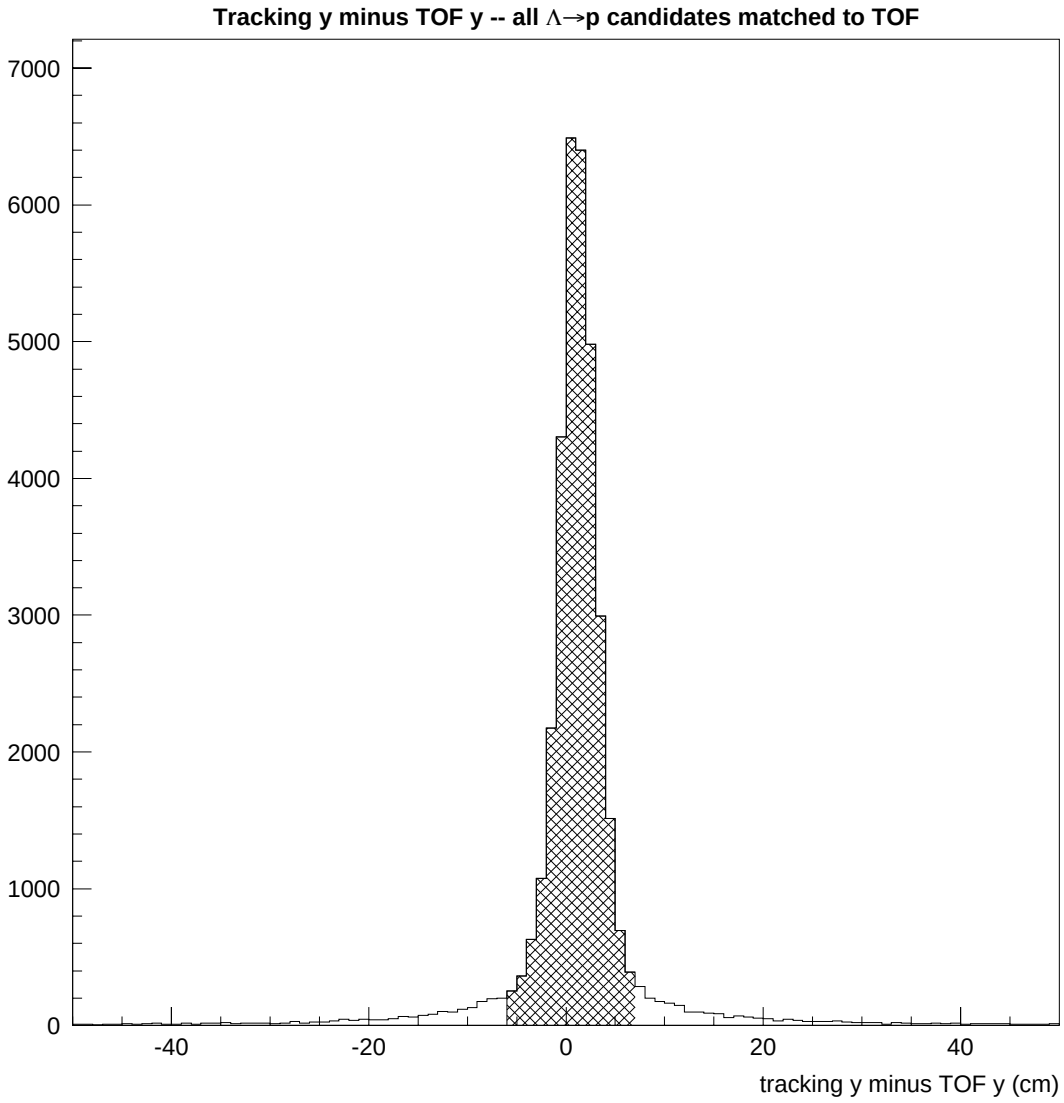

Figure 4.11 The distribution of $y_{tracking} - y_{TOF}$ for $\Lambda \rightarrow$ p candidates matched to TOF Central Wall slats.

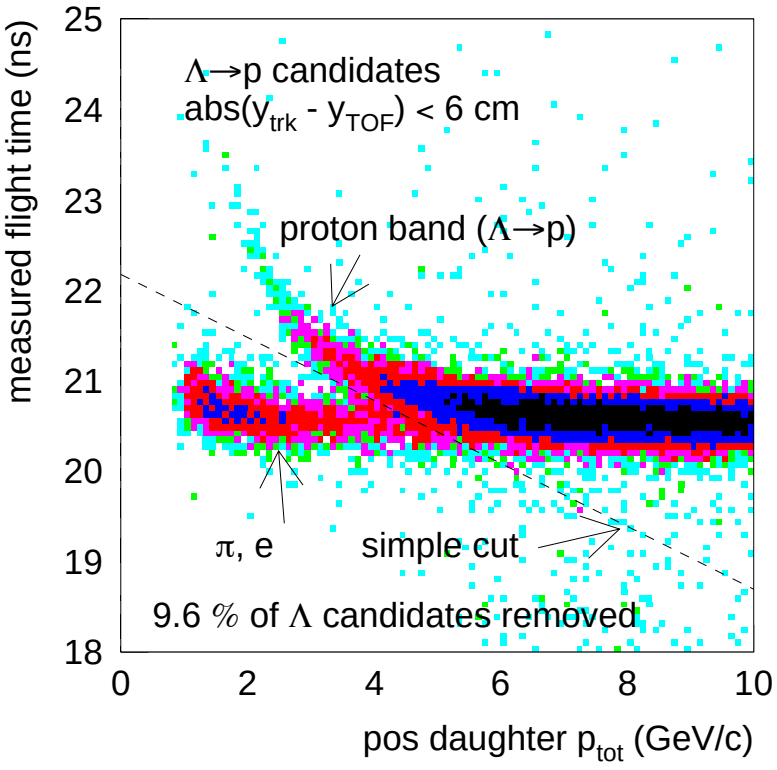

Figure 4.12 The measured flight time versus momentum for the positive daughter track of Λ hyperon candidates that are successfully matched to TOF Central Wall slats.

For $p_{tot} < 5$ GeV/c, a band separation is readily apparent. The dominant upper band, corresponding to longer flight times, is attributed to legitimate $\Lambda \rightarrow$ p candidates. The lower band is attributed to backgrounds such as $K_s \rightarrow \pi^+$, $\gamma \rightarrow e^+$, and combinatorial backgrounds. The dotted line defines the TOF PID cut.

A simple time-vs.-momentum cut is defined as a straight line on Figure 4.12 which separates the "p-band" from the "not-p-band" (attributed to lighter particles such as pions and electrons, as well as backgrounds).

An important statement made by Figure 4.12 is that, despite the best efforts of the geometric and kinematic cuts alone (*i.e.* all previous E896 Pass II analyses), there still exists recognizable background to the Λ hyperon sample when including TOF information. Approximately 9.6 percent of the Λ hyperon candidates surviving these cuts alone have positive daughters whose measured flight times are inconsistent with the proton hypothesis. This time-vs.-momentum information also provides a direct method to extract a K_s meson signal from the overwhelming Λ hyperon signal in the E896 data.

Thus, the time-vs.-momentum cut provides direct PID in the following manner. The "p-band" cut, defined as those hits which reside above the dotted line in Figure 4.12, removes daughters from K_s mesons and other backgrounds to yield a purer Λ hyperon sample. Approximately 9.6 percent of the Λ candidates are rejected by this cut. The "not-p-band" cut, defined as those hits below the dotted line, can, with additional cuts, yield a sample of K_s mesons separated from Λ hyperons.

4.1.4 Measured Λ Hyperon Yields and Spectra

Shown in the top two frames of Figure 4.13 are the distributions of the Λ hyperon invariant mass, before and after applying the "p-band" cut in Figure 4.12. The cut on time-vs.-momentum results in a 9.6 percent reduction in the Λ hyperon sample obtained from only the geometric, kinematic, and TOF-matching cuts. The lower left frame of Figure 4.13 shows the invariant mass distribution for $\Lambda \rightarrow p$ candidates that

do not pass the TOF PID cut. A peak centered about the accepted Λ hyperon invariant mass is apparent, even though the TOF flight time measurements are inconsistent with a $\Lambda \rightarrow$ p assumption.

Figure 4.14 shows the distribution of Λ hyperons in rapidity and transverse momentum space, before (left frame) and after (right frame) the time-vs.-momentum "p-band" cut. The cut tends to remove backgrounds mostly from the lower-momentum regions of (y,p_T) space in the E896 acceptance. Figure 4.15 plots the (y,p_T) distribution of Λ hyperon candidates that resided in the "not-p-band"; this is the difference between the two frames shown in Figure 4.14. The largest backgrounds to the E896 Λ analyses (recognizable with TOF) are at the lowest rapidity edge of the E896 acceptance.

Figure 4.16 shows a plot of the K_s meson invariant mass distribution for hits in the "not-p-band" region of Figure 4.12. A distinct peak centered near the kaon mass ($\sim$ 0.497 GeV/c^2) suggests the presence of $K_s \rightarrow \pi^+$ particles within the "not-p-band" region. Roughly one third of the entries in Figure 4.16 reside within this "kaon" peak. This suggests that about one third of the $\Lambda \rightarrow$ p candidate backgrounds identified by TOF are comprised of K_s mesons. Given the 9.6 percent background within the Λ candidate background, then, about one third of the TOF-identified Λ candidate background is comprised of K_s mesons.

Some of the hits in the "not-p-band" may be legitimate Λ hyperons whose positive

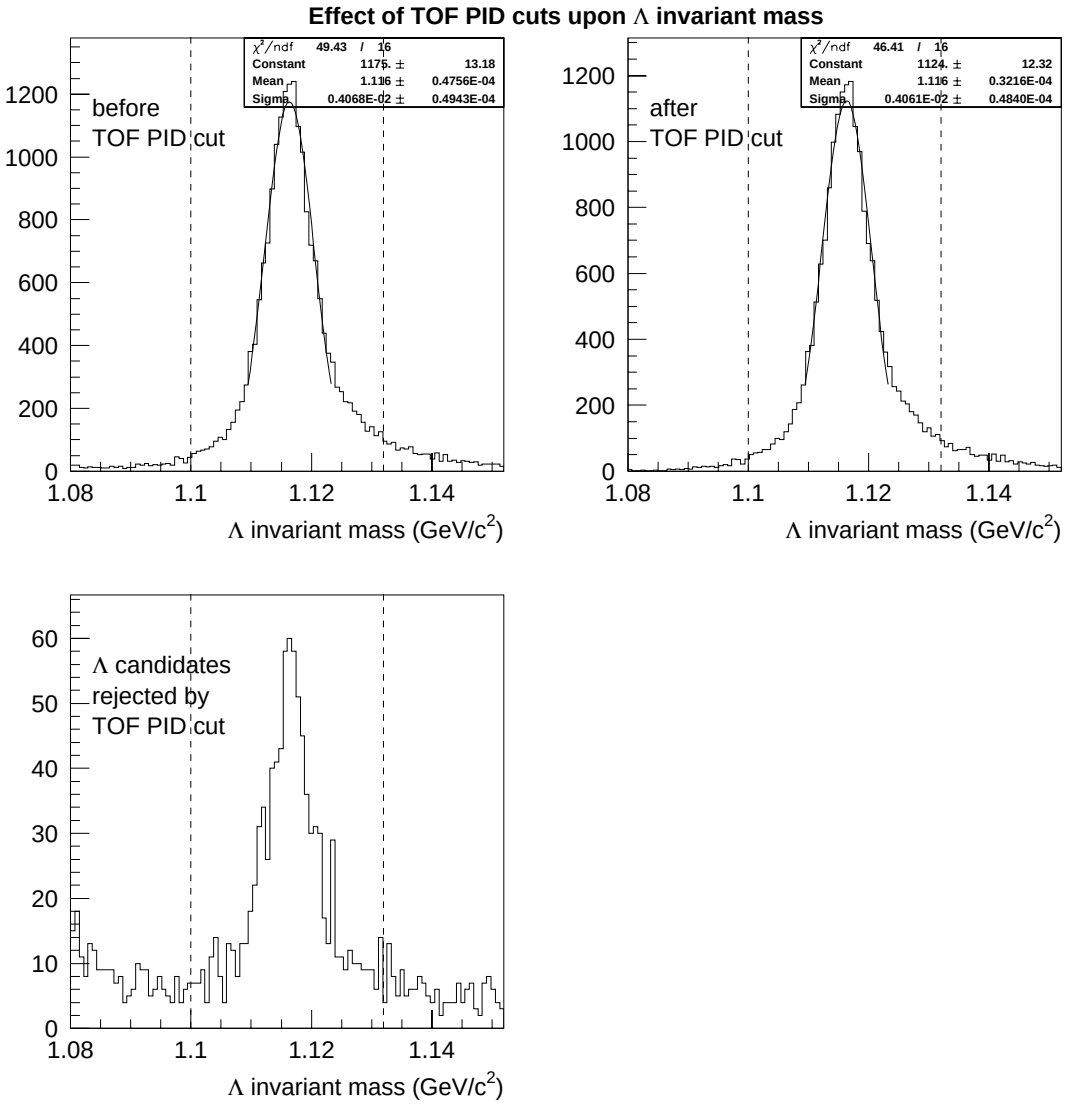

Figure 4.13 The Λ hyperon invariant mass distributions for Λ → p candidates matched to TOF slats, before (upper left frame) and after (upper right frame) applying the TOF "p-band" cut. The lower left frame shows the invariant mass distribution for Λ → p candidates rejected by the TOF PID cut.

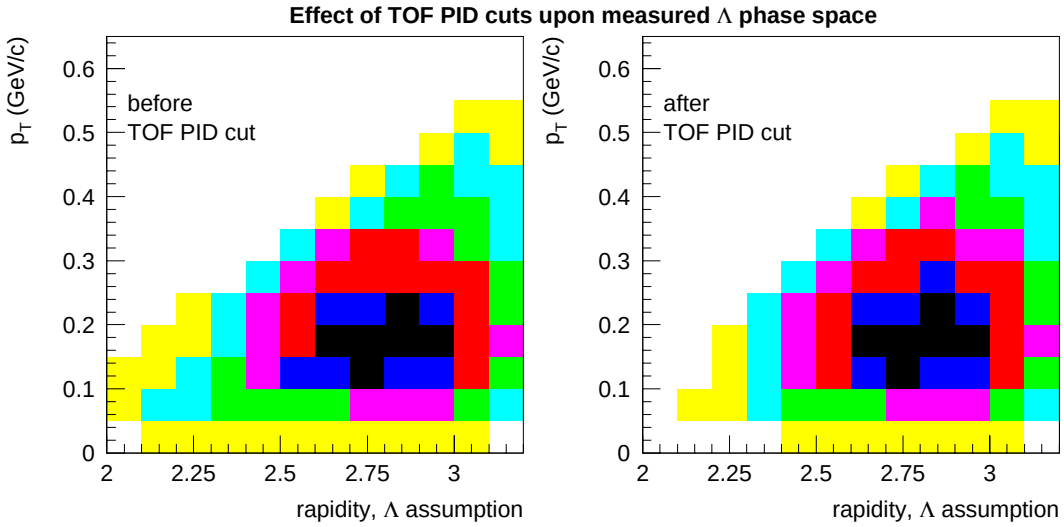

Figure 4.14 The (y, p_T) distributions for $\Lambda \rightarrow$ p candidates matched to TOF slats, before (left frame) and after (right frame) applying the TOF "p-band" cut.

daughter track was incorrectly matched to a slat that recorded a flight time consistent with a $K_s \rightarrow \pi^+$. Figure 4.17 presents Armenteros plots for V_0 candidates without TOF cuts (left frame) and with the "not-p-band" cut applied (right frame). An estimate of this "killed Λ hyperon" contribution was made by defining a zone on the Armenteros plot around the Λ hyperon region, and determining the fraction of "not-p-band" hits that remain in this Armenteros region. Of the number of Λ hyperon candidates that resided in this zone before the "not-p-band" cut, only 2 percent remained in this region after the cut. Given that many such hits in this region will actually be K_s mesons, this 2 percent is an upper bound on the "killed Λ hyperon" probability. In principle, the acceptance calculations should correct for any possible

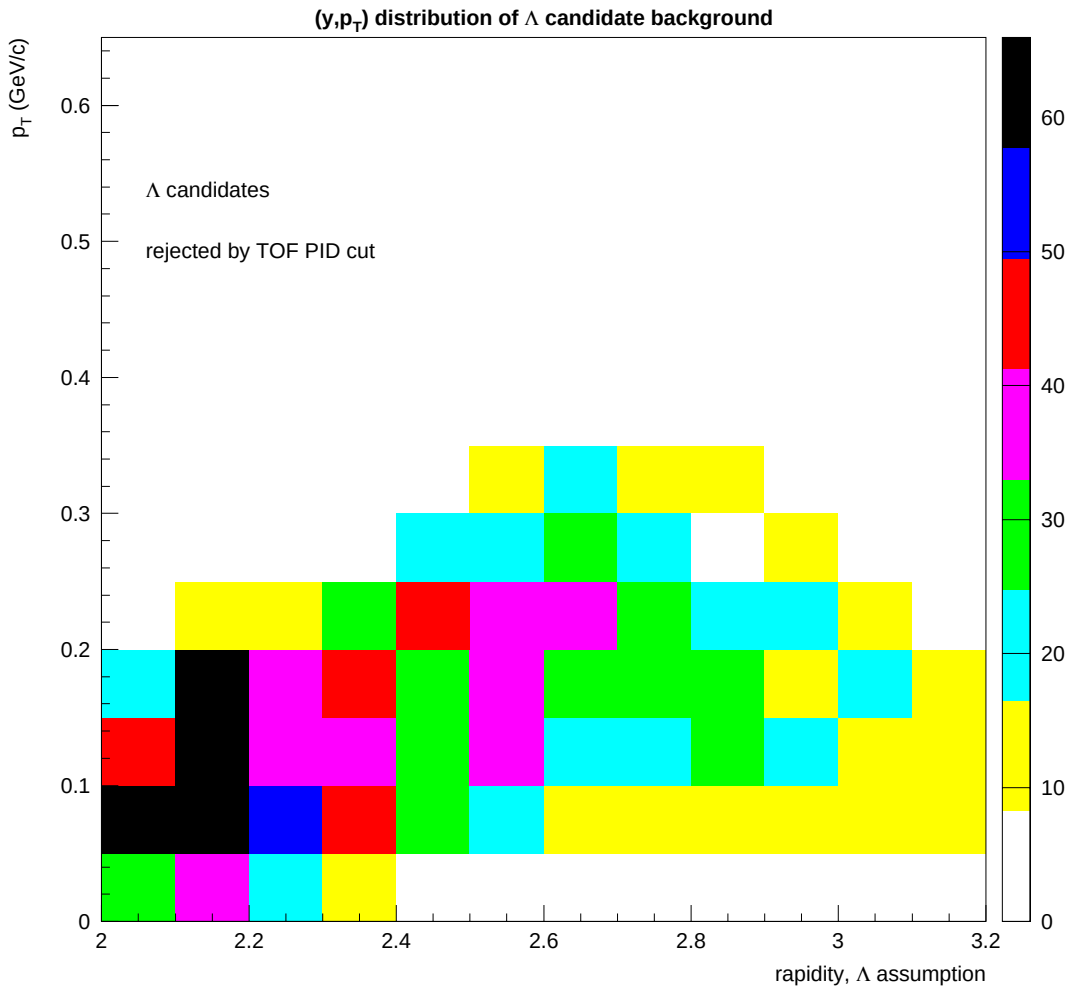

Figure 4.15 The (y, p_T) distribution for $\Lambda \rightarrow$ p candidates that reside in the "not-p-band" region.

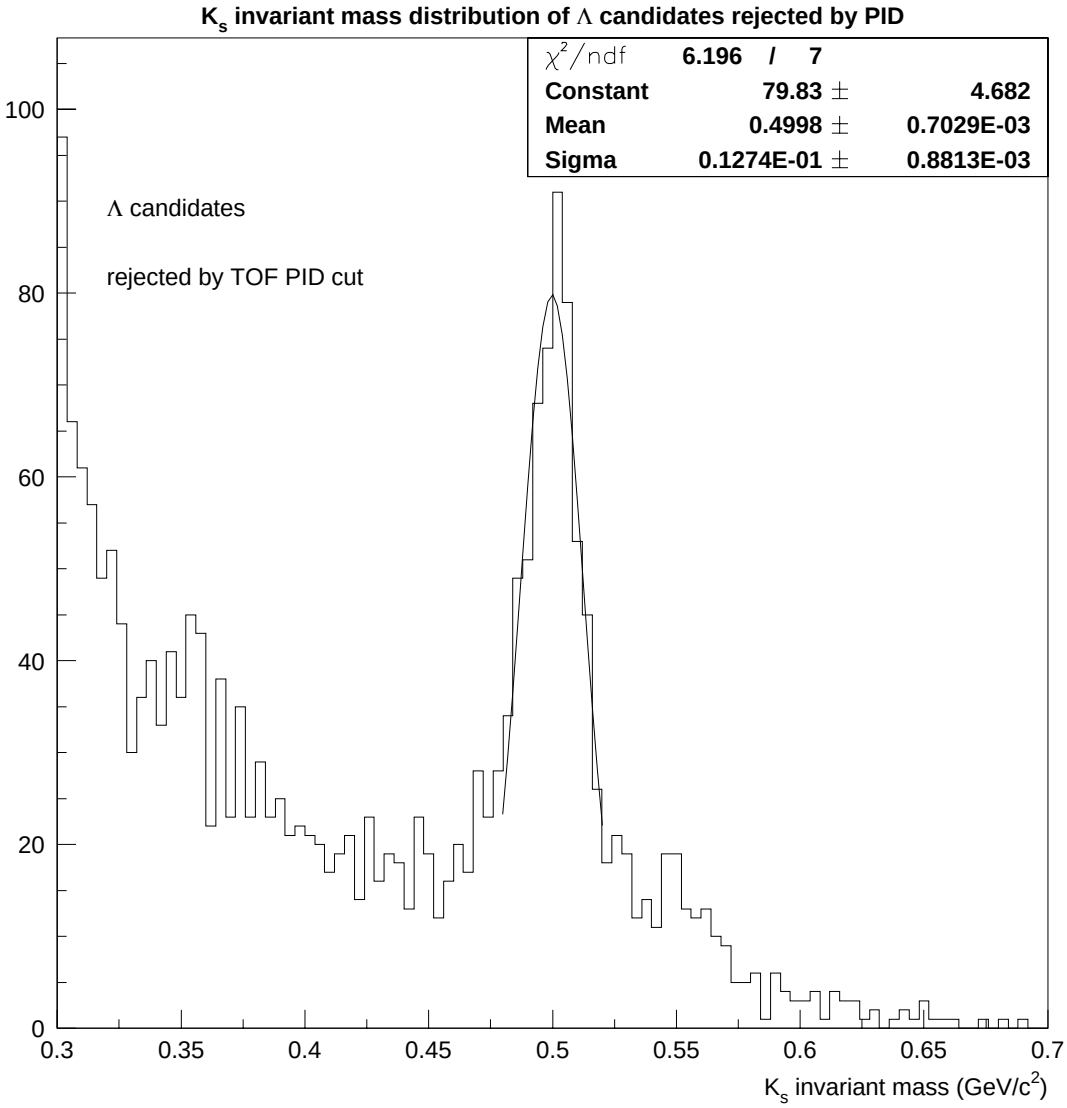

Figure 4.16 The K_s meson invariant mass distribution for V_0 candidates within the "not-p-band" region of Figure 4.12.

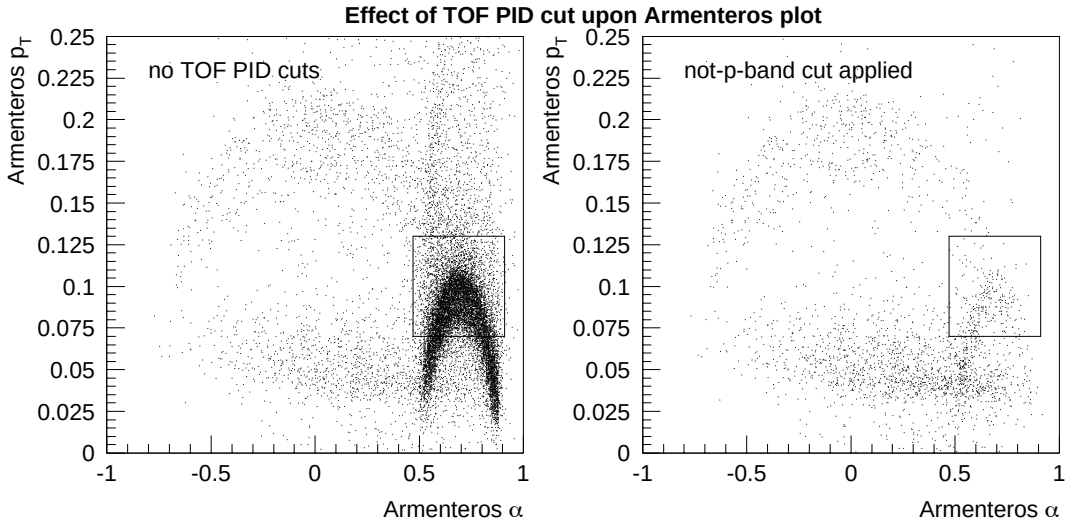

Figure 4.17 The left frame is an Armenteros plot of the Λ hyperon candidates before applying any TOF PID cuts. The right frame is the plot for hits in the "not-p-band" region of the time-vs.-momentum plot. The square on each frame defines the Armenteros region used to estimate the probability of a "true" $\Lambda \rightarrow$ p being matched to a TOF slat that gives a "not-p-band" measurement.

"killed Λ hyperons," since the flight times of the simulated Λ hyperons are "merged" with raw TOF information from Au98 events, in the same manner that Monte Carlo tracks are merged with raw DDC wire hits from Au98 data. With the K_s meson contribution of about 3 percent to the total sample of Λ hyperons, the remainder of the hits in the "not-p-band" region are attributed to $\gamma \rightarrow e^+e^-$ events and other backgrounds.

4.1.5 K_s Meson Observables

Figure 4.18 shows the K_s meson invariant mass distribution of all V_0 candidates that survive all cuts. Also displayed is the mean value and standard deviation of the K_s meson invariant mass distribution, which have values of 500 MeV/c^2 and 12 MeV/c^2, respectively.

Figure 4.19 shows the region of rapidity and transverse momentum over which these K_s mesons are detected. Shown in this figure is the transverse momentum versus rapidity for K_s mesons that survived all of the geometric, kinematic, and TOF-related cuts. In general, the K_s meson transverse momentum range is lower, and the rapidity range is higher than compared to the E896 acceptance for Λ hyperons. For $2.6 < y < 3.2$, both Λ hyperons and K_s mesons are observed.

With cleaner samples of Λ hyperons and K_s mesons now available, the next step is to determine, from these measured particle spectra, the primordial neutral spectra produced in the 11.6 GeV/c/nucleon Au+Au central collisions themselves. This is done by correcting for the E896 DDC and TOF detector geometric acceptance and V_0 candidate reconstruction efficiency as a function of rapidity and transverse momentum. These corrections and the physics results are described in the next section.

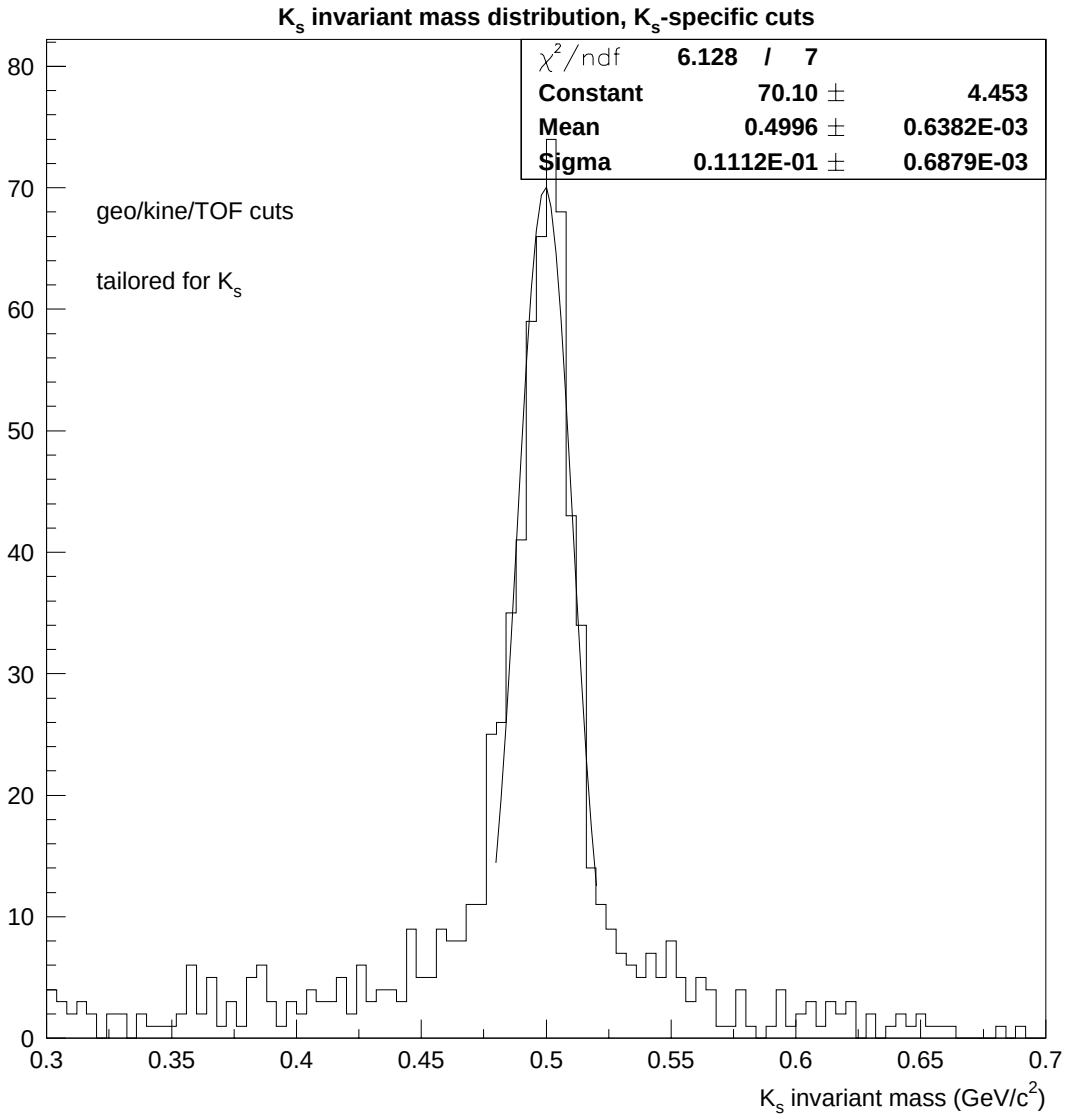

Figure 4.18 The K_s meson invariant mass distribution of those V_0 candidates which survive the geometric, kinematic, and TOF-related cuts that were optimized to purify the K_s meson sample.

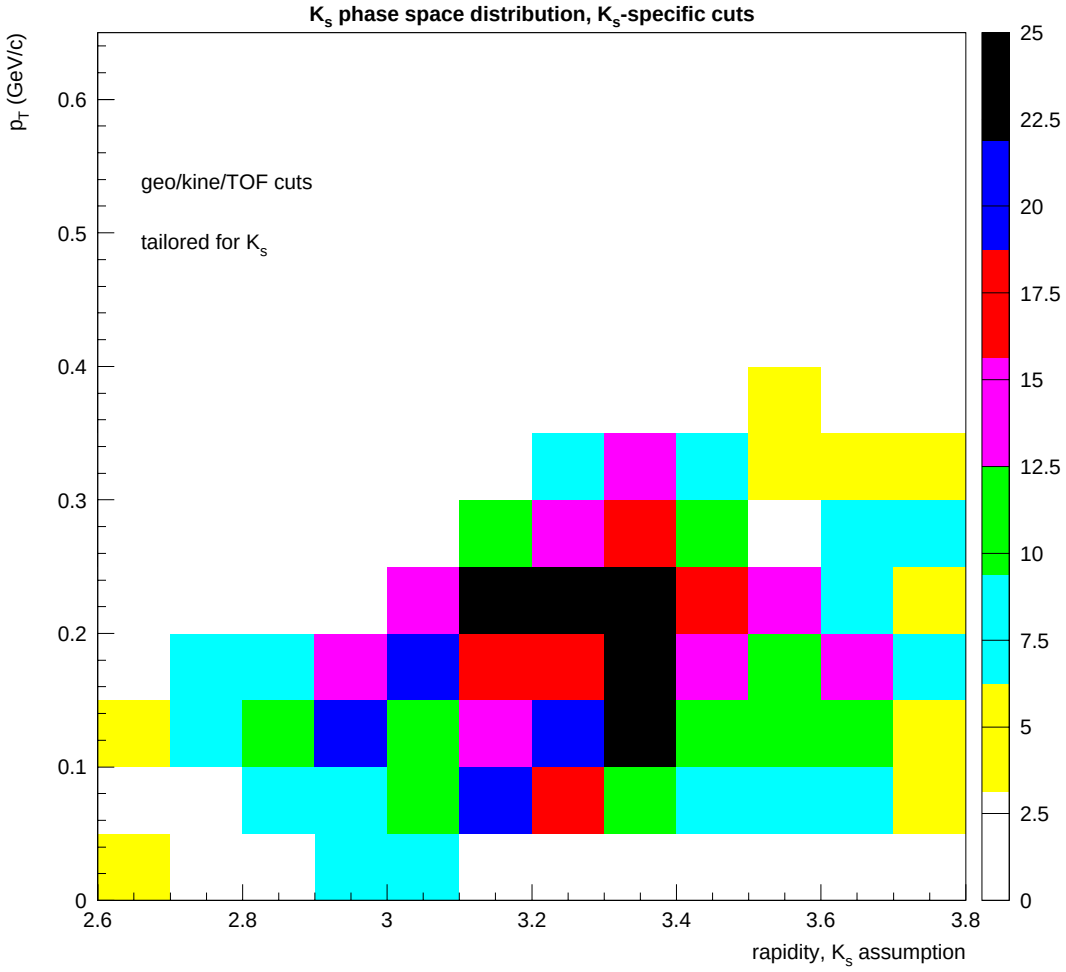

Figure 4.19 The (y, p_T) distribution of those V_0 candidates which survive the geometric, kinematic, and TOF-related cuts optimized to purify the K_s meson sample.

4.2 Acceptance Corrections

These analyses have shown that a measurable signal is observed for Λ hyperons and K_s mesons in the E896 forward detectors including TOF cuts. The formation of purified samples of events containing one of these parents involves the imposition of cuts based on experimental observables. A cut is intended to reject candidates if they are, according to specific observables, not actually a signal event but are actually a background. Cuts by definition have an efficiency, *i.e.* the probability that the event is correctly not rejected; and a discrimination power, *i.e.* the ratio of undesired events passing the cut to desired events. The conversion of experimentally observed spectra requires one to correct for the efficiencies of all of the experimental cuts to arrive at physical spectra that are comparable to other experiments and models. These corrections are described in this section.

There are two stages to the acceptance calculations. The first stage determines the *geometric acceptance*. This is the overall probability that a particle produced in a given (y,p_T) bin will decay within the acceptance of the downstream detectors. The second stage calculates the *reconstruction efficiency*. This is the overall probability that a detectable particle will be successfully reconstructed offline in Pass II and survive all of the V_0 candidate cuts described in the previous section. The overall *correction factor* for each (y,p_T) bin is the product of these two factors.

For both Λ hyperons and K_s mesons, the transverse momentum acceptance ranges

from zero to a maximum of 0.65 GeV/c. Corrections are calculated over the rapidity range $2.0 < y < 3.2$ for Λ hyperons, and $2.6 < y < 3.8$ for K_s mesons. The phase space is divided into a 12×13 grid, with rapidity bin sizes $\Delta y = 0.1$ and transverse momentum bin sizes $\Delta p_T = 0.05$ GeV/c.

Simulations were also performed to generate particles on a distribution of lifetime $c\tau$ for Λ hyperons and K_s mesons. These correction factors were used as part of a study to measure the proper lifetimes for Λ hyperons and K_s mesons, to compare with the accepted lifetimes.

The branching ratio of the charged channel decay in the simulations is set to 100 percent in the geometric acceptance calculations, as E896 is not sensitive to other Λ decay channels. The resulting correction factors are later scaled globally by applying this branching ratio, so that the spectra depicted using these correction factors corresponds to all produced Λ hyperons, not just those that decay into the charged channel $p + \pi^-$.

4.2.1 Geometric Acceptance

The method of geometric acceptance calculation was as follows. For each (y,p_T) bin, tens of thousands of Monte Carlo Λ hyperons or K_s mesons were generated with a uniform distribution within that given bin. The momentum coordinates of these Monte Carlo particles were input into GEANT, which was then used to propagate these neutral particles and their decay products through the E896 geometry. DDC

and TOF hit data from a simulated event were stored to GEANT ntuples if both daughters passed through the DDC active volume, and if the neutral decay vertex was downstream of $z = 379.49$ cm. Space points along the decay product's DDC path were stored on a 1 mm grid, to be used later in the simulation to convert the simulated energy depositions into simulated E896 detector signals.

4.2.2 Reconstruction Efficiency

The objective of the reconstruction efficiency calculations is to determine how efficiently a Monte Carlo Λ hyperon or K_s meson can be reconstructed amidst the ambient DDC wire hits and TOF slat hits that are present in central Au+Au events. First, the ntuple information extracted from the geometric acceptance calculation above is "digitized." This means that the ntuple information is converted into quantities that mimic actual detector output. The digitized Monte Carlo data is then embedded; that is, it is merged with the raw detector output from an actual Au98 central event. This allows exactly the same offline analysis code to reconstruct both experimental Au98 data and simulated data without any changes. Thus, direct measurements of the efficiency of the reconstruction can be made.

The Monte Carlo data are then embedded into raw unfiltered data from one of the experimental data runs used in the V_0 candidate analysis. The run was chosen such that the ramp ADC overflow problem was not present. The digitization and embedding processes for the DDC data and the TOF data are described separately

below.

DDC Digitization and Merging

The first step in digitizing DDC ntuple information is determining which DDC wires are in the proximity of the GEANT track. The distance of closest approach of the track to each wire is then converted into an equivalent raw TDC value for the relevant DDC wires. To simulate the sick or dead regions of the DDC, the digitized wire hit data are randomly "killed" using a per-plane efficiency table. [14] The per-plane efficiency table was compiled from one of the p98 runs by fitting single-particle tracks in the DDC, and determining the probability per DDC plane of a struck wire corresponding with the track. [14] The per-plane efficiency ranged from about 65 percent to about 95 percent across the depth of the DDC.

The simulated DDC wire hit data for the Monte Carlo daughter tracks is then merged with an experimental Au98 event. For a given digitized wire hit in the Monte Carlo event, if a DDC wire in the Au98 event registered no TDC value, the Monte Carlo TDC value was simply copied to the Au98 data bank. If the wire in the Au98 event registered a nonzero TDC value, the wire was then set to the lower of either the Au98 TDC value or the digitized Monte Carlo TDC value. This then results in simulated DDC raw data that contains the same backgrounds as do the experimental events (since the experimental events are actually used here), and that is known to contain one parent particle of interest in a specific detectable (y, p_T) bin. At this level,

acceptance correction factors comparable to those in Reference [14] can be extracted, as described below.

TOF Digitization and Merging

The objective of the TOF digitization is to convert the GEANT measured flight time and vertical slat coordinate information into simulated raw TDC and ADC values for the individual PMTs. This will allow the calculation of the efficiencies and hence correction factors for the additional TOF-related cuts of subsection 4.1.3.

For each TOF slat hit in the GEANT TOF ntuple, a 120 ps smearing is first applied to the GEANT flight time to include the TOF measurement resolution determined in the previous chapter. Next, the time-measurement calibrations, for timing offset, slew correction, and gain correction, are "undone," as they are in the raw experimental data. These are later recorrected by the main reconstruction and PID analysis software.

To simulate the slew effect, an "artificial" $\langle \mathrm{ADC} \rangle$ value consistent with a MIP response is assumed for the slat. The GEANT vertical hit coordinate, along with the correspondence between extrapolator y and TOF y observed in the track-to-slat matching studies, are used to determine the digitized raw TDC value for one PMT relative to the other. Finally, a pedestal "un-correction" is applied to the simulated PMT ADC values, using the ramp ADC value for the Au98 event that is also used in the embedding.

For a given GEANT slat hit, if the corresponding slat in the Au98 event does not register a hit (*i.e.* both TDCs are zero), the digitized TDC and ADC values are simply transferred to the Au98 TOF data bank. If the slat did record a hit in the Au98 event, the embedding is done in the following manner. First, the PMT ADC values for Monte Carlo TOF slat hits and Au98 data are added together. This simulates the response to two charged particles striking the same slat in an event, as both would be "inside the ADC gate" and hence both measured. Next, the PMT TDC value is taken to be the lower of the Monte Carlo TDC value and the Au98 raw TDC value (*i.e.* the faster of the two arrival times) at each end of the slat separately:

$$TDC_{merged} = \min(TDC_{MC}, TDC_{Au98}) \tag{4.13}$$

Monte Carlo V_0 Candidate Re-filtering and Re-cutting

After the digitized DDC and TOF data are embedded within the experimental Au98 event, the combined event is then put through the same analysis software chain as is used to analyze experimental data. The same V_0 candidate finding and filtering code and execution performed on the raw Au98 data are applied to the embedded data. The same geometric, kinematic, and TOF-related cuts that were applied to filtered V_0 candidates in the data are applied to Monte Carlo V_0 candidates found in embedded events. The daughter tracks of these found and fitted Monte Carlo V_0 candidates are extrapolated to the TOF wall and matched to TOF slats, and the ADC

and TDC calibrations are performed. This allows the measurement of experimental and software efficiencies using these simulations.

Counting the Reconstructed Monte Carlo V_0 Candidates

Not all of the V_0 candidates reconstructed within the embedded events will be "true" Monte Carlo Λ hyperons or K_s mesons. There may exist some "native" V_0 candidates which are inherent in the Au98 file before embedding, and which survive the geometric, kinematic, and TOF-related cuts. Also, some "hybrid" V_0 candidates may be formed by pairing a Monte Carlo track with a track in the "background" Au98 event. If not accounted, these "native" and "hybrid" V_0 candidates can lead to erroneous correction factors.

The number of "true" reconstructed Monte Carlo V_0 candidates is determined for a given (y,p_T) bin by plotting the invariant mass distribution for all reconstructed V_0 candidates, fitting a Gaussian function to the distribution, and taking the number of "true" Monte Carlo V_0 candidates to be the area under the Gaussian:

$$N_{rec\,MC\,V_0 s} = \sqrt{2\pi} C \sigma \tag{4.14}$$

where C is the height ("constant") of the Gaussian peak and σ is the width ("sigma") of the Gaussian in units of bin widths. An example of such a fitted invariant mass peak is shown in Figure 4.20. In this figure is plotted the invariant mass distribution of reconstructed Monte Carlo Λ hyperons that were generated within a given (y, p_T) bin,

propagated through E896 using GEANT, and digitized. A Gaussian fit is also shown on this distribution. For those regions of (y,p_T) space where geometric acceptance is very low, simply the total number of entries in the histogram is used instead of a Gaussian fit and integration.

4.2.3 Correction Factor Results

The validity of the above correction factors was checked by comparing the factors for Λ hyperons without TOF-related cuts with those obtained in a previous independent analysis. [14] Figure 4.21 displays, for separate rapidity bins, both sets of correction factors as a function of p_T. The solid points denote the correction factors obtained from this analysis (without TOF cuts), and the dotted points denote the factors from the previous analysis. For all rapidity bins in the E896 acceptance, the two correction factor calculations agree very well, despite differences in the algorithms used to calculate the reconstruction efficiency in the two cases. This instills confidence in the validity of the other sets of correction factors needed for this analysis, which include those that use TOF-related cuts in reconstructing V_0 candidates.

Figure 4.22 shows the correction factors for Λ hyperons, without TOF cuts (lines and error bars) and with TOF cuts (solid circles) obtained from the same simulations. The effect of the TOF PID cut can be seen primarily near the lower rapidity values in the E896 acceptance, *i.e.* $y < 2.9$. The TOF cuts and corrections have smaller effect upon the correction factors for $y > 2.9$.

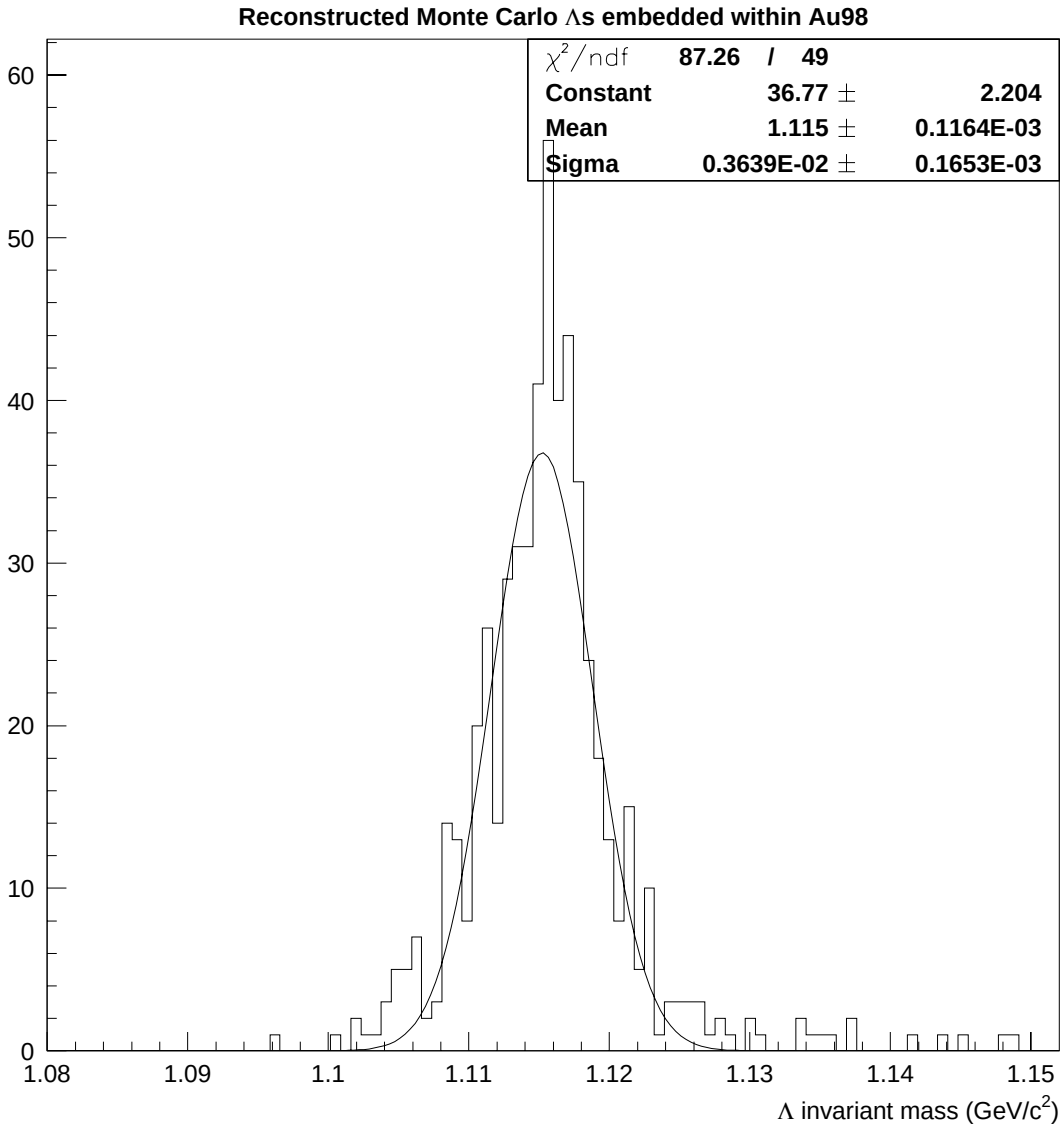

Figure 4.20 An example of the invariant mass distribution compiled from Monte Carlo V_0 candidates reconstructed within a particular (y, p_T) bin in the acceptance calculations.

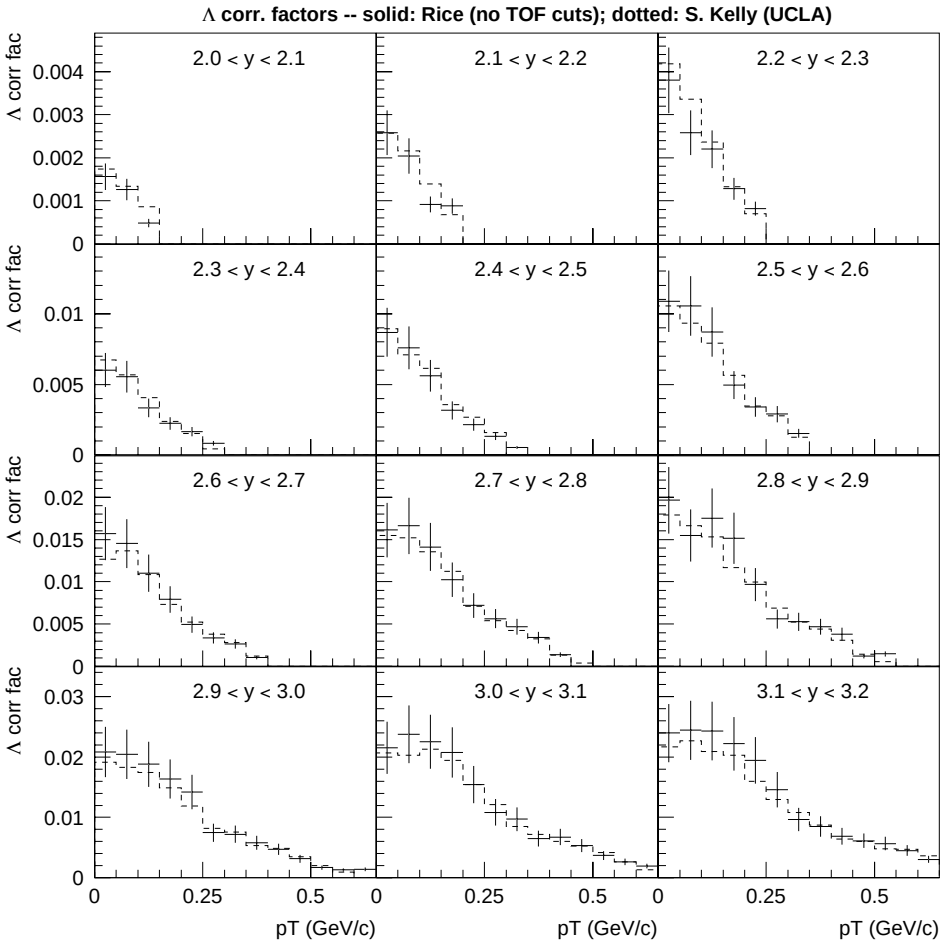

Figure 4.21 The Λ hyperon correction factors obtained in this analysis without TOF cuts (solid lines), compared with those obtained in the earlier DDC Λ hyperon analysis [14] (dotted lines).

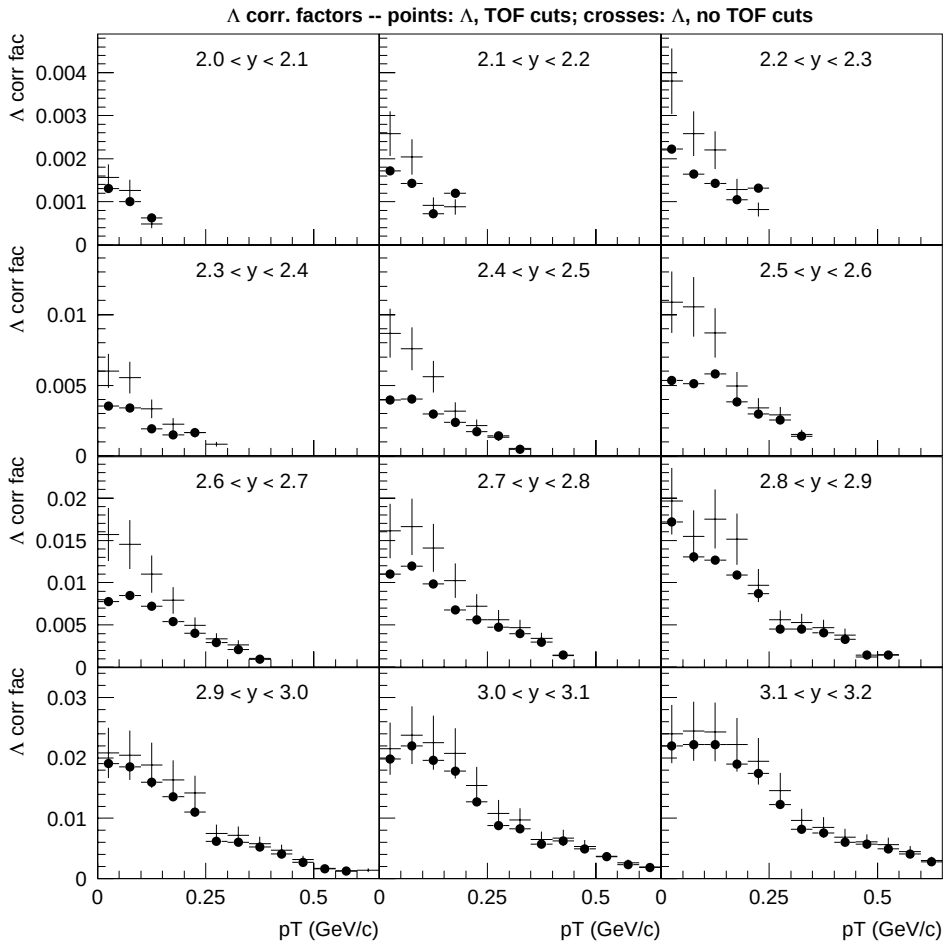

Figure 4.22 Comparison of the Λ hyperon correction factors including TOF cuts and corrections (crosses) with those obtained without the TOF cuts (solid circles).

Figure 4.23 compares the correction factors in specific (y, p_T) bins for Λ hyperons (crosses) and K_s mesons (solid circles) over the region of rapidity where the Λ hyperon and K_s meson acceptances in E896 overlap. The E896 DDC+TOF system's efficiency for K_s mesons is about two orders of magnitude smaller than that for Λ hyperons, due in part to the K_s meson's shorter lifetime.

For the results presented above, a systematic error was determined in the following manner. A "bin-leakage" error can be observed in a plot of the rapidity and the transverse momentum distributions for reconstructed V_0 candidates initially generated within a given (y,p_T) bin. Figure 4.24 shows the rapidity distribution for reconstructed Monte Carlo Λ hyperons relative to the rapidity bin within which they were originally generated. The rapidity distribution of reconstructed embedded V_0 candidates spreads outside the rapidity range within which the Λ hyperons were initially generated. Though this bin-leakage effect, a simply experimental resolution, becomes more pronounced as the parent particle momentum increases, an average bin-leakage error of about 20 percent over the relevant (y,p_T) space was found. The statistical errors tend to be negligible compared to the systematic experimental uncertainties.

4.3 Results, Comparisons, and Discussion

Now that the corrected yields of produced particles as a function of rapidity and transverse momentum have been obtained from the experimentally measured Λ hyperon and K_s meson yields, it remains to compare these produced-particle yields from

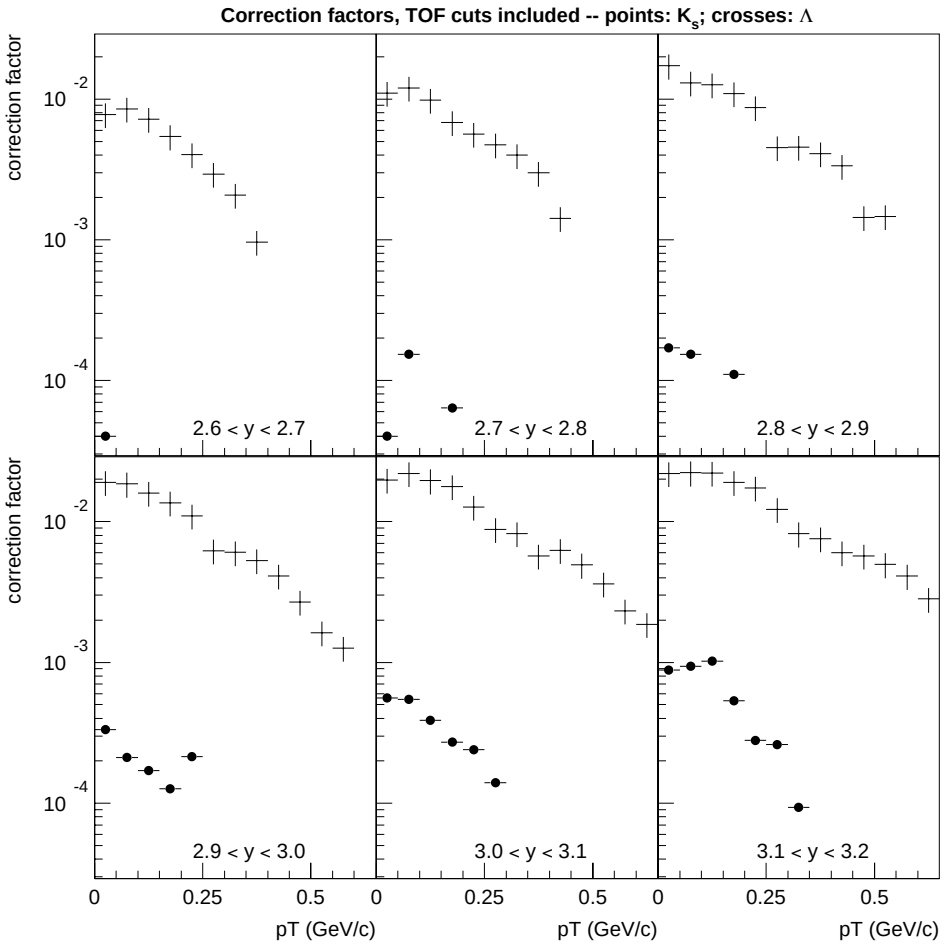

Figure 4.23 The correction factors (TOF cuts and corrections included) for Λ hyperons and K_s mesons in the regions of (y, p_T) where the DDC+TOF acceptances overlap.

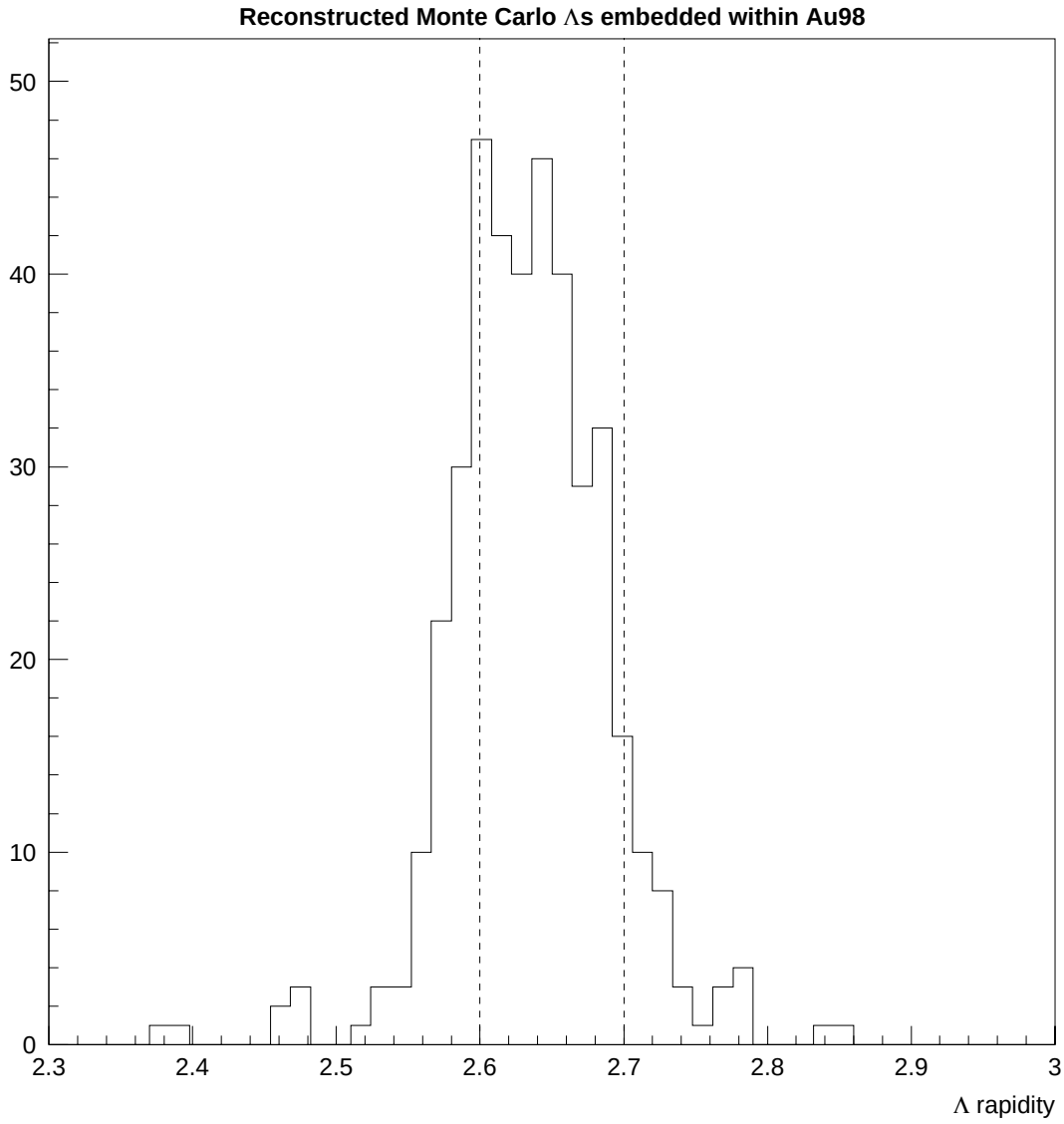

Figure 4.24 The rapidity distribution for V_0 candidates reconstructed from Monte Carlo Λ hyperons generated within a particular (y, p_T) bin. The dotted lines define the rapidity range within which the Monte Carlo Λ hyperons were originally generated.

the E896 TOF analysis with those predicted by RQMD and those reported in other AGS experiments. These comparisons are now described.

Certain AGS experiments have detected K_s mesons within their detector acceptance [27], but none have published results for acceptance-corrected K_s meson yields or spectra. Thus, the results presented below are the first measurement of very forward K_s meson production in 11.6 GeV/c/N Au+Au collisions. These will be compared to the predictions by RQMD in the same acceptance.

4.3.1 Transverse Mass Distributions

Several models for possible quark deconfinement within the participant matter of a heavy-ion collision impose requirements upon the energy density within the participant region. [28] [29] Thus, most relativistic heavy-ion experiments seek to infer the temperature of the participant matter produced in the beam-target interaction as this is related to the energy density via additional assumptions. A temperature measurement is done by measuring the transverse mass distributions of different particle species produced within the participant region, and fitting a Boltzmann distribution to them. The slope of the fitted distribution is interpreted as a "temperature."

Measured temperatures at the center-of-mass rapidity are the most pertinent to the temperature of the participant matter at freeze-out. The present detector systems only measure particles at near beam-like rapidities ($y \sim 3.2$). A model to extrapolate these near beam-rapidity temperatures to the mid-rapidity region is thus used. An

isotropic thermal model, or "fireball model," is just one option. This model [30] [31] predicts the temperature to be related to the rapidity in the following manner:

$$T(y) = \frac{T(y_{mid})}{\cosh(y - y_{mid})} \tag{4.15}$$

For different species of particles, there is experimental evidence suggesting that their mid-rapidity temperatures increase linearly with their mass. [32] [33] This linear dependence was shown to take the following form:

$$T_{eff} = T_{fo} + \frac{m}{2}\langle v_{flow}\rangle^2 \tag{4.16}$$

where T_{fo} is the temperature of the participant matter at freeze-out, and $\langle v_{flow}\rangle$ is the transverse velocity of the participant matter.

Though many prior analyses have used the above expression to calculate T_{fo} and $\langle v_{flow}\rangle$, for example [30] [34], it should be noted that there is also evidence of a breakdown of the above relation for Λ hyperons. While protons and Λ hyperons have similar mass, their mid-rapidity temperatures are quite different. [35] Several experiments [32] [36] have reported that protons and Λ hyperons exhibit different transverse motion characteristics.

In the following plots, the produced particle yields are plotted versus the "transverse mass" $m_T - m_0$, where m_0 is the rest mass of the particle, and:

$$m_T = \sqrt{p_T^2 + m_0^2} \tag{4.17}$$

The differential yield is assumed to have a Boltzmann-like (thermal) dependence upon the transverse mass [31] [37]:

$$\frac{1}{2\pi p_T N_{ev}} \frac{d^2N}{dy dp_T} = A m_T \exp(\frac{m_T - m_0}{T}) \tag{4.18}$$

where A and T are constants that depend only upon rapidity. The parameter T is referred to as the *inverse slope parameter*, and is often used directly as a measure of the source temperature of the particles at freeze out at that rapidity.

The experimental particle yields in (y, p_T) bins are mapped to the appropriate points in $m_T - m_0$ space and scaled by the factor $1/(2\pi p_T)$. The differential units of rapidity and transverse momentum are approximated by the bin sizes $\Delta y = 0.1$ and $\Delta p_T = 0.05$ GeV/c. The results are then plotted against $m_T - m_0$.

Plots of the differential yield versus transverse mass, for acceptance-corrected Λ hyperons that survive only the geometric and kinematic cuts, are shown in Figure 4.25. For clarity, the data in each rapidity bin are scaled by successive factors of ten. The points and solid line fits correspond to corrected yields using the locally determined correction factors that do not include TOF cuts. The dotted lines represent the fits to the Λ hyperon data corrected using the factors extracted from the earlier Λ hyperon analysis [14]. Error bars reflect the estimated 20 percent systematic error.

The statistical errors are smaller than the marker size.

The effect of the TOF-related cuts upon the transverse mass spectra is shown in Figure 4.26. The dotted lines are the fits to the corrected Λ hyperon data without TOF cuts. These dashed lines are the same as the solid lines in Figure 4.25. The results for Λ hyperons after applying the TOF-related cuts and corrections are represented by the points and the Boltzmann fits are shown as the solid lines. The error bars represent the 20 percent systematic error.

The rejection of Λ hyperon background in the lower rapidity regions ($y < 2.6$) by the TOF cuts is apparent in the dramatic difference in magnitudes between the dotted and solid lines. The differences in magnitude and slope (temperature) are smaller for higher rapidities, since the TOF-related cuts reject fewer V_0 candidates at these rapidities.

Figure 4.27 compares the transverse mass spectra for Λ hyperons from the TOF-cut data (points and solid lines) and the filtered GEANT simulation of RQMD v2.4 events (dotted lines). The magnitudes at $m_T - m_0 = 0$ for the TOF-cut data and for RQMD in the lower rapidity region are similar, suggesting that the TOF cuts are properly removing backgrounds in that region. Figure 4.28 shows a similar comparison of the $m_T - m_0$ distribution and fit results for K_s meson data (points and solid lines) and RQMD (dotted lines). For those rapidity bins where K_s meson transverse mass acceptance is higher, the measured temperatures are consistent with RQMD.

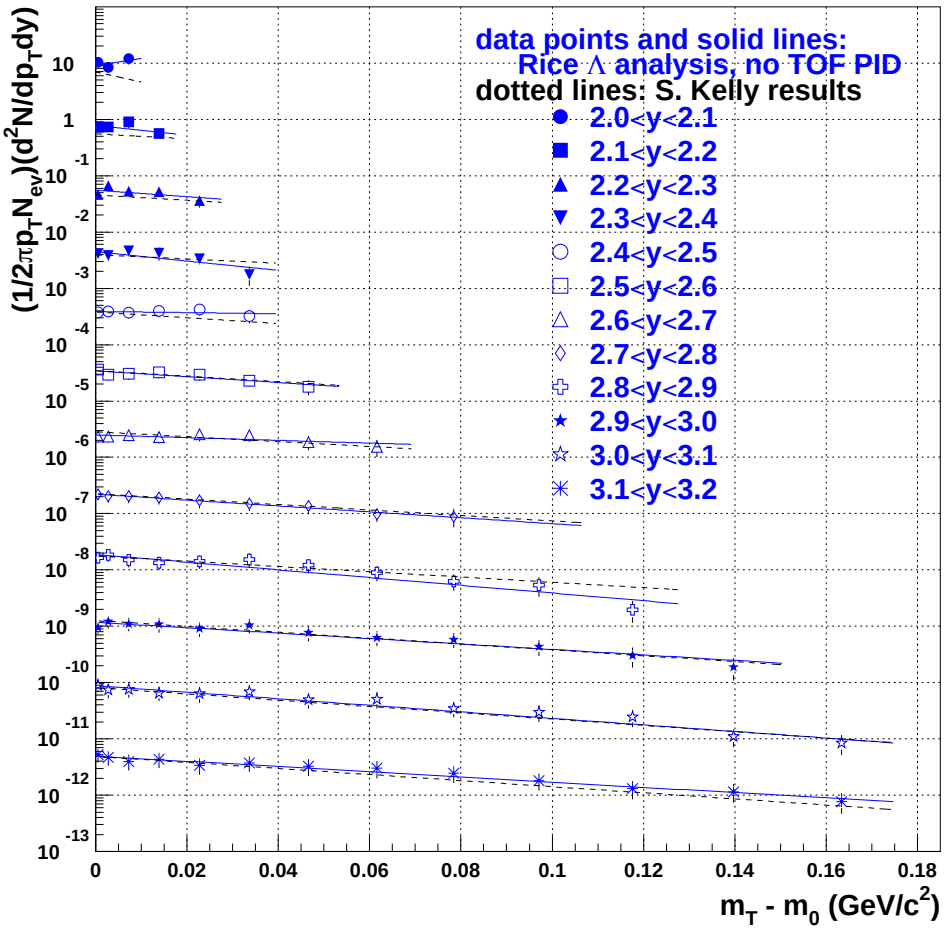

Figure 4.25 The differential yield versus transverse mass for corrected Λ hyperons in E896, without TOF cuts. The markers represent the data from this analysis; the solid lines denote the Boltzmann fit results. The dotted lines represent the fits to the produced Λ hyperon distribution from the analysis described in Reference [14].

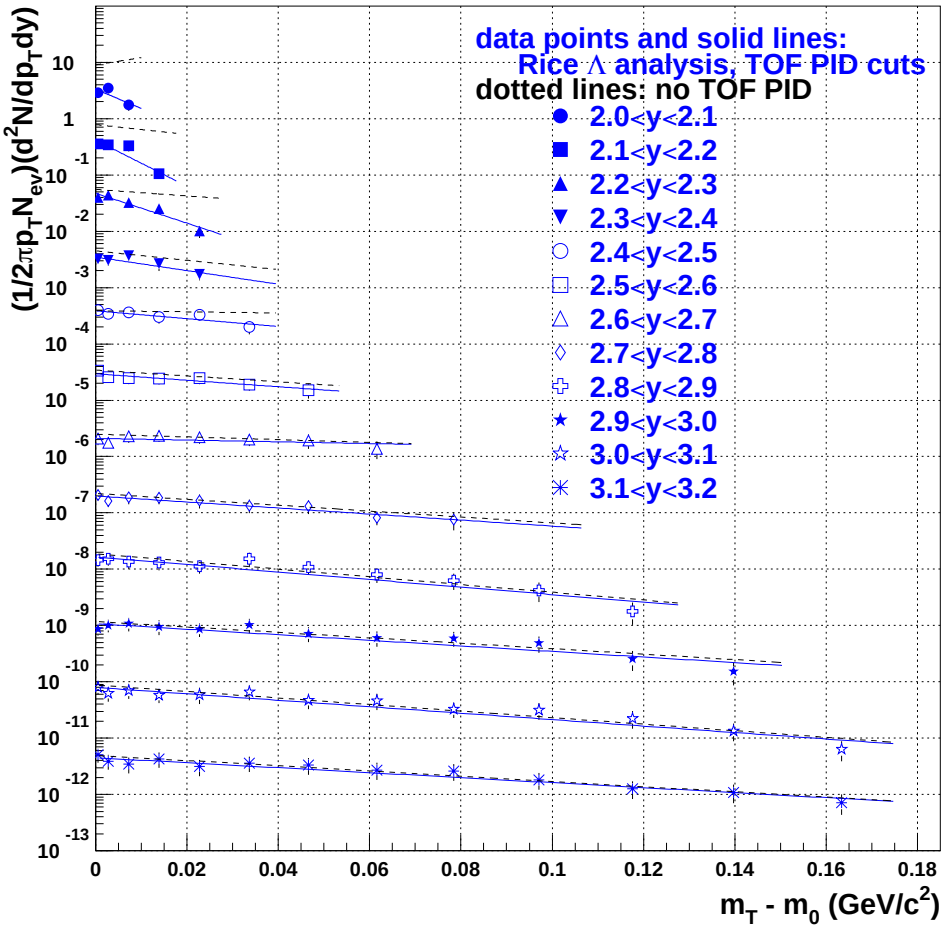

Figure 4.26 The Λ hyperon differential yields versus transverse mass for produced Λ hyperons in this analysis, with TOF cuts (markers and solid lines) and without TOF cuts (dotted lines).

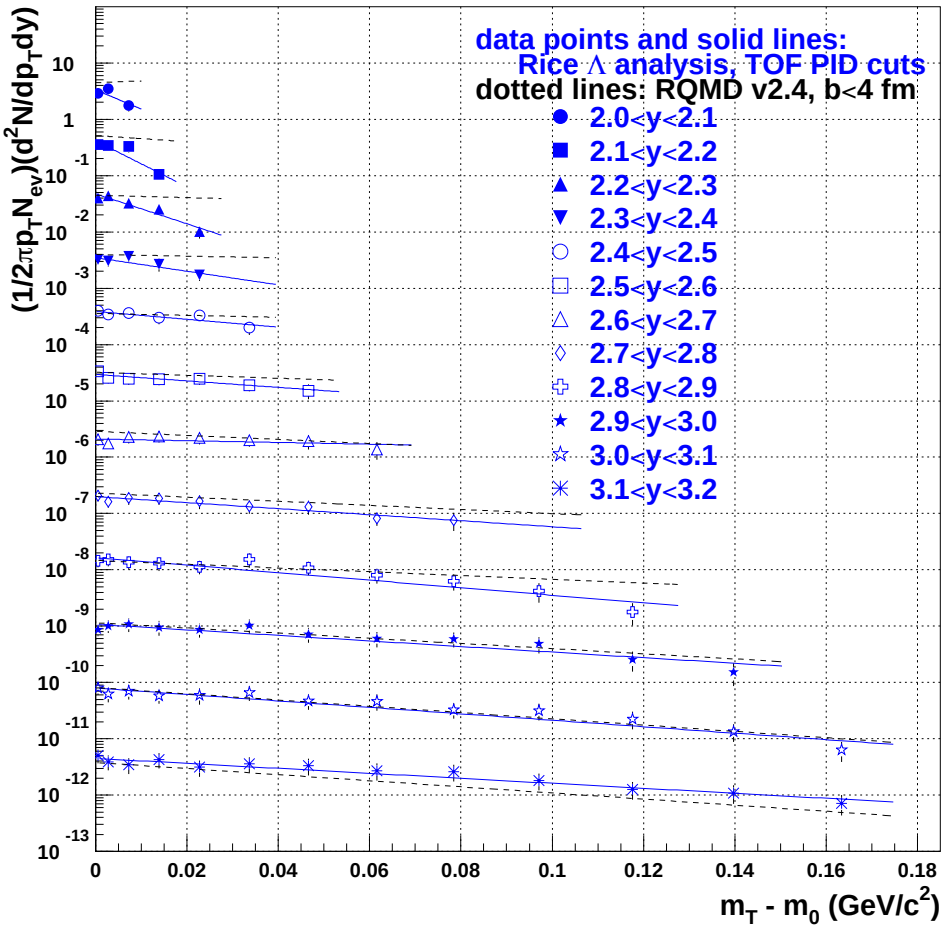

Figure 4.27 Λ hyperon differential yield versus transverse mass. The markers and solid lines represent corrected Λ hyperon spectra obtained using TOF cuts and corrections. The dotted lines are the fits to the Λ hyperon spectra from RQMD, $b < 4$ fm.

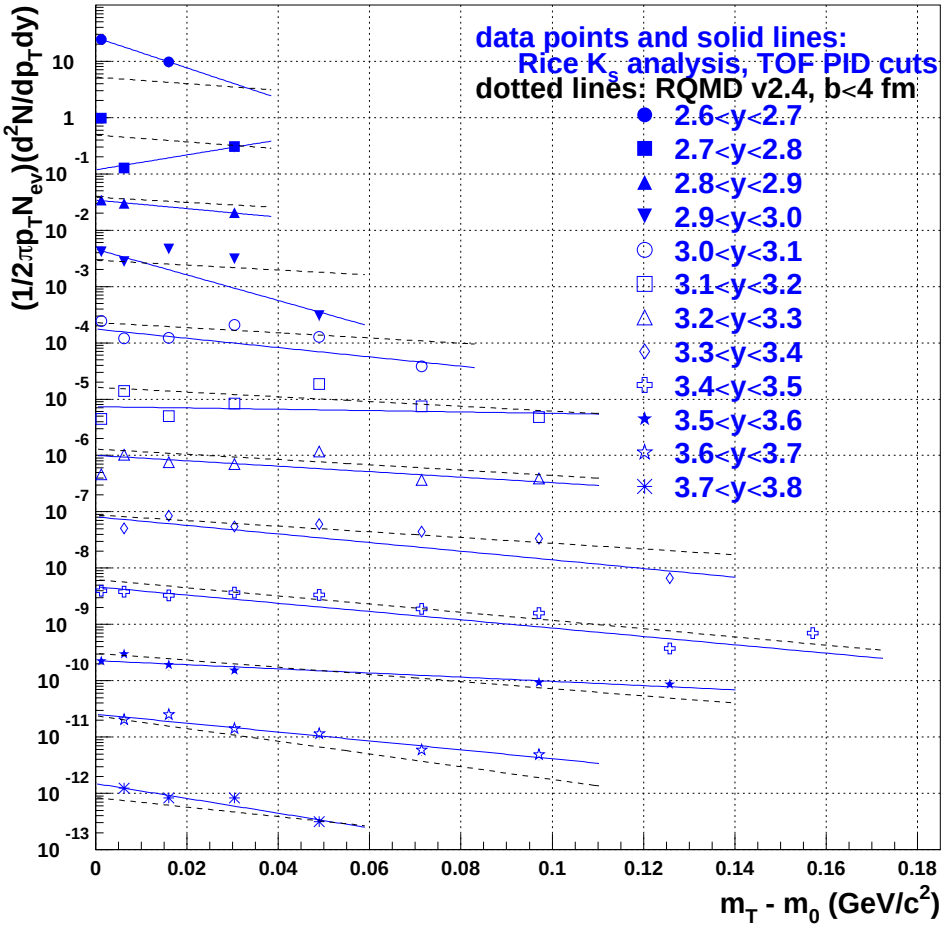

Figure 4.28 A comparison of the K_s meson transverse mass spectra obtained from this analysis with TOF cuts included (markers and solid lines), and from RQMD (dotted lines).

4.3.2 Slope Parameter Dependence upon Rapidity

For the transverse mass plots above, the rapidity interval size of 0.1 is too narrow (especially for K_s mesons in the data) to allow for enough statistics to yield a good Boltzmann-function fit. Thus, when measuring the inverse slope parameters to be compared with RQMD and with other experiments, a larger rapidity interval of 0.3 was used instead.

Λ Hyperon Temperature Dependence upon Rapidity

Shown in Figure 4.29 are the transverse mass distributions for Λ hyperons which survive all of the geometric, kinematic, and TOF-related cuts, and are corrected for acceptance. Also shown are the temperatures for these distributions, for the four $\Delta y = 0.3$ intervals spanned by the measured Λ hyperon data. The transverse mass range for the lower rapidities ($y < 2.6$) is too low to provide a reliable fit. The higher rapidity intervals exhibit inverse slope parameters of 108 MeV for $2.6 < y < 2.9$ (lower left frame) and 82 MeV for $2.9 < y < 3.2$ (lower right frame). The error bars in each frame represent the 20 percent systematic error for each bin.

The fitted inverse slope parameters for RQMD Λ hyperons in the same $\Delta y = 0.3$ rapidity intervals are shown in Figure 4.30. The measured temperatures are 164.1 ± 34.5 MeV for $2.0 < y < 2.3$, 137.9 ± 23.6 MeV for $2.3 < y < 2.6$, 108.8 ± 14.4 MeV for $2.6 < y < 2.9$, and 77.4 ± 8.4 MeV for $2.9 < y < 3.2$. The fitted temperatures

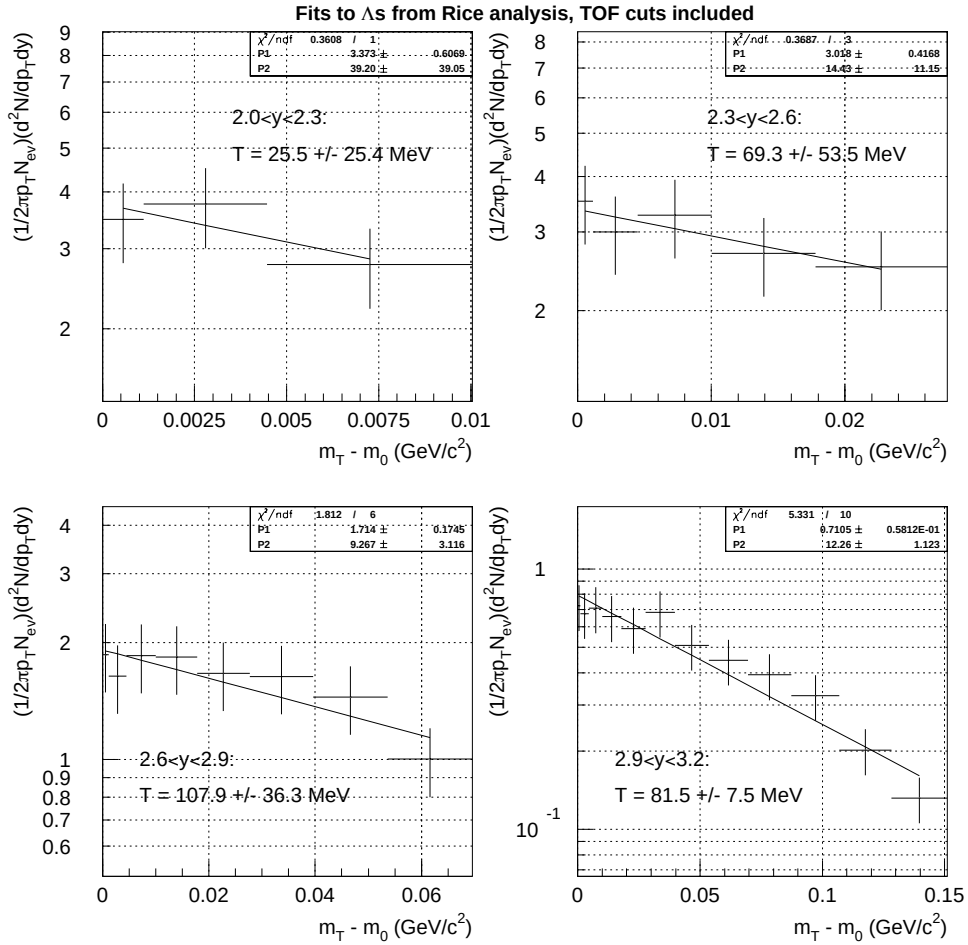

Figure 4.29 Transverse mass spectra for Λ hyperons, TOF cuts included, for four different rapidity bins. For each rapidity bin, the fit is performed over the m_T range covered by the DDC+TOF detector acceptance.

in RQMD agree well with those observed in the TOF-cut Λ hyperon data depicted in Figure 4.29.

Figure 4.31 plots the inverse slope parameters against rapidity for Λ hyperons from the present E896 TOF analysis (circles), from the simulations of RQMD (squares), and from the previous experiments E891 [38] (up triangles) and E877 [6] (down triangles and diamonds). Also shown are the results from the E896 SDDA analysis (stars) [30] [35]. E896 TOF's acceptance in rapidity overlaps with E891 and E877; however, the transverse momentum range for E891 and E877 is about twice as broad. Despite the more limited p_T acceptance in E896, the temperatures we observe are consistent with the values reported by E891 and E877.

An estimate of the Λ hyperon temperatures at mid-rapidity can be made by fitting the function of Equation 4.15 to various subsets of the temperature-vs.-rapidity points featured in Figure 4.31. Figure 4.32 shows the results of the fit to the E896 TOF data alone (left frame), and to the RQMD values alone (right frame). The resulting mid-rapidity Λ hyperon temperatures, 183.55 ± 16.29 MeV for the TOF data and 182.33 ± 12.95 MeV for the RQMD prediction, are quite consistent with each other.

The effective Λ hyperon temperatures inferred from the high-rapidity data alone are slightly lower than the temperatures expected from the E896 SDDA analysis. Figure 4.33 shows the results of the fit to E896 SDDA data alone (left frame), and the fit to both the SDDA and the TOF data sets (right frame). Inclusion of the SDDA

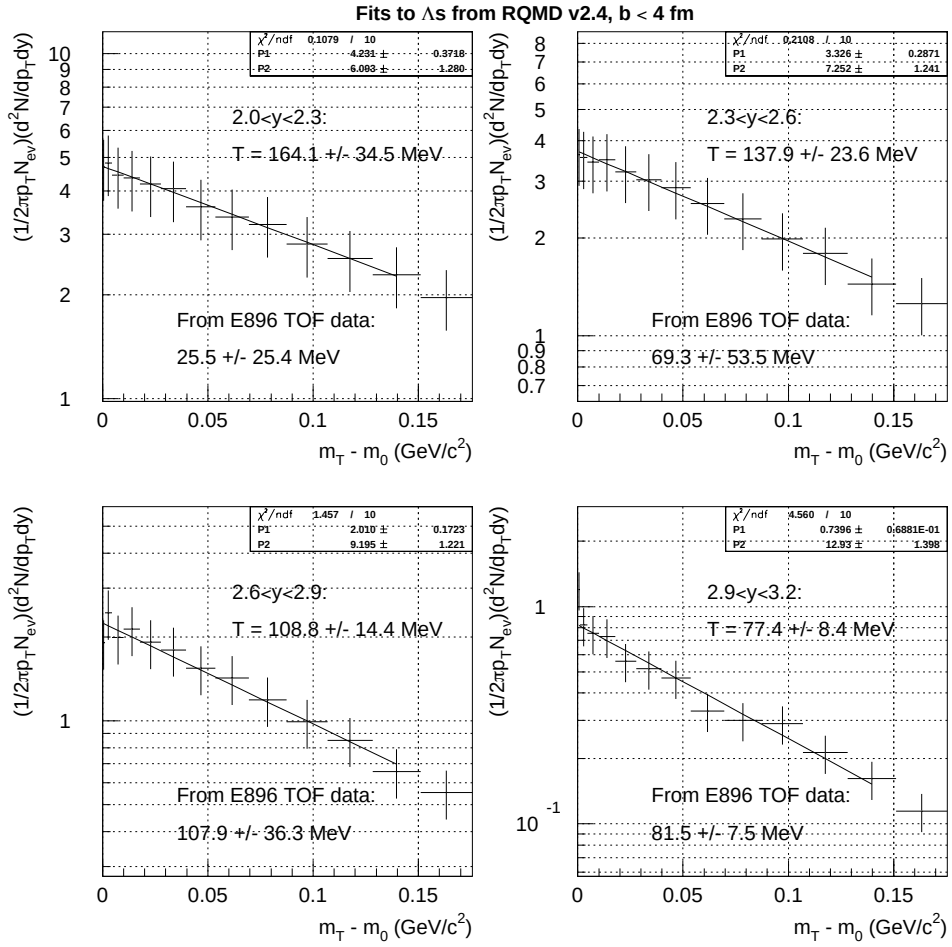

Figure 4.30 Transverse mass spectra for Λ hyperons from RQMD, $b < 4$ fm, for four different rapidity bins. Denoted at the bottom of each frame are the E896 TOF Λ hyperon temperatures measured for each rapidity bin.

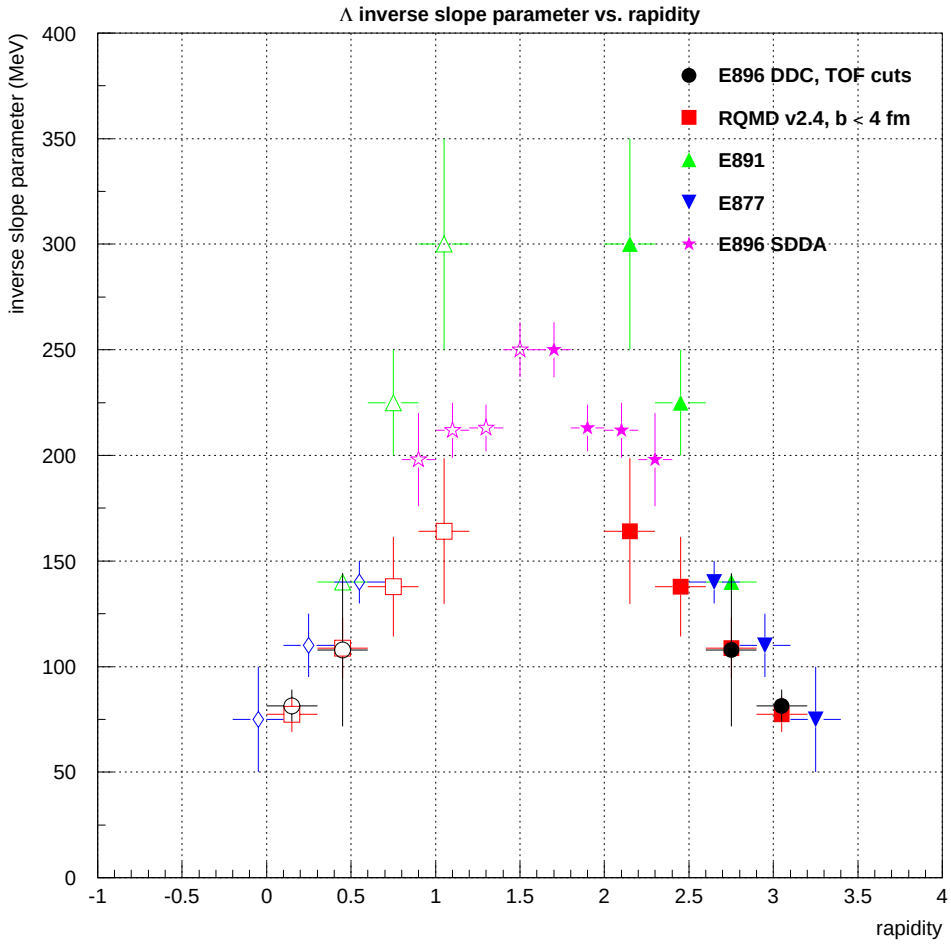

Figure 4.31 The Λ hyperon inverse slope parameter versus rapidity, for the E896 TOF-cut data (circles), RQMD (squares), E891 [38] (up triangles), E877 [6] (down triangles and diamonds), and the E896 SDDA data [30] [35] (stars).

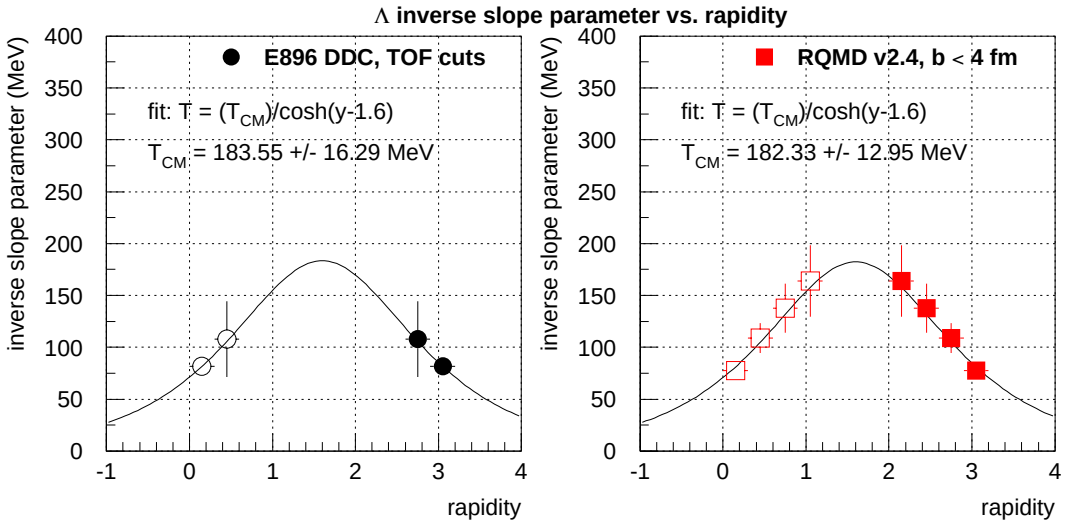

Figure 4.32 Results of the "fireball model" fit to the temperature-vs.-rapidity values for E896 TOF-cut Λ hyperons (left frame) and for RQMD Λ hyperons (right frame).

data suggests a higher Λ hyperon effective temperature than that inferred from the present high-rapidity Λ hyperons alone, although both fit results are approximately consistent with each other. Including the TOF Λ hyperon data points reduces the extracted effective temperature slightly, from 237.0 ± 7.2 MeV to 228.3 ± 6.6 MeV.

K_s Meson Temperature Dependence upon Rapidity

The transverse mass spectra for K_s mesons, using rapidity bin widths of 0.3 and measured over the rapidity range $2.6 < y < 3.8$, are shown in Figure 4.34, along with the same kinds of Boltzmann fit results. The temperatures measured are 72.6 ± 24.8 MeV for $2.9 < y < 3.2$, 90.0 ± 19.7 MeV for $3.2 < y < 3.5$, and 43.8 ± 12.0 MeV for

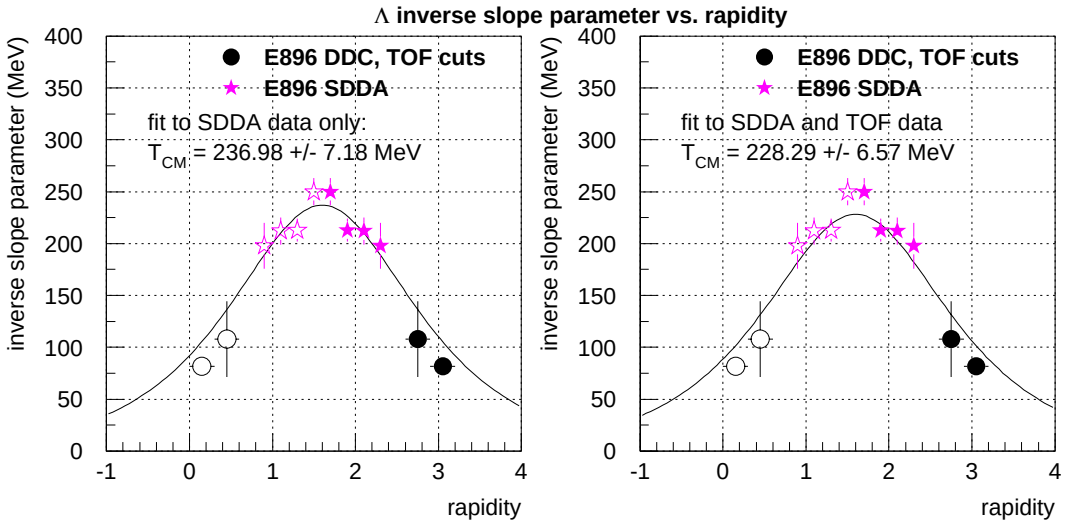

Figure 4.33 Results of the "fireball model" fit to E896 SDDA Λ hyperon data alone (left frame) and to the SDDA and TOF Λ hyperon data taken together (right frame).

$3.5 < y < 3.8$.

The temperatures of the RQMD K_s mesons in the same rapidity bins are summarized in Figure 4.35. The measured temperatures are 109.3 ± 7.0 for $2.6 < y < 2.9$, 96.3 ± 5.2 for $2.9 < y < 3.2$, 77.9 ± 3.5 for $3.2 < y < 3.5$, and 72.5 ± 3.5 for $3.5 < y < 3.8$.

Figure 4.36 displays the inverse slope parameter versus rapidity for K_s meson TOF-cut data and K_s mesons from the RQMD simulations. The present results are again consistent with RQMD. Mid-rapidity K_s meson spectra from $\sim 11A$ GeV/c Au+Au interactions have not been reported by any other AGS experiments. One can instead compare these neutral kaon temperatures with charged kaon temperatures

more commonly measured in other experiments (although none of these charged kaon temperature measurements were made in the present E896 K_s acceptance). Thus, also included in Figure 4.36 are the inverse slope parameters for K^+ (up triangles) and K^- (down triangles and diamonds) mesons from E866 [39], and K^+ mesons from E877 [40] (stars).

Estimates of effective K_s meson temperatures via fits to the temperature-vs.-rapidity plots are made in Figure 4.37, for K_s mesons from data (left frame), and K_s mesons from RQMD (right frame). The solid curves show the results of the fits to K_s meson temperatures. Included for comparison are the dotted curves that denote the results of the fits to the Λ hyperon data from Figure 4.32. The K_s meson effective temperature extracted from the "fireball model" fit to the E896 TOF data is 195.96 ± 30.71 MeV, and the K_s meson effective temperature from the RQMD simulation is 227.68 ± 5.91 MeV. The results from both fits are consistent, although the RQMD data does not appear to conform quite as well to a $1/\cosh(y - y_{mid})$ distribution.

Figure 4.38 shows the results of fits to the temperature versus rapidity distributions for the E866 K^+ (up triangles) and E877 K^+ (stars) data alone (left frame), and for the E896 TOF K_s temperatures included in the fit. The K_s meson temperatures are consistent with the temperatures extrapolated from the mid-rapidity charged kaon data.

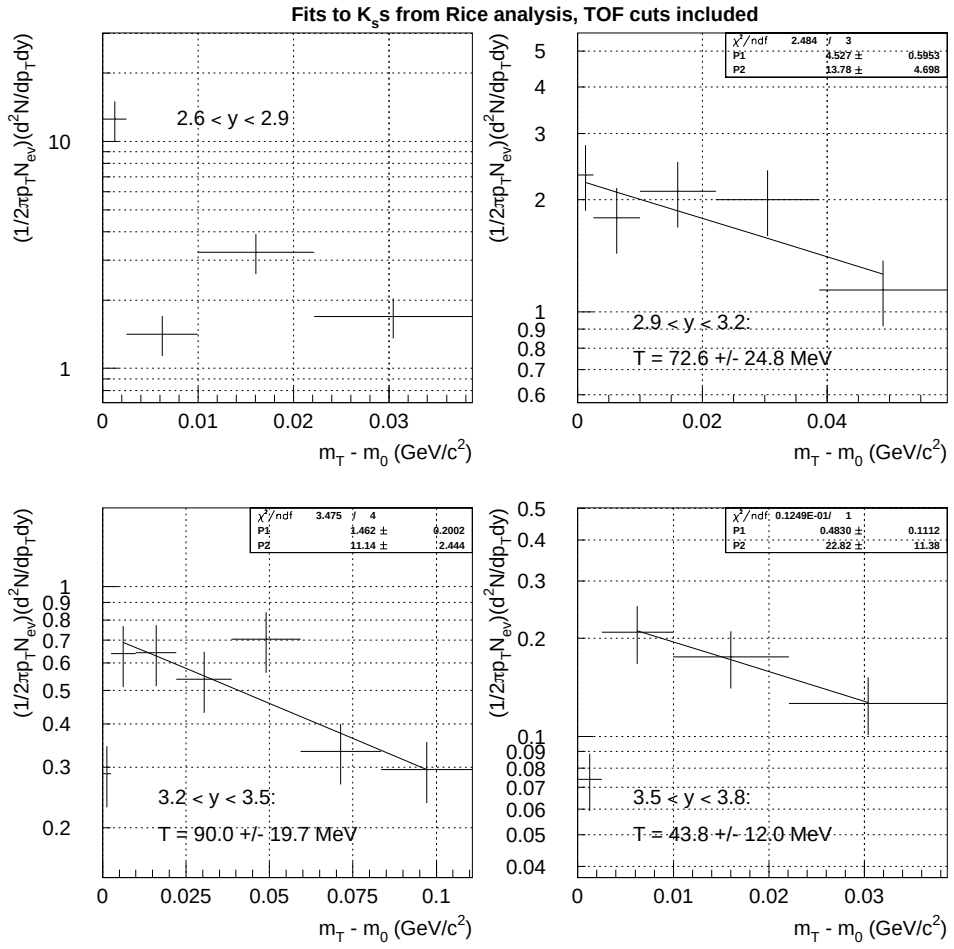

Figure 4.34 The transverse mass plots and Boltzmann fits for K_s mesons obtained from the E896 TOF analysis.

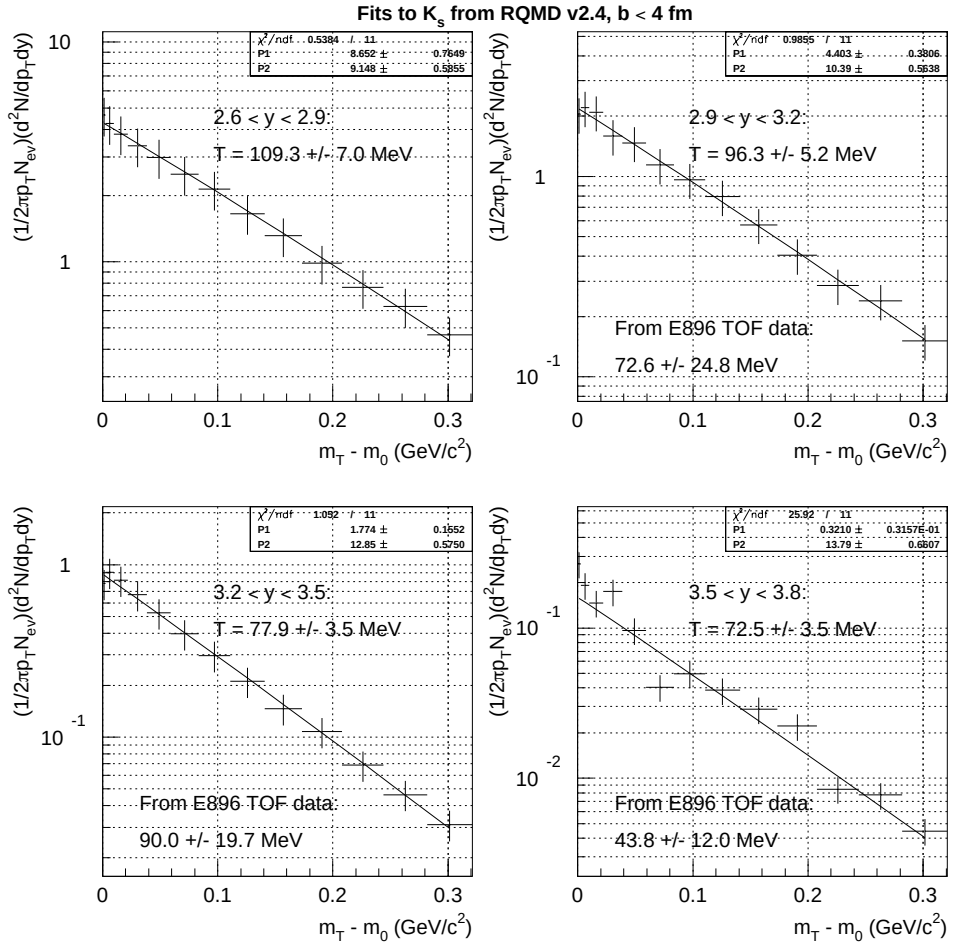

Figure 4.35 The transverse mass plots and Boltzmann fits for K_s mesons obtained from RQMD, $b < 4$ fm. Denoted at the bottom of each frame are the E896 TOF K_s meson temperatures measured for each rapidity bin.

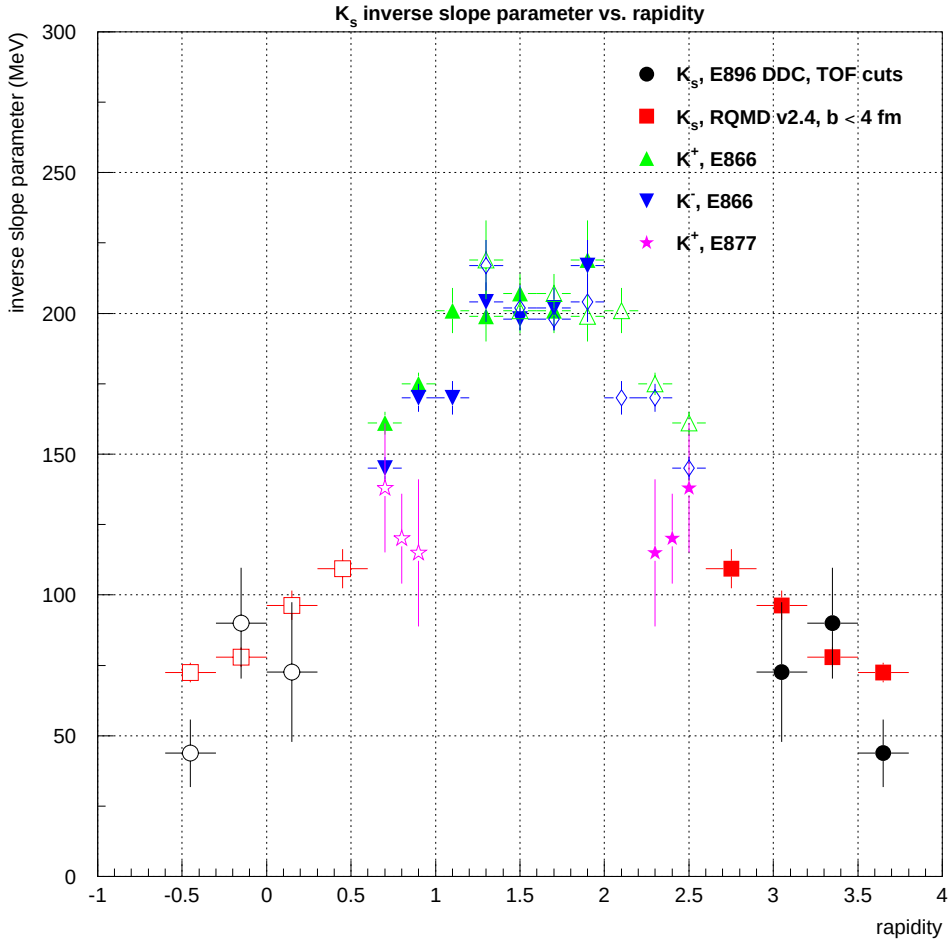

Figure 4.36 The K_s meson inverse slope parameter versus rapidity, for K_s mesons from the E896 TOF analysis (circles) and from RQMD $b < 4$ (squares). Also included are charged kaon temperatures from E866 [39] (up triangles for K^+, down triangles and diamonds for K^-) and K^+ meson temperatures reported by E877 [40] (stars).

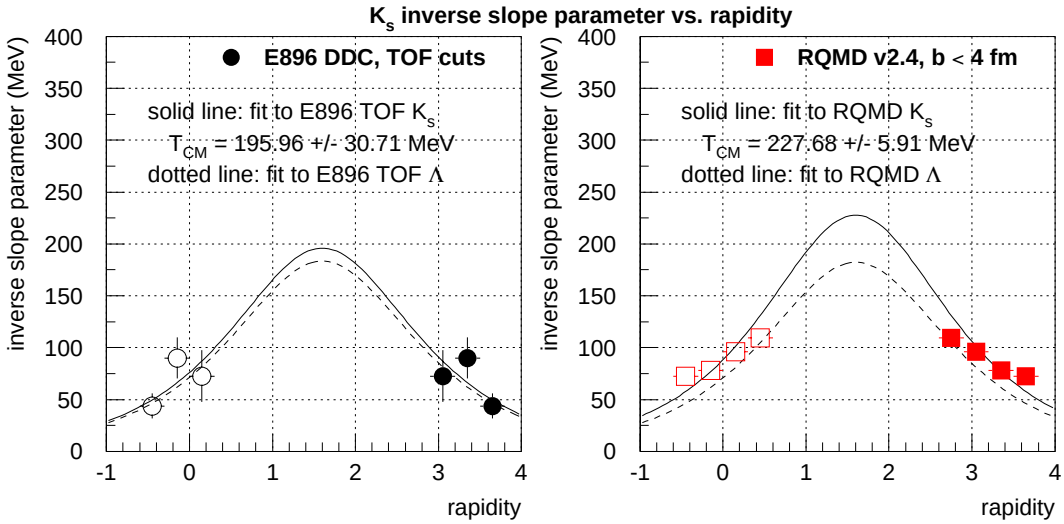

Figure 4.37 The solid curves represent fits of the "fireball model" function to the temperature-vs.-rapidity plots for K_s mesons from the E896 TOF analysis (left frame) and for K_s mesons from RQMD (right frame). The dotted lines show the fits to the Λ hyperon values from Figure 4.32.

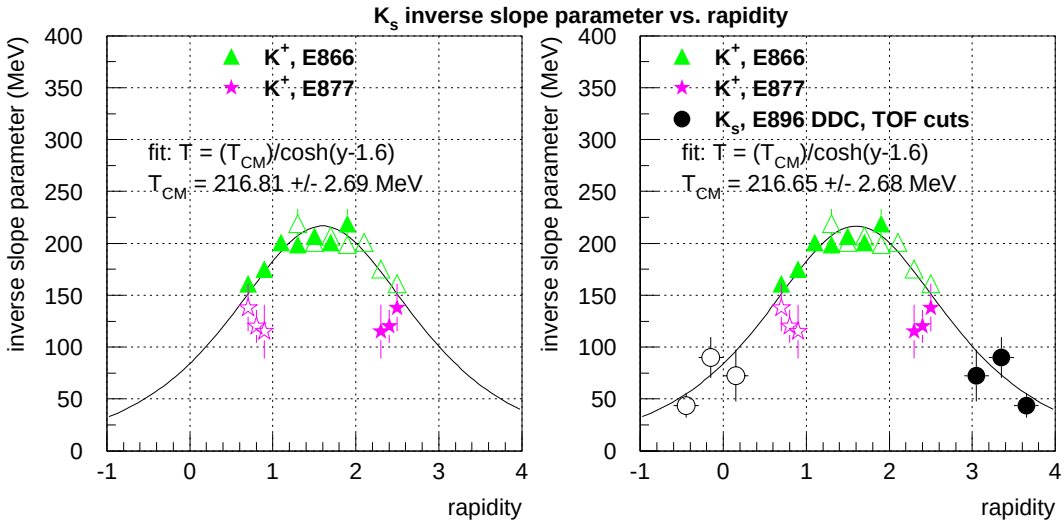

Figure 4.38 Fits of the "fireball model" function to the temperature-vs.-rapidity plots for kaons when fitting only to the mid-rapidity charged kaons (left frame) and when including the E896 TOF K_ss in the fit as well (right frame).

4.3.3 Production Magnitudes for Λ Hyperons and K_s Mesons

Along with the inverse slope parameter comparisons in the previous subsection, a comparison of the intercepts at the $m_T - m_0$ axes among various experiments and the RQMD simulation is now described. Specifically, the vertical axis intercepts of the exponential that is fitted to the transverse mass spectra are extracted from the present analyses and from independent sources. The intercept is defined to be the point on the $(1/2\pi p_T N_{ev})(d^2N/dydp_T)$ axis crossed by the fitted Boltzmann curve.

Λ Hyperon Intercepts

Figure 4.39 plots the intercepts for the TOF-cut data (circles) and the RQMD simulations (squares) versus rapidity. For all rapidities, the error bars for the two data sets overlap. For beam-like rapidities ($y > 2.6$), the intercepts are in very good agreement.

The transverse mass data in E891 were plotted using the expression

$$\frac{1}{N_{ev}}\frac{d^2N}{dyd(p_T^2)} \tag{4.19}$$

for the vertical axis. This quantity is the same as $(1/2\pi p_T N_{ev})(d^2N/dydp_T)$ multiplied by π; $d(p_T^2)$ is equal to $2p_T dp_T$. With this redepiction of the E896 TOF data, and a fit of the form $Am_T\exp(-Bm_T)$ applied, the intercepts at $m_T \sim 1.1$ were determined and plotted versus rapidity in Figure 4.40. The E896 TOF data are represented by

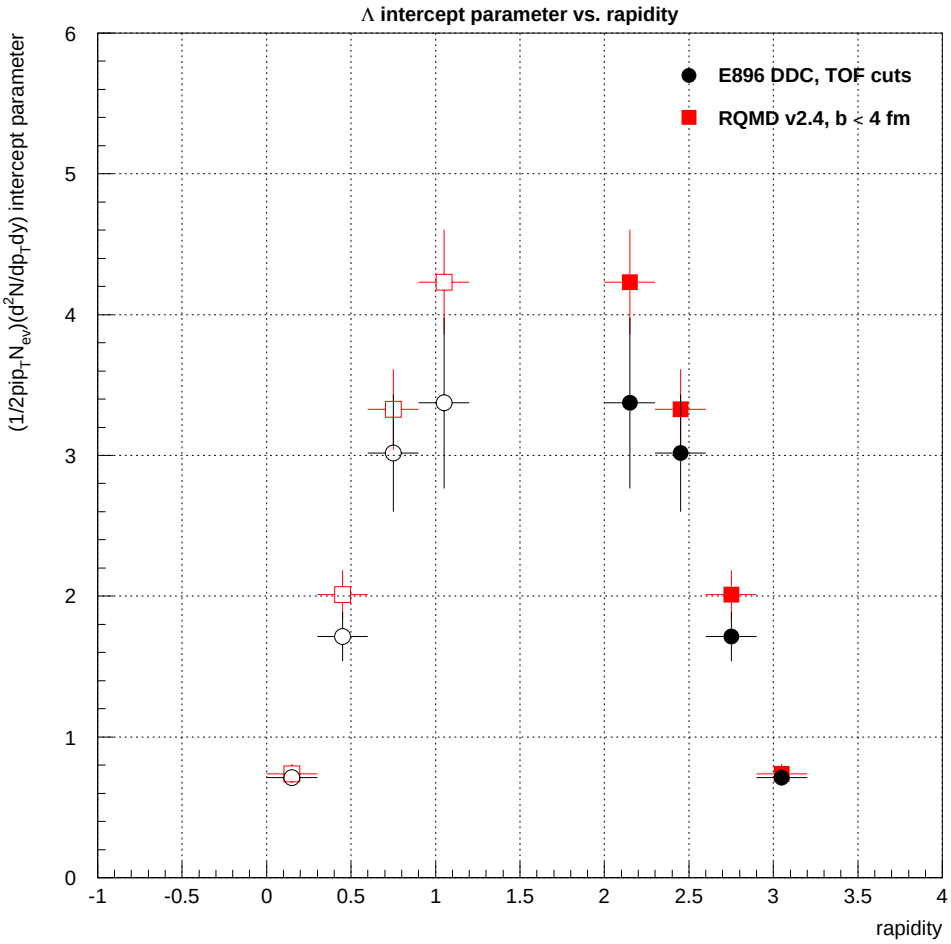

Figure 4.39 The "intercept parameter" (the point on the $m_T - m_0 = 0$ axis crossed by the fitted Boltzmann curve) versus rapidity, for Λ hyperons from the E896 TOF analysis (circles) and from RQMD (squares).

circles on that frame. Also shown are the intercepts obtained from E891 [38] (up triangles). The E891 intercepts not only appear to be considerably higher, but also appear to be quite constant with respect to rapidity.

E877 produced their transverse mass spectra with the definition of their vertical axis as

$$\frac{1}{m_T^2 N_{ev}} \frac{d^2N}{dy dm_T} \tag{4.20}$$

and applied a fit of the simple exponential form $A\exp(-B(m_T - m_0))$. Again, the E896 TOF yields are thus scaled using the identity $p_T dp_T = m_T dm_T$ and multiplying by $2\pi/m_T$. In Figure 4.41, the resulting E896 TOF intercepts (circles) are compared to E877's intercepts (down triangles and diamonds). The error bars for the E896 TOF intercepts are smaller than the marker size. The E896 TOF intercepts are slightly above those obtained from E877, but the agreement is somewhat better than with E891.

Given the narrow transverse momentum acceptance in the present analysis, it involves excessive extrapolation to use the fitted temperatures and intercepts to integrate over the entire p_T space for the determination of the rapidity density $(1/N_{ev})(dN/dy)$ versus the rapidity. Such an integration of the TOF data was performed anyway. The results are plotted as circles on Figure 4.42 along with the rapidity densities obtained from RQMD (squares), E891 (up triangles), E877 (down

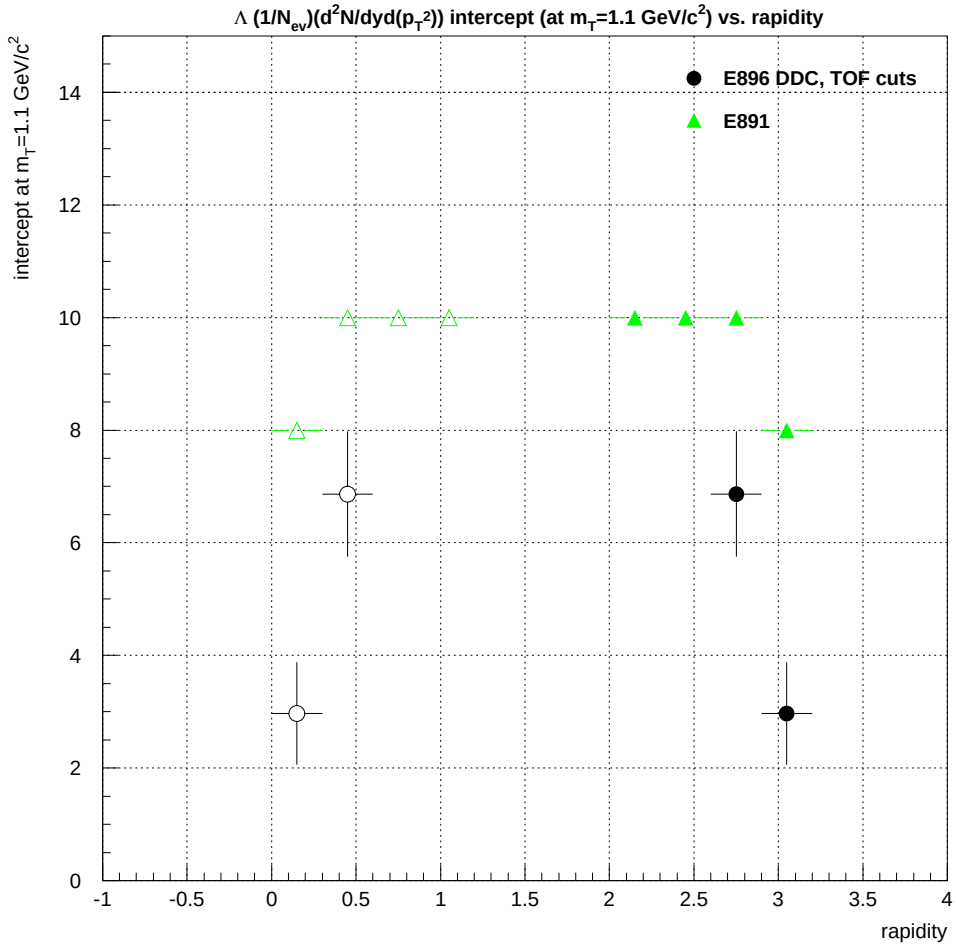

Figure 4.40 The intercept parameter (scaled to conform to Equation 4.19) versus rapidity, for Λ hyperons from the E896 TOF analysis (circles) and from E891 [38] (up triangles).

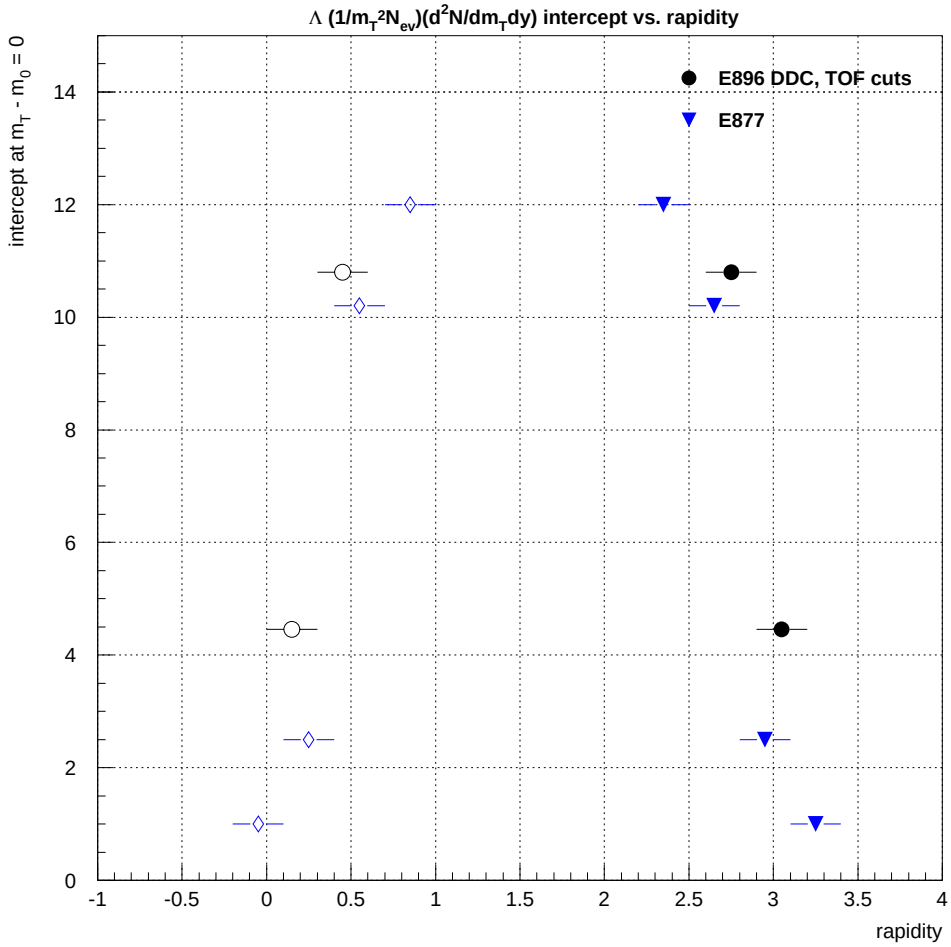

Figure 4.41 The intercept parameter (scaled to conform to Equation 4.20) versus rapidity, for Λ hyperons from the E896 TOF analysis (circles) and from E877 [6] (down triangles and diamonds). The error bars for the E896 TOF intercepts are smaller than the marker size.

triangles and diamonds), and the SDDA analysis (stars). The dN/dy values from TOF data are consistent with those reported by E891 and E877, and with those from the RQMD simulations.

If the rapidity density is assumed to be a Gaussian [30], the E896 SDDA and TOF results can be compared. This is shown in Figure 4.42. Figure 4.43 plots and fits to dN/dy values extracted for E896 TOF Λ hyperons and E896 SDDA Λ hyperons. Integrating the area underneath this Gaussian, using Equation 4.14 provides a measurement of the number of Λ hyperons produced per central event. The value we observe is 16.1 ± 0.9. This is compared with RQMD's estimate of 15.0 ± 0.1. That is, despite the limited p_T coverage, estimates of the total Λ hyperon yield are not inconsistent with the predictions.

K_s Meson Production Magnitudes

Figure 4.44 shows a plot of the intercept parameter versus rapidity for K_s mesons from E896 TOF (circles) and from RQMD simulations (squares). Despite the low statistics for K_s mesons in the present data set, the intercepts agree well with those obtained from RQMD.

Despite the same caveats with E896's narrow p_T acceptance, a $(1/N_{ev})(dN/dy)$ integration was performed for E896 TOF selected K_s mesons as well. Figure 4.45 plots the integrated dN/dy values versus rapidity for K_s mesons from E896 TOF data (circles) and from RQMD simulations (squares). Due to the lack of mid-rapidity

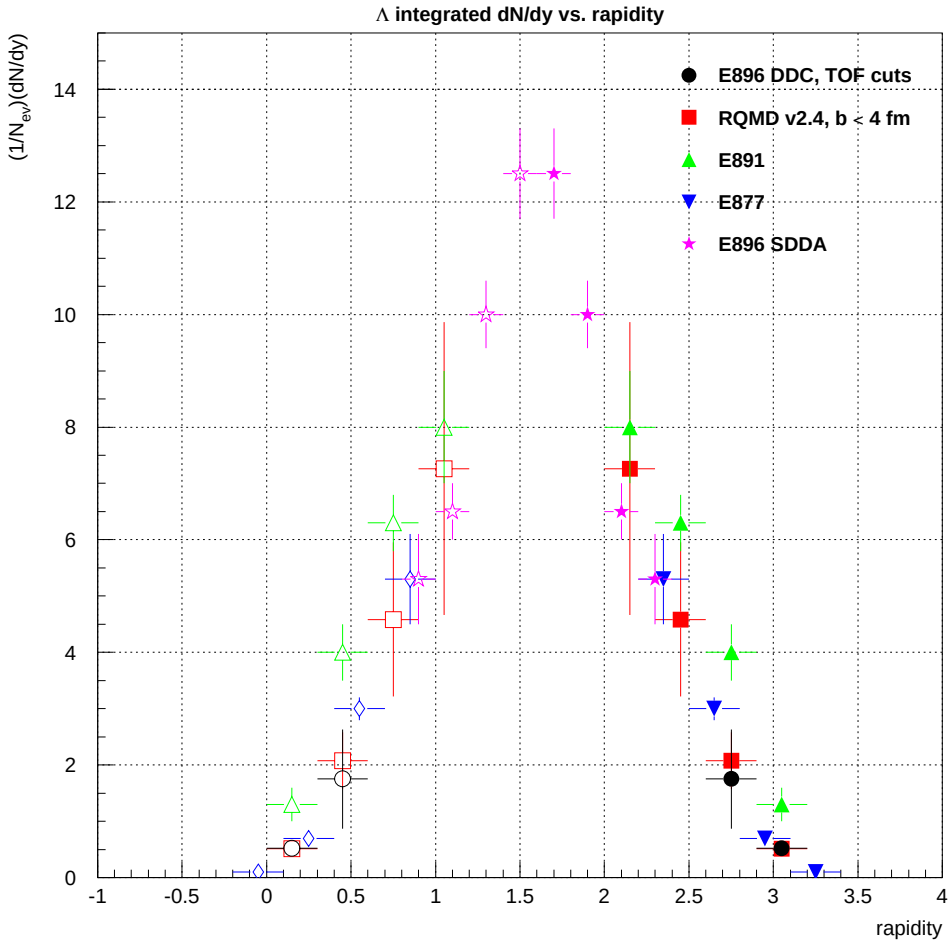

Figure 4.42 The integrated dN/dy values versus rapidity for Λ hyperons from the E896 TOF analysis, RQMD, E891, E877, and the E896 SDDA analysis.

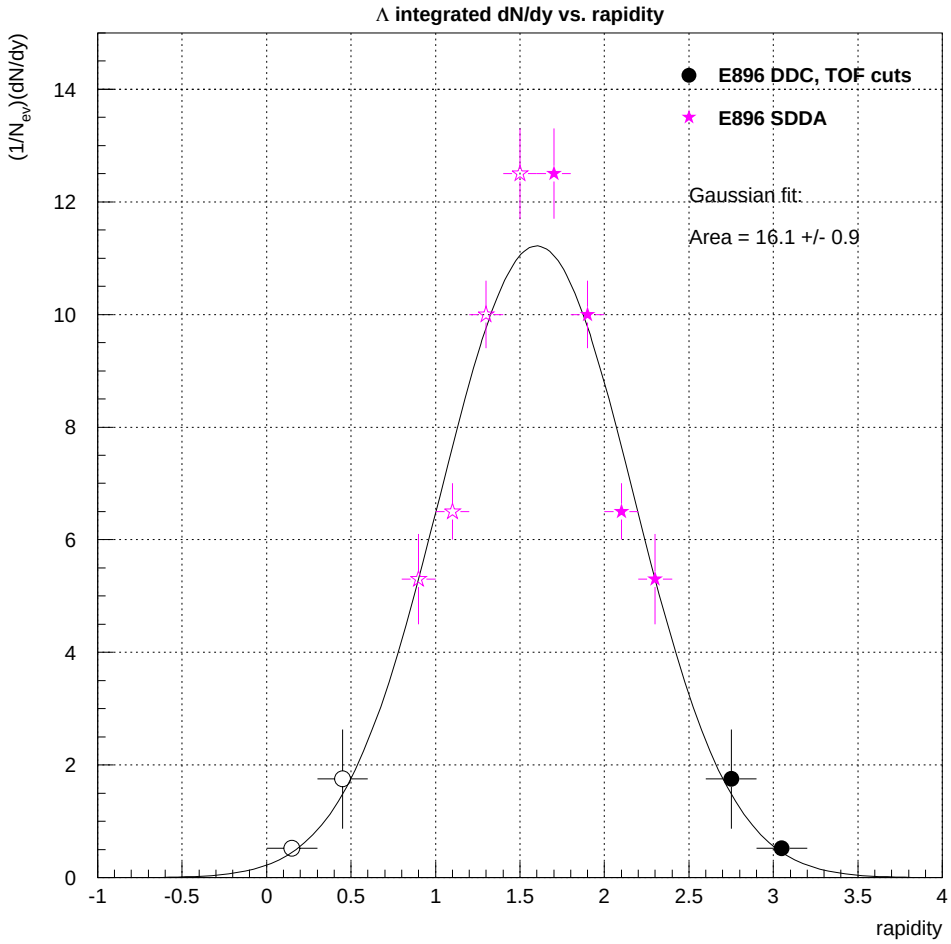

Figure 4.43 The dN/dy values versus rapidity for SDDA and TOF Λ hyperons, along with a Gaussian fit applied to these data.

K_s meson data, however, a Gaussian fit to this distribution is less certain. The uncertainties for the $(1/N_{ev})(dN/dy)$ values at rapidity closer to mid-rapidity are too large.

4.3.4 Λ Hyperon and K_s Meson Proper Lifetimes

In the previous sections, results on the apparent temperatures and production rates for Λ hyperons and K_s mesons in the present analyses were presented and compared to those from independent studies. These results were obtained by starting with the E896 Collaboration's "Pass II" data set and applying additional cuts based on TOF for the first time to purify the E896 Pass II data set. A generally good agreement was seen in all comparisons of the present results to independent analyses of the same data [14], to the RQMD model, and to other AGS experiments. The invariant mass distributions of daughter tracks of the Λ hyperon and K_s meson decays studied here and in the previous analysis [14] are in close agreement with the known masses of these particles [41]. These distributions were shown for example in Figures 4.9 and 4.13 for the Λ hyperon, and in Figures 4.16 and 4.18 for the K_s meson.

There is, however, an additional experimentally accessible quantity that must also be consistent with known properties of these particles. This quantity is the "proper lifetime" of the particle of interest. The proper lifetime, τ, of a particle multiplied by the speed of light, c, is a tabulated quantity [41] which has well-established values of $c\tau$=7.89 cm for the Λ hyperon and $c\tau$=2.68 cm for the K_s meson. To further ex-

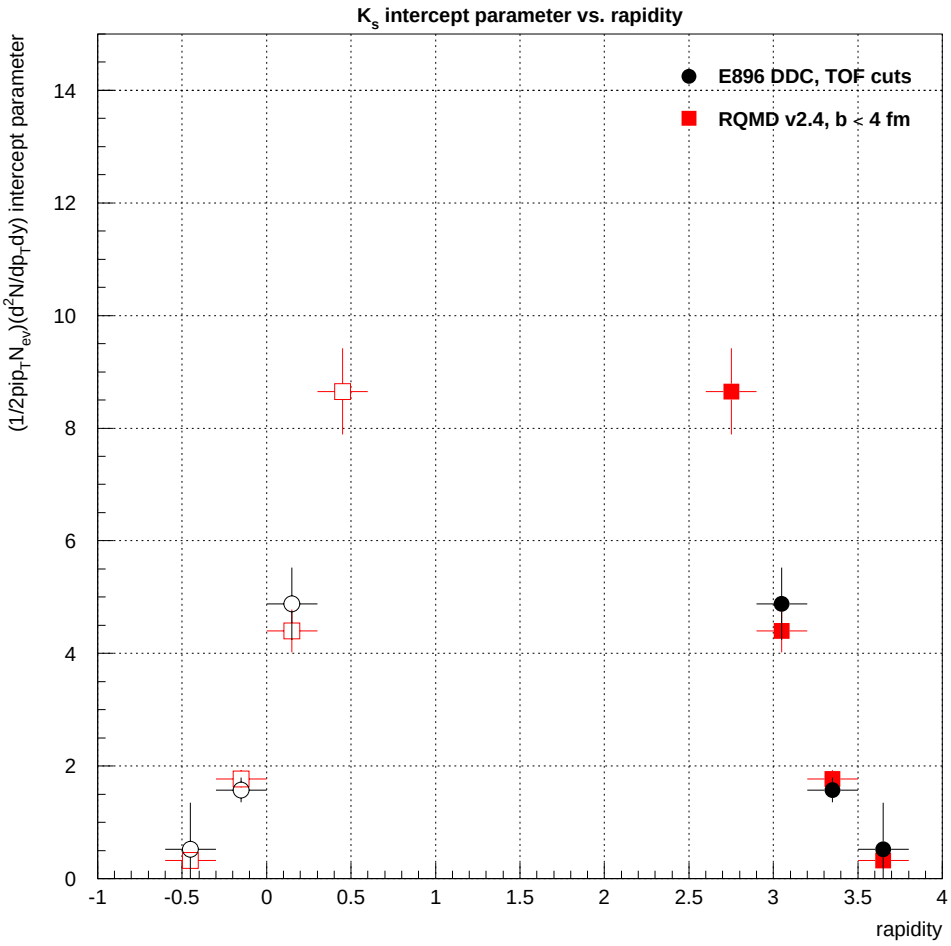

Figure 4.44 The intercept parameter versus rapidity for K_s mesons from the E896 TOF analysis (circles) and from RQMD (squares).

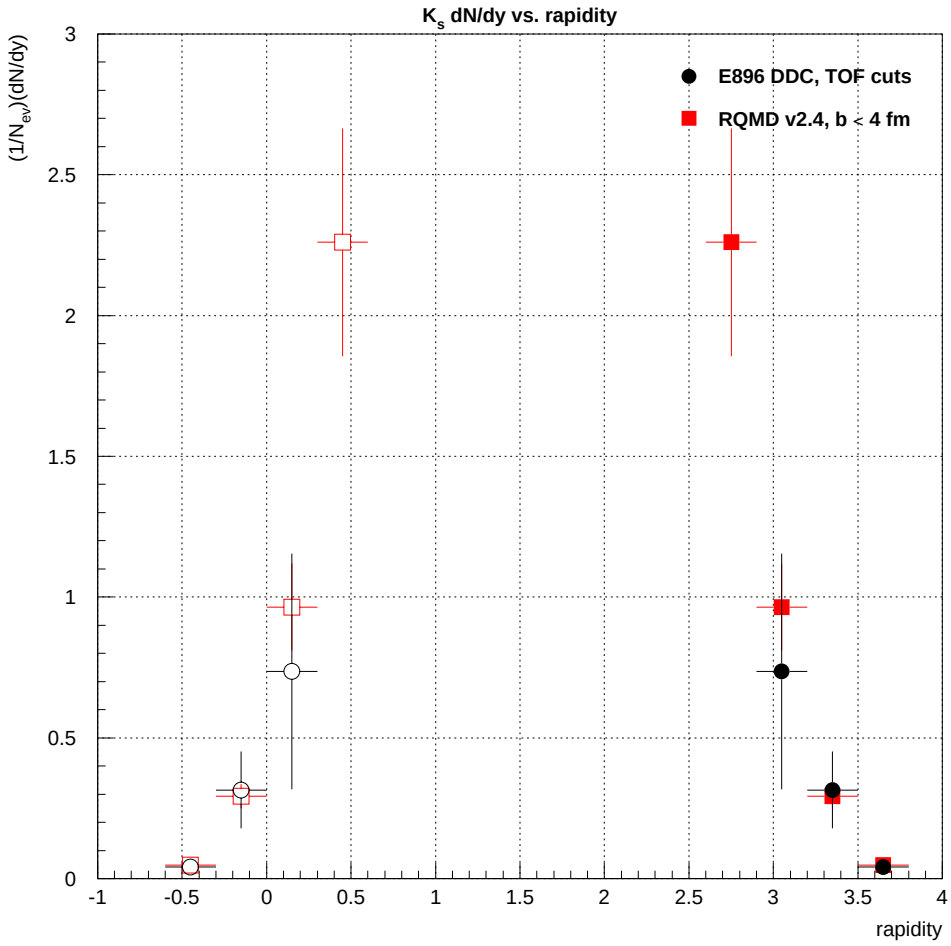

Figure 4.45 The integrated dN/dy values versus rapidity for K_s mesons from the E896 TOF analysis (circles) and from RQMD (squares).

plore the information content of the present data, this subsection will concentrate on describing the measurement of proper lifetimes and the comparison of the present results to the tabulated values. To our knowledge, such a measurement and comparison was not performed in the independent analysis [14] of the E896 data.

There are two ways to infer the proper lifetime of a sample of particles that move in the laboratory with some momentum and then decay. The first method involves the reconstruction of the invariant mass of decaying parents and the measurement of the variance of that distribution. This mass-width of a particle, ΔM, measured in MeV, and the particle's proper lifetime are related by the formulas $1/\tau = \Delta M$ or $c\tau = c/\Delta M$. In practice, however, the experimental resolution necessary to obtain a sufficiently precise measurement of ΔM for this purpose is practically never achievable in heavy-ion experiments. According to Figures 4.13 and 4.18, the experimental variance of the invariant mass distributions in E896 are of order 4 MeV for the Λ hyperon and 11 MeV for the K_s meson, which are many orders of magnitude larger than the known values of the intrinsic widths of these particles respectively.

The alternative method involves the experimental measurement of the target to particle decay distances, and the conversion of these to lifetimes in the particle rest frame using special relativity. This involves the depiction of the experimental distribution of the quantity $d/\gamma\beta$, where d is the distance from the target to the decay vertex in centimeters, and γ and β are the Lorentz variables for the transformation

from the laboratory frame to the particle frame. Over a sample of measured decays of a specific particle, the experimental distribution of count rate versus the quantity $d/\gamma\beta$ is an exponential that has a slope parameter which is the experimental value of $c\tau$ for this sample in centimeters.

Shown in Figure 4.46 is such a count rate versus $d/\gamma\beta$ distribution extracted from the present sample of K_s mesons with the TOF-based cuts. These count rates have been corrected for the experimental acceptance and cut efficiencies using the simulations described in Section 4.2. The error bars represent the combined uncertainties, for each $d/\gamma\beta$ bin, of the K_s meson data sample and the correction factor applied to that bin. The solid line denotes an exponential fit ($A\exp(-Bd/\gamma\beta)$) over the entire $d/\gamma\beta$ range. The proper lifetime measurement is obtained from the inverse of the slope parameter B; it is 2.68 ± 0.82 cm. This compares very well with the K_s meson lifetime of 2.6762 ± 0.0027 cm quoted by the Particle Data Group [41].

The corrected experimental distribution of proper decay lengths for the present Λ hyperon sample is shown in Figure 4.47. The distribution without TOF cuts is featured in the left frame, and the right frame shows the distribution with TOF cuts included. The meaning of the axes, points, and lines is the same as those in Figure 4.46. Again, the error bars represent the combined uncertainties of the data and the correction factors. The TOF cuts appear to correctly remove the additional counts at the higher $d/\gamma\beta$ values, between 40 cm and 60 cm. The solid lines indicate

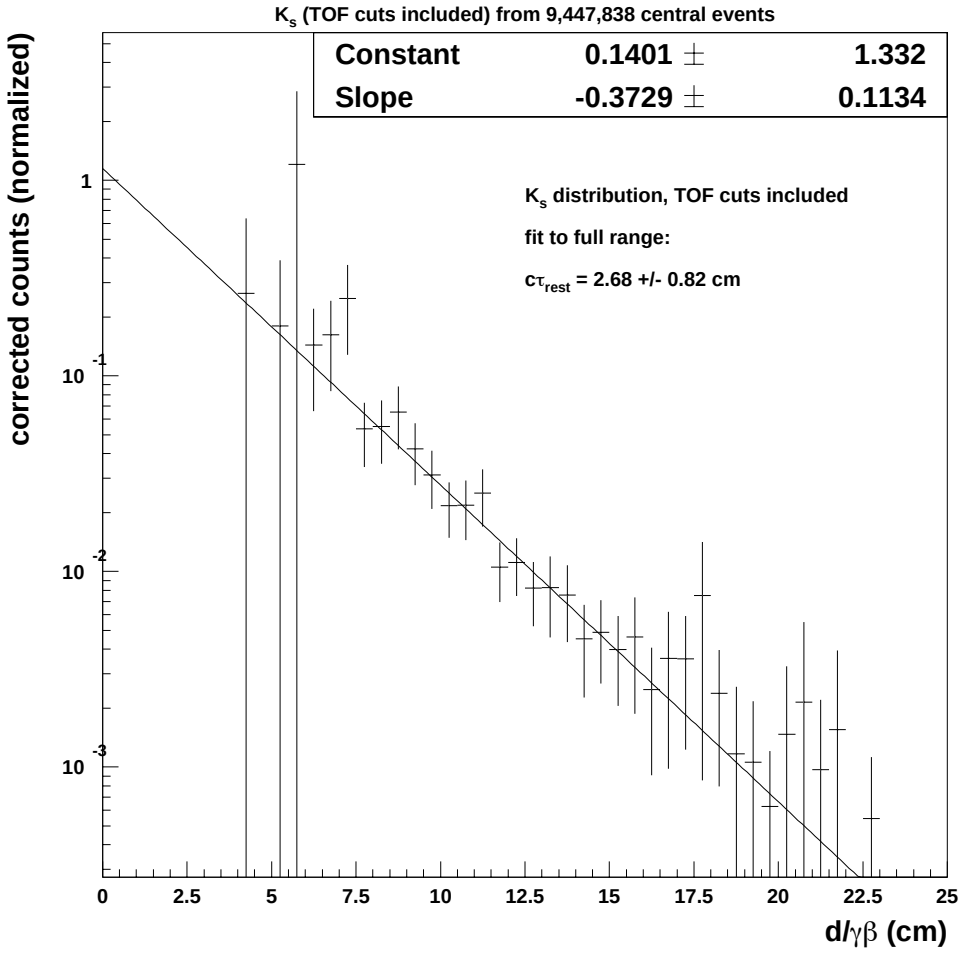

Figure 4.46 Distribution of $d/\gamma\beta$ for K_s mesons from the present analysis, corrected for acceptance. The error bars represent the combined uncertainties of the data sample and the correction factors.

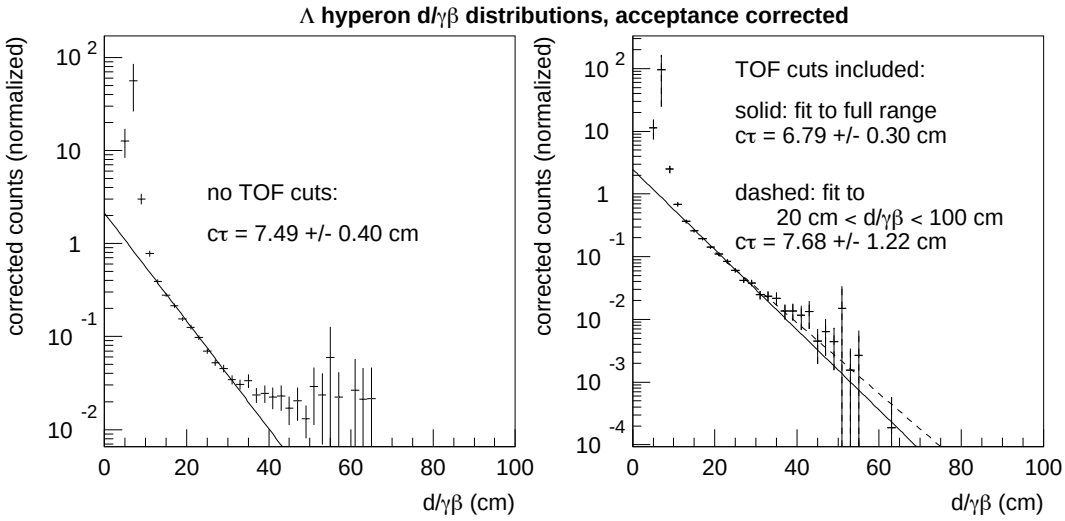

Figure 4.47 Acceptance-corrected distributions of $d/\gamma\beta$ for Λ hyperons in the present analysis, without TOF cuts (left frame) and with TOF cuts included (right frame). The solid lines denote exponential fits over the full $d/\gamma\beta$ range. The dotted line in the right frame denotes the fit over the range 20 cm $< d/\gamma\beta <$ 100 cm.

exponential fits to the full $d/\gamma\beta$ range. According to those fits, the apparent proper lifetime without TOF cuts is 7.49 ± 0.40 cm, and 6.79 ± 0.30 cm with TOF cuts included. The dashed line in the right frame indicates a fit applied over a restricted range of $d/\gamma\beta$ from 20 cm to 100 cm. That fit result yields a lifetime measurement of 7.68 ± 1.22 cm, which is more consistent with the Λ hyperon lifetime of 7.89 ± 0.06 cm quoted by the Particle Data Group [41]. There is, however, a significant excess of counts above the trend established by the restricted-range fit, for values of $d/\gamma\beta$ that are less than $\sim$15 cm. This section closes with a brief discussion of an investigation of this excess.

Shown in Figure 4.48 are the separate distributions of uncorrected count rates versus the product $\gamma\beta$ (left frame) and versus the decay length d (right frame) for the same sample of Λ hyperons shown in Figure 4.47. In both frames the solid histogram depicts the uncorrected count rate for all Λ hyperons in the sample, while the dashed (dotted) histograms depict the rate for those hyperons with $d/\gamma\beta$ larger (smaller) than 15 cm. On the right frame one sees that there is not a significant correlation between $d/\gamma\beta$ and d in the present sample. There is, however, a rather strong correlation of $d/\gamma\beta$ and $\gamma\beta$. Those Λ hyperons in the "excess" region, $d/\gamma\beta<15$ cm, have values of $\gamma\beta$ generally greater than $\sim$9, and there is relatively little overlap with the significantly lower velocity Λ hyperons with $d/\gamma\beta>15$ cm.

Also compared were the distributions of the decay vertex x, y, and z values within the DDC active volume for the two classes of Λ hyperons based on their $d/\gamma\beta$ values. These comparisons are shown respectively in the three frames of Figure 4.49. The line styles have the same meaning as in Figure 4.48. In the upper right and lower left frames, respectively, no correlation between these classes and the decay vertex y or z coordinates was observed. A weak correlation is seen in the upper left frame with respect to the decay vertex x location. The two distributions overlap completely, but those Λ hyperons with $d/\gamma\beta>15$ cm tend toward slightly larger values of x (*i.e.* more leftward when looking downstream from the target) than those with $d/\gamma\beta<15$ cm.

Shown in Figure 4.50 is the same type of comparison, but now versus the rapidity

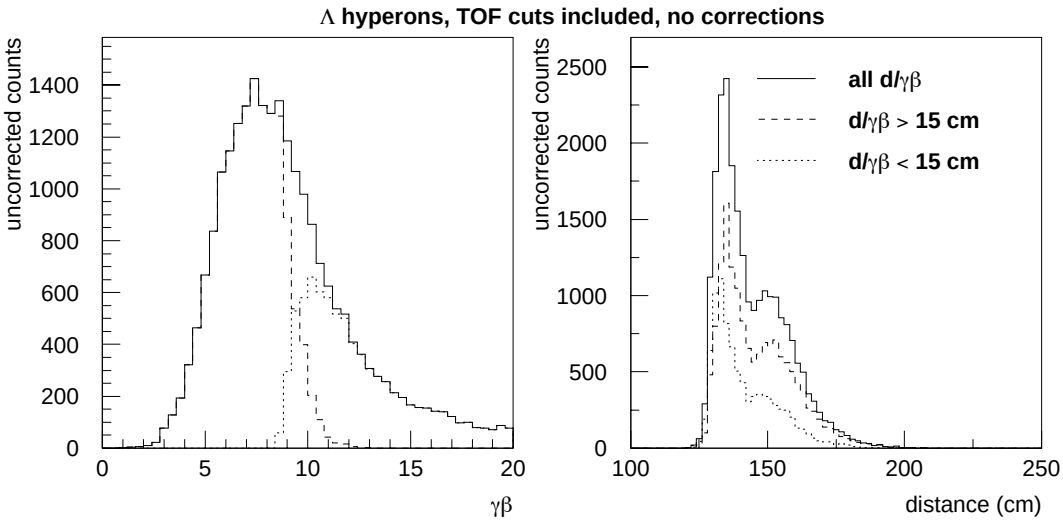

Figure 4.48 Uncorrected count rates for Λ hyperons versus the quantity $\gamma\beta$ (left frame) and decay length d (right frame). Solid lines denote count rates for all Λ hyperons in the sample. Dashed (dotted) lines represent Λ hyperons with $d/\gamma\beta$ greater than (less than) 15 cm.

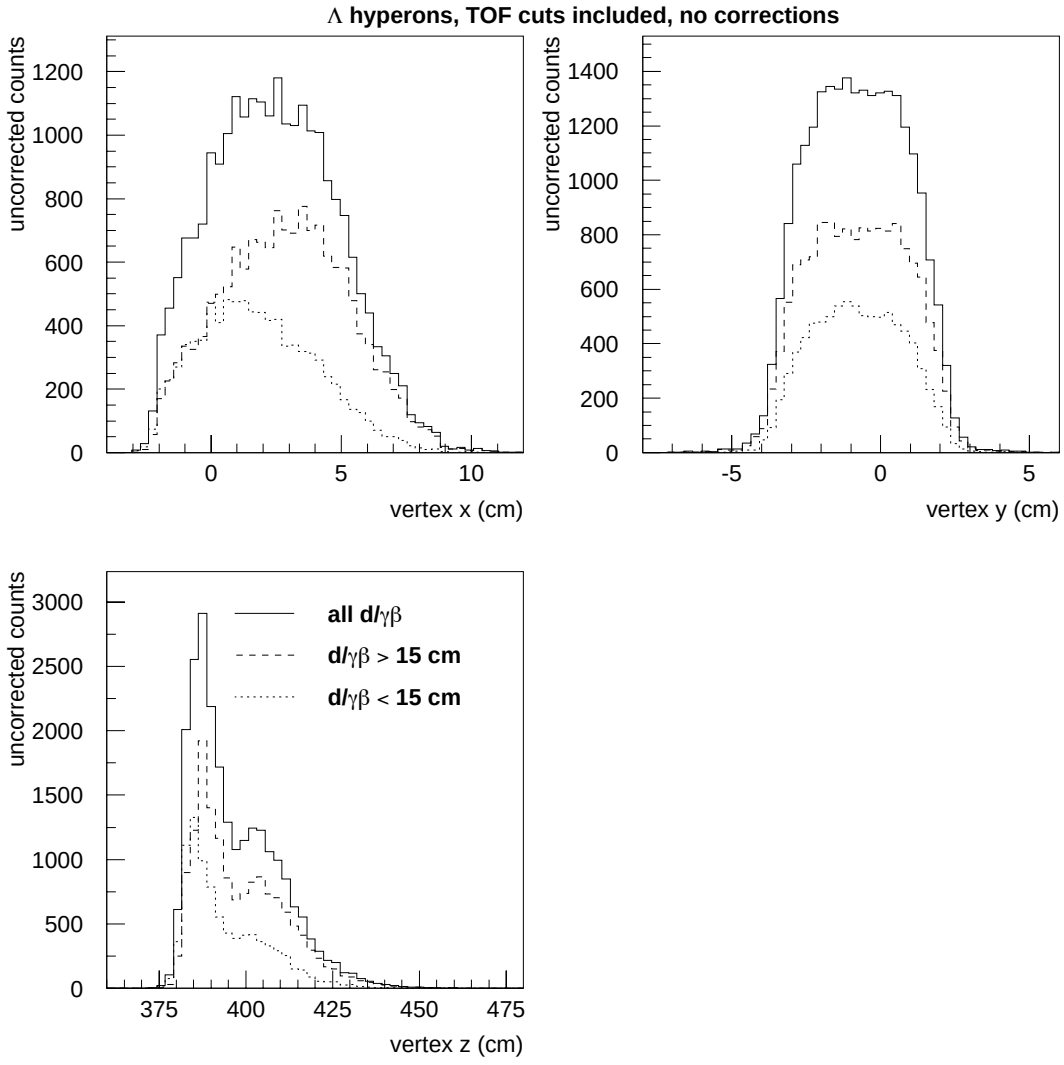

Figure 4.49 Uncorrected count rates for Λ hyperons versus the x (upper left), y (upper right), and z (lower left) coordinates of the decay vertex. Solid lines denote count rates for all Λ hyperons in the sample. Dashed (dotted) lines represent Λ hyperons with $d/\gamma\beta$ greater than (less than) 15 cm.

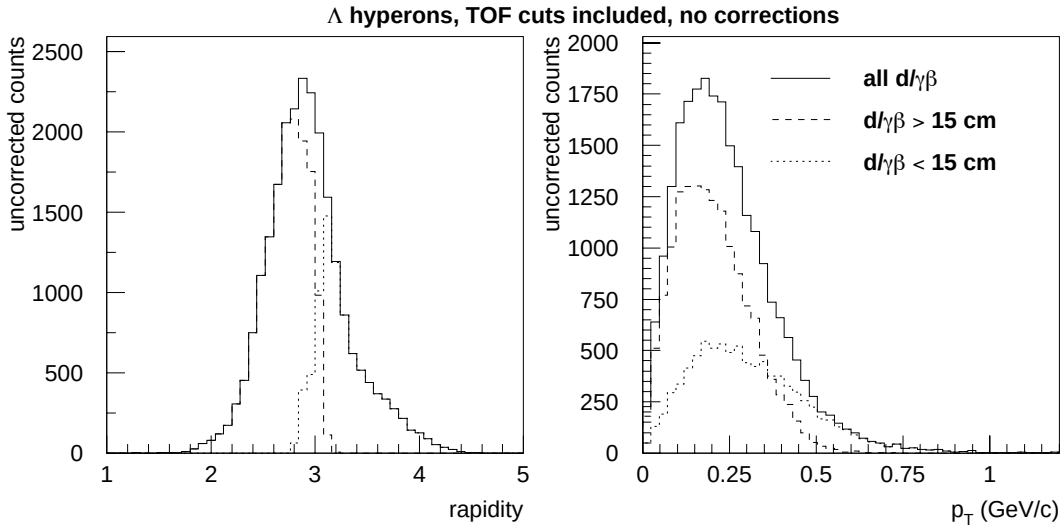

Figure 4.50 Uncorrected count rates for Λ hyperons versus rapidity (left frame) and transverse momentum (right frame). Solid lines denote count rates for all Λ hyperons in the sample. Dashed (dotted) lines represent Λ hyperons with $d/\gamma\beta$ greater than (less than) 15 cm.

(left frame) and the transverse momentum (right frame) of these Λ hyperons. On the right frame one notices a modest difference in the transverse momentum distributions in the two classes of decays. On the left frame, however, one sees a rather sharp distinction in the two classes. Those Λ hyperons with $d/\gamma\beta$>15 cm generally have laboratory rapidities less than 3.0, while the other class of Λ hyperons in the "excess region" of $d/\gamma\beta$<15 cm have rapidities larger than 3.0. There is little overlap between these distributions.

Shown in Figure 4.51 are the corrected count rates for Λ hyperons versus $d/\gamma\beta$ under the two cases of rapidity less than (left frame) and greater than (right frame)

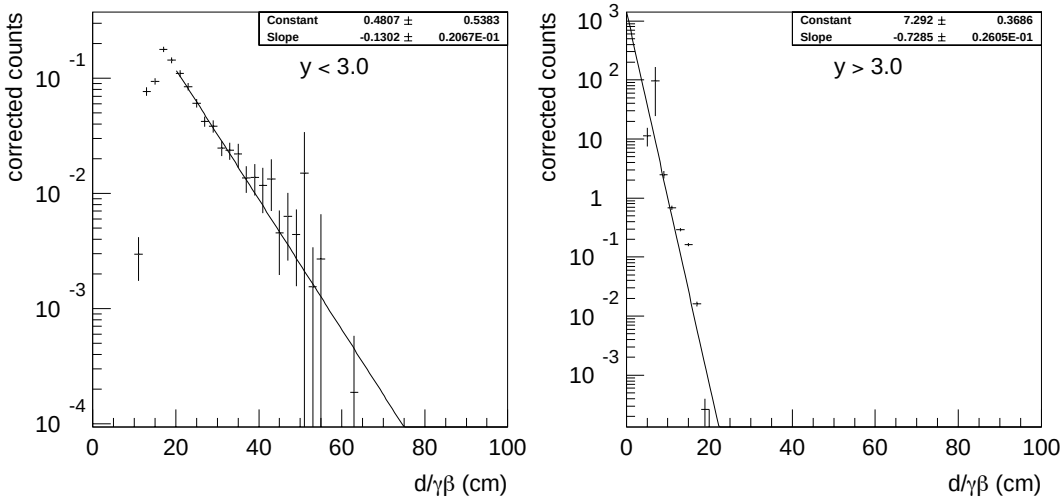

Figure 4.51 Acceptance-corrected distributions of $d/\gamma\beta$ for Λ hyperons, TOF cuts included, for rapidity less than 3.0 (left frame) and rapidity greater than 3.0 (right frame). The solid lines denote exponential fits.

a value of 3.0. In the left frame, the proper lifetime $c\tau = 7.68 \pm 1.22$ cm, obtained from a fit over the range $d/\gamma\beta > 20$ cm, is consistent to the 0.2σ level with the known value. In the right frame, for a fit over the full $d/\gamma\beta$ range, the apparent lifetime is $c\tau = 1.37 \pm 0.05$ cm.

While there is a good agreement between the measured and expected proper lifetimes for the K_s meson in the present analyses, it is clear that this observable is not completely understood for Λ hyperons in the E896 data with $y > 3.0$. This is an issue that will be presented to the Collaboration for wider discussion. One possible cause of this effect would be a physical background process that is not completely suppressed by the present track-quality and TOF-related cuts. If this is the case,

and if one considers the results of subsection 4.1.4, then this implies that the largest backgrounds to the present Λ hyperon measurements occur at the extreme edges of the E896 experimental acceptance in rapidity, which one might expect. The K_s spectra are apparently unaffected by this process.

Chapter 5
Summary and Conclusions

The initial PID scheme in E896 involved cuts to Armenteros variables. However, such a plot cannot conclusively separate Λ hyperons, K_s mesons, and background. This absence of direct PID capabilities in E896 motivated the implementation of a TOF array downstream of the DDC, to intercept charged daughters of neutral strange particle decays and to separate K_s mesons from Λ hyperons using cuts to plots of measured flight time versus daughter track momentum.

Implementation of the TOF system was completed in time for the Au98 run. Three TOF walls were constructed and conditioned to record data. Much repair, recabling, cable connector reinstallation, and cable mapping for about 800 channels was necessary to bring the TOF Central Wall and TOF Side Walls on line. The TOF Side Walls, built by Rice University and positioned to collect pions from Λ hyperon decay, were brought on line during the Au98 run, and used as a Λ hyperon trigger during the p98 run.

During the p98 run, about 24 hours of dedicated TOF calibration data were recorded, in which the beam was stepped horizontally across the entire TOF array and through the DDC as well. A subset of this data, in which single tracks are present in the DDC with the analyzer magnet at full field and at opposite polarities,

was highly useful in developing and optimizing the track extrapolation software.

The Time-Of-Flight hodoscope system and the complementary data analysis software developed by the Rice University effort in E896 possess the following capabilities:

TOF slat hit information, along with the DDC track extrapolation, verified the correct positioning of the TOF array, the DDC, the magnetic fields, and the target with respect to each other. This verification could not have been performed offline without the TOF detector and track extrapolation software together. The track extrapolation software relied solely upon the particle's track in the $\sim$1 m long DDC fiducial volume and the mapped magnetic fields, with TOF providing the only source of additional particle space points downstream of the DDC. Extrapolated DDC tracks were uniquely matched to the appropriate struck TOF slat (among several struck slats in the vicinity of the track) using the TOF TDCs' sensitivity to the y coordinate of the slat hit to compare with the extrapolated track's y coordinate.

Distortions in the TOF system's time measurements due to 60 Hz noise contamination, time-walk effects, and time-dependent drifts in the TDC offsets were corrected using actual Au98 data, without requiring any special calibration runs. The flight times for secondary charged particles produced in E896 can be measured with a resolution of 120 ps.

Neutral strange particles were identified by measuring the flight time of the parent plus charged-daughter particles, and exploiting the flight-time separation of charged

decay daughters of different masses. This is in distinction to the typical use of TOF systems, which is to identify *primary* charged particles. Much work was required to condition the TOF analysis software to perform PID on secondary particles within the E896 apparatus.

This TOF system was used to remove background V_0 candidates from the Λ hyperon sample, and to identify K_s mesons within that mostly Λ hyperon sample. Along with providing a "cleaner" Λ hyperon sample, the TOF analysis provided the first very forward K_s meson spectra not just from this experiment, but from any AGS experiment which studied $\sim$11 GeV/c Au+Au interactions. No similar experiment has published K_s meson transverse mass or rapidity spectra to our knowledge. Thus, the E896 K_s meson sample provides the first opportunity to verify RQMD's prediction for very forward K_s meson production.

By using the DDC+TOF system, the inverse slope parameters and production magnitudes for Λ hyperons and K_s mesons were measured at near-beam rapidities. For Λ hyperons and K_s mesons, these measurements and their dependence upon rapidity were consistent with RQMD v2.4, $b < 4$ fm. The E896 TOF Λ hyperon temperatures were consistent with those reported by similar AGS experiments.

For Λ hyperons, the high-rapidity inverse slope parameters were consistent with an isotropic thermal model. Without including the Λ hyperon data from the SDDA, however, the apparent Λ hyperon center-of-mass temperature determination is some-

what low. However, the high-rapidity temperatures from E896 TOF are consistent with those predicted by extrapolating the E896 SDDA measurements to higher rapidity.

The Λ hyperon and K_s meson production rates and temperatures measured in E896 at high rapidity were compared with the predictions of the RQMD model, operated in "cascade mode." The measured production rates and temperatures are consistent with the predictions from the RQMD model in the acceptance of E896's downstream detectors. This suggests that RQMD's representation of nucleon+nucleon interactions alone in central Au+Au collisions is all that is necessary to reproduce the present experimental results. In the present, very forward, acceptance, the production rates and spectra of Λ hyperons and K_s mesons are insensitive to the physical mechanisms simulated in RQMD beyond the proper superposition of nucleon+nucleon collisions.

References

1. "A Proposal to the BNL AGS: To Search for a Short-Lived H_0 Di-Baryon, Short Lived Strange Matter, and to Investigate Hyperon Production in 11.6 A GeV/c Au+Au Collisions," E896 proposal, Brookhaven National Laboratory AGS Program Advisory Committee, June 1993.

2. Jaffe, R. L., "Perhaps a stable dibaryon," *Phys. Rev. Lett.* **38** (1977) pp. 195-198.

3. Sorge, H., "Flavor production in Pb(160A GeV) on Pb collisions: effect of color ropes and hadronic rescattering," *Phys. Rev. C* **52** (1995) pp. 3291-3314.

4. Sorge, H., H. Stöcker, and W. Greiner, "Poincaré Invariant Hamiltonian Dynamics: Modelling Multi-hadronic Interactions in a Phase Space Approach," *Ann. Phys.* **192** (1989) pp. 266-306.

5. Lacasse, Roger, "Hadron Production in 10.8A GeV/c Au+Au Collisions," Ph.D. Thesis, McGill University (1997).

6. Barrette, J. *et al.*, "Λ production and flow in Au+Au collisions at 11.5A Gev/c," *Phys. Rev. C* **63** (2001) pp. 014902-1 to 014902-8.

7. Llope, W. J. for the E896 Collaboration, "The BNL-AGS Experiment 896," proceedings from the 12th Winter Workshop on Nuclear Dynamics, Snowbird, Utah, *Advances in Nuclear Dynamics 2*, Plenum Press, New York (1996) pp. 19-28.

8. Debbe, Ramiro, Brookhaven National Laboratory, private communication.

9. Mitchell, John W., NASA Goddard Space Flight Center, private communication.

10. Kumar, B. S. *et al.*, "High-rate multiplicity detector for relativistic heavy-ion collisions," *Nucl. Inst. Meth. Phys. Res. A*, **357** (1995) pp. 283-291.

11. Brun, R. *et al*, GEANT *Detector Description and Simulation Tool*, CERN Program Library (1993).

12. Kainz, Kristofer, "Design, Construction, and Commissioning of an Exit Charge Detector for BNL AGS Experiment 896," M.A. Thesis, Rice University (1998).

13. Bellwied, R. *et al.*, "Distributed Drift Chamber Design for Rare Particle Detection in Relativistic Heavy Ion Collisions," to be submitted to *Nucl. Inst. Meth. Phys. Res. A*.

14. Kelly, Sean, "Lambda Production and Polarization in 11.6 A GeV/c Au+Au Collisions at the AGS," Ph.D. Thesis, University of California Los Angeles (2000).

15. Albergo, S. *et al.*, "Position sensitive scintillator discs for intermediate and high energy neutron spectroscopy," *Nucl. Inst. Meth. Phys. Res. A*, **311** (1992) pp. 280-286.

16. Takahashi, J. *et al.*, "Silicon drift detectors as tracking devices," *Nucl. Inst. Meth. Phys. Res. A*, **453** (2000) 131-135.

17. Leo, W. R. *Techniques for Nuclear and Particle Physics Experiments*, Second Revised Edition, Springer-Verlag (1994).

18. Stokely, Christopher, "Design, Construction, and Commissioning of a Time-of-Flight Detector for BNL AGS Experiment 896," M.A. Thesis, Rice University (1998).

19. Lacasse, R. *et al.*, "A time-of-flight hodoscope for the E877 spectrometer," *Nucl. Inst. Meth. A* **408** (1998) pp. 408-424.

20. Sugitake, T. *et al.*, "100 cm long time-of-flight scintillation counters with RMS resolution of 50 ps," *Nucl. Inst. Meth. A* **249** (1986) 354-360.

21. Trentalange, Stephen, University of California Los Angeles, private communication.

22. Llope, W. J. *et al.*, "An electronic clock for correlated noise corrections," *Nucl. Inst. Meth. A* **443** (2000) pp. 451-463.

23. HBOOK Reference Manual, CERN Program Library (1995).

24. `http://www.lecroy.com/lrs/dsheets/1875a.htm`

25. Smith, E. S. *et al.*, "The time-of-flight system for CLAS," *Nucl. Inst. Meth. A* **432** (1999) pp. 265-298.

26. Miake, Yasuo, "Time of Flight Techniques in High Energy Heavy Ion Experiments," from the AIP Conference Proceedings *Strangeness in Hadronic Matter* **340**, J. Rafelski ed., AIP Press (1995) pp. 78-89.

27. Chung, P. *et al.*, "Neutral strange particle production and flow at AGS energies," *J. Phys. G: Nucl. Part. Phys.* **25** (1999) pp. 255-261.

28. Rafelski, J. and B. Müller, "Strangeness production in the quark-gluon plasma," *Phys. Rev. Lett* **48** (1982) pp. 1066-1069.

29. Stachel, J. and G. R. Young, "Relativistic heavy ion physics at CERN and BNL," *Annu. Rev. Nucl. Part. Sci.* **42** (1992) pp. 537-597.

30. Sheen, Jeffrey M., "Lambda and Anti-lambda Production in Relativistic Heavy Ion Collisions of Au+Au at 11.6A GeV/c," Ph.D. Thesis, Wayne State University (2001).

31. Dobler, H., J. Sollfrank and U. Heinz, "Kinetic freeze-out and radial flow in 11.6 *A* GeV Au+Au collisions," *Phys. Lett. B* **457** (1999) pp. 353-358.

32. Van Hecke, H., H. Sorge, and N. Xu, "Evidence of early multistrange freeze-out in high energy nuclear collisions," *Phys. Rev. Lett.* **81** (1998) pp. 5764-5767.

33. Bearden, I. G. *et al.*, "Collective expansion in high energy heavy ion collisions," *Phys. Rev. Lett.* **78** (1997) pp. 2080-2083.

34. Lo Curto, Gaspare, "Strange Particle Production in 11.6 GeV per Nucleon Au Au Collisions," Ph.D. Thesis, The Ohio State University (1999).

35. Albergo, S. *et al.*, "Λ spectra in 11.6 A GeV/c Au-Au collisions," submitted to *Phys. Rev. Lett.* (2001).

36. Chung, P. *et al.*, "Directed flow of Λ-hyperons in 2 - 6 AGeV Au + Au collisions," *Phys. Rev. Lett.* **86** (2001) pp. 2533-2536.

37. Braun-Munzinger, P., J. Stachel, J. P. Wessels, and N. Xu, "Thermal equilibration and expansion in nucleus-nucleus collisions at the AGS," *Phys. Lett. B* **344** (1995) pp. 43-48.

38. Ahmad, S. *et al.*, "Λ production by 11.6 GeV/c Au beam on Au target," *Phys. Lett. B* **382** (1996) pp. 35-39.

39. Ahle, L. *et al.*, "Kaon production in Au+Au collisions at 11.6*A* GeV/*c*," *Phys. Rev. C* **58** (1998) pp. 3523-3538.

40. Wessels, J. P. *et al.*, "Particle Production and Hydrodynamic Flow: Recent Results from E877 for Au+Au Collisions at AGS Energy," *Nucl. Phys. A* **638** (1998) pp. 69c-80c.

41. Barnett, R. M. *et al.*, "Review of Particle Properties," *Phys. Rev. D* **54** (1996) p. 1.